MICROTEXTURAL, ELASTIC AND TRANSPORT PROPERTIES OF SOURCE ROCKS

A DISSERTATION

SUBMITTED TO THE DEPARTMENT OF GEOPHYSICS

AND THE COMMITTEE ON GRADUATE STUDIES

OF STANFORD UNIVERSITY

IN PARTIAL FULFILLMENT OF THE REQUIREMENTS

FOR THE DEGREE

OF DOCTOR OF PHILOSOPHY

SRB VOLUME 127

Ramil Surhay oglu Ahmadov

JUNE 2011

I certify that I have read this dissertation and that, in my opinion, it is fully adequate in scope and quality as a dissertation for the degree of Doctor of Philosophy.

_____

Gary Mavko (Principal Adviser)

I certify that I have read this dissertation and that, in my opinion, it is fully adequate in scope and quality as a dissertation for the degree of Doctor of Philosophy.

_____

Mark Zoback

I certify that I have read this dissertation and that, in my opinion, it is fully adequate in scope and quality as a dissertation for the degree of Doctor of Philosophy.

_____

Tapan Mukerji

Approved for the University Committee on Graduate Studies

Abstract

"Science progresses best when observations force us to alter our preconceptions"

--Vera Rubin

This dissertation addresses recurrent questions in hydrocarbon reservoir characterization. In particular, the major focus of this research volume is microtextural characterization of source rock fabric as well as elastic and transport properties of source rocks. Source rocks are one of the most complicated and intriguing natural materials on earth. Their multiphase composition is continually evolving over various scales of length and time, creating the most heterogeneous class of rocks in existence. The heterogeneities are present from the submicroscopic scale to the macroscopic scale, and all contribute to a pronounced anisotropy and large variety of shale macroscopic behavior. Moreover, the effects of the multiphase composition are amplified within organic-rich rocks that contain varying amounts of kerogen. Despite significant research into the properties of kerogen,

fundamental questions remain regarding how the intrinsic rock-physics properties of the organic fraction affect the macroscopic properties of host rocks.

Because we do not fully understand the elastic properties of either the organic matter or the individual clay minerals present in source rocks, seismic velocity prediction in organic-rich shales remains challenging. Conventional measurements of 'macroscopic' or 'average' properties on core plugs are not sufficient to fully address the degree of property variation within organic-rich rocks. Alternatively, most analyses of organic matter rely on samples that have been isolated by dissolving the rock matrix. The properties of the organic matter before and after such isolation may be different, and all information about sample orientation is lost. In addition, comprehensive characterization of organic-rich rocks has been hindered by several factors: sample preparation is time-consuming, and the nanogranular nature of this rock type makes it difficult to link effective elastic properties to maceral properties, such as elastic moduli, composition, maturity, and quality. These difficulties have prevented us from building large databases, without which we cannot establish the accurate rock-physics models needed for inverting field geophysical data. I approach this issue using atomic-force microscopy based nanoindentation, coupled with scanning electron and confocal laser-scanning microscopy as a tool for visualization and identification of the organic part within shale, and to perform nanoscale elastic-property measurements. First, the microfabric of a set of source rock samples is characterized. The spatial and temporal link between organic matter and the *stiff* silicate mineral matrix is established, which leads to proposal of alternative Rock Physics modeling approach to organic-rich source rocks. Based on the nanoindentation measurements, I obtain elastic properties of source rock *phases* and provide several applications of these (nanoindentation-derived) elastic properties within a number of geomechanical problems. Finally, transport properties of various source rock formations are discussed based on comparison to *more* conventional reservoir rocks.

Acknowledgments

I would like to thank all the friends, professors, and students that made my stay at Stanford a most unique and enjoyable experience.

First, I want to express my gratitude to my advisers. My principal adviser Gary Mavko had a particularly large impact on high level of science that I have learned while at Stanford and was a guiding force for completion of this work; he is the one that made me feel that the door to Rock Physics was open when I was applying to Geophysics Department. Without his guidance, constructive criticism, and encouragement, this dissertation was not possible. Second, I thank Jack Dvorkin for all the help I received from our interaction. Throughout my time here, the questions Jack asked helped me to set the specific goals laid out in this dissertation. Next is Tapan Mukerji. If I was looking for an answer, Tapan was the one person I knew who could answer it and explain it to me. Thanks to Mike Moldowan; through his courses and laboratory experiments I have discovered a new world of organic geochemistry and realized how powerful the methods used there could be. Mark Zoback, with his clear sense of practicality, provided many enjoyable conversations that kept me from deviating from my main route. Steve Graham always provided that bit of rationale on the geologic side and kept me thinking about applications on larger scale. Thank you, Gary, Jack, Tapan, Steve, Mike and Mark for the outstanding help and friendship. It was an honor and privilege to have you all as advisers.

I am grateful to the following faculty, students and research staff who guided and assisted me in various parts of my research and provided constructive discussion: Lev Vernik, Tiziana Vanorio, Atilla Aydin, William Nix, Kitty Lee, Lydia-Marie Joubert, Seok-Woo Lee, Ronny Hofmann, Ezequiel González and Maria Spletter.

A great deal of thanks goes to the SRB program and all its sponsors for the funding and support during my time here. Generous financial support for this research was provided by GCEP Grant " Linking Chemical and Physical Effects of CO2 injection to Geophysical Parameters ", US Department of Energy, Office of Basic Energy Sciences Grants "Porous Rock With Fluid: Impact of Heterogeneity on Reservoir Transport and Elastic Properties and Application to Unconventional Probe-Filling materials " and "Porous Rock With Fluid: Impact of Heterogeneity on Reservoir Transport and Elastic Properties and Application to Unconventional Probe-Filling materials", American Association of Petroleum Geologists Harold J. Funkhouser Memorial Grant "Application of Confocal Laser Scanning and Atomic-Force Microscopy in Elastic Properties Estimation of Organic-Rich Rocks" and Geological Society of America Grant " Quantifying the Links between Rock Physics and Geochemical Properties of Oil Shales". Without this generous support, the time here would not have been possible.

I would like to thank Geophysics and Geology Department administrative staff. I express thanks to Fuad Nijim for his amazing ability to help with every situation that presented itself. Thanks to Tara Ilich, Elaine Andersen, Arlene Abucay and Felicia Morales for making sure all the forms were completed ahead of every turn in the road.

Thank you to all my officemates over my time at Rock Physics Laboratory: Kevin Wolf, Kyle Spikes, Carmen Gomez and Kenichi Akama. All were always willing to lend a hand and tolerate both good and bad behavior.

I feel really proud to have been a member of the Rock Physics Laboratory at Stanford and had the opportunity to work with so many talented people, many of whom have become friends over the years. Thanks to my fellow graduate students: Kevin, Kyle, Kaushik, Ratna, Richa, Tanima, Carmen, Franklin, Cinzia, Indrajit, Madhur, Piyapa, Danica, Fabian, Stephanie, Kenichi, Nishank, Adam, Amrita, Dario, Yu and Xi

for providing a friendly, open and stimulating working environment, *Gens una sumus*. In particular, I thank Kaushik and Indrajit for providing ideas and support, for research and other matters. I also would like to thank my friend Elnur Aliyev from Energy Resources Engineering Department for numerous coffee breaks and chance to practice Azeri language while on campus. You all taught me more than you know, so I wish the best of luck to everyone.

Last but certainly not least, I thank my family in Azerbaijan, US, and Turkey. Without them, I would not have accomplished this goal. One person who helped me get this far and has been my lodestar is my Grandfather – Mahmoud Akhundov who dedicated 60 years of his life to oil and gas exploration. Years ago he introduced me to the world of Earth Sciences. He is the one in family I could speak the *Geo-language* with and the person who throughout my studies always supported me. Thanks, *Baba*. I owe you a great deal of appreciation these words cannot fully describe.

I dedicate this dissertation with all my heart and soul to my family. Thank you.

RA, June 20th, 2011

List of contents

List of Tables

List of Figures

Chapter 1

Introduction

"Before I came here I was confused about this subject. Having listened to your lecture I am still confused. But on a higher level."

---Enrico Fermi

1.1 Motivation and objectives

Shales are one of the most complex, and hence challenging to characterize and to model, sediments on earth. Their multiphase composition is continually evolving due to diagenesis over various scales of length and time, resulting in the most heterogeneous class of rocks in existence. The heterogeneities are present from the submicroscopic scale to the macroscopic scale, and all contribute to a pronounced anisotropy and large variety

of shale macroscopic behavior (Ulm and Abousleiman, 2006). Moreover, the effects of the multiphase composition are amplified within organic-rich shales (source rocks or potential source rocks) that contain varying amounts of kerogen dispersed within inorganic matrix. Migration of hydrocarbons during the natural petroleum generation process is instrumental for the formation of gas and oil accumulations. The first step in this process, the primary migration within the source rock in which the hydrocarbons are generated, is facilitated by the chemical decomposition of the organic matter in the rock and a consequent microstructural evolution of the inorganic rock matrix. The chemical changes resulting from the thermal maturation of the organic matter in source rocks have been long studied and the processes involved are relatively well understood (Tissot and Welte, 1978). By contrast, the microstructural evolution ~i.e., microscopic changes in geometry and topology of the inorganic and organic components of the rocks upon maturation remained unknown, although much speculated about (Mann, 1994; Radlinski et al., 1996). Despite significant research into the properties of kerogen, fundamental questions remain regarding how the intrinsic rock-physics properties of the organic fraction affect the macroscopic properties of host shales (Ahmadov et al, 2009a).

In this dissertation we improve our understanding of all aforementioned issues by addressing the following questions:

(a) One of the most challenging questions is how do mineral matrix and organic fraction of shale evolve over the course of diagenesis and maturation, respectively?

(b) Furthermore, what is the spatial and temporal link between deposited mineral framework and authigenic fractions formed during the processes of diagenesis and maturation?

(c) Also, is there any difference in spatial distribution of kerogen at early and late stages of maturation that may affect the way organic-rich rocks are modeled?

(d) And finally, what is the influence of all aforementioned variations on Rock Physics properties such as porosity, permeability, elastic properties.

1.2 Chapter Descriptions

This dissertation broadly covers the following topics: source rock microfabric characterization and implications for Rock Physics modeling approaches (Chapter 2 and Chapter 3), elastic properties of source rocks (Chapter 4), application of elastic properties of source rocks in geomechanical problems (Chapter 5) and transport properties of source rocks (Appendix A).

In Chapter 2 a suite of six source rock samples from Kimmeridge, Bakken, Bazhenov, Monterey and Lockatong Formations is analyzed using Confocal Laser Scanning- (CLSM) and Scanning Electron Microscopy (SEM). The combined application of SEM and CLSM imaging provides the microscopic basis for analysis of these microscopically complex and heterogeneous rock samples. Organic matter is successfully imaged within the matrix of the source rock samples despite inherent lithologic differences of the phases. A number of valuable observations of spatial distribution of clay, pyrite and kerogen are made. In addition to these observations, we report deformation of clay minerals, quartz grains and presence of pressure solution surfaces in some samples, all attributed to the diagenetic processes within source rocks. The fractional volumes of minerals and kerogen obtained from image analysis of SEM and CLSM photomicrographs is in good agreement with values previously reported by Vernik and Landis (1996). The observations and methodology described in this section create a framework for evaluation of spatial distribution of kerogen discussed in detail in Chapter 3 and elastic property estimation at microscale discussed in detail in Chapter 4. Part of this work was presented at the 29th Oil Shale Symposium (Ahmadov et al., 2009b).

In *Chapter 3* the microtexture of three shale samples at mature and postmature hydrocarbon generation stages - two from the Bakken Formation and one from the Kimmeridge Formations documented. The simple principle of contrasting microfabric observations against each other is used. To gain an insight into shale's intrinsic structure, SEM and CLSM based images and subsequent 3D volume reconstruction based on CLSM images is employed. Based on the microstructural observations we establish

spatial and temporal links between organic matter and corresponding maturity stages. We then compute Hashin-Shtrikman as well as Voigt-Reuss-Hill bounds for a mixture of silicate mineral matrix and organic matter in order to explain the microtextural observations within two Bakken Formation source rocks and compare them to larger set of Bakken Formation samples (Vernik and Landis, 1996; Bandyopadhyay, 2009) forming a natural maturity sequence for hydrocarbon generation. Furthermore, following these observations, we explain anisotropy variation within two Bakken Formation source rocks. Part of this chapter was presented at combined SEG/SPE/AAPG Workshop on shales (Ahmadov and Dvorkin, 2010).

Chapter 4 discusses a combined application of SEM, CLSM imaging and nanoindentation characterization, which provides the microscopic basis to analyze these macroscopically complex and heterogeneous rock samples. Organic matter is successfully imaged within the matrix of the Bazhenov and Lockatong Formations samples despite inherent lithologic differences of the phases. The experimental system proved capable of determining the physical properties of the organic matter without requiring extraction from the matrix. Nanoindentation measurements showed organic matter within both samples to be softer than the surrounding mineral matrix. In particular, the indentation modulus of organic matter from the Bazhenov Formation varies between 6 and 11 GPa, whereas for the Lockatong Formation sample it is about 12 GP. Moreover, values of Indentation modulus of organic matter, as well as elastic properties of stiffer minerals as dolomite, quartz and pyrite are in very good agreement with previously published data. Sensitivity analysis of Young's modulus to varying Poisson's ratios of organic matter shows minor dependence throughout the range of Poisson's ratios (ν=0.05-0.45). Part of this work was published in *The Leading Edge* (Ahmadov et al., 2009c).

In *Chapter 5*, based on the measured properties of organic matter, quartz, dolomite and pyrite, we derive P-wave, S-wave and Lamb-wave velocities by estimating Young's modulus and assuming appropriate Poisson's ratio. The computed velocity values are in excellent agreement with data previously published by Mavko et al (2009).

The largest computed difference in velocity values is that of pyrite and does not exceed 10%.

The closure stresses of two- and three-dimensional cracks with a wide range of aspect ratios are computed in all phases. The relative difference of stress values for a given aspect ratio within *softest* (kerogen) and *stiffest* (pyrite) phases is in excess of an order of magnitude. The analysis of tensile rock failure conducted herein provides a scheme for computation of stress intensity factors of analyzed fractures. Furthermore, we consider flow through a Mode I fracture based on a parallel plate approximation for fluid flow through a planar fracture and compute maximum aperture of a crack under given stress in all phases. The computed fracture aperture values are in good agreement with previously reported values of Zoback (2007). Alternatively, we derived a thermodynamic criterion of crack propagation due to an applied load according to Griffith (1920, 1924). This allows computation of the tensile stress of a crack as a function of the surface energy per unit area for pyrite, dolomite, quartz and organic matter in three different scenarios: *general case*, *plane strain* and *3-D penny-shaped* cracks. Our findings suggest that in the case of 3-D penny-shaped cracks, higher tensile stresses are require in all phases compared to other scenarios. Next, conditions for microhydraulic fracturing within organic layers according to Vernik (1994) were analyzed. Throughout these computation*s* we show a relative difference in the maximum aperture of the crack as a function of bounding medium. The results are in very good agreement with values previously reported by Vernik (1994) and corroborate the suggestion that the bedding-parallel microcracks originate and propagate within the weakest constituent of the rock matrix-organic matter assemblage or along interfaces with other mineral phases.

In *Appendix A*, we compile published permeability data in shale and contrast these data to classical datasets, including Fontainebleau sandstone, North Sea, and tight gas sandstone laboratory measurements. As expected, shale permeability is much smaller than that in sands and sandstones. Moreover, the fluid transport mechanisms in shale are likely to be different from those in conventional reservoir rocks. The main reason is the very small size of pores in shale, so small that it is often commeasurable with the size of

a gas molecule. The main goal of this compilation is to serve as a reference guide for assessing permeability in new plays as well as a quality-control tool for new physical and computational data.

1.3 References

Ahmadov R., and Dvorkin J, 2010, "Looking inside organic-rich shales", SEG/SPE/AAPG Workshop on shales: Seal, reservoir, source, Austin, Texas, USA, June 6-9, 2010

Ahmadov R., Dvorkin J, Mavko G., 2009a, "Method of the determination of elastic coefficients of combustible shales" proceedings of 3rd International Scientific Conference of Young Scientists and Students "New Directions of Investigations in Earth Sciences", Baku, Azerbaijan, October 5-6, 2009

Ahmadov R., Dvorkin J, Mavko G., 2009b, "Elastic properties of source rocks" proceedings of 29th Oil Shale Symposium, Golden, Colorado, USA, October 18-23, 2009.

Ahmadov, R., Vanorio, T., and Mavko, G., 2009c, Confocal laser scanning and atomic-force microscopy in estimation of elastic properties of the organic-rich Bazhenov Formation, The Leading Edge, 28, 19.

Bandyopadhyay K., 2009, Seismic Anisotropy: Geological Causes and Its Implications to Reservoir Geophysics, Stanford University, Ph.D. Thesis, p.254

Griffith,A. A., 1920, The phenomena of flow and rupture in solids, Phil. Trans. Roy. Soc. Lond. Ser. A,221,163–198.

Griffith,A. A., 1924, Theory of rupture,in Proc. 1st Int. Cong. Appl. Mech.,C . B. Biezano and J. M. Burgers,eds .,J .Waltman Jr,Delft, pp. 53–63.

Mavko, G., T. Mukerji, and J. Dvorkin, 2009, The Rock Physics Handbook: Cambridge University Press.

Mann U., 1994, Origin, Migration and Evolution of Fluids in Sedimentary Basins, in Geofluids: edited by J. Parnell, Geological Society Special Publication No. 78 ~Geological Society, London, pp. 233–260.

Radlinski, A.P., Boreham, C.J., Wignall, G.D. and Lin, J.-S., 1996, Microstructural evolution of source rocks during hydrocarbon generation: a small-angle-scattering study. Physical Review B53, pp. 14152–14160

Tissot, B.P., Welte, D.H., 1978, Petroleum Formation and Occurrence. Berlin-Heidelberg-New York: Springer, p. 699.

Ulm, F. J. and Abousleiman, Y, 2006, The nanogranular nature of shale, Acta Geotechnica, 1, 77-88

Vernik L., 1994, Hydrocarbon-generation-induced microcracking of source rocks, Geophysics, v. 59, n. 4, p. 555-563.

Vernik, L., and Landis, C., 1996, Elastic Anisotropy of Source Rocks: Implications for Hydrocarbon Generation and Primary Migration: AAPG Bulletin, 80, 531-544.

Zoback, M. D., 2007, Reservoir Geomechanics, Cambridge University Press, The Edinburgh Building, Cambridge CB2 8RU, UK, Published in the United States of America by Cambridge University Press, New York, 464 pp.

Chapter 2

Samples and Their Characterization by SEM and CLSM

"Possibly many may think that the deposition and consolidation of fine-grained mud must be a very simple matter, and the results of little interest. However, when carefully studied experimentally it is soon found to be so complex a question, and the results dependent on so many variable conditions, that one might feel inclined to abandon the inquiry, were it not that so much of the history of our rocks appears to be written in this language."

--Henry Clifton Sorby, 1908

2.1. Abstract

A suite of six source rock samples from Kimmeridge, Bakken, Bazhenov, Monterey and Lockatong Formations is analyzed using Confocal Laser Scanning- and Scanning Electron Microscopy. The combined application of SEM and CLSM imaging provides the microscopic basis for analysis of these microscopically complex and heterogeneous rock samples. Organic matter was successfully imaged within the matrix of the source

rock samples despite inherent lithologic differences of the phases. A number of valuable observations of spatial distribution of clay, pyrite and kerogen was made. In addition to these observations, we report deformation of clay minerals, quartz grains and presence of pressure solution surfaces in some samples, all attributed to the diagenetic processes within source rocks. The fractional volumes of minerals and kerogen obtained from image analysis of SEM and CLSM photomicrographs is in good agreement with values previously reported by Vernik and Landis (1996). The observations and methodology described in this section create a framework for evaluation of spatial distribution of kerogen discussed in detail in Chapter 3 and elastic property estimation at microscale discussed in detail in Chapter 4.

2.2. Introduction

A large fraction of sedimentrary rocks are the fine grained rocks composing about 60-70% of sedimentary basins (Broichhausen et al., 2005). These clay-rich rocks as well as some dolomites and porcelanites are important, as they form source rocks, seals and sometimes unconventional reservoirs. Due to low matrix permeability, these rocks play an important role in controlling fluid flow (Sayers, 2005). Source rocks are often elastically anisotropic, as observed in the field (Banik, 1984; Alkhalifah and Rampton, 2001) and laboratory measurements (Jones and Wang, 1981 Vernik and Nur, 1992a,b; Hornby et al., 1994; Johnston and Christensen, 1995; Wang, 2002). The geological processes that result in microscopic and macroscopic structures in source rocks affect their elastic properties both isotropic and anisotropic. Despite being volumetrically significant part of most clastic sedimentary basins, the elastic properties and microstructure of source rocks are known to a lesser degree compared to siliciclastic rocks formed by inorganic processes, or deposited through some mechanical process. Not surprisingly, even less knowledge is available about the rock physics links between the seismic measurements and the microstructural properties for these rocks. With the increasing importance of unconventional resources (e.g., shale gas, oil shale) there has

been increasing effort on understanding the rock properties for these fine grained rocks (Bandyopadhyay, 2009).

Most of the source rocks (due to the small grain size) pose difficulty in visualization and quantification of their microstructures. Shales and mudstones, unlike sandstones, usually contain a larger variety of minerals and higher amount of organics. These minerals are often chemically reactive with pore fluids as well as due to the overburden (at elevated pressures and temperatures) and form a complex rock microstructure. Therefore, the heterogeneity of source rocks requires investigation at multiple scales in order to characterize their microfabric. In contrast to common sedimentary rock-forming minerals (quartz, feldspar, etc.), the elastic properties and microfabric of clays and spatial distribution of organic matter in source rocks are not well known.

Over the past two decades, studies of the microfabric of clay minerals in shales have been an intensive area of research for geologists and mineralogists (e.g., Bennett, 1976; Bryant et al., 1981; O`Brien, 1981; Bennett et al., 1981; Katsube and Williamson, 1994; Kim et al., 1999). Bennett et al. (1977) proposed a fabric model for smectite-rich and illite-rich clay sediments with varying void ratios (ratios of the pore volume to the volume of solids). In contrast to illite-rich clays, smectite-rich clays have wavy structures, many dislocations (layer terminations), and disoriented fabrics. Katsube et al. (1991) showed decreased effective porosity with depth of clay-rich sediments, caused by compaction. O`Brien (1986), on the other hand, emphasized the biological factors that disturb some original clay fabrics, causing an increase of permeability. Davies et al. (1991) observed three different types of fabric in shale: (1) chaotic fabric caused by intense burrowing activity with random orientation of the platelets of illite/muscovite components; (2) subparallel fabric distinguished by the combination of chaotic and subparallel grain alignment and an absence of burrows; and (3) well-defined parallel fabric formed by oriented platelets of illite-muscovite.

The characterization of microfabric of source rocks and its effect on elastic properties becomes even more complex when considerable amounts of organic matter are

present. Organism-derived organic matter generates the bulk of the petroleum hydrocarbons by thermocatalytic degradation and occurs finely disseminated in source rocks (Philippi, 1965; Hunt, 1968; Tissot et al., 1971; Tissot and Welte, 1978; Hunt, 1979). Source rocks are usually fine-grained sediments, shales and siltstones which are often calcareous, as well as argillaceous limestones rich in organic matter. The bulk of the finely disseminated organic matter is insoluble and is called kerogen. It has to be of a certain chemical structure and nature to make a good source for hydrocarbons. The term kerogen refers collectively to the solid organic matter which is of a highly polymerized nature and hence insoluble in low-boiling organic solvents.

The study of spatial and temporal distributions of kerogen within host rock microfabric is essential for source rock characterization. Kerogen can be characterized by chemical and microscopical techniques. Many chemical techniques require separation of the kerogen from the inorganic matrix of a rock, i.e. exhaustive treatment of a sample with hydrochloric and hydrofluoric acid to destroy the minerals. Based on elemental analysis the atomic H/C and O/C ratios characterize the basic nature of kerogens occurring in sediments.

In this chapter, we will focus on two powerful non-destructive techniques for microfabric characterization - Confocal Laser Scanning Microscopy and Scanning Electron Microscopy.

2.3. Principles of Confocal Laser Scanning Microscopy

There has been a tremendous explosion in the popularity of confocal microscopy in recent years, in part because of the relative ease with which extremely high-quality images can be obtained from specimens prepared for conventional optical microscopy. Confocal Laser Scanning Microscopy (CLSM) was conceptualized in 1953 and was later used for biological research, chemical analysis, and material testing. CLSM has seen a wide variety of applications, but only very recently has it been applied to studying the morphology of macerals within coals (Teerman et al. 1987), source rocks (Ahmadov et al., 2009) and oil shales (Stasiuk et al. 1999, Vanorio et al., 2008), to thermal-maturity

determination (Wilkins et al. 1995), and to characterization of algae fossils (Chi et al. 2006).

The confocal principle in fluorescence laser-scanning microscopy is schematically presented in Figure 2.1. Coherent light emitted by the laser system (excitation source) travels through a pinhole aperture that is positioned in a conjugate plane (confocal) with a scanning point on the specimen and a second pinhole aperture situated in front of the detector (a photomultiplier tube). As the laser is reflected by a dichromatic mirror and scanned across the specimen in a defined focal plane, secondary fluorescence emitted from points on the specimen (in the same focal plane) pass back through the dichromatic mirror and are focused as a confocal point at the detector pinhole aperture.

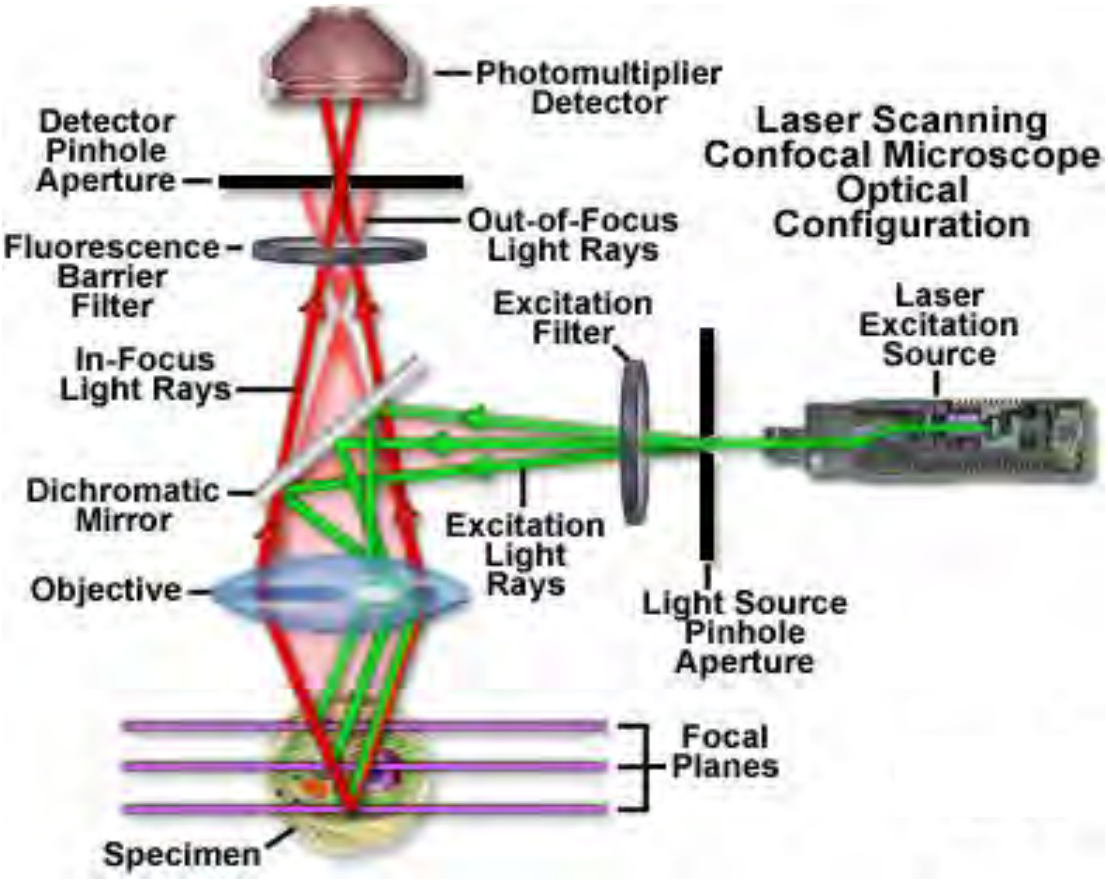

Figure 2.1: Schematic representation of the confocal principle in fluorescence laser-scanning microscopy. Courtesy Fellers and Davidson.

The significant amount of fluorescence emission that occurs at points above and below the objective focal plane is not confocal with the pinhole (termed Out-of-Focus Light Rays in Figure 2.1) and forms extended Airy disks in the aperture plane. Since only a small fraction of the out-of-focus fluorescence emission passes through the pinhole aperture, most of this extraneous light is undetected by the photomultiplier, providing very sharp resulting images.

We have used the Stanford Cell Sciences Imaging Facility to collect and analyze confocal images via *Leica SP2 AOBS* Confocal Laser Scanning Microscope. The *SP2 AOBS* utilizes state of the art Acousto-Optical Beam Splitters (AOBS) in place of traditional glass di- or multichroics allowing user selection of reflecting excitation and transmitting emission wavelengths. The microscope is equipped with a prism spectrometer detector which allows for spectral scanning of emission profiles as well as selection of emission detection bandwidth. For image post-processing we employed *Java* platform-based public domain open source image processing software *ImageJ* , as well as *Volocity-4D* imaging, rendering and de-convolution software in order to construct and visualize 3-D rock cubes.

2.4. General Principles of Electron Microscopy

There is a limit to the resolution that one can obtain in microscopes that operate with visible light. The resolution increases with increasing frequency of the light beam, and electron microscopes use a beam of electrons to examine specimens on a much smaller scale than a light or optical microscope. The interaction of the electron beam with the specimen gives information concerning its morphology, topography, crystallographic arrangement and elemental composition (Egerton, 2005).

The electron microscope consists of an electron source, an anode, magnetic lenses, apertures, specimen stage and image recording system all of which operate in a high vacuum (Figure 2.2). The electron source can be made of various types of materials. The most common is the tungsten filament which, when heated, produces electrons which are attracted by the anode and are accelerated down the column and interact with the

specimen. The electrons are focused using magnetic lenses in the column and the apertures filter out scattered electrons so the resulting beam is monochromatic. This monochromatic beam is focused and interacts with the specimen in different ways, depending on the type of electron microscope. As the primary electron beam is scanned across the surface, electrons of a wide range of energies will be emitted from the surface in the region where the beam is incident. These electrons will include backscattered primary electrons and Auger electrons, but the vast majority will be *secondary electrons* formed in multiple inelastic scattering processes. The secondary electron current reaching the detector is recorded and the microscope image consists of a "plot" of this current, against probe position on the surface. The contrast in the photomicrograph arises from several mechanisms, but first and foremost from variations in the surface topography. Consequently, the secondary electron micrograph is virtually a direct image of the real surface structure (Reimer, 1998).

Two types of electron microscopes are normally available, the *Scanning Electron Microscope (SEM),* and the *Transmission Electron Microscope (TEM)*. Our microtextural characterization of source rock samples is based on SEM, therefore basic principles of this type of electron microscope are discussed below.

2.4.1. **Principles of Scanning Electron Microscopy**

In the SEM, a set of scan coils moves the electron beam across the specimen in a two-dimensional grid fashion. When the electron beam scans across the specimens, different interactions take place. These interactions are decoded with various detectors situated in the chamber above the specimen. Some electrons from the surface material are knocked out of their orbitals by the electron beam, and are called Secondary Electrons. These electrons are detected by the secondary electron detector. Different interactions give images based on topography, elemental composition or density of the sample. A SEM can magnify up to about ×100,000.

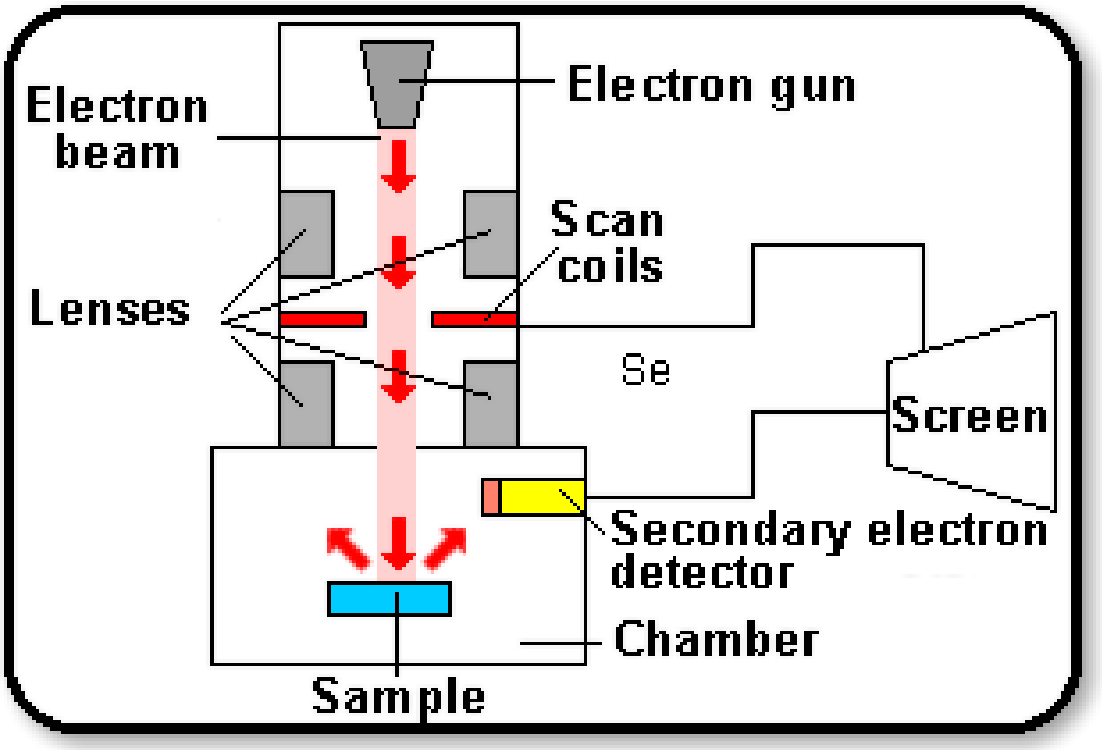

Figure 2.2: Schematic representation of the electron microscopy.

The high performance Hitachi S-3400N scanning electron microscope operated in both *SE* and *BSE* modes was employed to obtain source rock photomicrographs of various sizes ranging from few microns up to a cm. Hitachi S-3400N SEM has unique variable-pressure-mode (as well as high vacuum mode) that allows microscopy of wet, oily and non-conductive samples in their natural state without the need of conventional sample preparation. High vacuum mode guarantees 3 nm resolution, whereas resolution drops to 4.0 nm in variable-pressure-mode.

2.4.2. **BSE and SE modes of Scanning Electron Microscopy**

Accelerated electrons in an SEM carry significant amounts of kinetic energy, and this energy is dissipated as a variety of signals produced by electron-sample interactions when the incident electrons are decelerated in the solid sample. These signals include *secondary electrons* (SE), *backscattered electrons* (BSE), *diffracted backscattered electrons* (EBSD that are used to determine crystal structures and orientations of

minerals), *photons* (characteristic X-rays that are used for elemental analysis and continuum X-rays), *visible light* (cathodoluminescence - CL), and *heat* (Goldstein, 2003). Secondary electrons and backscattered electrons are commonly used for imaging samples: secondary electrons are most valuable for showing morphology and topography on samples and backscattered electrons are most valuable for illustrating contrasts in composition in multiphase samples (since resulting color in an image is directly proportional to the atomic number of the sample).

2.5. Microtextural Characterization of Source Rock Samples

Source rock samples were selected from source rock core collection previously analyzed by Vernik and Landis (1996). All characterization of microfabric is performed on six (6) source rock samples from Kimmeridge (Sample NS), Bakken (Sample M and F), Bazhenov (Sample E), Monterey (Sample D) and Lockatong (Sample H) Formations. In preparation for imaging, the samples were dry-cut (without water in order to eliminate any possible physical and chemical reactions between water, clays and kerogen) perpendicular to the bedding to better expose their heterogeneity and then polished to reduce the surface roughness down to 1 to 2 μm.

The summary of properties from this study and from Vernik and Landis (1996) is provided in Tables 2.1-2.6. Vernik and Landis (1996) combined acoustic velocities and anisotropy measurements with x-ray diffraction mineralogy, Rock-Eval organic geochemical analyses, vitrinite reflectance, and scanning electron microscope observations on 69 cores of hydrocarbon source rocks collected from eight sedimentary basins. Rock-Eval pyrolisis evaluates the type and the maturity of the organic matter as well as determining its petroleum potential. Rock-Eval reveals the amount of generated oil and gas in the source rock sample, the amount of oil and gas generated through thermal breakdown of organic matter by heating, the amount of CO_2 released during pyrolysis, and the temperature of maximum release of hydrocarbons.

Total organic carbon (TOC) was measured using Rock-Eval pyrolysis and reported in weight fraction. This value along with kerogen and mineral densities was then

used to compute volume of organic matter for analyzed lithologies. The hydrocarbon potential of a source rock sample is expressed by the hydrogen index (HI), which is the ratio of the amount of convertible hydrocarbon to the organic richness of the rock (Tissot and Welte, 1978). The study of vitrinite reflectance is a key method for identifying the temperature history of sediments in sedimentary basins. The reflectance of vitrinite was first studied by coal explorationists attempting to diagnose the thermal maturity, or *rank*, of coal beds. More recently, its utility as a tool for the study of sedimentary organic matter metamorphism from kerogens to hydrocarbons has been increasingly exploited. The key attraction of vitrinite reflectance in this context is its sensitivity to temperature ranges that largely correspond to those of hydrocarbon generation (i.e. 60 to 120°C). This means that, with a suitable calibration, vitrinite reflectance can be used as an indicator of maturity in hydrocarbon source rocks. Generally, the onset of oil generation is correlated with a reflectance of 0.5-0.6% and the termination of oil generation with reflectance of 0.85-1.1%.

SEM photomicrographs (grey-scale intensity) were collected in both *BSE* and *SE* modes. CLSM images were collected in 3-4 main light excitation wavelengths corresponding to red, green, blue and magenta light. The original intensity (grey-scale) CLSM images were then assigned an ‗artificial' color corresponding to the excitation wavelengths under which images were captured. Fractional areas of minerals and kerogen were obtained from image analysis of SEM and CLSM photomicrographs. Fractional volumes of minerals and kerogen were obtained from 3-D cubes reconstructed from sequences of CLSM images.

2.5.1. **Kimmeridge Formation - Sample NS**

Table 2.1: Petrophysical and image analysis properties of Kimmeridge Formation (sample NS) obtained in this study and from Vernik and Landis (1996).

Lithology	Shale	Source
Depth	4449 m	Vernik and Landis (1996)
Density	2.54 g/cc	Vernik and Landis (1996)
Total Organic Carbon (TOC, % weight)	5.02%	Vernik and Landis (1996)
Vitrinite Reflectance (R_o, %)	1.25	Vernik and Landis (1996)
Hydrogen Index (HI)	67mg/g	Vernik and Landis (1996)
Porosity (helium porosimetry)	1.2%	Vernik and Landis (1996)
P-Wave Velocity --$V_p(0^\circ)$	3.86 km/s	Vernik and Landis (1996)
S-Wave Velocity --$V_s(0^\circ)$	2.22 km/s	Vernik and Landis (1996)
Kerogen Volume	13.5%	Vernik and Landis (1996)
Kaolinite Volume (XRD of 5 samples)	40.0%	Vernik and Landis (1996)
Kerogen Volume (543nm exc. wavelength)	13.4%	(this study)
Volume of Pyrite (488nm exc.)	0.9%	(this study)
Volume of Pyrite (458nm exc.)	1.3%	(this study)
Area of Pyrite (image analysis)	1.7%	(this study)
Porosity (image analysis of BSE)	1.8%	(this study)

Figure 2.3 shows backscatter SEM images of Kimmeridge Formation Sample NS. Sample NS is dominated by very-fined grained (< 2μm) particles with varying amounts of silt (2-60μm) and fine quartz (> 60μm) as shown in Figure 2.3. Porosity is very low (part of the black color) and usually does not exceed 2% (Vernik and Nur, 1992a) with pore sizes dominated by micron size rarely reaching 30μm. Low porosity is usually associated with high organic matter content but mineral composition and diagenetic processes also have an effect. Intergranular permeability is very low, due to very small pore sizes. The white inclusions represent relatively denser mineral, pyrite. The round white inclusions are pyrite framboids (spheroids). Pyrite is commonly a component of fine-grained, organic-rich marine sediments, where iron and sea water sulfate are normally present in abundance, and pyrite formation and distribution is apparently controlled by the concentration of organic carbon (Berner 1980, 1984). According to

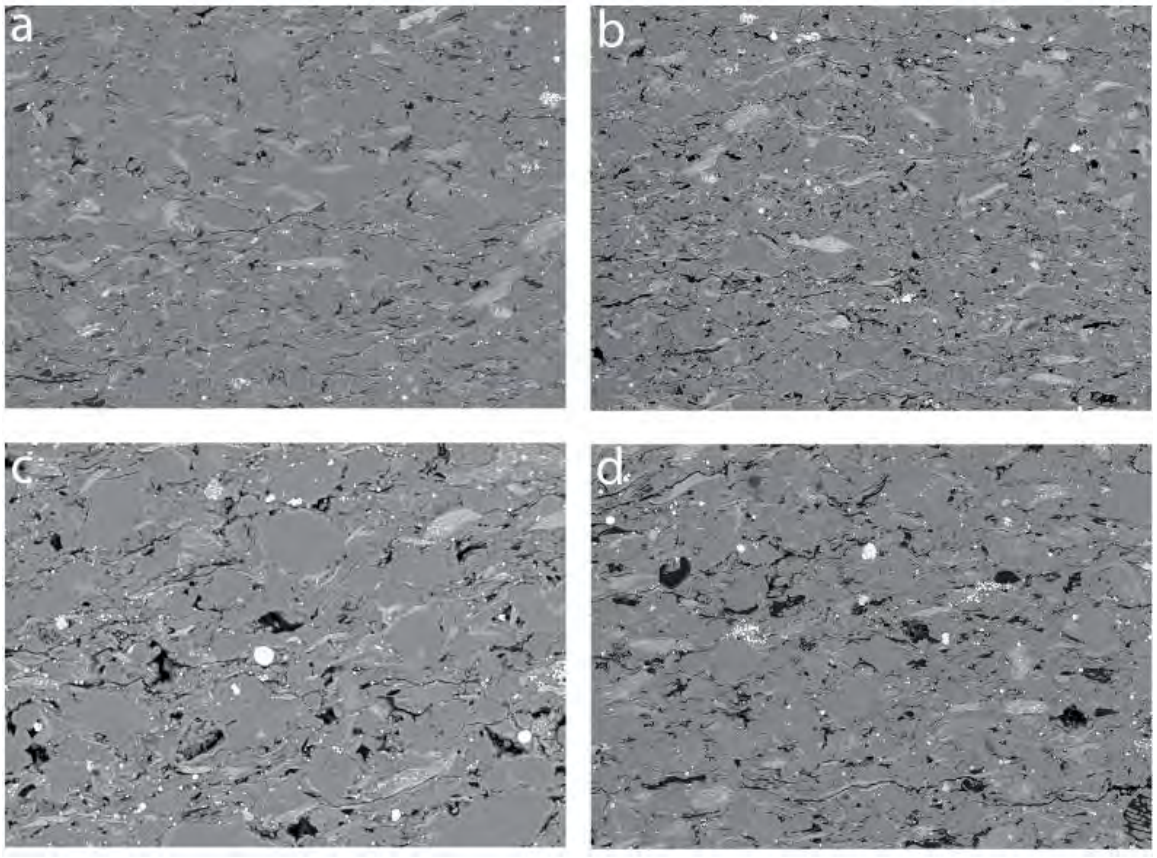

Figure 2.3: Backscatter SEM photomicrographs of Kimmeridge Formation Sample NS. Size of longer side of image: a) is 1600 µm; b) is 2100 µm; c) is 800 µm; c) is 950 µm.

Canfield and Raiswell (1991), pyrite forms in sediments deposited in oxygenated bottom waters only when anoxic conditions are established within the sediments, where formation is generally limited either by the concentrations of metabolizable organic matter or by the concentrations of iron that are reactive towards dissolved sulfide. The chronological formation and evolution of pyrite is depicted on Figure 2.4. At initial stages, the pyrite crystals are formed at periphery (Fig. 2.4a), consequentially growing towards the center of framboid (Fig. 2.4b-c), and finally, the framboid is formed (Fig. 2.4d). The average size of spheroidal aggregates is 5-30µm in diameter of closely packed individual crystals of pyrite. The shapes of the inclusions are typical of pyrite: smaller round clasts consist of even smaller crystals (Fig. 2.4d) – pore-filling framboidal pyrite formed from solutions highly supersaturated with both Fe monosulfides and pyrite.

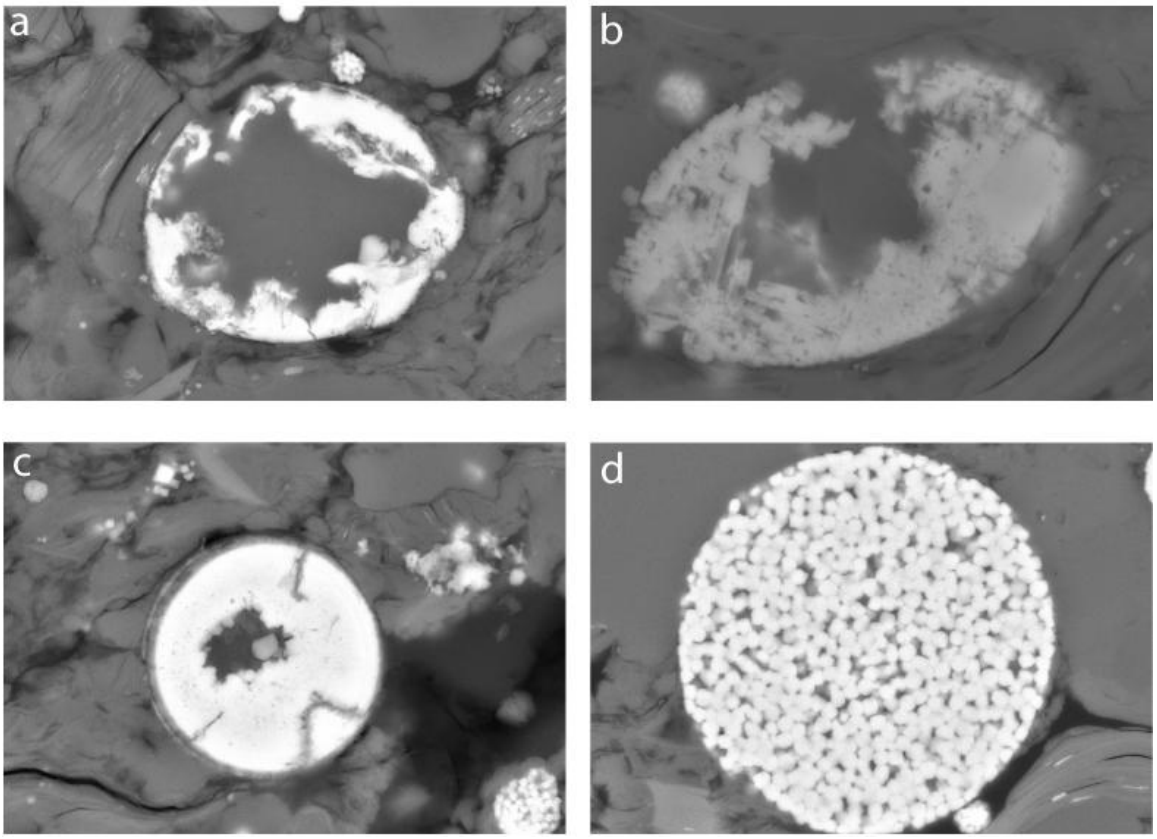

Figure 2.4: Backscatter SEM photomicrographs of Kimmeridge Formation Sample NS showing the chronological formation and evolution of framboidal pyrite. Size of longer side of image: a) is 60 μm; b) is 35 μm; c) is 45 μm; d) is 35 μm.

Sample NS was subjected to at least 4500m burial depth and as a result, a number of deformational features are present at close examination of microtexture. These features are indicated by arrows on Figure 2.5. The clay particle shown in Figure 2.5a is broken and displaced in left-lateral direction. Vermiform kaolinite (vc) particle is deformed between several medium-grained quartz particles (qz) in Figures 2.5b and 2.5c, below a clast of framboidal pyrite (fp). According to Ehrenberg *et al.* (1993), large vermiform aggregates, several hundreds of micrometers long, are predominant within Kimmeridge Formation at depth of 2500–3000 m. At depth of 3700–3800 m, kaolin minerals occur with more uniform size and morphology. From 3000 to 5000 m, kaolin crystals become progressively thicker (Beaufort *et al.*, 1998). McAulay *et al.* (1994) and Beaufort *et al.* (1998) observed intercalated blocky and lamellar crystals, interpreted as a transient phase from vermiform to blocky habit. Wilkinson *et al.,* (2006) suggested that kaolin originated

by the dissolution of feldspars in meteoric porewater. Vermicular kaolin formed during early burial (surface to 40˚C) recrystallized to blocky kaolin at 40-80˚C in pore waters with a predominantly meteoric signature.

The framboidal pyrite clasts in Figure 2.5d are deformed compared to spheroidal rounded shape suggesting that pyrite formed prior to considerable amounts of compaction. Figures 5e and 5f display an example of quartz grain deeply penetrating into kaolinite particle in BSE and SE modes, respectively. Another example of highly deformed kaolinite particle is shown in Figures 2.5g (BSE mode) and 2.5h (SE mode). Substantial compaction is also implied from preferred orientation of aligned clay particles.

Several authors (Heald, 1959; Lerbekmo and Platt, 1962; Geiser and Sansone, 1981) have proposed that inhomogeneities due to fabric and/or compositional variations act as precursors for dissolution of quartz and the generation of stylolites (indicated by arrows in Figure 2.6). Some authors emphasize that the influence of clay and micas in quartz dissolution is textural, as the internal structure of these minerals situated between dissolving grains provide as a rapid diffusion pathway for silica-saturated water (Weyl, 1959). Others have proposed that the presence of mica raises the pH-value of the intergranular fluid above the mica surface, which favours quartz dissolution (Thompson, 1959; Boles, 1984). Whatever the process is, clays and micas clearly facilitate pressure solution of quartz grains. Figure 2.7 shows a pressure solution surface formed at the border between two quartz grains (indicated by arrow).

Sample NS contains fusinite macerals of inertinite maceral group. The inertinite macerals show well-preserved cellular structure derived from plant material that has been strongly altered and degraded, typical of fusinite (Fig. 2.8). Chemically, fusinite is characterized by relatively high carbon content and low contents of hydrogen, oxygen and other volatile components and originates from ligno-cellulosic cell walls. According to ICCP (2001) mainly the resistant lignified portions of the cell walls –survived" during fusinitization.

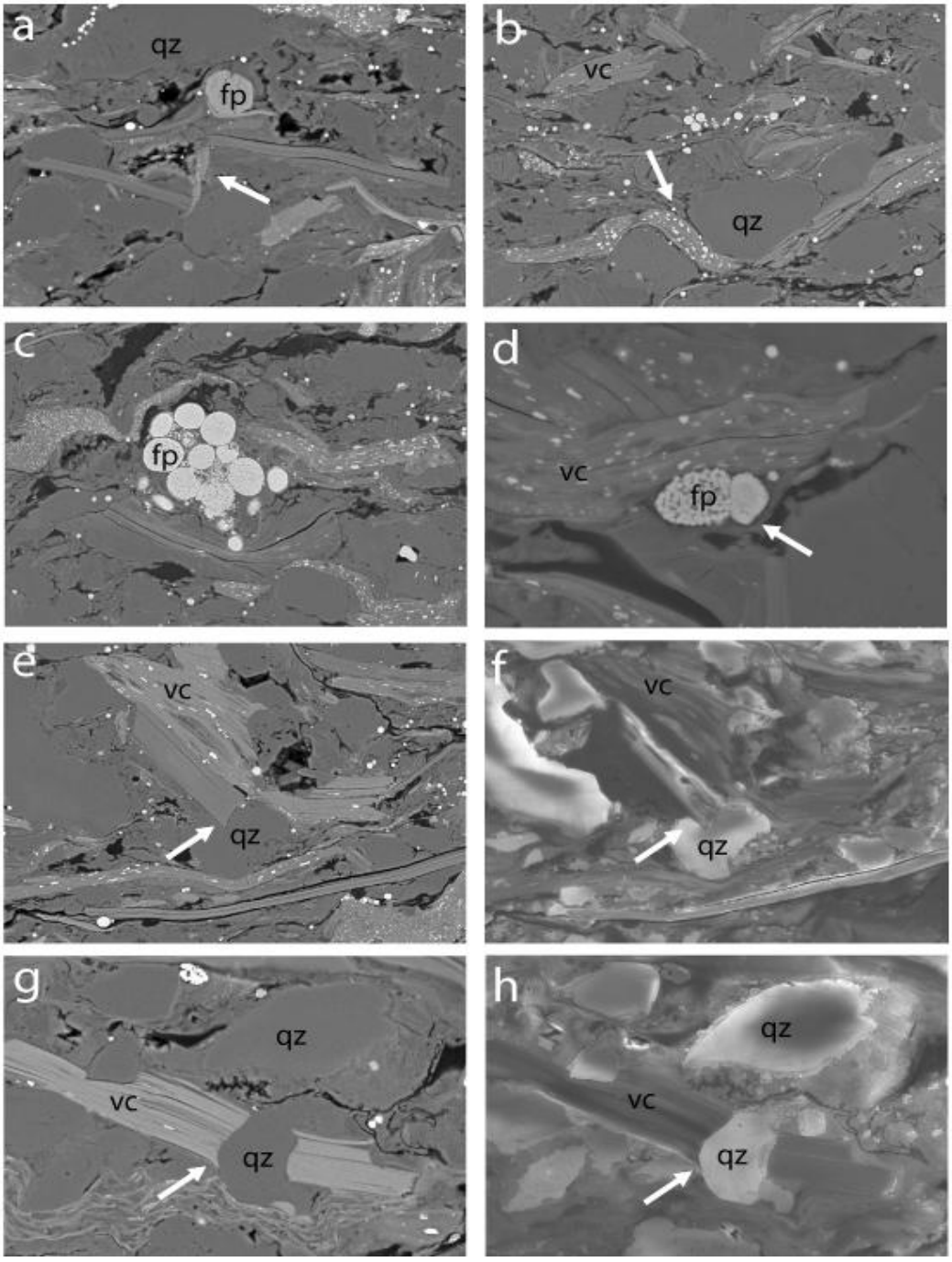

Figure 2.5: SEM photomicrographs of Kimmeridge Formation Sample NS showing the deformational features indicated by arrows. a) broken and displaced clay particle in BSE mode, b-c) Vermiform kaolinite (vc) particle is deformed between several medium-grained quartz particles (qz) in BSE mode, d) deformed framboidal pyrite clasts (fp) in BSE mode, e) quartz grain deeply penetrating into kaolinite particle in BSE mode, f) area shown in e) in SE mode, g) highly deformed kaolinite particle in BSE mode, h) area shown in g) in SE mode. Size of longer side of image: a) is 300 μm; b) is 250 μm; c) is 300 μm; d) is 100 μm e-f) is 300 μm; g-h) is 150 μm.

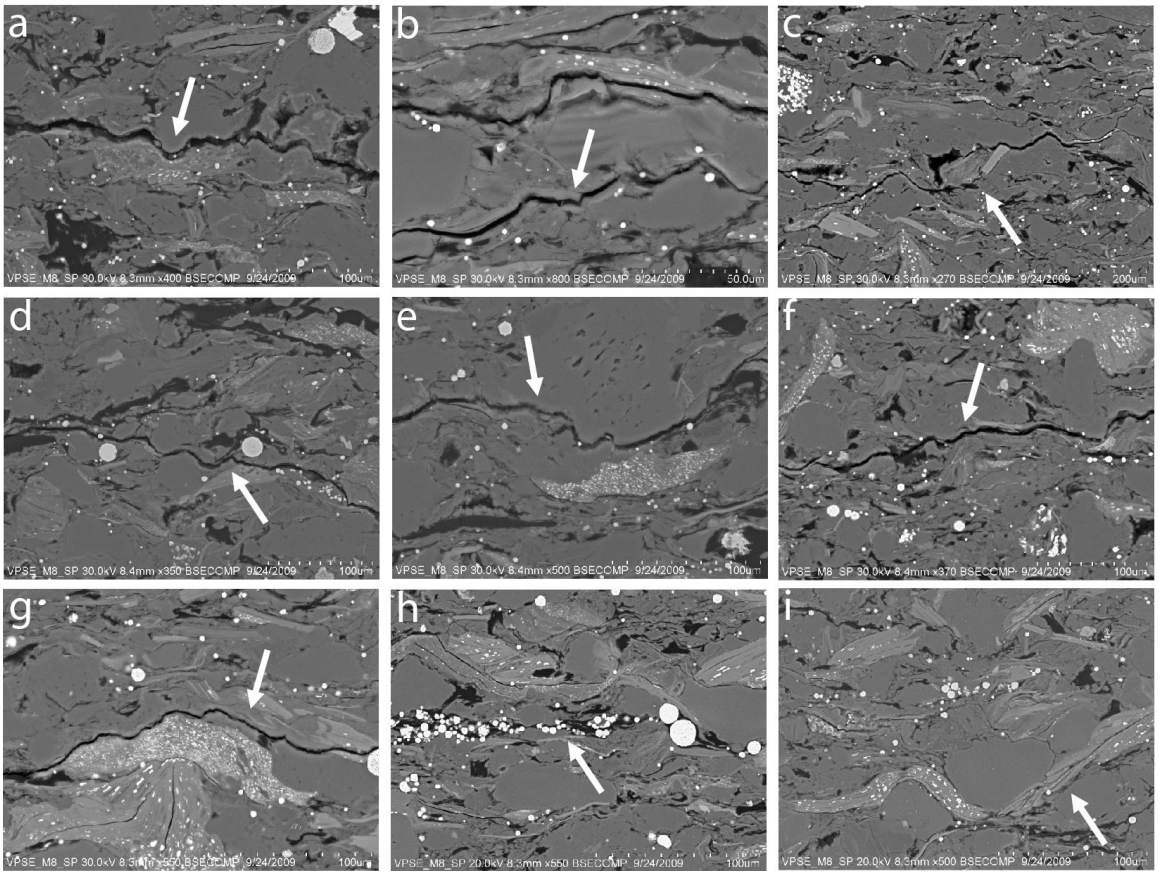

Figure 2.6: a-i) Backscatter SEM photomicrographs of Kimmeridge Formation Sample NS showing the morphology of pressure solution surfaces. Size of longer side of image: a) is 60 µm; b) is 35 µm; c) is 45 µm; c) is 35 µm. NOTE: Pressure solution surfaces are east-west cutting bed-parallel features (orthogonal to the direction of normal stress) in all photomicrographs.

Some fusinite is derived from wild fires which resulted in the formation of fossil charcoal (pyrofusinite) (Goodarzi, 1985; Varma, 1996; Scott, 1989; Jones et al., 1991. According to Varma (1996) and Taylor et al. (1998) fusinite can also generate by decarboxylation of plant tissues with the aid of fungi and bacteria, or by dehydration and weathering (degradofusinite). In contrast, Guo and Bustin (1998) and Bustin and Guo (1999) consider all fusinite to be the product of incomplete combustion.

CLSM images of the area covered in Figure 2.3c are displayed in Figure 2.9. These images were obtained under varying excitation wavelengths. From left to right and top to bottom, the excitation wavelength was (a) 543 nm; (b) 488 nm; and (c) 458 nm.

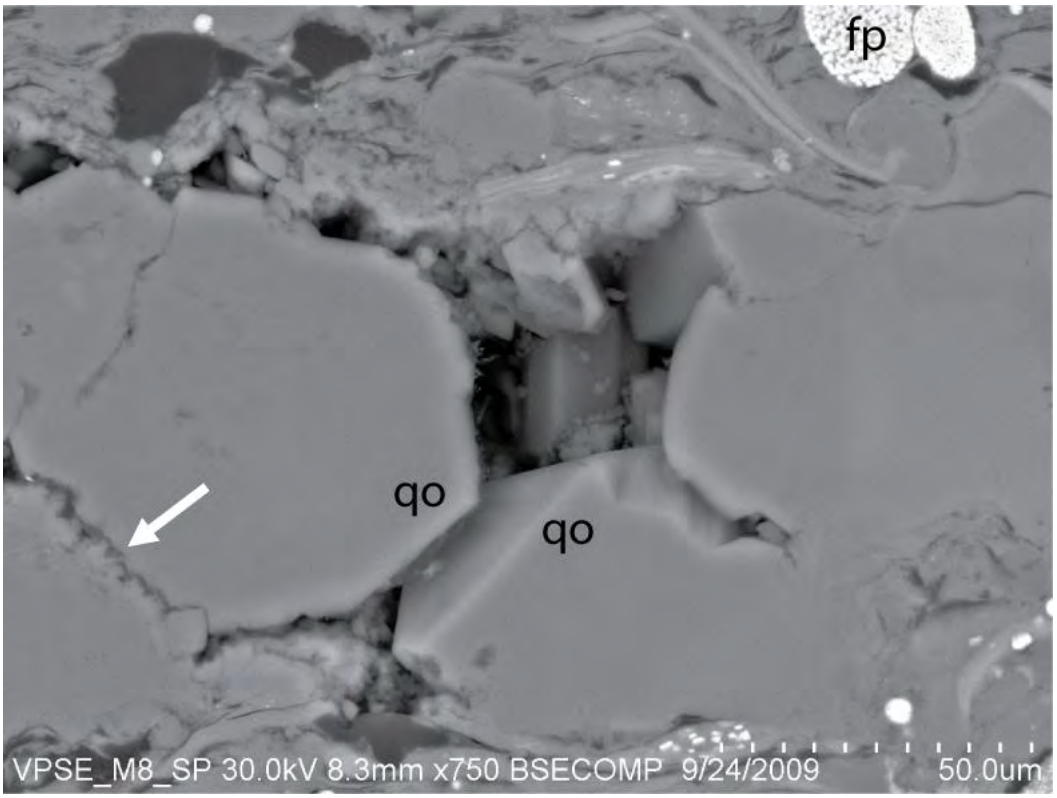

Figure 2.7: Backscatter SEM photomicrographs of Kimmeridge Formation Sample NS showing the formation of pressure solution surface (indicated by arrow) formed at the border between two quartz grains. NOTE: quartz overgrowth (qo) and deformed shape of framboidal pyrite (fp), both indicative of considerable amount of overburden and diagenesis.

The framboidal pyrite inclusions fluoresce at all wavelength excitations (appear as bright disks or dots). In images (a) and (c), the organic matter is visible scattered around silica grains and filling pores adjacent to mineral matrix. Image (d), a composite image where the previous three images were superimposed, both the organic matter and pyrite are visible, while the grey (non-fluorescing) background is predominantly quartz, feldspar and clay.

In Figure 2.10 (false-color image) we display a 3D volume reconstruction based on 27 sequential CLSM images 1μm apart obtained under red and blue light excitation. Figures 2.10a-c show side views of the 3D volume reconstructed based on 27 sequential CLSM images. These images are thresholded in order to emphasize three-dimensional character of organic matter in Figure 2.9a (under red light excitation) and Figure 2.9c

(under blue excitation). Organic matter is scattered throughout the sample somewhat uniformly without any reference to the depositional bedding.

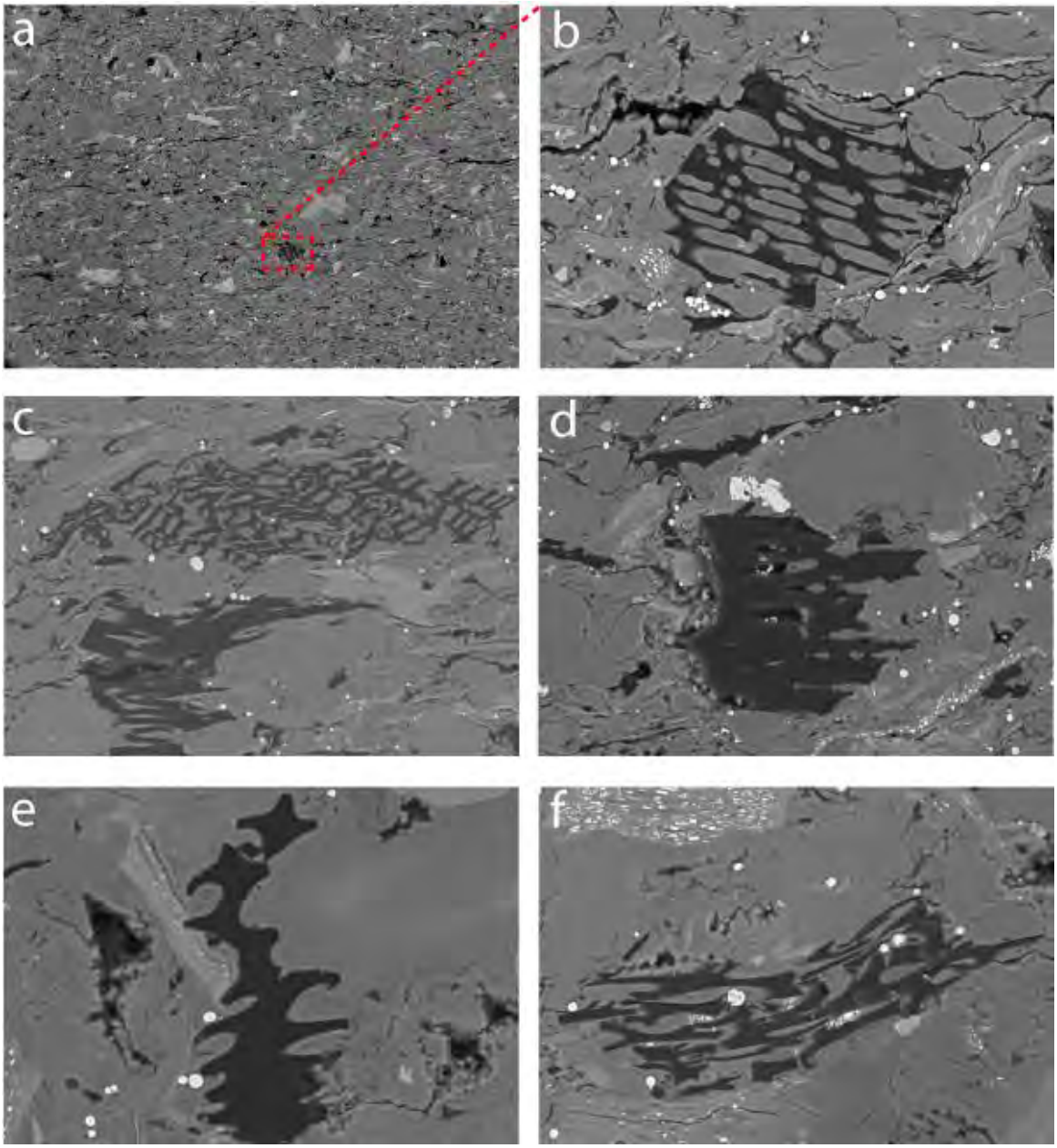

Figure 2.8: Backscatter SEM photomicrographs of North Sea Kimmeridge Formation sample NS showing fusinite maceral a) general view of microstructure of NS sample, b) close-up view of fusinite maceral with visible intercellular pores, c) two fusinite macerals: with thin-walled structure (on the top) and thick-walled structure (at the bottom), d) thick-walled structure of fusinite, e) , f) . Longer side of image a) is 2800 µm, b) is 250 µm, c) is 260 µm, d) is 260 µm; e) is 180 µm, f) is 180 µm.

Given the post-mature character of the sample and pore-filling nature of some of the kerogen adjacent to silica grains, it is rational to suggest that this portion of kerogen is residual organic matter left from primary generation and expulsion.

In order to better visualize 3D geometry of the organic matter within Sample NS, we focus on the different areas of kerogen part shown in Figure 2.10 (middle left image). Figures 2.10a-c represents a combination of high magnification insets from various organic-rich parts. Considerable amount of organic matter is localized in elongated pores along quartz grain boundaries (center of Figure 2.10c).

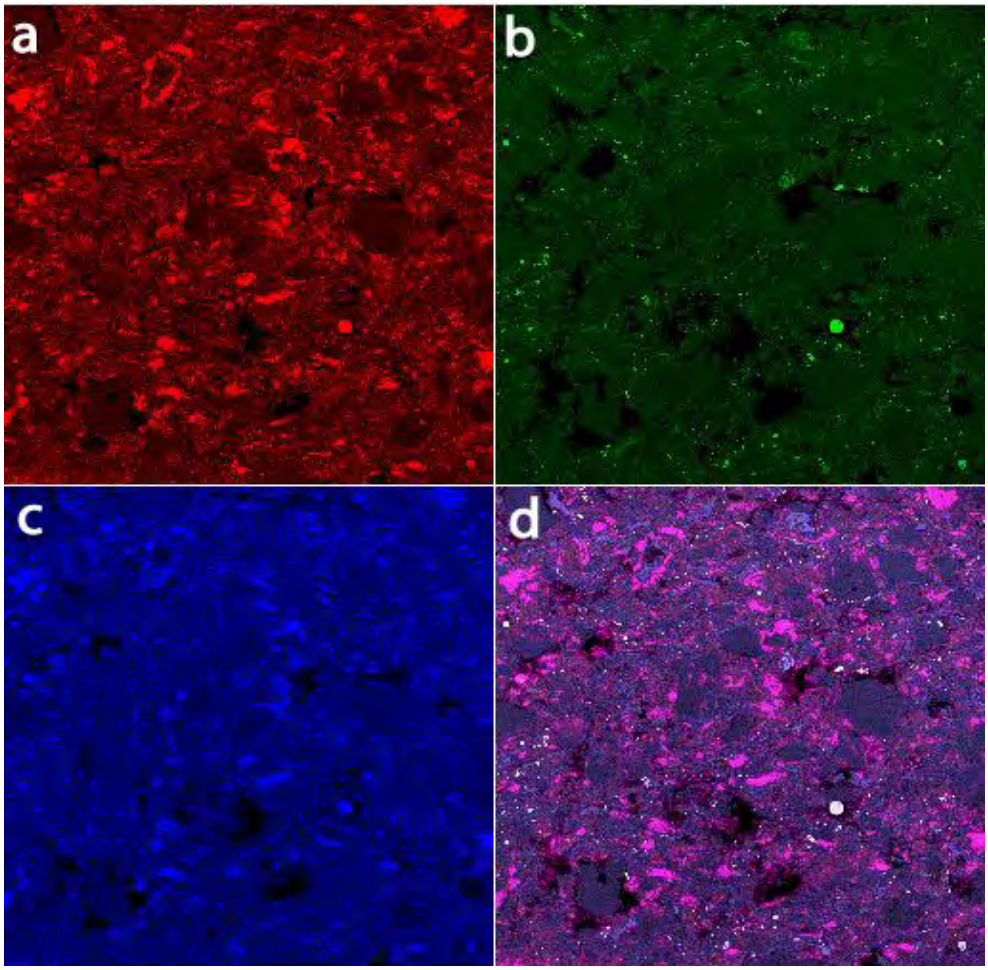

Figure 2.9: CLSM images of North Sea Kimmeridge Formation sample NS (the area covered in Figure 2.3c) showing spatial distribution of organic matter. a) obtained under red light excitation, b) obtained under green light excitation, c) obtained under blue light excitation, d) composite image of three previous images (a-c). Organic matter is detected mainly under red light excitation. Image size is 750×750 μm.

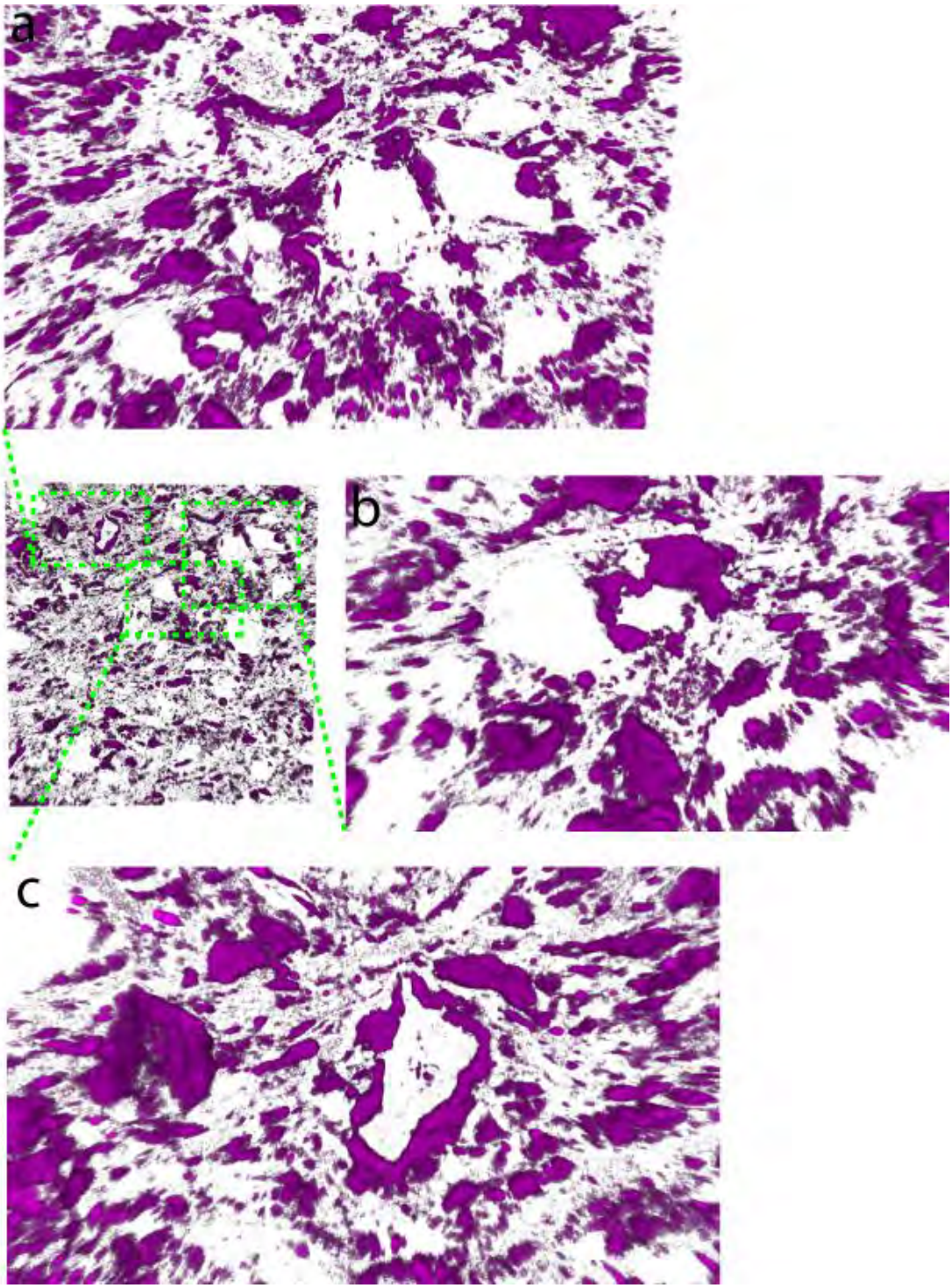

Figure 2.10: 3D volume reconstruction based on 27 sequential CLSM images of organic matter. (a-c) side view of 3D volume of organic matter from Figure 2.9. Size of 3D volume (middle left image) is 750×750×27 μm. Distance between two consecutive images is 1 μm.

2.5.2. **Bakken Formation - Sample M**

Table 2.2: Petrophysical and image analysis properties of Bakken Formation (sample M) obtained in this study and from Vernik and Landis (1996).

Lithology	Shale	Source
Depth	3223 m	Vernik and Landis (1996)
Density	2.49 g/cc	Vernik and Landis (1996)
Total Organic Carbon (TOC, % weight)	7.01%	Vernik and Landis (1996)
Vitrinite Reflectance (R_o, %)	0.69	Vernik and Landis (1996)
Hydrogen Index (HI)	447mg/g	Vernik and Landis (1996)
Porosity (helium porosimetry)	0.75%	Vernik and Landis (1996)
P-Wave Velocity --$V_p(0^\circ)$	3.36 km/s	Vernik and Landis (1996)
S-Wave Velocity --$V_s(0^\circ)$	2.06 km/s	Vernik and Landis (1996)
Kerogen Volume	20.5%	Vernik and Landis (1996)
Kerogen Volume (543nm exc. wavelength)	22.6%	(this study)
Volume of Pyrite (488nm exc.)	9.2%	(this study)
Volume of Pyrite (458nm exc.)	8.8%	(this study)
Area of Pyrite (image analysis)	10.6%	(this study)
Porosity (image analysis of BSE)	0.51%	(this study)

Figure 2.11 shows a backscatter SEM image of Bakken Formation Sample M. Sample M is dominated by very-fined grained (< 2μm) particles with varying amounts of silt (2-60μm) and fine sand (> 60μm) as shown in Figure 2.11. Porosity is very low (not visible in image) and usually does not exceed 2% (Vernik and Nur, 1992b) with pore sizes dominated by submicron size. Low porosity is usually associated with high organic matter content, but mineral composition and diagenetic processes also have an effect. Intergranular permeability is very low, due to very small pore sizes. The white circular inclusions in Figure 2.11 represent relatively denser mineral, pyrite. The larger white inclusions are euhedral (angular) pyrite. Kerogen occurs in bed-parallel (horizontal in Figure 2.11) lenses (in black).

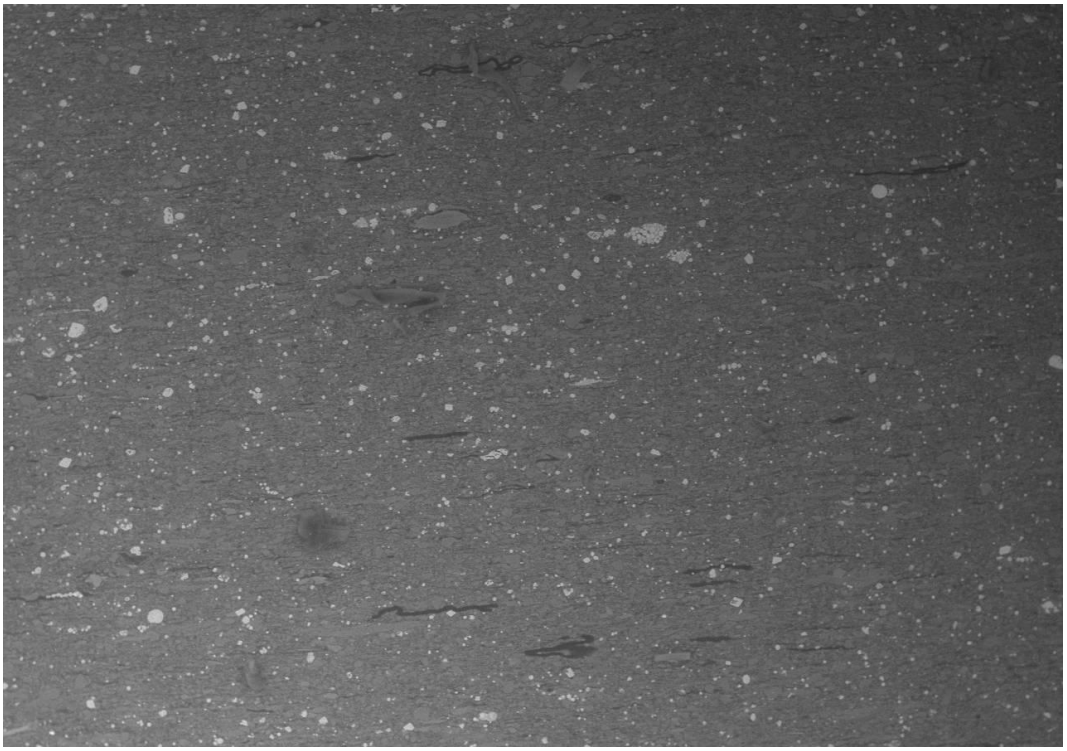

Figure 2.11: Backscatter SEM photomicrographs of Bakken Formation Sample M. Horizontal black features are kerogen. White dots and clusters of dots are pyrite. Longer side of image is 1550 μm.

The partial replacement of organic matter by pyrite is depicted on Figure 2.12. Initially, the pyrite crystals are formed at periphery of organic cyst (Fig. 2.12a-b), consequentially replacing organic matter and growing towards the center. The average size of cyst aggregates is 15-20μm in diameter. Figures 2.12c-e show replacement of organic matter in a kerogen lens composed of a liptinite group maceral. The replacement here differs from pyrite replacement in cysts. Within the kerogen lenses both framboidal and euhedral pyrite is formed in the central parts of the lens preserving the organic periphery shown in black in Figure 2.12. The shapes of the inclusions are typical of pyrite: smaller round clasts consist of even smaller crystals (Fig. 2.12d) – pore-filling framboidal pyrite formed from aqueous solutions highly supersaturated with both Fe monosulfides and pyrite. Figure 2.12e shows an extreme degree of pyrite occurrence in shale sample photomicrograph, close to ~30%. Figure 2.13 shows kerogen lenses (in black) composed of liptinite group macerals. Kerogen lenses are bed-parallel (horizontal in images)

preserving depositional configuration. The size of lenses consistently varies between 150-250 μm in length and 10-20 μm in thickness, with aspect ratio of the lenses between 1:20 to 1:10.

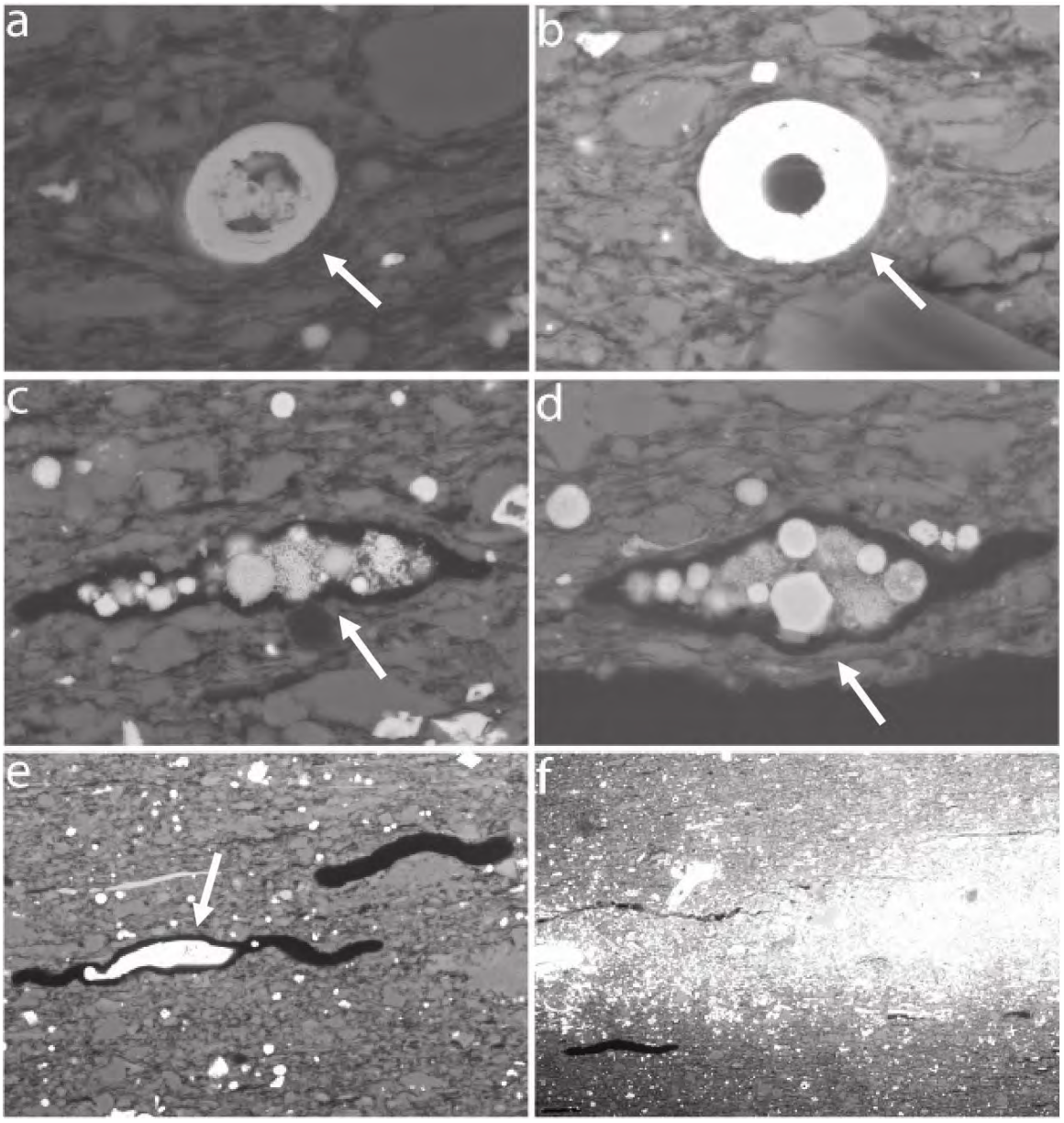

Figure 2.12: Backscatter SEM photomicrographs of Bakken Formation Sample M showing a-b) pyrite partially replacing organic cyst, c-e) euhedral and framboidal pyrite partially replacing liptinite maceral in kerogen lens, f) extreme degree of pyritization. Longer side of image a) is 70 μm, b-d) is 100 μm, e) is 310 μm, f) is 1000 μm

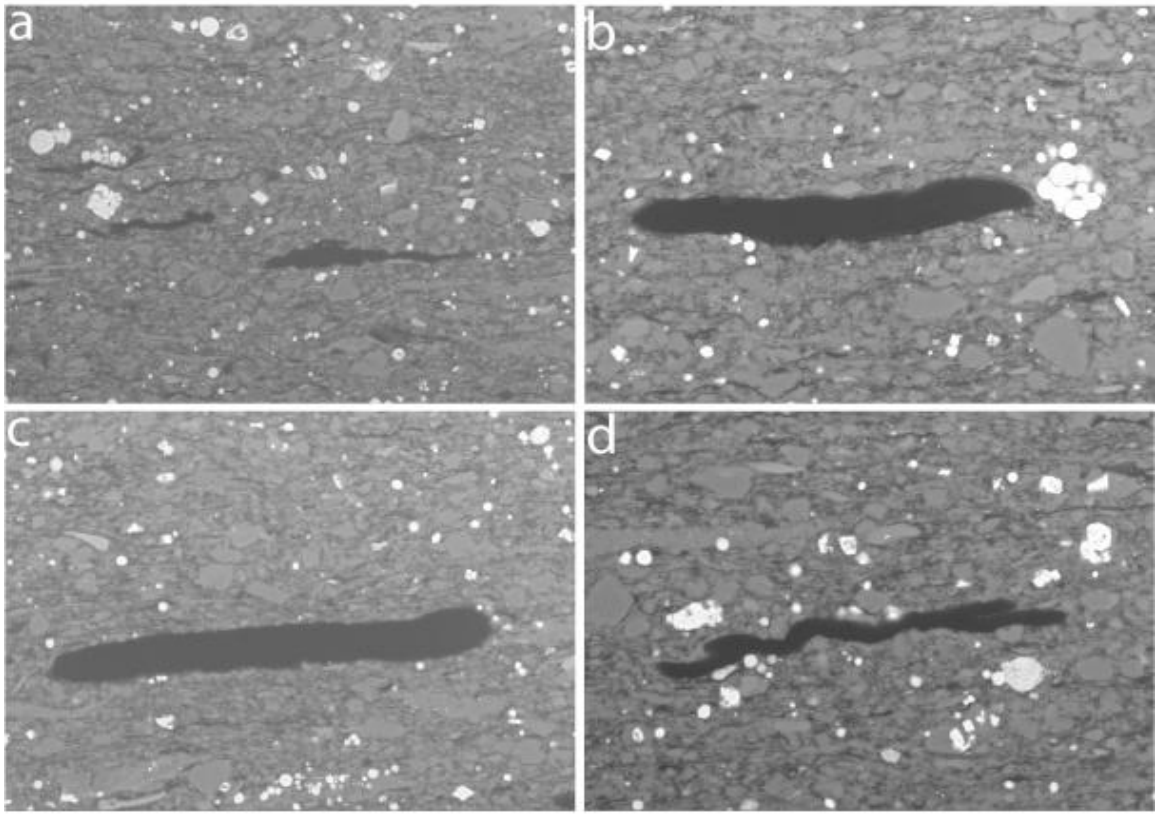

Figure 2.13: Backscatter SEM photomicrographs of Bakken Formation Sample M showing a-d) kerogen lenses (in black) composed of liptinite group macerals. Kerogen lenses are bed-parallel (horizontal in images) preserving depositional geometry. The size of lenses varies between 150-250 µm in length and 10-20 µm in thickness. The aspect ratio of the lenses is consistent and varies between 1:20 to 1:10. Longer side of image a) is 360 µm, b) is 230 µm, c) is 290 µm, d) is 230 µm.

CLSM images of the Bakken Formation Sample M are displayed in Figure 2.14. These images were obtained under varying excitation wavelengths: (a) 458 nm; (b) 488 nm; (c) 543 nm and (d) 512 nm. In these images both the organic matter and pyrite are visible, while the nonfluorescing white background, which is predominantly quartz, feldspar and clay, are removed.

The pyrite inclusions fluoresce under 458, 488 and 543 nm wavelength excitation. In the image (d) obtained at excitation wavelength 512 nm, the pyrite is invisible while the bright-magenta features represent organic matter. The difference in the illumination (pyrite versus organic matter) is determined by the amount of photons released from the surface of the samples under each given wavelength excitation. Images 2.14a-c depict

horizontal lenses similar to organic matter, however, the close examination of these lenses confirms the presence of both euhedral and framboidal pyrite that occurs within lenses of organic-rich matter as was shown earlier in Figures 2.12c-e

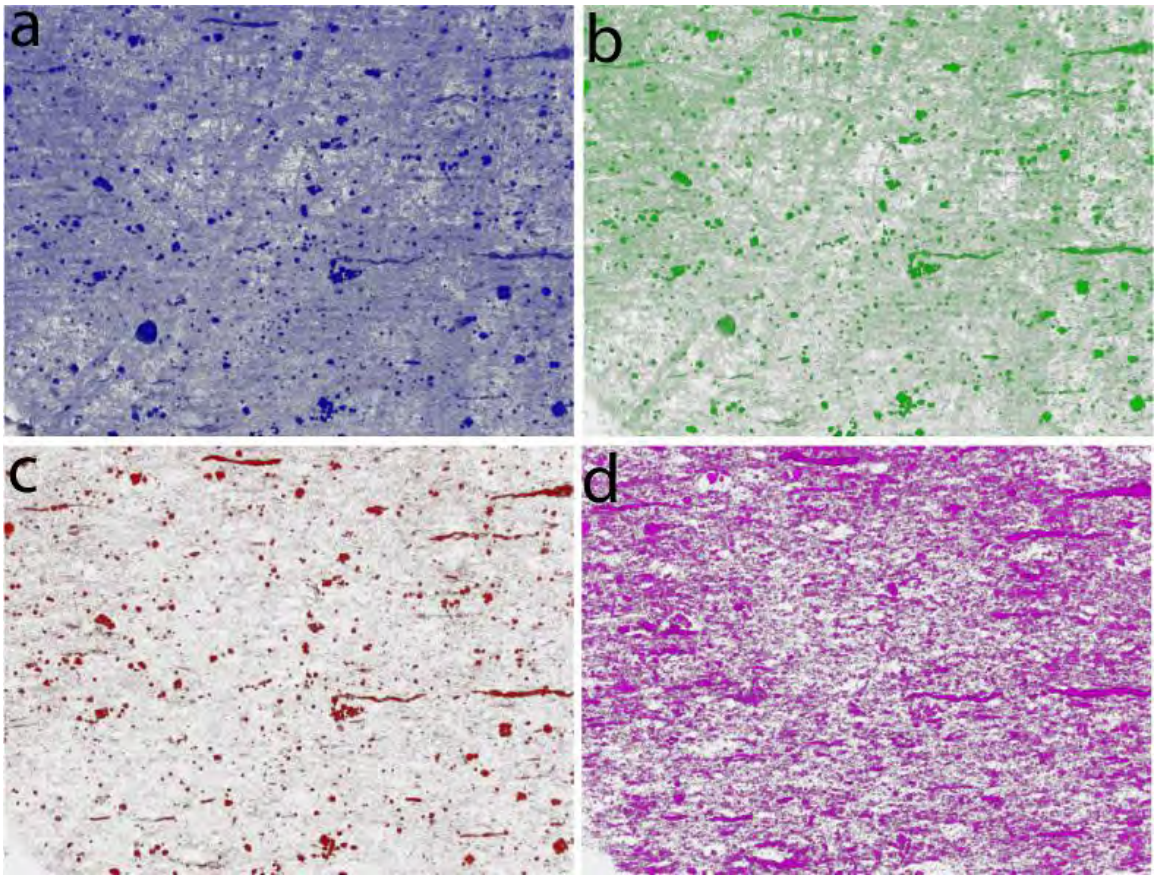

Figure 2.14: CLSM images of the Bakken Formation sample M (the area covered in Figure 2.11) showing spatial distribution of organic matter. a) obtained under blue light excitation, b) obtained under green light excitation, c) obtained under red light excitation, d) obtained under magenta light excitation. Organic matter is detected mainly under magenta light excitation. Longer side of images is 800 μm.

We display side views of 3D volume reconstruction of kerogen based on 27 sequential CLSM images 1μm apart (Figures 2.15). Images are thresholded in order to eliminate non-fluorescing background and to reveal the three-dimensional nature of organic lenses. The left image shows several lenses of kerogen aligned with bedding plane (horizontal), whereas the right image is a close-up view of the smaller area from the image on the left.

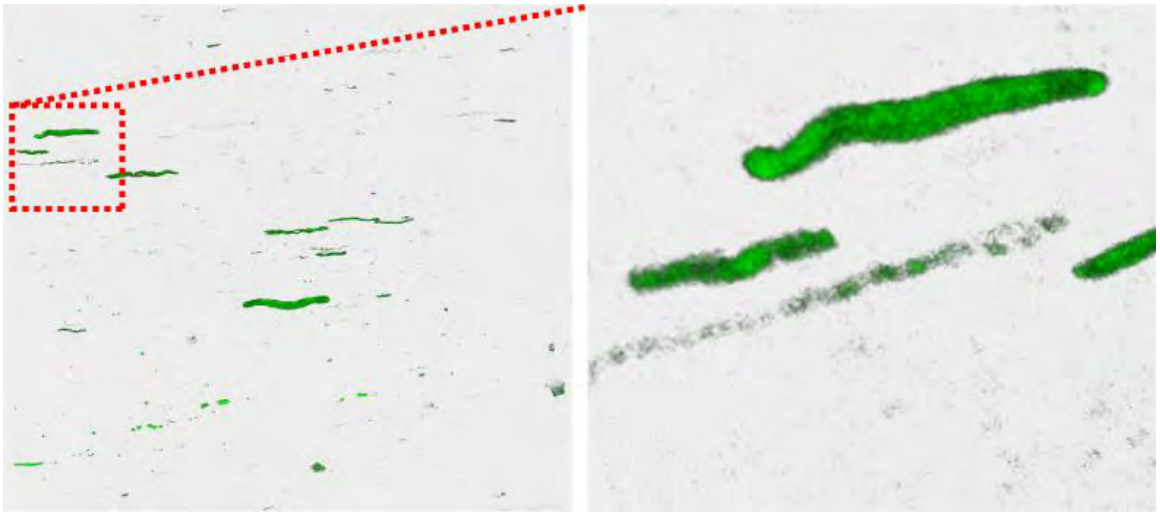

Figure 2.15: Side view of 3D volume reconstructed from series of 27 images under 512 nm light excitation: Volume of images on the: (left) is 800×700×27 µm; (right) is 210×185×27 µm. Distance between two consecutive images is 1 µm.

Figure 2.16 shows side views of 3D volumes reconstructed based on 27 sequential CLSM images. These images are thresholded in order to emphasize three-dimensional character of organic matter and pyrite. In addition, only volumes obtained under green (representing pyrite) and magenta (representing kerogen) light excitation were used to illustrate the spatial link between pyrite and organic matter. Figures 2.16a, 2.16b and 2.16c (under green light excitation) show distribution of both euheral and framboidal pyrite. Figures 2.16a', 2.16b' and 2.16c' are obtained under both green and magenta light excitation and correspond to the area shown in Figures 2.16a, 2.16b and 2.16c, respectively. Images show partial to full replacement of original organic matter lenses by pyrite (indicated by arrows). The vitrinite reflectance data (R_o=0.69) indicates that kerogen lenses are not composed of residual organic matter left from primary generation and expulsion. Unlike kerogen from post-mature sample F from Bakken Formation (discussed in the next section), most of the organic matter is not scattered throughout the sample uniformly without any reference to the depositional bedding, but localized in bed-parallel lenses, indicating preserved depositional character of the organic matter.

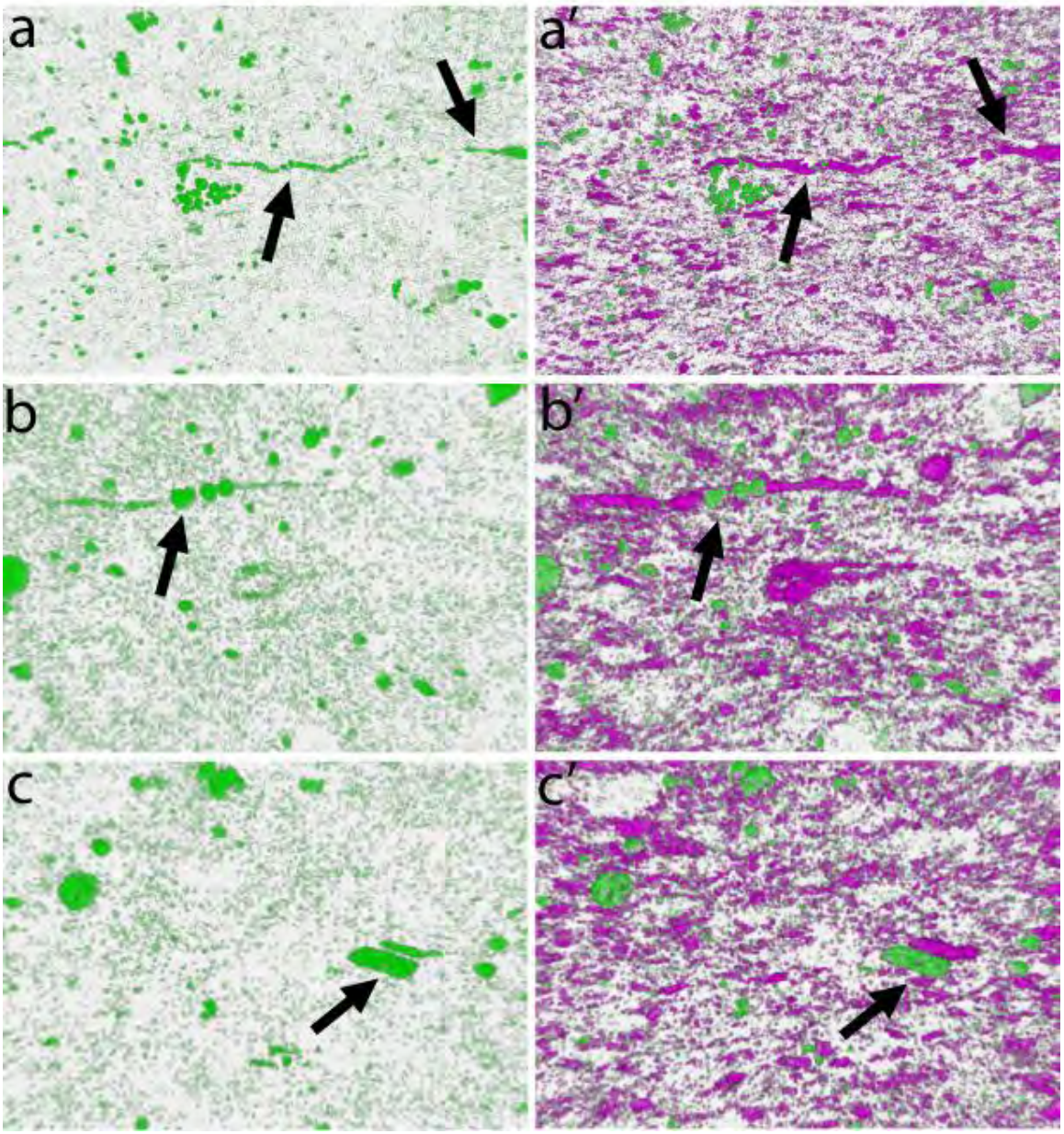

Figure 2.16: 3D volume reconstruction based on 27 sequential CLSM images of organic matter and pyrite. (a) side view of 3D volume of organic matter under red light excitation; (b) side view of 3D volume of pyrite a under blue light excitation; c) side view of 3D volume of pyrite under green light excitation; d) side view of 3D volume of combined organic matter and pyrite; and (e) close-up view of d) arrows indicate partial substitution of organic macerals (red) by framboidal and euhedral pyrite (green). Size of 3D volume is 450×450×27 µm. Distance between two consecutive images is 1 µm.

2.5.3. **Bakken Formation - Sample F**

Table 2.3: Petrophysical and image analysis properties of Bakken Formation (sample F) obtained in this study and from Vernik and Landis (1996).

Lithology	Shale	Source
Depth	3438 m	Vernik and Landis (1996)
Density	2.48 g/cc	Vernik and Landis (1996)
Total Organic Carbon (TOC, % weight)	5.95%	Vernik and Landis (1996)
Vitrinite Reflectance (R_o, %)	1.27	Vernik and Landis (1996)
Hydrogen Index (HI)	97mg/g	Vernik and Landis (1996)
Porosity (helium porosimetry)	1.12%	Vernik and Landis (1996)
P-Wave Velocity --$V_p(0^\circ)$	3.89 km/s	Vernik and Landis (1996)
S-Wave Velocity --$V_s(0^\circ)$	2.42 km/s	Vernik and Landis (1996)
Kerogen Volume	15.8%	Vernik and Landis (1996)
Kerogen Volume (543nm exc. wavelength)	13.3%	(this study)
Volume of Pyrite (488nm exc.)	4.9%	(this study)
Volume of Pyrite (458nm exc.)	5.0%	(this study)
Area of Pyrite (image analysis)	4.1%	(this study)
Porosity (image analysis of BSE)	1.93%	(this study)

Figure 2.17 shows backscatter SEM (left) and secondary electron (SE) images of Bakken Formation Sample F. Sample F is dominated by very-fined grained (< 2μm) particles with varying amounts of silt (2-60μm) and fine sand (> 60μm) as shown in Figure 2.17. Porosity is very low (black color on the left image of Figure 3) and usually does not exceed 2% (Vernik and Nur, 1992b) with pore sizes dominated by submicron size. Low porosity is usually associated with high organic matter content, but mineral composition and diagenetic processes also have an effect. Intergranular permeability is very low, due to very small pore sizes. On the left image of Figure 2.17, as in the case of the previous Bakken Formation sample M, the white inclusions represent pyrite. The larger angular inclusions are euhedral (angular) pyrite that appear dark as well as do pyrite framboids (spheroids) in the SE image on the right.

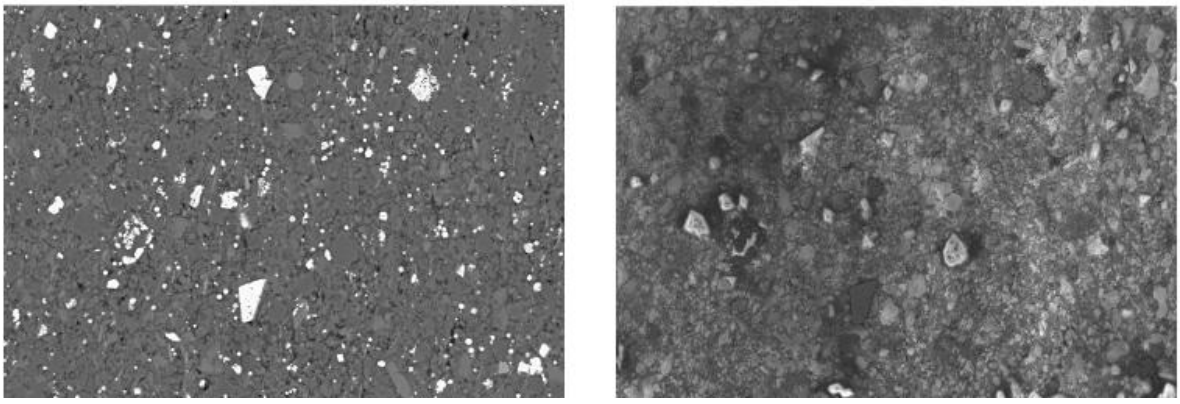

Figure 2.17: Backscatter SEM (left) and secondary electron (right) photomicrographs of Bakken Formation Sample F. Bright white features are both euhedral (angular) and framboidal (circular) pyrite. Longer side of each image is 460 µm.

Pyrite is commonly a component of fine-grained, organic-rich marine sediments, where iron and sea water sulfate are normally present in abundance, and pyrite formation and distribution is apparently controlled by the concentration of organic carbon (Berner 1980, 1984). The shapes of the inclusions are typical of pyrite: smaller round clasts consist of even smaller crystals (Figures 2.18a and 2.18b) – pore-filling framboidal pyrite forming as a result of rapid pyrite formation from aqueous solutions highly supersaturated with both Fe monosulfides and pyrite, in which reaction kinetics favor the formation of Fe monosulfides before pyrite. By contrast, euhedral pyrite (Figures 2.18c and 2.18d) forms more slowly at saturation levels that are below those of Fe monosulfides (e.g., Sweeney and Kaplan, 1973; Goldhaber and Kaplan, 1974; Raiswell, 1982; Rickard, 1997), as confirmed by pyrite synthesis experiments (Wang and Morse, 1996) which show that pyrite morphology changes from cubic to octahedral to spherulitic with increasing degree of supersaturation. Framboidal pyrite generally is very early diagenetic in origin (Coleman and Raiswell, 1995).

The average size of spheroidal aggregates is 5-20µm in diameter of closely packed individual crystals of pyrite. The framboidal pyrite clasts in Figures 2.18a and 2.18b are deformed compared to spheroidal rounded shape suggesting that pyrite formed prior to considerable amounts of compaction. Substantial compaction is also implied from preferred orientation of aligned clay particles as well as from broken clay particles.

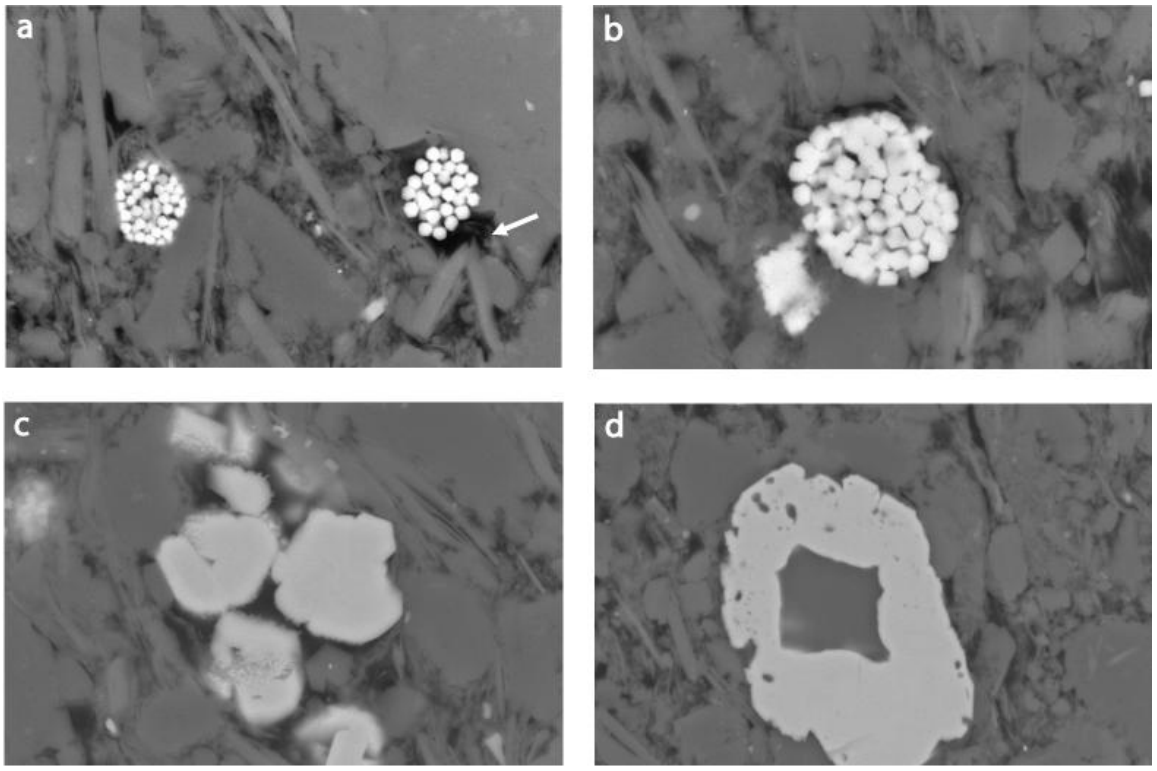

Figure 2.18: Backscatter SEM photomicrographs of Bakken Formation Sample F showing a) and b) pore-filling framboidal pyrite, c) pore-filling euhedral pyrite, d) euhedral pyrite partially replacing maceral. Note broken clay particle (white arrow) and preferred alignment of clay particles as well as deformed shape of framboidal pyrite clast indicating considerable amount of compaction. Longer side of image a) is 25 µm, b is 15 µm, c) is 20 µm, d) is 35 µm

CLSM images of the area covered in Figure 2.17 are displayed in Figure 2.19. These images were obtained under varying excitation wavelengths. From left to right and top to bottom, the excitation wavelength was (a) 488 nm; (b) 543 nm; and (c) 458 nm. Image (d) is a composite image where the previous three images were superimposed. The pyrite inclusions fluoresce at 488 and 458 nm wavelength excitation. In the image (b) obtained at excitation wavelength 543 nm, the pyrite is invisible while the bright-red features represent organic matter. The difference in the illumination (pyrite versus organic matter) is determined by the amount of photons released from the surface of the samples under given wavelength excitation. In the composite image (d) both the organic matter and pyrite are visible, while the dark background is predominantly quartz, feldspar and clay.

In Figures 2.20 we display 3D volume reconstruction based on 10 sequential CLSM images 1µm apart obtained under green light excitation. Image in Figure 2.20b is thresholded in order to eliminate non-fluorescing background and to reveal the three-dimensional nature of framboidal (spheroidal) and euhedral (angular) pyrite. Smaller pyrite clasts are pore-filling, and occur between clay platelets and silica grains.

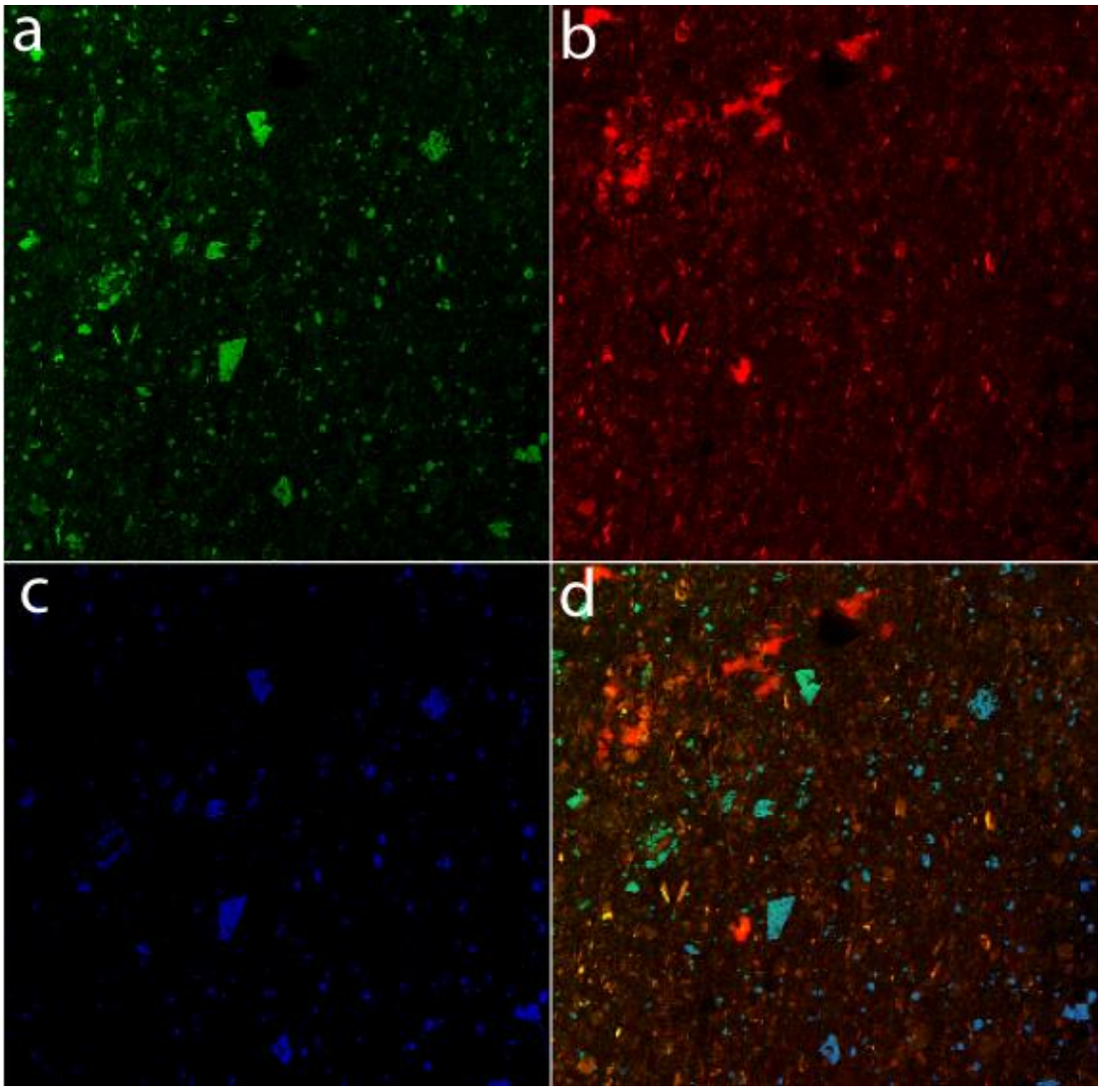

Figure 2.19: CLSM images of the Bakken Formation sample F (the area covered in Figure 2.17) showing spatial distribution of organic matter. a) obtained under green light excitation, b) obtained under red light excitation, c) obtained under blue light excitation, d) is a composite CLSM image where the previous three images (a-c) were superimposed. Organic matter is detected mainly under red light excitation. Image size is 374×374 µm.

As implied from Figure 2.19d, unlike framboidal pyrite, that preserves its original round shape irrespective of the shape of the pore, euhedral pyrite occupies most (if not all) of available pore space. Its growth is dictated by the size and shape of the available pore space.

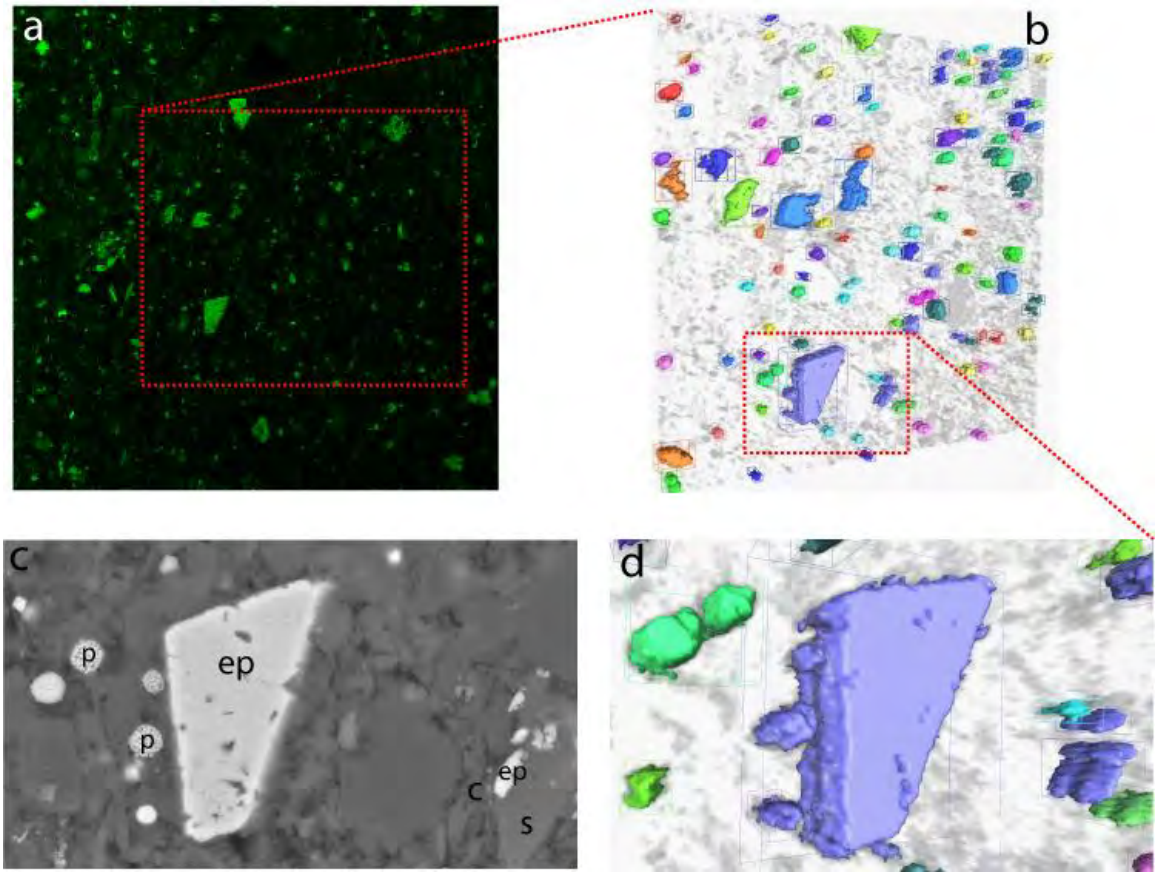

Figure 2.20: (a) CLSM image under green light excitation; (b) side view of 3D volume reconstructed from series of 10 images: two types of heavy mineral inclusions are observed – framboidal pyrite (p) and euhedral pyrite (ep); (c) BSE photomicrograph of pore-filling pyrite adjacent to silicate grain (s) and clay sheet (c); and (d) CLSM close-up view of b). Size of a) is 450×450 μm. Size of 3D volume in b) is 300×270×9 μm. Distance between two consecutive images is 1 μm.

Figure 2.21a-c shows side view of 3D volume reconstructed based on 10 sequential CLSM images. These images are thresholded in order to emphasize three-dimensional character of organic matter in Figure 2.21a (under red light excitation) and pyrite in Figures 2.21b and 2.21c (under blue and green light excitations). Three-dimensional volumes of organic matter and pyrite are combined in Figures 2.21d and 2.21e which

show partial to full replacement of original organic matter by pyrite. Organic matter is scattered throughout the sample somewhat uniformly without any reference to the depositional bedding. Given the post-mature character of the sample and pore filling nature of some of the kerogen adjacent to silica grains, it is rational to suggest that this portion of kerogen is residual organic matter left from primary generation and expulsion. In order to better visualize 3D geometry of the organic matter within Sample F, we focus on the different areas of kerogen part shown in Figure 2.21a. Figures 2.22 and 2.23 represent a combination of high magnification insets from various organic-rich parts.

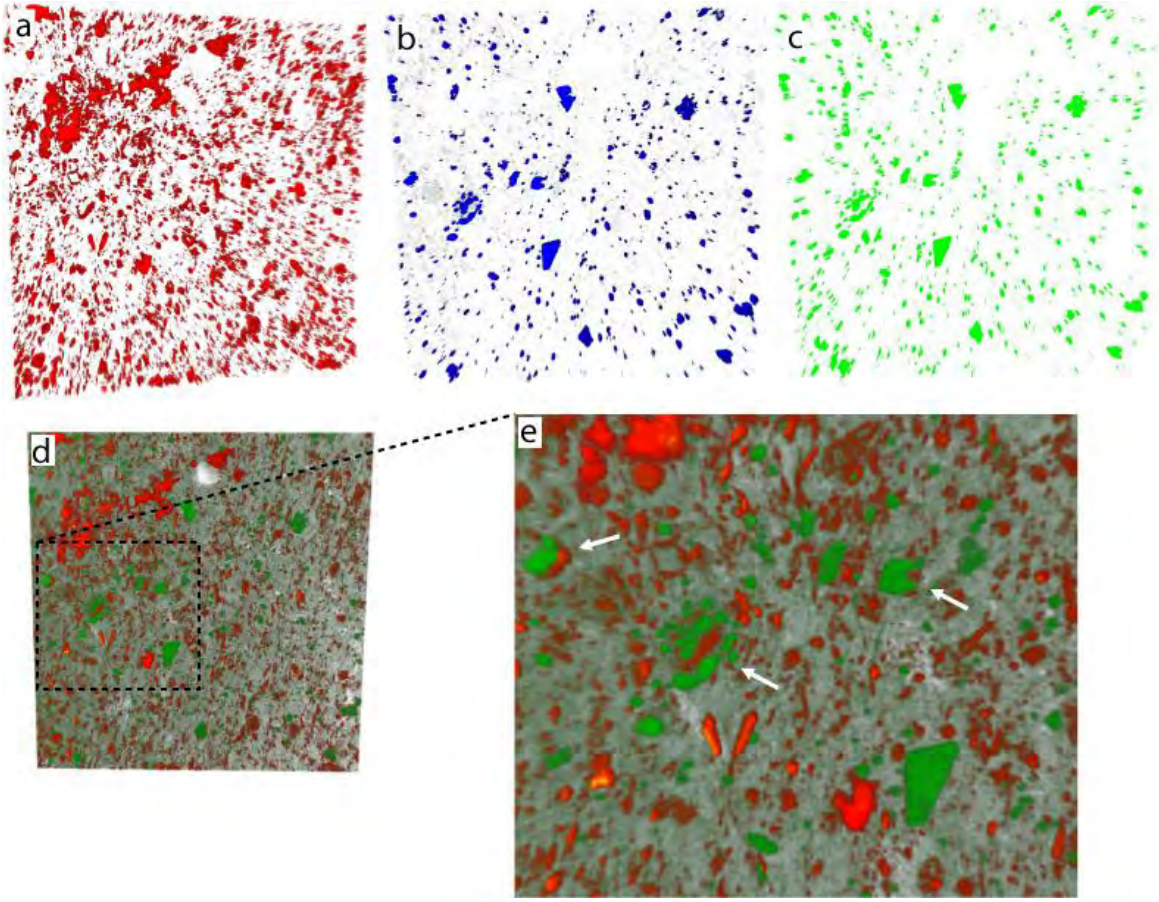

Figure 2.21: 3D volume reconstruction based on 10 sequential CLSM images of organic matter and pyrite. (a) side view of 3D volume of organic matter under red light excitation; (b) side view of 3D volume of pyrite a under blue light excitation; c) side view of 3D volume of pyrite under green light excitation; d) side view of 3D volume of combined organic matter and pyrite; and (e) close-up view of d) arrows indicate partial substitution of organic macerals (red) by framboidal and euhedral pyrite (green). Size of 3D volume is 450×450×9 µm. Distance between two consecutive images is 1 µm.

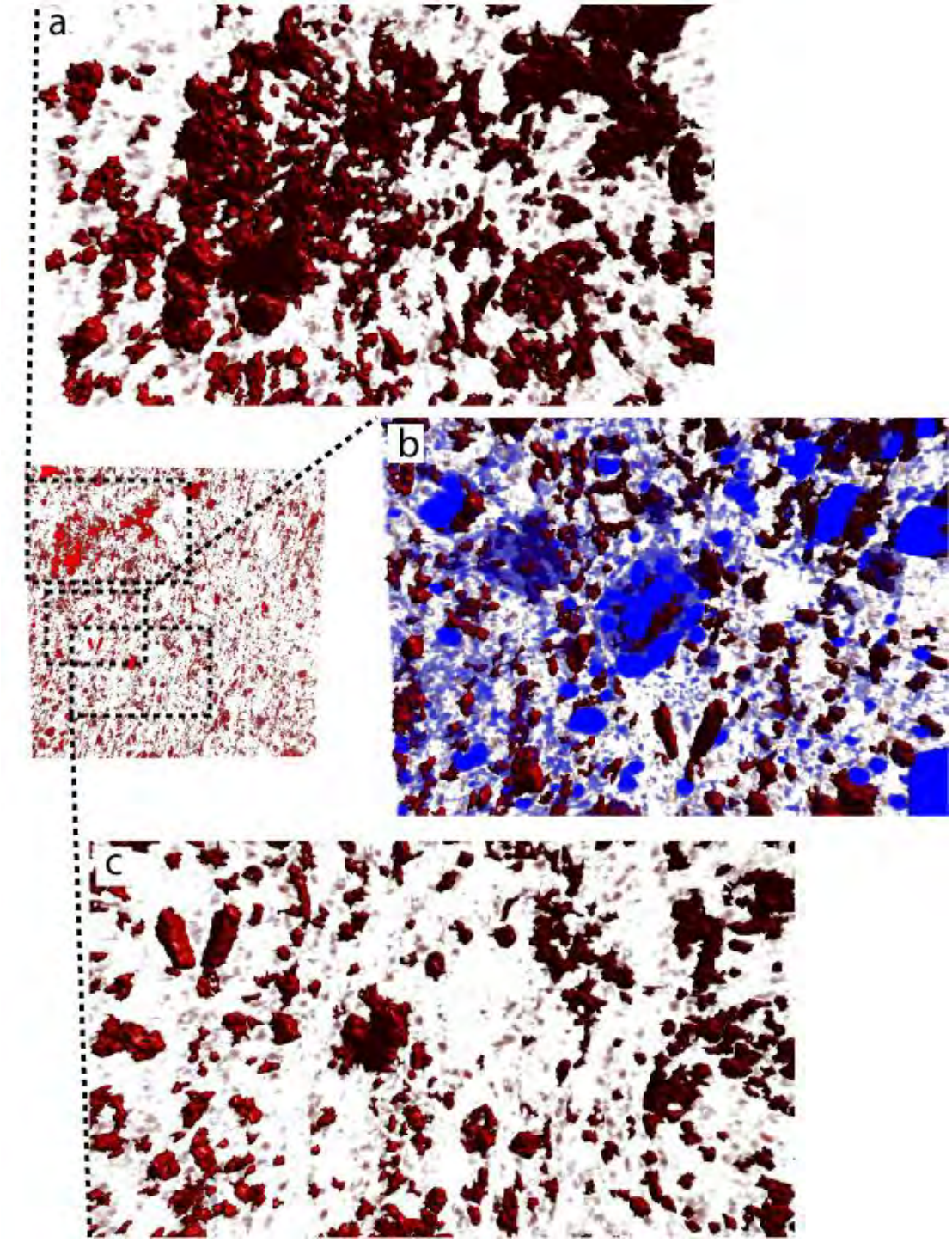

Figure 2.22: 3D volume reconstruction based on 10 sequential CLSM images of organic matter. (a) side view of 3D volume of organic matter from Figure 2.21a; (b) side view of 3D volume of pyrite (blue) replacing organic matter (red) from Figure 2.21a; c) side view of 3D volume of organic matter from Figure 2.21a. Size of 3D volume is 450×450×9 µm. Distance between two consecutive images is 1 µm.

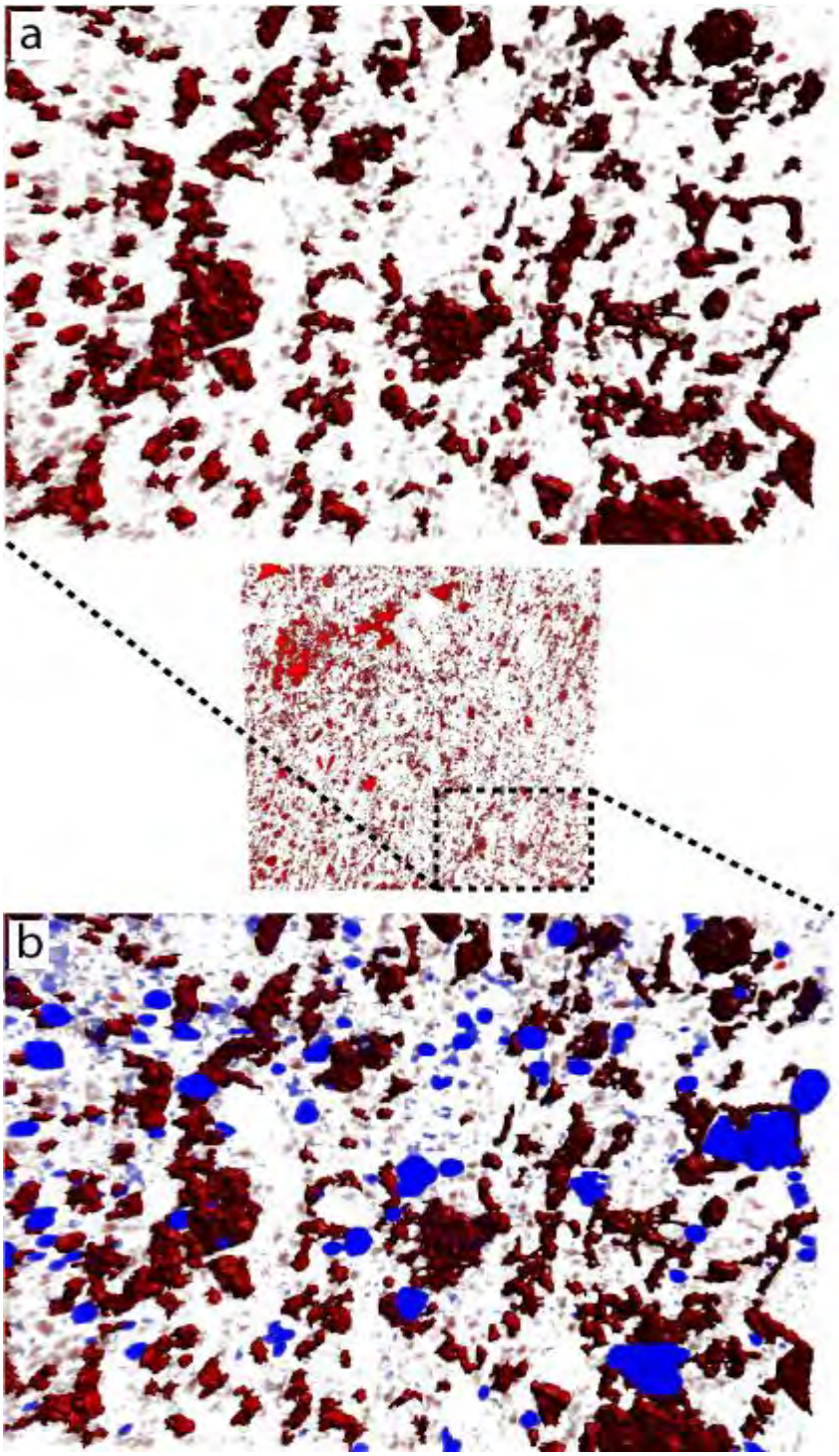

Figure 2.23: 3D volume reconstruction based on 10 sequential CLSM images of organic matter. (a) side view of 3D volume of organic matter from Figure 2.21a; (b) side view of 3D volume of pyrite (blue) replacing organic matter (red) from Figure 2.21a.

Partial replacement of organic matter is best observed in Figures 2.22b and 2.23, where pyrite (blue) closely associated with organic part (red). Considerable amount of reworked organic matter is localized in elongated pores along silicate and pyrite grain boundaries (right side of Figure 2.23a).

2.5.4. **Bazhenov Formation - Sample E**

Table 2.4: Petrophysical and image analysis properties of Bazhenov Formation (sample E) obtained in this study and from Vernik and Landis (1996).

Lithology	Shale	Source
Depth	3822 m	Vernik and Landis (1996)
Density	2.63 g/cc	Vernik and Landis (1996)
Total Organic Carbon (TOC, % weight)	2.83%	Vernik and Landis (1996)
Vitrinite Reflectance (R_o, %)	0.78	Vernik and Landis (1996)
Hydrogen Index (HI)	279mg/g	Vernik and Landis (1996)
Porosity (helium porosimetry)	2.26%	Vernik and Landis (1996)
P-Wave Velocity --$V_p(0^\circ)$	3.82 km/s	Vernik and Landis (1996)
S-Wave Velocity --$V_s(0^\circ)$	2.56 km/s	Vernik and Landis (1996)
Kerogen Volume	8.7%	Vernik and Landis (1996)
Kerogen Volume (543nm exc. wavelength)	6.6%	(this study)
Volume of Pyrite (488nm exc.)	2.5%	(this study)
Volume of Pyrite (458nm exc.)	3.5%	(this study)
Area of Pyrite (image analysis)	2.2%	(this study)
Porosity (image analysis of BSE)	1.3%	(this study)

Figure 2.24 shows backscatter SEM image of Bazhenov Formation Sample E. Photomicrograph shows pyrite and bed-parallel kerogen lenses along elongated clay platelets and rounded silt fraction. Porosity is below 3% (Vernik and Nur, 1992b) with pore sizes dominated by submicron size.

Figures 2.25a and 2.25b are photomicrographs obtained under *BSE* and *SE* modes, respectively. Figures 2.25c is a magnified view of the area within Figure 2.25a showing extensive presence of framboidal pyrite. Figures 2.25d is a magnified view of the area within Figure 2.25a showing broken clay particle (red arrow).

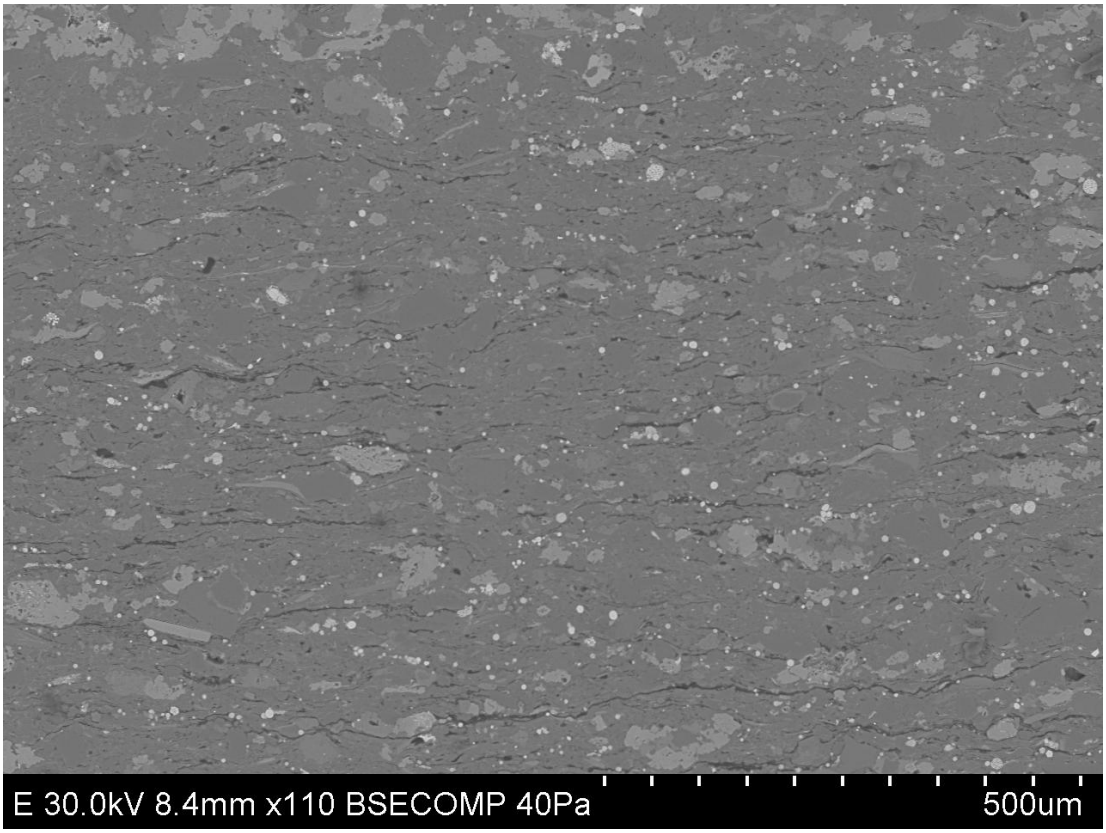

Figure 2.24: Backscatter SEM photomicrographs of Bazhenov Formation Sample E showing microfabric including frarmboidal pyrite (white dots) and bed-parallel kerogen lenses (in black). Longer side of each image is ~1mm.

Sample E (Figure 2.26) contains two distinct maceral types. Images 2.26a and 2.26b show alginate macerals. Alginite macerals, predominantly derived from blue-green and green algal precursors, are dispersed throughout Phanerozoic (e.g. Cook et al., 1981, Goodarzi et al., 1987) and late Precambrian rocks (Crick et al., 1988) and are of particular interest because of their excellent potential as a source for petroleum (Stasiuk, 1994). Figures 2.26c and 2.27d (magnified view of Figure 2.26c) show fusinite (inertinite maceral group) maceral with well-preserved cell structure. The well-preserved cellular structure is derived from plant material that has been strongly altered and degraded, typical of fusinite. Chemically, fusinite is characterized by relatively high carbon content and low contents of hydrogen, oxygen and other volatile components and originates from ligno-cellulosic cell walls.

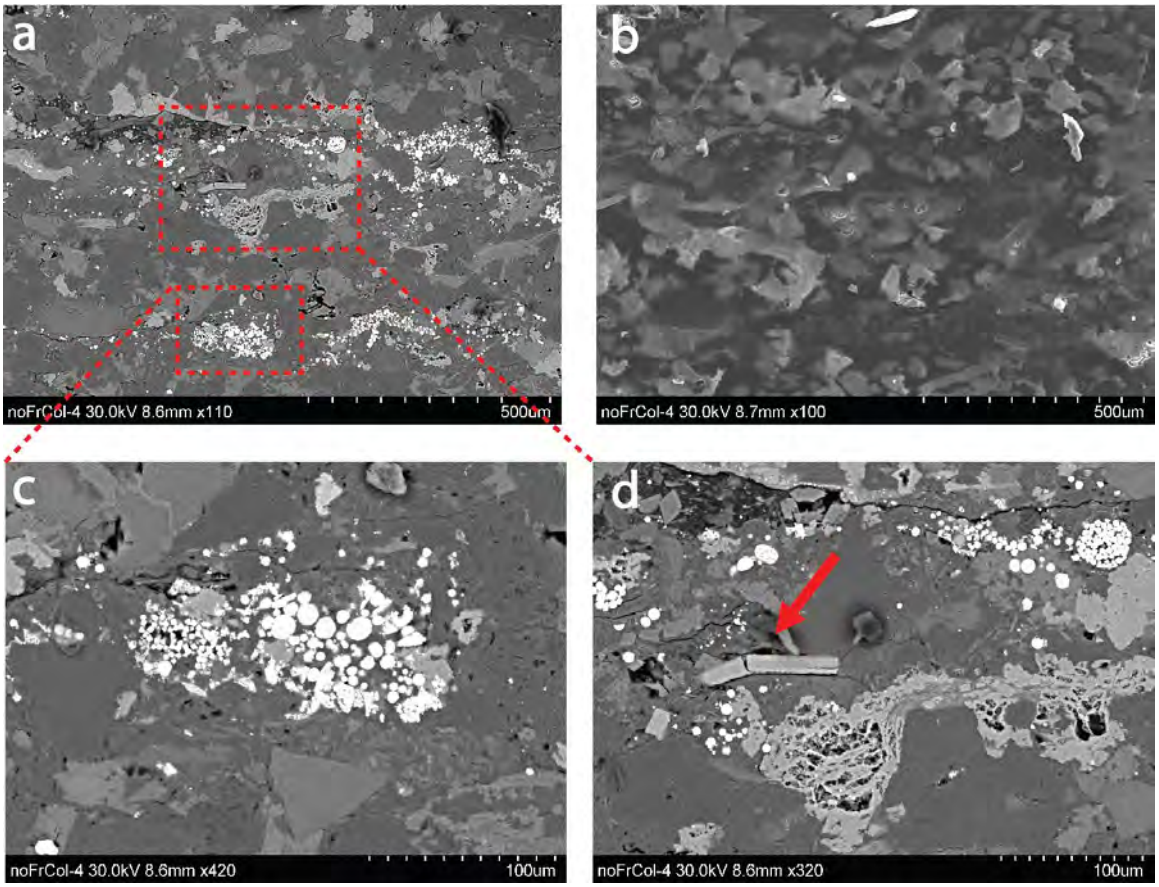

Figure 2.25: Photomicrographs of Bazhenov Formation Sample E microfabric a) Backscatter SEM, b) secondary electron SEM, c) is a magnified view of the area within Figure 2.25a showing extensive presence of framboidal pyrite, d) is a magnified view of the area within Figure 2.25a showing broken clay particle indicated by the red arrow.

According to ICCP (2001) mainly the resistant lignified portions of the cell walls ―survived" during fusinitization. Some fusinite is derived from wild fires which resulted in the formation of fossil charcoal (pyrofusinite) (Goodarzi, 1985; Varma, 1996; Scott, 1989; Jones et al., 1991. According to Varma (1996) and Taylor et al. (1998), fusinite can also generate by decarboxylation of plant tissues with the aid of fungi and bacteria, or by dehydration and weathering. In contrast, Guo and Bustin (1998) and Bustin and Guo (1999) consider all fusinite to be the product of incomplete combustion.

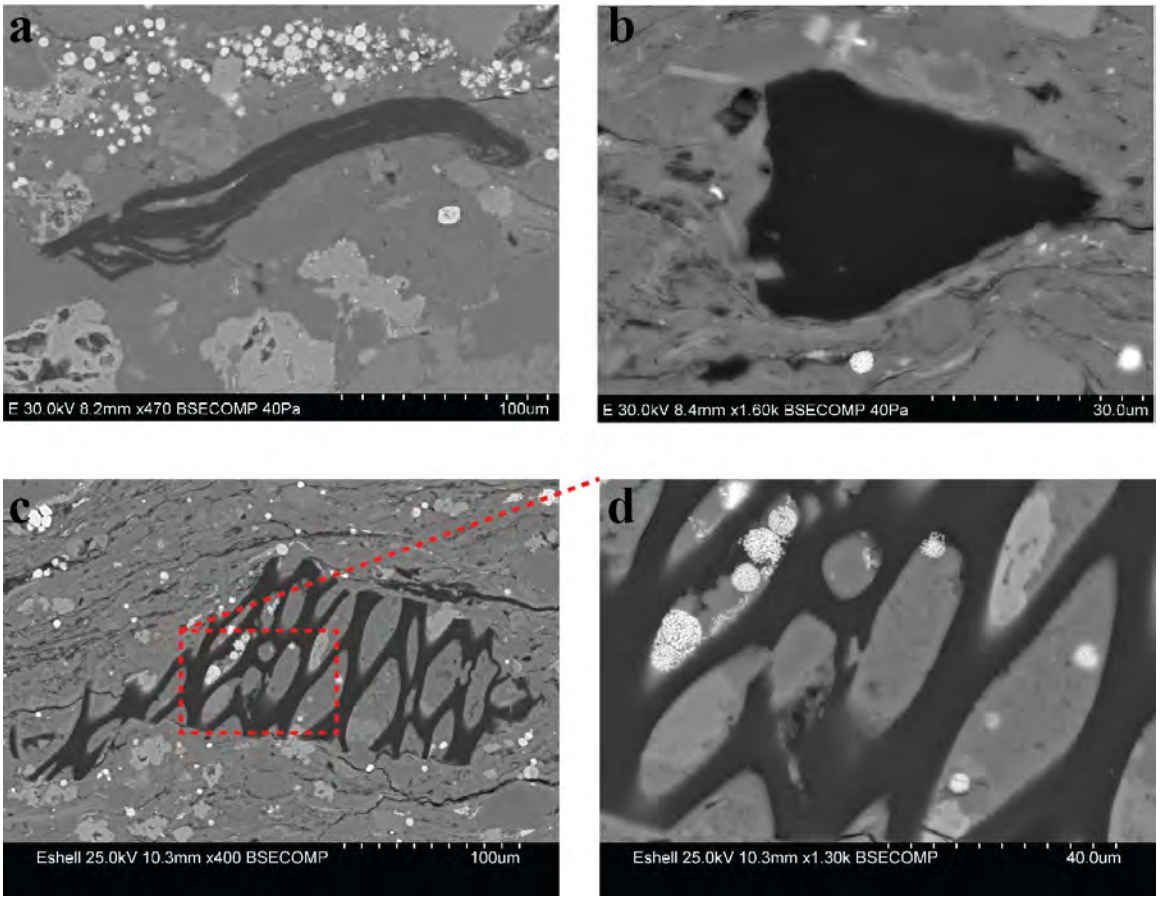

Figure 2.26: Backscatter SEM photomicrographs of Bazhenov Forrmation sample E showing two maceral types a) alginite, b) portion of alginate, c) fusinite macerals with well-preserved cellular structure, d) close-up view of fusinite maceral with visible intercellular pores depicted in (c).

Figures 2.27a and 2.27b display CLSM images of the area covered in *BSE* SEM photomicrograph (Figure 2.27c) and Figure 2.27d is a composite CLSM image where the previous two images were superimposed (2.27a and 2.27b). The CLSM images were obtained under two excitation wavelengths: (a) 543 nm; (b) 488 nm. The pyrite inclusions fluoresce at 488 wavelength excitation. In the image (a) obtained at excitation wavelength 543 nm, the pyrite is invisible while the bright-red features represent organic matter. In the composite image (d) both the organic matter and pyrite are visible, while the dark greenish background is predominantly quartz, feldspar and clay.

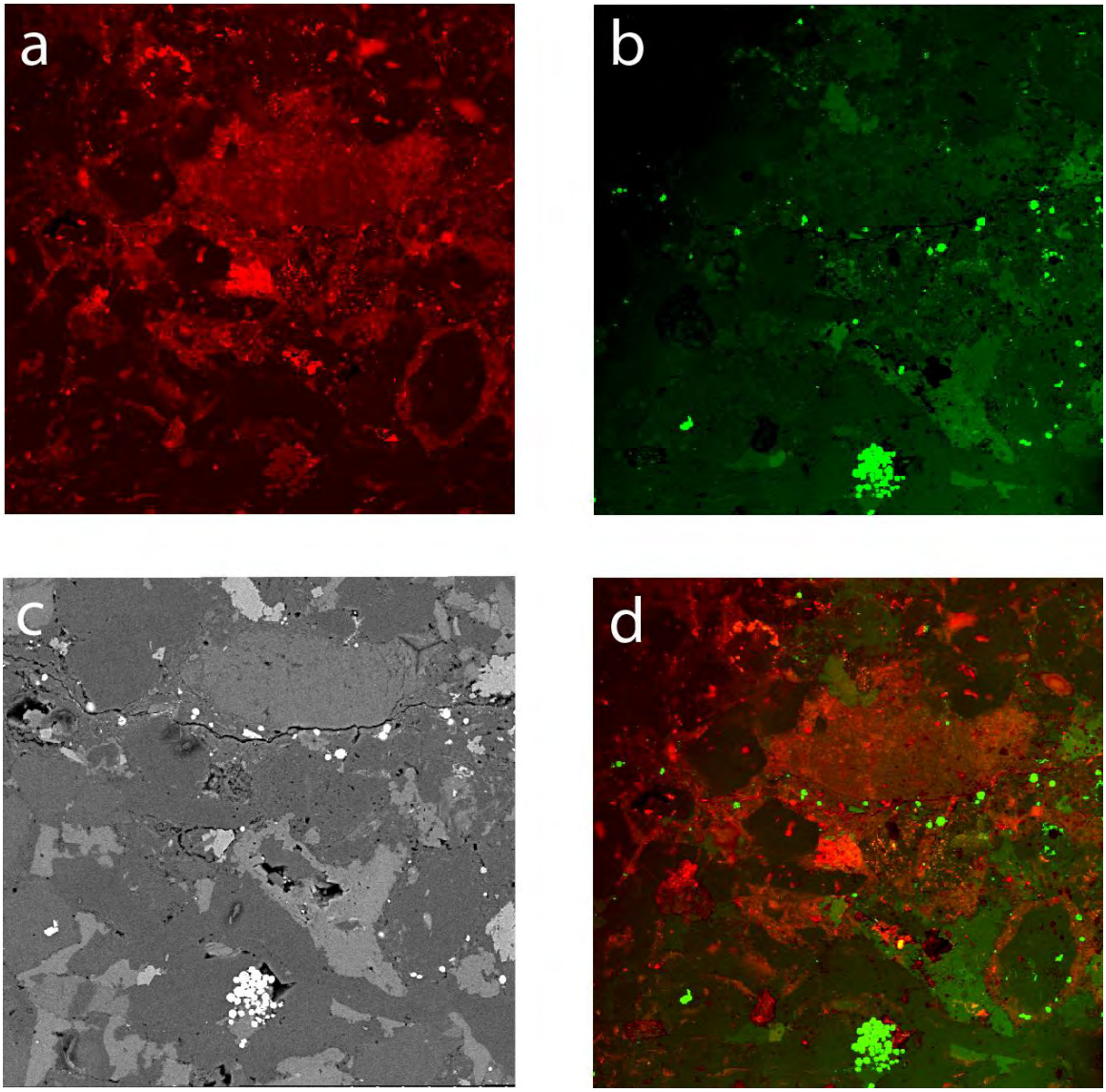

Figure 2.27: CLSM image of the area covered in *BSE* SEM photomicrograph (c), a) under red light excitation (543nm), b) under green light excitation (488nm), c) *BSE* SEM photomicrograph, d) is a composite CLSM image where the previous two images were superimposed (a and b). Image size is 311×311 μm.

2.5.5. **Monterey Formation - Sample D**

Table 2.5: Petrophysical and image analysis properties of Monterey Formation (sample D) obtained in this study and from Vernik and Landis (1996).

Lithology	Opal-CT Porcelanite	Source
Depth	1390 m	Vernik and Landis (1996)
Density	2.17 g/cc	Vernik and Landis (1996)
Total Organic Carbon (TOC, % weight)	2.40%	Vernik and Landis (1996)
Vitrinite Reflectance (R_o, %)	0.38	Vernik and Landis (1996)
Hydrogen Index (HI)	537mg/g	Vernik and Landis (1996)
Porosity (helium porosimetry)	11.4%	Vernik and Landis (1996)
P-Wave Velocity --$V_p(0^\circ)$	3.91 km/s	Vernik and Landis (1996)
S-Wave Velocity --$V_s(0^\circ)$	2.57 km/s	Vernik and Landis (1996)
Kerogen Volume	5.8%	Vernik and Landis (1996)
Kerogen Volume (515nm exc. wavelength)	4.4%	(this study)
Volume of Pyrite (488nm exc.)	1.9%	(this study)
Volume of Pyrite (458nm exc.)	1.1%	(this study)
Area of Pyrite (image analysis)	0.9%	(this study)
Porosity (image analysis of BSE)	4.4%	(this study)

Sample D, unlike previously described samples, is lithologically classified as an opal-CT porcelanite (Figure 2.28). Porcelanites are composed primarily of microcrystalline silica and, according to the Bramlette (1946), Murata and Larson (1975), Williams (1982), and Dholakia et al. (1998), are characterized by a subvitreous luster that resembles broken unglazed porcelain. Porcelanite of the Monterey Formation is the product of a diagenetic process that begins with deposits of siliceous diatom tests. The conversion from diatomite to quartz is well documented in the literature (i.e., Murata and Larson, 1975; Isaacs, 1981; and Graham and Williams, 1985). The process begins with tests of diatoms that consist of amorphous hydrated silica (opal-A phase). Deposits of high concentrations of diatoms, where lithified as diatomite, have an extremely high porosity ~55–60% (Isaacs, 1981). Hurd (1983) suggested Monterey Formation silica originated as biochemically precipitated siliceous skeletal elements, such as sponge spicules, radiolarian tests, and diatom frustules—that is, as amorphous silica colloids.

With burial and increasing time, formation pressure, and temperature, the opal-A chemical structure becomes unstable and dissolves, yielding precipitation of a more stable mixture of cristobalite and tridymite (opal-CT phase) (Williams et al., 1985). The principle elements of opal-A (silica and oxygen) combine in a more tightly packed crystalline structure that has less surface area (Williams et al., 1985).

Opal-CT–phase porosity decreases to 25–35% in the most silica-rich samples (Isaacs, 1981). The opal-CT–phase mineralogy in turn becomes unstable over time, as the overburden thickness increases and formation pressure and temperature continue to rise. Cristobalite and tridymite dissolve, and more stable microcrystalline quartz precipitate - quartz phase (Williams et al., 1985). Generally, the transformation of opaline silica in these sediments undergoes diagenetic change over time to the stable silica polymorph, quartz, through the pathway opal-A → opal-CT → quartz (Murata and Larsen, 1975; Oehler, 1975; Isaacs, 1980; Williams et al., 1985). In the coastal basins of California, chert and porcelanite can form as precipitating quartz fills much of the remaining porosity resulting in porosity of 10- 20% (Isaacs, 1981). The diagenetic process of converting opal-A to chert is accompanied by fluid flow due to dehydration reactions and chemical compaction (Eichhubl and Behl, 1998). The porosity reduction occurs as the matrix framework collapses and the rock compacts (Reid and McIntyre, 2001), and if the diagenetic water cannot be released, high pore fluid pressures may result in the formation of significant fracture networks, as observed in Monterey rocks in the coastal basins of California (Eichhubl and Boles, 1998).

Opal-A reservoirs are matrix porosity–dominated reservoirs, whereas opal-CT and quartz reservoirs, although sometimes maintaining some matrix porosity, are commonly fracture dominated (Chaika and Williams, 2001). Within opal-CT phase, porosity averages between 20-25% and is evenly distributed throughout the porcelanite in the form of extremely small pores ranging in size from 1 to 10 μm, thus resulting in matrix permeability values <1md, with flow of oil and gas primarily through fractures parallel with and perpendicular to bedding (Reid and McIntyre, 2001).

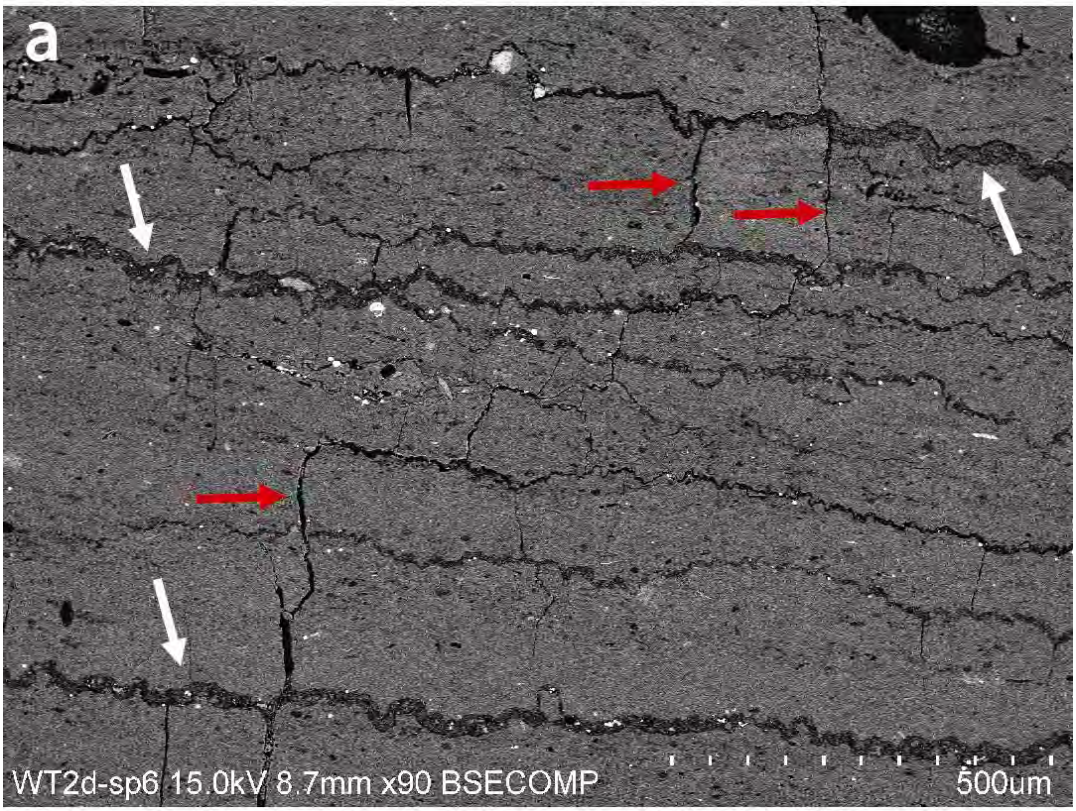
a
WT2d-sp6 15.0kV 8.7mm x90 BSECOMP
500um

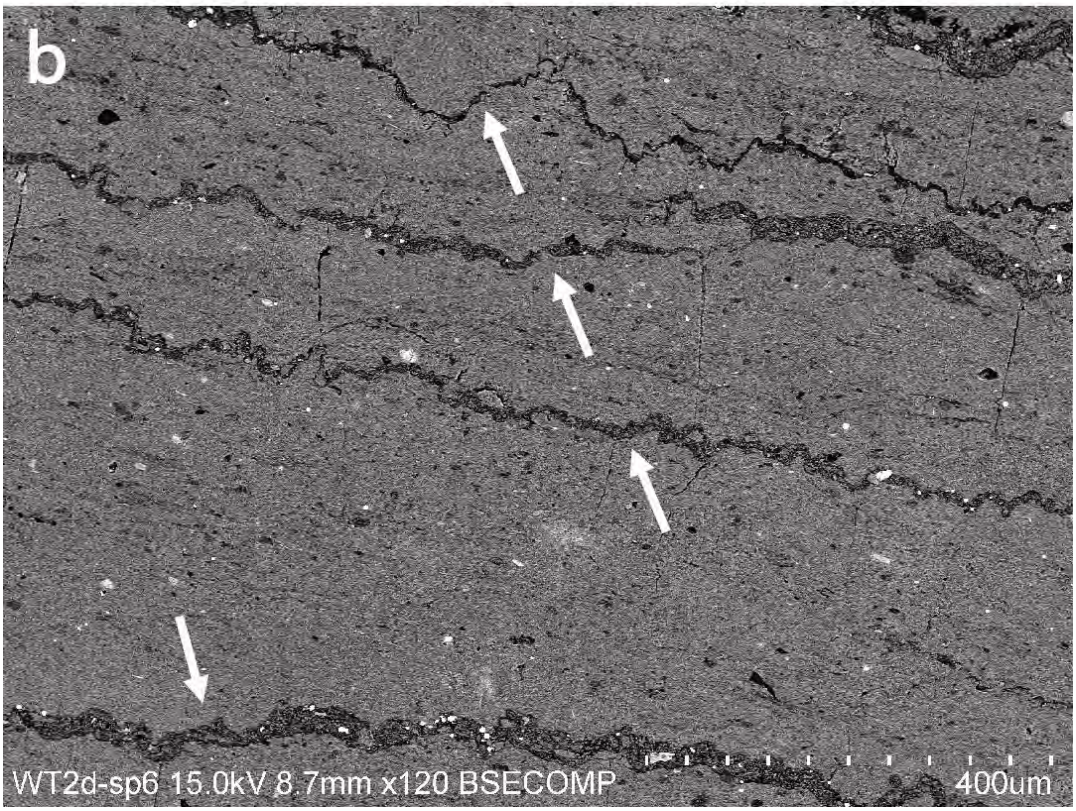
b
WT2d-sp6 15.0kV 8.7mm x120 BSECOMP
400um

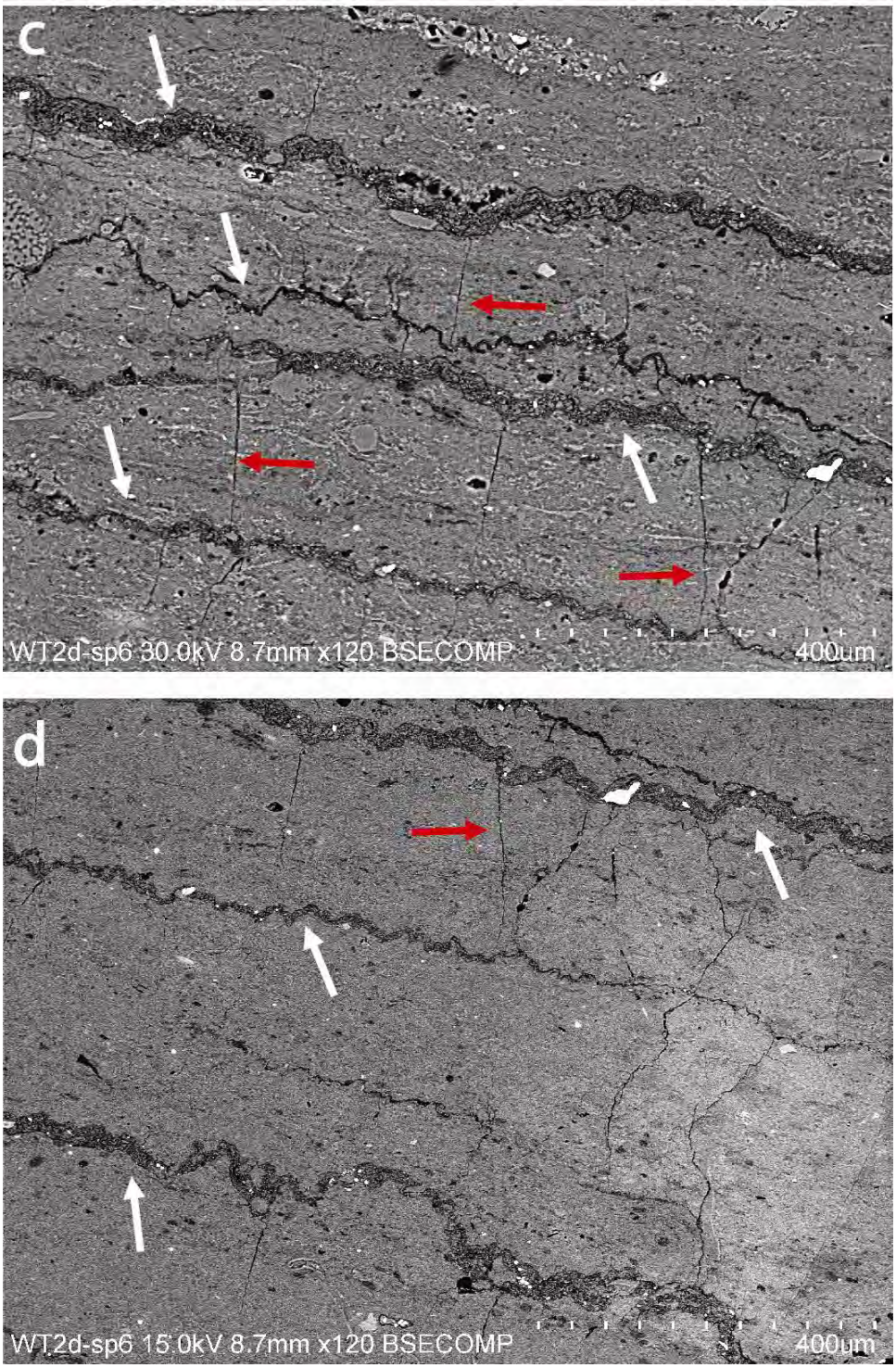

Figure 2.28a-d: Backscatter SEM photomicrographs of Monterey Formation Sample D showing microfabric of opal-CT porcelanite including frarmboidal pyrite, bed-parallel stylolites stained by organic matter (dark infill within stylolites marked by white arrows) and bed-othogonal opening mode (Mode I) fractures (marked by red arrows). Note the presence of large number of pyrite framboids within the pressure solution surfaces compared to the host rock. Longer side of each image is ~1mm.

In addition to fractures within porcelanite (marked in Figure 2.28 by red arrows), visual evidence of mechanical compaction based on thin section analysis and common presence of pressure solution seams known as stylolites (marked in Figure 2.28 by white arrows) are documented in Monterey Formation by Williams (1982, 1988). Pressure solution can decrease porosity effectively both by chemical compaction and by cementation (Rittenhouse, 1971). Figure 2.28 shows a collage of four photomicrographs from opal-CT porcelanite sample within Monterey Formation. The most striking feature of all images within Figure 2.28 is a presence of bed-parallel pressure solution seams filled with organic matter, which has darker color than host rock (it means its lighter than host rock in Backscatter SEM). In addition, extensive presence of vertical (orthogonal to bedding) fractures is documented. These fractures are bound by parallel stylolites in most cases, making them younger structural elements compared to the pressure solution seams. An interesting observation is the presence of large number of pyrite framboids within the pressure solution bodies compared to the host rock. According to Durand (1980), pyrite could only be chemically destroyed in the lab via complex application of reactive agents. The mechanical compaction due to overburden, has very small (if any) effect on pyrite because elastic moduli of pyrite (as discussed in Chapter 4) and according to Woeber et al (1963), Le Page and Rodgers (2005), Mavko et al., (2009) are much larger than those of the stiffest silicate mineral present in the rock (in this case, of amorphous silica). Therefore, we speculate that pyrite present within pressure solution seams was originally formed within mineral matrix, and then, as progressively more rock mass was dissolved within pressure solution surfaces and transported through stylolites and fractures, the pyrite framboids (stable to the chemical and physical influence) remained within these seams.

Figures 2.29a-c display CLSM images of the Monterey Formation sample D and Figure 2.28d is a composite CLSM image where the previous three images were superimposed (2.28a, 2.28b and 2.27c). The CLSM images were obtained under three excitation wavelengths: (a) 488 nm; (b) 543 nm and (c) 515 nm. The pyrite inclusions within bed-parallel pressure solution surface fluoresce primarily under green and red light

wavelength excitation. Organic matter fluoresces primarily under yellow light. In the composite image (d) both the organic matter and pyrite are visible. The fluorescence intensity is higher within pressure solution seam.

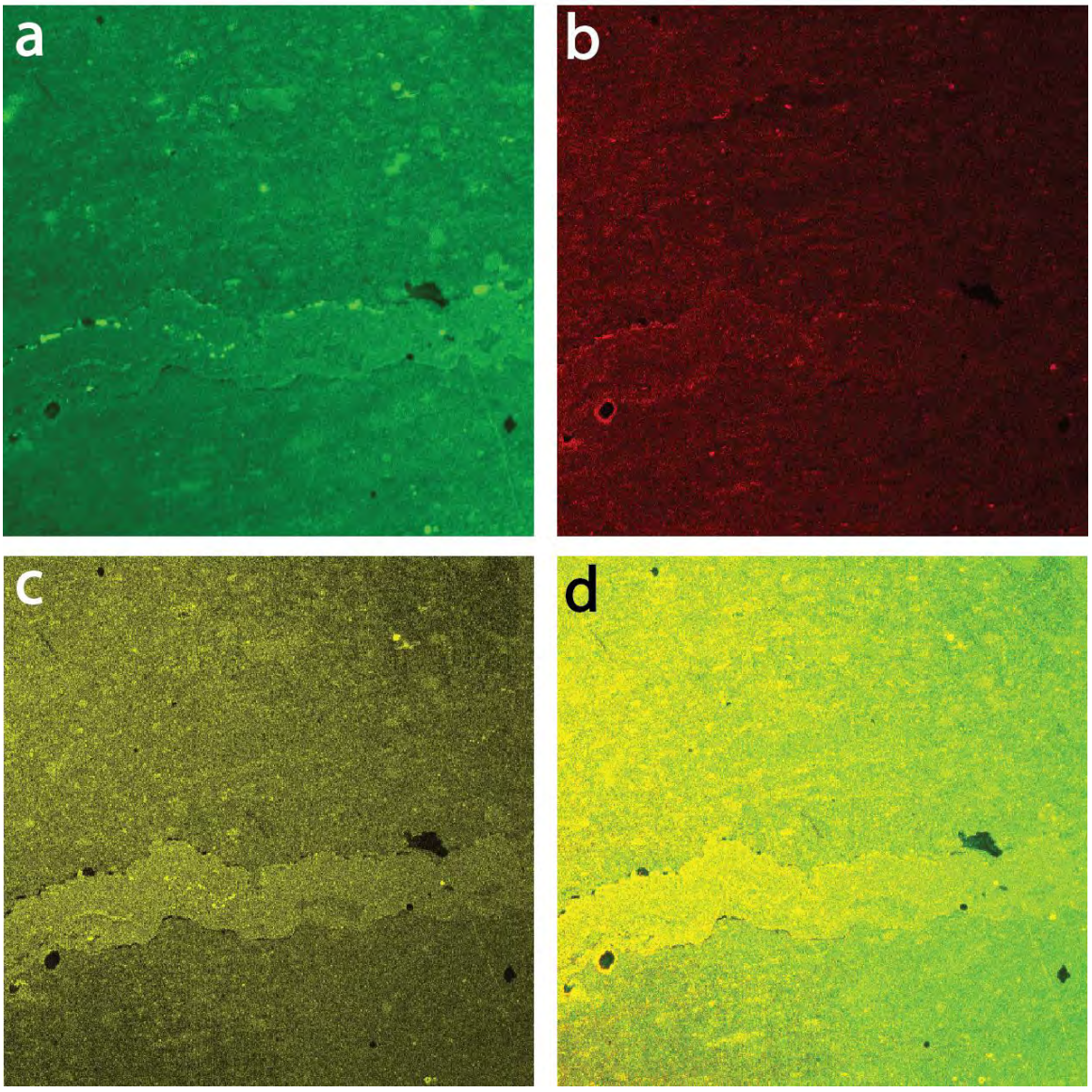

Figure 2.29: CLSM image of the Monterey Formation sample D, a) under green light excitation (488nm), b) under red light excitation (543nm), c) under yellow light excitation (515nm), d) is a composite CLSM image where the previous two images were superimposed (a and b). Image size is 500×500 μm.

2.5.6. **Lockatong Formation - Sample H**

Table 2.6: Petrophysical and image analysis properties of Lockatong Formation (sample H) obtained in this study and from Vernik and Landis (1996).

Lithology	Siliceous dolomite	Source
Depth	549 m	Vernik and Landis (1996)
Density	2.70 g/cc	Vernik and Landis (1996)
Total Organic Carbon (TOC, % weight)	2.84%	Vernik and Landis (1996)
Vitrinite Reflectance (R_o, %)	2.58	Vernik and Landis (1996)
Hydrogen Index (HI)	2mg/g	Vernik and Landis (1996)
Porosity (helium porosimetry)	0.3%	Vernik and Landis (1996)
P-Wave Velocity --$V_p(0^\circ)$	5.69 km/s	Vernik and Landis (1996)
S-Wave Velocity --$V_s(0^\circ)$	3.28 km/s	Vernik and Landis (1996)
Kerogen Volume	8.2%	Vernik and Landis (1996)
Kerogen Volume (543nm exc. wavelength)	5.6%	(this study)
Volume of Pyrite (488nm exc.)	2.9%	(this study)
Volume of Pyrite (458nm exc.)	2.1%	(this study)
Area of Pyrite (image analysis)	1.8%	(this study)
Porosity (image analysis of BSE)	n/a	(this study)

Sample H, unlike previously described samples, lithologically classified as siliceous dolomite (Figure 2.30). Dolomite is a major component of limestone. It is ususally secondary, replacing pre-existing carbonate minerals. Unlike calcite, it often occurs as euhedral rhomb-shapes crystals (Figure 2.31). On the degree of dolomitisation, carbonate rocks can be divided into four categories: limestones (up to 10% dolomite), dolomitic limestone (10–50% dolomite), calcitic dolomite (50–90% dolomite) and dolomite (90–100% dolomite). Even though Sample H falls within *calcitic dolomite* nomenclature, it is composed of 73% dolomite and 20% of quartz-feldspar (Venik and Landis, 1996), therefore term *siliceous dolomite* is more appropriate.

The majority of dolomites, especially those of the Phanerozoic (including Upper Jurassic Lockatong Formation), have formed by replacement of limestones. This dolomitisation can take place soon after deposition, i.e., contemporaneously and notably upon high intertidal– supratidal flats in semi-arid regions, or later during shallow-burial

or deeper burial diagenesis. Early-formed, peritidal dolomite is typically very fine-grained and is associated with structures indicative of supratidal conditions: desiccation cracks, evaporites and their pseudomorphs, microbial laminites and fenestrae (Tucker, 2003). Fine-grained dolomites like these usually preserve the structures of the original sediment very well. Later diagenetic dolomitisation can vary from local replacement of certain grains, or just the lime–mud matrix and not the grains, or just burrows, or it may affect the whole limestone bed, the formation or just a particular facies. Rhombs of dolomite may be seen concentrated along stylolites. The dolomite may occur in veins cutting through the limestone, or in vugs- irregular holes lined with dolomite crystals. In these cases other minerals, such as calcite, fluorite or galena, may be associated (Tucker, 2003).

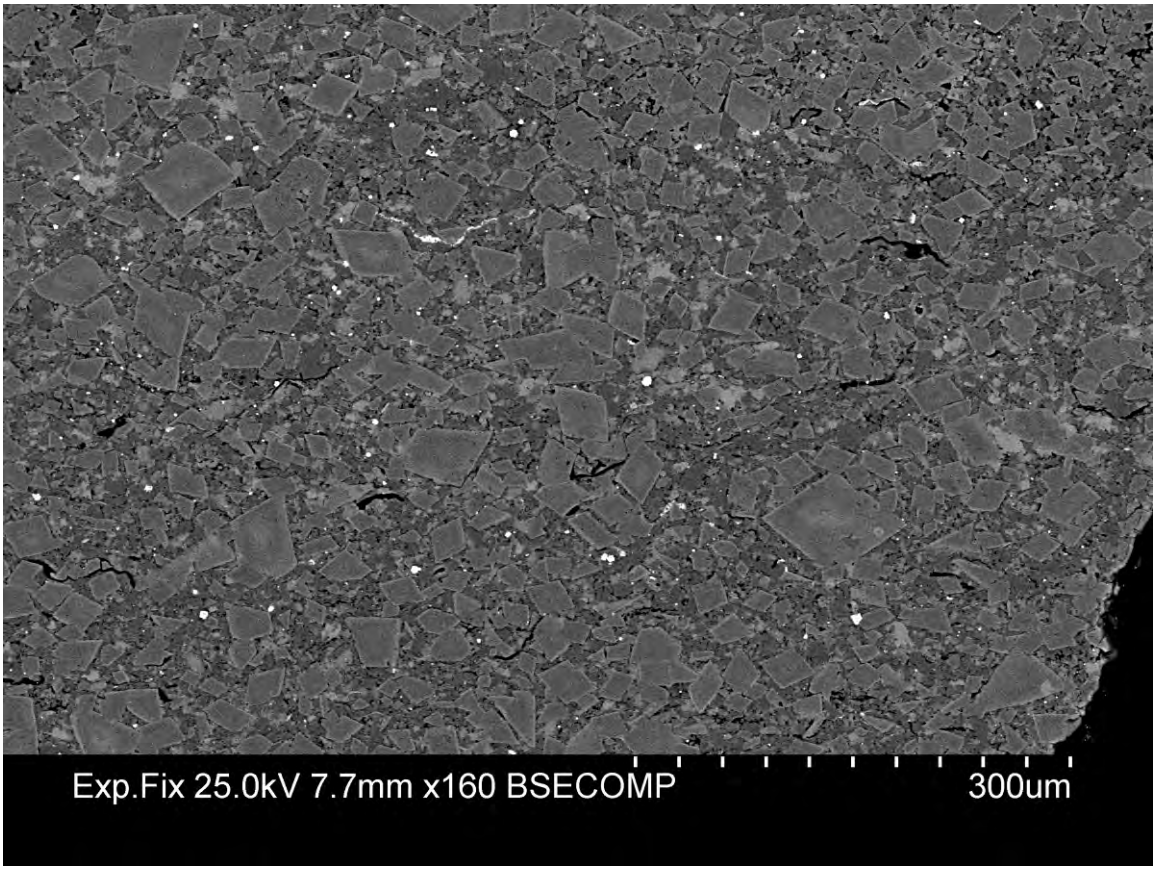

Figure 2.30: *BSE* SEM photomicrograph of Lockatong Formation sample H showing microfabric composed primary of coarse-grained euhedral dolomite (in the shape of rhombs). Elongated black lenses represent organic matter. Bright white dots are pyrite framboids.

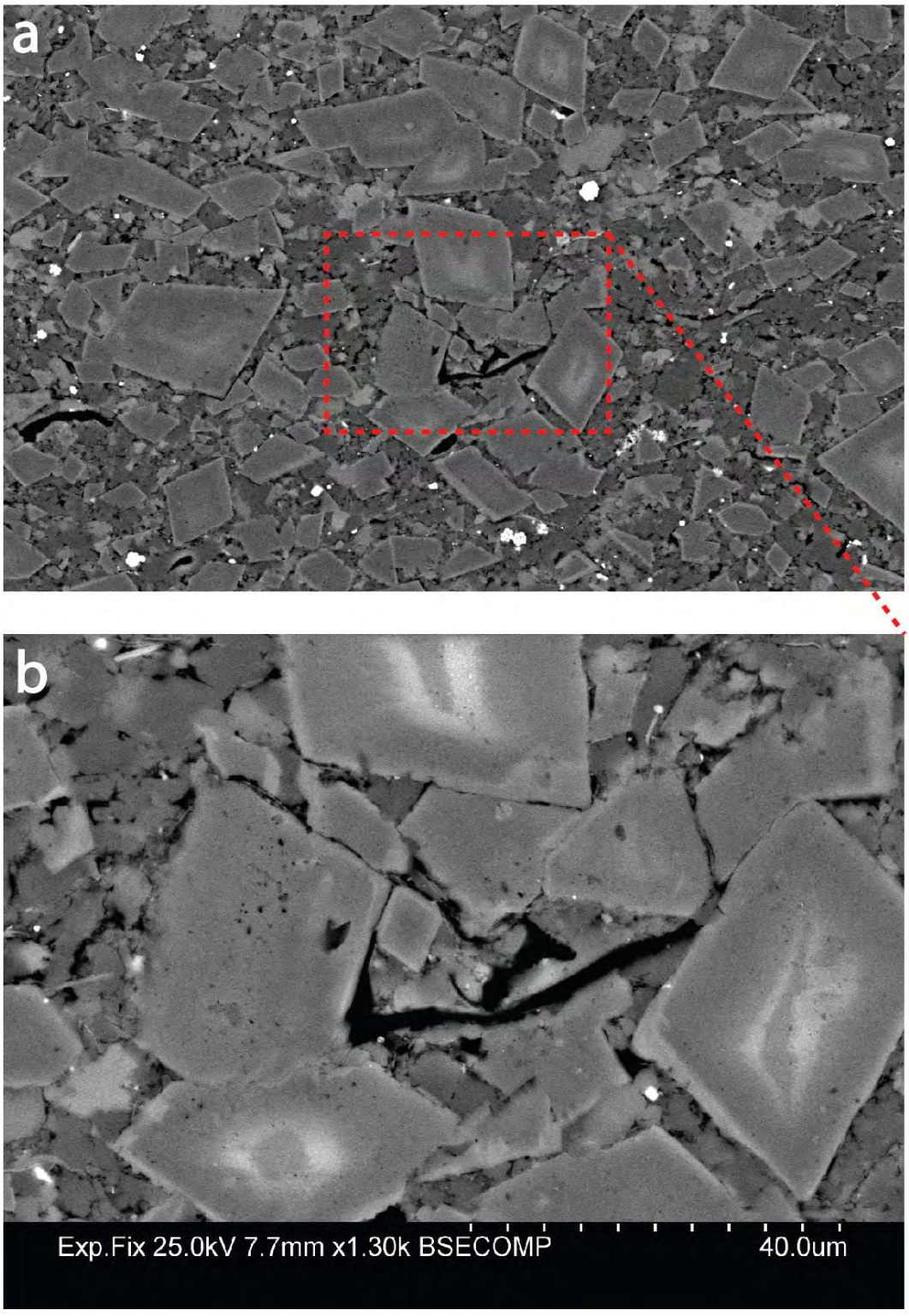

Figure 2.31: *BSE* SEM photomicrograph of Lockatong Formation sample H showing microfabric composed primary of a) coarse-grained euhedral dolomite with black pore-filling organic matter, b) magnified view of (a).

Many limestones are pervasively dolomitised, and then there is commonly an obliteration of the original structure of the sediment, so that fossils are poorly preserved and sedimentary structures ill-defined. With some dolomites the dolomitisation relates to tectonic structures; for example, the dolomite may occur adjacent to a fault (up which the dolomitising fluids migrated) or to major joints. The dolomitisation may be restricted to a particular stratigraphic level or certain facies, or relate to a certain stratigraphic horizon, such as occurring beneath an unconformity (Tucker, 2003).

Figures 2.32a-d display CLSM images of the Lockatong Formation sample H and Figure 2.32d is a composite CLSM image where the previous four images were superimposed (2.32a, 2. 32b, 2.32c and 2.32d).

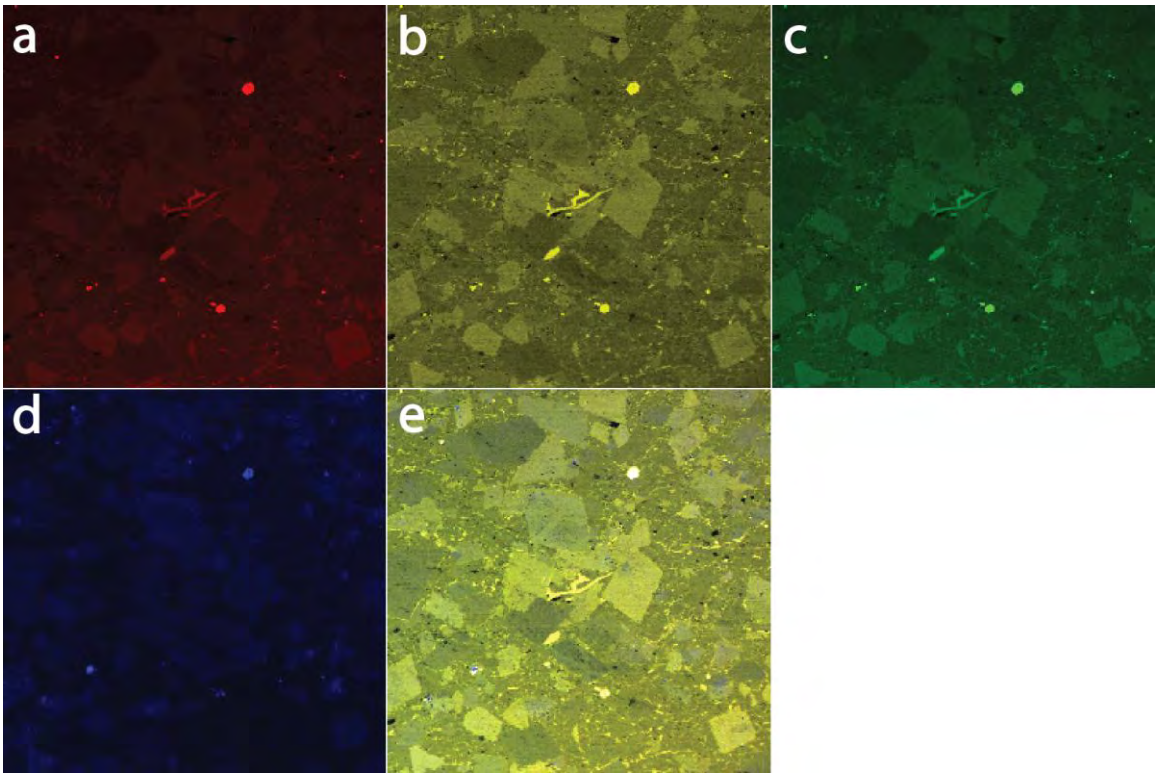

Figure 2.32: CLSM images of Lockatong Formation sample H captured under (a) red light (543 nm), (b) yellow light (515 nm), (c) green light (488 nm), (d) blue light (458 nm) and (e) composite CLSM image where the previous four images were superimposed. Longer side of each image is 225×255µm.

The CLSM images were obtained under three excitation wavelengths: (a) 543 nm; (b) 515 nm (c) 488 nm and (d) 458 nm. The pyrite inclusions within matrix fluoresce under all light wavelength excitations. Organic matter fluoresces primarily under yellow

light, as well as under red and green lights, eventhough in the latter images the fluorescence intensity is weaker. Figure 2.33 shows *BSE* SEM photomicrograph (the area previously shown in Figure 2.31) of Lockatong Formation sample H with corresponding CLSM image captured under green light. Organic matter in this sample fills predominantly fractures and elongated pores at dolomite grain boundaries.

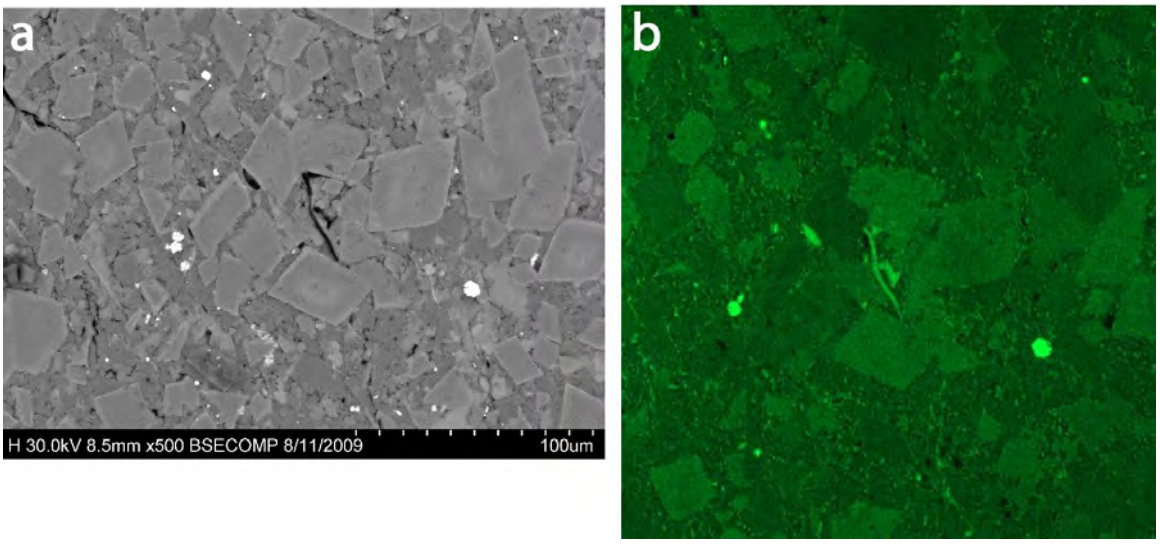

Figure 2.33: a) *BSE* SEM photomicrographs of Lockatong Formation sample H, b) corresponding CLSM image captured under green light (488 nm).

2.6. Chapter Summary

We have analyzed a suite of six source rock samples from Kimmeridge, Bakken, Bazhenov, Monterey and Lockatong Formation using Confocal Laser Scanning- and Scanning Electron Microscopy. The analysis proves that combined application of SEM and CLSM imaging for the microscopic characterization of complex and heterogeneous rock samples is a powerful technique. Organic matter was successfully imaged within the matrix of the source rock samples despite inherent lithologic differences of the phases. A number of valuable observations of spatial distribution of clay, pyrite and kerogen was made. In addition to these observations, we report deformation of clay minerals, quartz grains and presence of pressure solution surfaces in some samples, all attributed to the diagenetic processes within source rocks. The fractional volumes of minerals and organic

matter obtained from image analysis of SEM and CLSM photomicrographs is in good agreement with values previously reported by Vernik and Landis (1996). The organic matter in postmature shale samples of Kimmeridge and Bakken Formations primarily occupies pores at grain boundaries, whereas in mature samples of Bazhenov and Bakken Formations organic matter is bed-parallel and forms elongated lenses. In opal-CT sample of Monterey Formation, the organic matter is predominantly localized within pressure solution surfaces. Within the dolomitic sample of Lockatong Formation, the organic matter fills predominantly fractures and elongated pores at dolomite grain boundaries. The observations and methodology described in this section create a framework for evaluation of spatial distribution of kerogen discussed in detail in Chapter 3 and elastic property estimation at microscale discussed in detail in Chapter 4.

2.7. References

Ahmadov, R., Vanorio, T., and Mavko, G., 2009, Confocal laser scanning and atomic-force microscopy in estimation of elastic properties of the organic-rich Bazhenov Formation, The Leading Edge, 28, pp. 19.

Alkhalifah, T., and D., Rampton, 2001, Seismic anisotropy in Trinidad: a new tool for lithology determination: The Leading Edge, 20, 420–424.

Bandyopadhyay K., 2009, Seismic Anisotropy: Geological Causes and Its Implications to Reservoir Geophysics, Stanford University, Ph.D. Thesis, p.254

Banik, N. C., 1984, Velocity anisotropy in shales and depth estimation in the North Sea basin: Geophysics, 49, 1411–1419.

Beaufort, D., Cassagnabere, A., Petit, S., Lanson, B., Berger, G., Lacharpagne, J.C., and Johansen, H., 1998, Kaolinite-to-dickite reaction in sandstone reservoirs. Clay Miner., 33, 297-316.

Bennett R. H., 1976, Clay fabric and geotechnical properties of selected submarine sediment cores form Mississippi Delta. PhD dissertation, Texas A&M University, College Station, TX, 269 pp

Bennett RH, Bryant WR, and Keller GH, 1977, Clay fabric and geotechnical properties of selected submarine sediment cores from the Mississippi Delta. NOAA Professional Paper 9, US Department of Commerce, 86 pp

Bennett RH, Bryant WR, and Keller GH, 1981, Clay fabric of selected submarine sediments: fundamental properties and models. Journal of Sedimentary Petrology 51(1), 127-152

Berner, R.A., 1980. Early Diagenesis: A Theoretical Approach: Princeton, NJ (Princeton Univ. Press).

Berner, R.A., 1984, Sedimentary pyrite formation: An update, Geochim. Cosmochim. Acta 48, pp. 605–615.

Broichhausen, H., R., Littke, and T., Hantschel, 2005, Mudstone compaction and its influence on overpressure generation, elucidated by a 3D case study in the North Sea: International Journal of Earth Sciences, 94, 956–978.

Boles, J.R., 1984, Influence of mica surface on pore water PH. Chem. Geol., 43: 303-317.

Bramlette, M. N., 1946, The Monterey Formation of California and the origin of its siliceous rocks: U.S. Geological Survey Professional Paper 212, 57 p.

Bryant WR, Bennett RH, and Katherman C, 1981, Shear strength, consolidation, porosity, and permeability of ocean sediments. In: Emiliani C (Ed), The Sea 7. The Oceanic Lithosphere. New York: Wiley, pp 1555-1616

Bustin R. M, and Guo Y., 1999, Int J Coal Geol, v.38, p.237.

Canfield, D.E., and Raiswell, R., 1991, Pyrite formation and fossil preservation, in Allison, P.A., and Briggs, D.E.G., eds., Taphonomy: Releasing the Data Locked in the Fossil Record: New York, Plenum Press, p. 337–387.

Chaika C., and Williams, A, 2001, Density and Mineralogy Variations as a Function of Porosity in Miocene Monterey Formation Oil and Gas Reservoirs in California, AAPG Bulletin, v. 85, no. 1 (January 2001), pp. 149–167

Chi, H. M. Xiao, Z. D. Fu, D. G. and Lu, Z. H., 2006, Analysis of fluorescence from algae fossils of the Neoproterozoic Doushantuo formation of China by confocal laser scanning microscope. Microsc Res Tech, 69, 253-259.

Coleman, M., Raiswell, R., 1995, Source of carbonate and origin of zonation in pyritiferous carbonate concretions: evaluation of a dynamic model. Am. J. Sci. 295, 282–308.

Cook, A. C., Hutton, A. C. and Sherwood, N. R., 1981, Classification of oil shales Bull. Cent. Rech. ExpL Prod. Elf-Aquitaine 5, 353-381

Crick, I. H., Boreham, C. J., Cook, A. C. and Powell, T. G., 1988, Petroleum geology and geochemistry of Middle Proterozoic McArthur Basin, Northern Australia I1: assessment of source rock potential Am. Assoc. Petrol GeoL Bull. 72, 1495-1514

Davies D. K., Bryant W. R., Vessell R. K., and Burkett P. J., 1991, Porosities, permeability, and microfabrics of Devonian shales. In: Bennett RH, Bryant WR, and Hulbert M.H., (Ed.), Microstructure of Fine-Grained Sediments from Mud to Shale. New York: Springer-Verlag, pp 109-119

Dholakia, S. K., A. Aydin, D. D. Pollard, and M. D. Zoback, 1998, Fault-controlled hydrocarbon pathways in the Monterey Formation, California: AAPG Bulletin, v. 82, p. 1551–1574.

Durand, B., 1980, Kerogen: Insoluble Organic Matter from Sedimentary Rocks, Imperimerie Bayeusaine, Editions Technip, p.519.

Egerton, R. F., 2005, Physical principles of electron microscopy : an introduction to TEM, SEM, and AEM. Springer, p. 202.

Ehrenberg, S.N., Aagaard, P., Wilson, M.J., Fraser, A.R., and Duthie, D.M.L.,1993, Depth-dependent transformation kaolinite to dickite in sandstones of the Norwegian Continental Shelf. Clay Miner., 28, 325-352.

Eichhubl, P., and R. J. Behl, 1998, Diagenesis, deformation, and fluid flow in the Miocene Monterey Formation, in P. Eichhubl, ed., Diagenesis, deformation, and fluid flow in the Miocene Monterey Formation: Pacific Section SEPM, book 83, p. 5–13.

Eichhubl, P., and J. R. Boles, 1998, Vein formation in relation to burial diagenesis in the Miocene Monterey Formation, Arroyo Burro Beach, Santa Barbara, California, in P. Eichhubl, ed., Diagenesis, deformation, and fluid flow in the Miocene Monterey Formation: Pacific Section SEPM, book 83, p. 15–36.

Geiser, P.A. and Sansone, S., 1981, Joints, microfractures and the formation of solution cleavage in limestones. Geology, 9: 280-285.

Goldhaber, M.B., and Kaplan, I.R., 1974. The sulfur cycle. In Goldberg, E.D. (Ed.), The Sea (v. 5): Marine Chemistry: The Sedimentary Cycle: New York (Wiley-Interscience), p. 569–655.

Goldstein, J., 2003, Scanning electron microscopy and x-ray microanalysis. Kluwer Adacemic/Plenum Pulbishers, p. 689.

Goodarzi F., 1985, Int J Coal Geol, v.5, p.337.

Goodarzi, F., Davies, G. R., Nassichuk, W. W. and Snowdon, L. R., 1987, Organic petrology and Rock-Eval analysis of Lower Carboniferous Emma Fiord Formation in Sverdrup Basin, Canadian Arctic Archipelago Mar. Petrol. Geol. 4, 132-145

Graham, S. A., and L. A. Williams, 1985, Tectonic, depositional, and diagenetic history of Monterey Formation (Miocene), central San Joaquin basin, California: AAPG Bulletin, v. 69, p. 365–411.

Guo Y., and Bustin R. M., 1998, Int J Coal Geol, v.37, p.29.

Heald M.T., 1959, Significance of stylolites in permeable sandstones. J. Sediment. Petrol., 29: 251-253.

Hornby, B. E., L. M., Schwartz, and J. A., Hudson, 1994, Anisotropic effective-medium modeling of the elastic properties of shales: Geophysics, 59, 1570-1583.

Hunt, J.M., 1968, World Oil 167, 140

Hunt, J.M., 1979, Petroleum Geochemistry and Geology. San Francisco: Freeman.

ICCP (International Committee for Coal and Organic Petrology), 2001, Fuel v.80, p. 459–471

Isaacs, C. M., 1980, Diagenesis in the Monterey Formation examined laterally along the coast near Santa Barbara, California: Ph.D. dissertation, Stanford University, Stanford, California, 329 p.

Johnston, J. E., and N. I., Christensen, 1995, Seismic anisotropy of shales: Journal of Geophysical Research B, 100, 5991–6003.

Jones T. P., Scott A. C., and Cope M., 1991, Bull Soc Geol Fr, v. 162, n.2, p.193.

Jones, L. E. A., and H. F., Wang, 1981, Ultrasonic velocities in Cretaceous shales from the Williston basin: Geophysics, 46, 288–297.

Katsube T. J. and Williamson M. A., 1994, Effects of diagenesis on shale nano-pore structure and implications for sealing capacity. Clay Minerals 29 : 451-461

Katsube T. J., Wires K., Cameron B. I., and Franklin, J. M., 1991, Porosity and permeability of ocean ßoor sediments from the Middle Valley Zone in the northeast Pasific; borehole PAR90-1. Geological Survey of Canada, Paper 91-E : 91-97

Kim, J.-W., Bryant, W.R., Watkins, J.S. & Tieh, T.T., 1999, Electron microscopic observations of shale diagenesis, offshore Louisiana, USA, Gulf of Mexico. Geo Marine Letters, 18, 234–240.

Le Page, Y., Rodgers, J. R., 2005, Ab Initio Elasticity of FeS_2 Pyrite from 0 to 135 GPa. Physics and Chemistry of Minerals, 32(8–9): 564–567.

Lerbekmo, J.F. and Platt, R.L., 1962, Promotion of pressure solution of silica in sandstones, J. Sediment. Petrol., 32: 514-519.

Mavko, G, Mukerji, T. and Dvorkin, J., 2009, The Rock Physics Handbook, Cambridge University Press, p. 511.

McAulay, G.E., Burley, S.D., Fallick, A.E., and Kusnir, N.J., 1994, Paleohydrodymanic fluid flow regimes during diagenesis in the Brent Group in the Hutton-NW Hutton reservoirs: constraints from oxygen isotope studies of authigenic kaolin and reverse flexural modeling. Clay Miner., 29, 609-626.

Murata, K. J., and R. R. Larsen, 1975, Diagenesis of Monterey siliceous shales, Temblor Range, California: United States Geological Survey Journal of Research, v. 3, p. 553–566.

Oehler, J. H., 1975, Origin and distribution of silica lepispheres in porcelanite from the Monterey Formation of California: Journal of Sedimentary Petrology, v. 45, p. 252–257.

O`Brien NR, 1981, SEM study of shale fabric: a review, Scanning Electron Microscopy/1981/I, SEM Inc., pp 569-575

O`Brien NR, 1986, The effects on bioturbation on the fabric of shale. Journal of Sedimentary Petrology 57, 449-455

Philippi, G.T., 1965, Geochim. Cosmochim. Acta 29, 1021

Raiswell, R., 1982, Pyrite texture, isotopic composition and the availability of iron: American Journal of Science, v. 82, p. 1244–1263.

Reid and McIntyre, 2001, Monterey Formation porcelanite reservoirs of the Elk Hills field, Kern County, California, AAPG Bulletin, v. 85, no. 1, pp. 169–189

Reimer, L., 1998, Scanning electron microscopy: physics of image formation and microanalysis. Springer, p. 527.

Rickard, D., 1997, Kinetics of pyrite formation by the H2S oxidation of iron (II) monosulfide in aqueous solutions between 25 and 125°C: The rate equation: Geochimica et Cosmochimica Acta, v. 61, p.

Ritenhouse G., 1971, Pore-space reduction by solution and cementation: Am. Assoc. Petroleum Geologists Bull., v. 55, p. 80-91.

Sayers, C. M., 2005, Seismic anisotropy of shales: Geophysical Prospecting, 53, 667–676.

Scott AC., 1989, Int J Coal Geol, v.12, p.443.

Stasiuk L.D., 1994, Oil-prone alginite macerals from organic-rich Mesozoic and Paleozoic strata, Saskatchewan, Canada, Marine and Petroleum Geology 11, pp. 207–218.

Stasiuk, L.D. Tomica, M. Wong, J. and Pratt, K., 1998, Fluorescence confocal laser scanning microscopy of dispersed organic matter in hydrocarbon source rocks. The Society for Organic Petrology, Abstracts and Programs 15, 88-89.

Sweeney, R. E., and Kaplan, I. R., 1973, Pyrite framboid formation: Laboratory synthesis and marine sediments: Economic Geology, v. 68, p. 618–634.

Taylor G. H., Teichmuller M., Davis A., Diessel C. F. K., Littke R., and Robert P., 1998, Organic petrology. Stuttgart, Berlin: Gebruder Borntraeger.

Thompson, A.F., 1959, Pressure solution and porosity. Soc. Econ. Paleontol. Mineral.. Spec, Publ., 7: 92-110.

Teerman, S.C. Crelling, J.C. and Glass, G.B., 1987, Fluorescence spectral analysis of resinite macerals from coals of the Hanna Formation, Wyoming, U.S.A.: International Journal of Coal Geology, 7, 315-334.

Tissot, B. Califet-Debyser, Y. Deroo G.and Oudin, J.L., 1971, Origin and evolution of hydrocarbons in Early Toarcian shales, Paris Basin, France, Amer. Assoc. Petrol. Geol. Bull. **55**, pp. 2177–2193.

Tissot, B.P., Welte, D.H., 1978, Petroleum Formation and Occurrence. Berlin-Heidelberg-New York: Springer, p. 699.

Tribble JS, Mackenzie ET, and Urmos J., 1991, Physical property changes accompanying deep burial of clay-rich sediments. In: Bennett RH, Bryant WR, and Hulbert M.H., (Ed.), Microstructure of Þne-grained sediments from mud to shale. New York: Springer-Verlag, pp 93-108

Tucker M. E., 2003, Sedimentary rocks in the field, Wiley; 3rd edition, p. 244

Vanorio, T., T. Mukerji, and G. Mavko, 2008, Emerging methodologies to characterize the rock physics properties of organic-rich shales: The Leading Edge, 27, no. 6, 780–787

Varma AK., 1996, Int J Coal Geol, v.30, p.327.

Vernik, L., and Landis, C., 1996, Elastic Anisotropy of Source Rocks: Implications for Hydrocarbon Generation and Primary Migration: AAPG Bulletin, 80, 531-544.

Vernik, L. and Nur, A., 1992a, Petrophysical Analysis of the Cajon Pass Scientific Well: Implications for Fluid Flow and Seismic Studies in the Continental Crust, J. Geophys. Res. 97, 5121–5134.

Vernik, L., and A., Nur, 1992b, Ultrasonic velocity and anisotropy of hydrocarbon source rocks: Geophysics, 57, 727–735.

Wang, Q., and Morse, J.W., 1996, Pyrite formation under conditions approximating those in anoxic sediments I. Pathway and morphology: Marine Chemistry, v. 52, p. 99–121.

Wang, Z., 2002, Seismic anisotropy in sedimentary rocks: Part 2—Laboratory data: Geophysics, 67, 1423–1440.

Weyl, P.K., 1959, Pressure solution and the force of crystallization a phenomenological theory. J. Geophys. Res., 64: 2001-2025

Wilkins, R. W. T,. Wilmshurst, J. R Hladky, G. Ellacott, M. V.and Buckingham, C. P., 1995, Should fluorescence alteration replace vitrinite reflectance as a major tool for thermal maturity determination in oil exploration?, Organic Geochemistry, 22, 191–209.

Wilkinson M., Haszeldine R.S., and Fallick A.E., 2006, Jurassic and Cretaceous clays of the northern and central North Sea hydrocarbon reservoirs reviewed: Clay Minerals, v. 41, p. 151– 186

Williams, L. A., 1982, Lithology of the Monterey Formation (Miocene) in the San

Joaquin Valley of California, in L. A. Williams and S. A. Graham, eds., Monterey Formation and associated coarse clastic rocks, central San Joaquin basin, California: Pacific Section SEPM Publication 25, p. 17–36.

Williams, L. A., 1988, Origins of reservoir complexity in the Miocene Monterey Formation of California, in S. A. Graham, ed., Studies of the geology of the San Joaquin basin: Pacific Section SEPM, v. 60, p. 261–279.

Williams, L. A., Parks G. A., and Crerar D. A., 1985, Silica diagenesis I: solubility controls: Journal of Sedimentary Petrology, v. 55, p. 301–311.

Woeber, A.F., Katz, S., and Ahrens, T.J., 1963, Elasticity of selected rocks and minerals. Geophys., 28, 658–663.

Chapter 3

Spatial and Temporal Distribution of Kerogen in Source Rocks

"A thinker sees his own actions as experiments and questions—as attempts to find out something. Success and failure are for him answers above all."

--Friedrich Nietzsche

3.1. Abstract

We study microtexture of three shale samples at mature and postmature hydrocarbon generation stages: two from the Bakken Formation and one from the Kimmeridge Formation. Fisrt, simple principle of contrasting microfabric observations against each other is used. To gain an insight into shale's intrinsic structure, Scanning Electron Microscopy (SEM) and Confocal Laser Scanning Microscopy (CLSM) based images and

subsequent 3D volume reconstruction based on CLSM images is employed. Based on the microstructural observations we attempt to establish spatial and temporal link between oranic matter and corresponding maturity stages. Following these observations, an attempt to explain anisotropy variation within two Bakken Formation source rocks is made. Furthermore, a possible modeling approach based on Rock Physics mixing laws is provided to support microtextural observations within two Bakken Formation source rocks and compare them to larger set of Bakken Formation samples forming a natural maturity sequence for hydrocarbon generation.

3.2. Introduction

Shales are one of the most complex, and hence challenging to characterize and to model sediments on earth. Their multiphase composition is continually evolving due to diagenesis over various scales of length and time, resulting in the most heterogeneous class of rocks in existence. The heterogeneities manifest themselves from the submicroscopic scale to the macroscopic scale, and all contribute to a pronounced anisotropy and large variety of shale macroscopic behavior (Ulm and Abousleiman, 2006). Moreover, the effects of the multiphase composition are amplified within organic-rich shales (source rocks or potential source rocks) that contain varying amounts of kerogen dispersed within inorganic matrix. Migration of hydrocarbons during the natural petroleum generation process is instrumental for the formation of gas and oil accumulations. The first step in this process, the primary migration within the source rock in which the hydrocarbons are generated, is facilitated by the chemical decomposition of the organic matter in the rock and a consequent microstructural evolution of the inorganic rock matrix. The chemical changes resulting from the thermal maturation of the organic matter in source rocks have been long studied and the processes involved are relatively well understood (Tissot and Welte, 1978). By contrast, the microstructural evolution ~i.e., microscopic changes in geometry and topology of the inorganic and organic components of the rocks upon maturation remained unknown, although much speculated

about (Mann, 1994; Radlinski et al., 1996). Despite significant research into the properties of kerogen, fundamental questions remain regarding how the intrinsic rock-physics properties of the organic fraction affect the macroscopic properties of host shales (Ahmadov et al, 2009). One of the most challenging questions is how do mineral matrix and organic fraction of shale evolve over the course of diagenesis and maturation, respectively? Furthermore, what is the spatial and temporal link between deposited mineral framework and authigenic fractions formed during the processes of diagenesis and maturation? Also, is there any difference in spatial distribution of kerogen at early and late stages of maturation that may affect the way organic-rich rocks are modeled? And finally, what is the influence of all aforementioned variations on Rock Physics properties such as porosity, permeability, elastic properties. In this paper we attempt to provide answers to the formulated questions. To achieve our goal, we use relatively simple principle of contrasting against each other three shale samples, two from the Bakken Formation and one from the Kimmeridge Formation (described in the detail in the previous chapter). To gain an insight into shale's intrinsic structure, Scanning Electron Microscopy (SEM) and Confocal Laser Scanning Microscopy (CLSM) based images and subsequent 3D volume reconstruction based on CLSM images is employed. Based on the microstructural observations we attempt to explain anisotropy variation within two Bakken Formation source rocks. Furthermore, a possible modeling approach based on Rock Physics mixing laws is provided to support microtextural observations within two Bakken Formation source rocks and compare them to larger set of Bakken Formation samples forming a natural maturity sequence for hydrocarbon generation.

3.3. Sample Preparation and Properties

Samples were cut perpendicular to the bedding, so that all imaging and subsequent measurements were performed orthogonal to the bedding plane. Samples were polished to reduce surface roughness below 1-2 μm. SEM and CLSM imaging was performed on two samples of Bakken shale (samples F and M) and one sample of Kimmeridge shale (sample NS) previously analyzed by Vernik and Liu (1997) and described in detail in the

previous chapter. All samples were subjected to more than 3.2km of burial, resulting in loss of porosity with values varying between 0.75 and 1.2% (Table 3.1). Total organic carbon (TOC) values range between 5-7%. Computed kerogen volume fraction lies in the range between 13.5 and 20.5%. Measured Vitrinite Reflectance (R_o) and Hydrogen Index (HI) data values verify postmature stage in samples F and NS, and mature stage in sample M. Table 3.1 also shows measured values of porosity and area of pyrite from SEM images and kerogen and pyrite content from 3D reconstruction of CLSM volumes.

Table 3.1. Petrophysical, geochemical and image analysis data of 3 analyzed shale samples.

	Sample F	**Sample NS**	**Sample M**
Vernik and Liu (1997)			
Depth, m	**3438**	**4449**	**3223**
Density, gr/cm^3	**2.48**	**2.54**	**2.49**
Porosity, %	**1.12**	**1.2**	**0.75**
TOC, %	**5.95**	**5.02**	**7.01**
R_o, %	**1.27**	**1.25**	**0.69**
HI, mg/g	**97**	**67**	**447**
Kerogen volume, %	**15.8**	**13.5**	**20.5**
P-Wave Velocity - $V_p(0^\circ)$, km/s	**3.85**	**3.86**	**3.36**
S-Wave Velocity - $V_s(0^\circ)$, km/s	**2.40**	**2.22**	**2.06**
P-Wave Velocity - $V_p(90^\circ)$, km/s	**4.76**	**4.70**	**4.48**
S-Wave Velocity - $V_s(90^\circ)$, km/s	**2.79**	**2.66**	**2.55**
This sudy (image analysis)			
Kerogen volume, %	**13.3**	**13.4**	**22.6**
Pyrite volume, %	**4.9**	**1.3**	**9.0**
Area of pyrite, %	**4.1**	**1.7**	**10.6**
Porosity, %	**1.93**	**1.8**	**0.5**

3.4. Microfabric characterization using SEM

Figure 3.1 shows backscatter SEM images of shale samples dominated by very-fined grained (< 2μm) particles with varying amounts of silt (2-60μm) and fine quartz (> 60μm). Porosity is very low (part of the black color) and usually does not exceed 2% (Vernik and Nur, 1992) with pore sizes dominated by micron size rarely reaching 30μm.

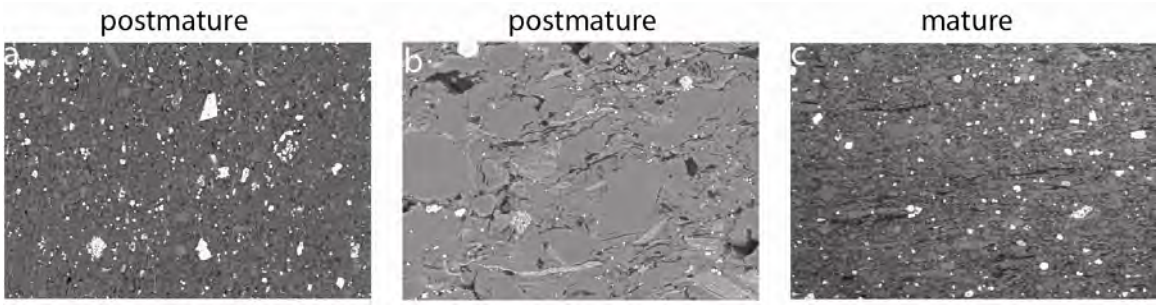

Figure 3.1. Backscatter SEM photomicrographs of shale samples: a) postmature Bakken Formation (F), bright features are pyrite framboids; b) postmature Kimmeridge Formation (NS), elongated white features are vermiform kaolinite; c) mature Bakken Formation (M), elongated black features are kerogen lenses. Longer side of images is 450 μm.

Striking feature present in all three samples is occurrence of relatively denser mineral, pyrite at different stages and modes of formation shown as white inclusions. The round white inclusions are pyrite framboids (spheroids), whereas angular ones are euhedral pyrite. All three samples show drastic difference when compared against each other. The major difference between the two Bakken samples which were located just 200 m apart in vertical direction and Kimmeridge Formation sample is the absence of any apparent features indicating bedding in postmature samples (Fig. 3.1a,b), and presence of aligned kerogen lenses parallel to the bedding in mature sample (shown in black in Fig. 3.1c).

The Kimmeridge Formation (Sample NS) was subjected to at least 4500m burial depth and as a result, a number of deformational features are present at close examination of microtexture. These features are indicated by arrows on Figure 3.2. Clay particle shown in figure 3.2a is broken and displaced in left-lateral direction below clast of framboidal pyrite (Py) which is also deformed compared to spheroidal rounded shape suggesting that pyrite formed prior to considerable amounts of compaction. Vermiform

kaolinite (Kaol) particle is deformed between several medium-grained quartz particles (Q) in Figure 6b. Figures 3.2c and 3.2c` (obtained under *BSE* and *SE* modes, respectively) display an example of a quartz grain deeply penetrating into a kaolinite particle.

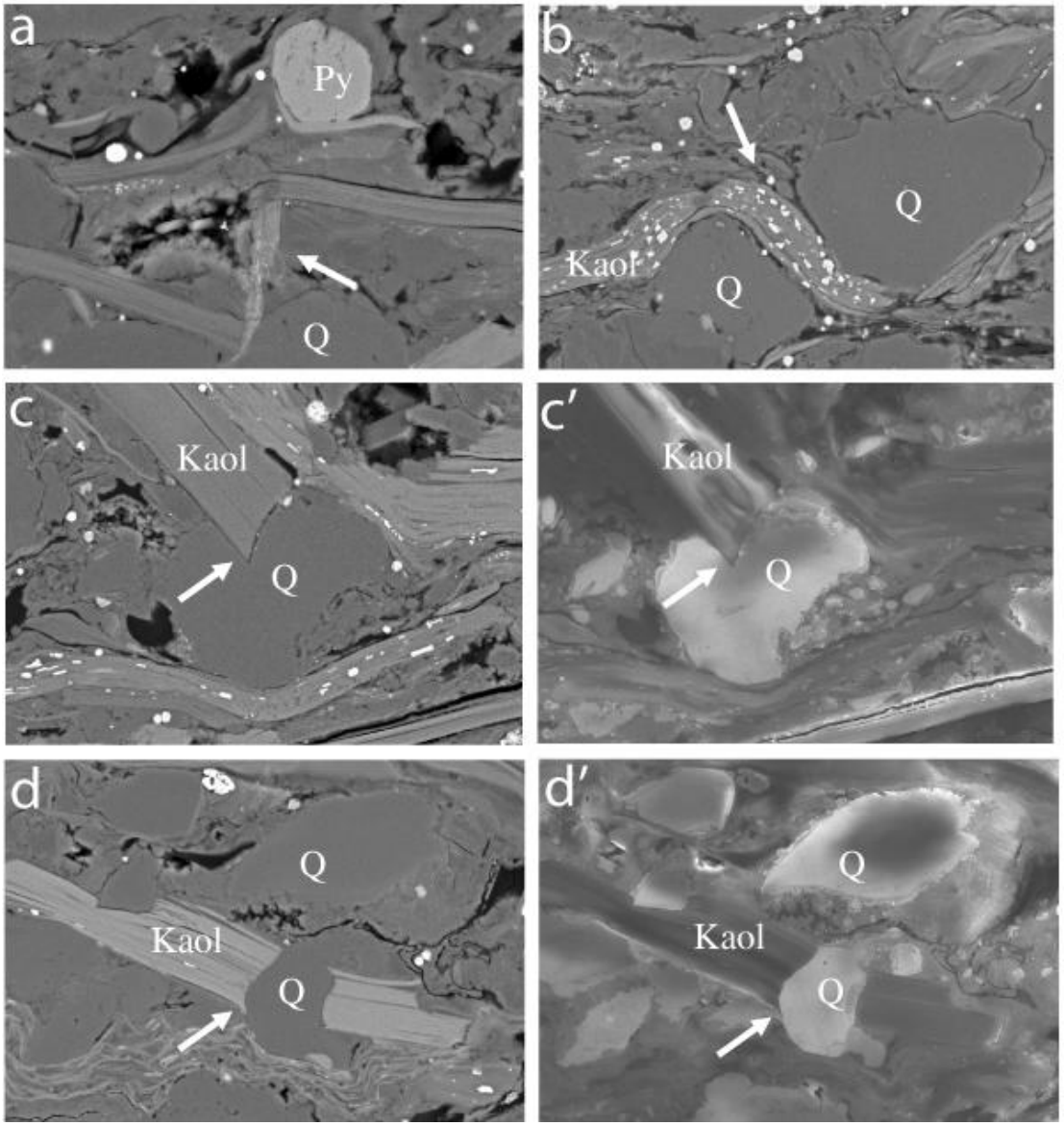

Figure 3.2. SEM photomicrographs of Kimmeridge Formation Sample NS showing deformed vermiform kaolinite indicated by arrows. a) Broken and displaced particle in *BSE* mode; b) vermiform kaolinite (k) particle is deformed between several medium-grained quartz particles (q), image in *BSE* mode; c) quartz grain deeply penetrating into kaolinite particle in *BSE* mode, c`) area shown in d) in *SE* mode; d) quartz grain deeply penetrating into kaolinite particle in *BSE* mode, d`) area shown in d) in *SE* mode. Size of longer side of image: a) is 300 μm; b) is 250 μm; c-d`) is 150 μm.

Another example of a highly deformed kaolinite particle is shown in figures 3.2d (BSE mode) and 3.2d` (SE mode). Substantial compaction is also implied from preferred orientation of aligned clay particles. Figure 3.3 shows kerogen lenses (in black) composed of liptinite group macerals in Bakken Formation (Sample M). Kerogen lenses are bed-parallel (horizontal in images) preserving depositional configuration. The size of lenses consistently varies between 150-250 μm in length and 10-20 μm in thickness, with aspect ratio of the lenses between 0.05 and 0.1.

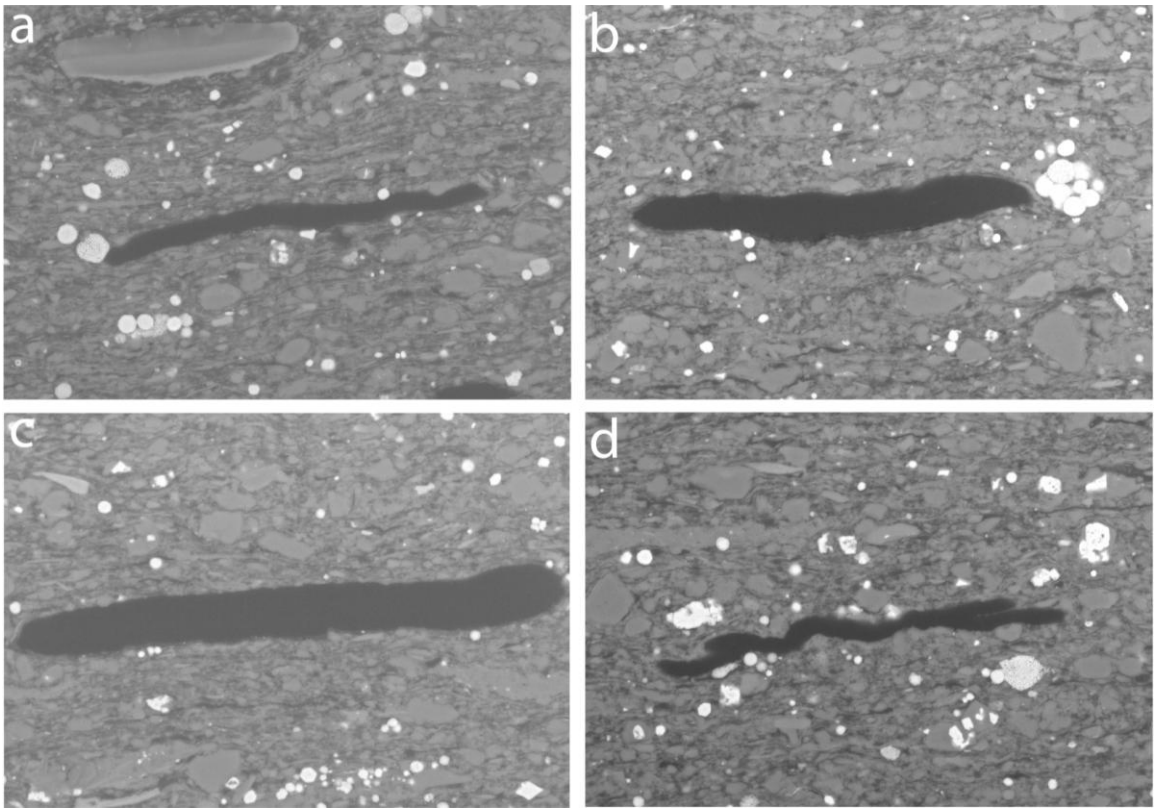

Figure 3.3. Backscatter SEM photomicrographs of Bakken Formation Sample M showing a-d) kerogen lenses (in black) composed of liptinite group macerals. Kerogen lenses are bed-parallel (horizontal in images) preserving depositional geometry. The size of lenses varies between 150-250 μm in length and 10-20 μm in thickness. The aspect ratio of the lenses is consistent and varies between 0.05 and 0.1. Longer side of images is 230 μm.

3.5. *Microfabric characterization using CLSM*

In Figures 3.4 we display CLSM images of three shale samples obtained under red light excitation (λ=543nm). Images in Figure 3.4 are not thresholded showing non-fluorescing background silicate mineral matrix (in black). The major attribute of spatial distribution of kerogen in postmature samples of both Bakken and Kimmeridge Formations (Fig. 3.4a and b, respectively) is that organic matter is scattered throughout the samples somewhat uniformly without any reference to the depositional bedding.

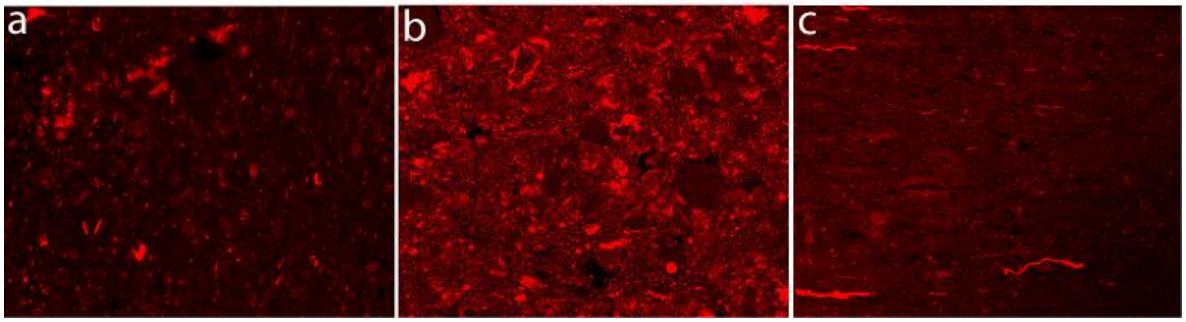

Figure 3.4. CLSM images (under red light excitation, λ=543nm) of the of shale samples: a) postmature Bakken Formation (F); b) postmature Kimmeridge Formation (NS); c) mature Bakken Formation (M). Bright features are kerogen. Size of longer side of image is 450 μm.

Given the postmature character of the samples and pore-filling nature of some of the kerogen adjacent to silica grains, it is rational to suggest that this portion of kerogen is residual organic matter left from primary generation and expulsion.

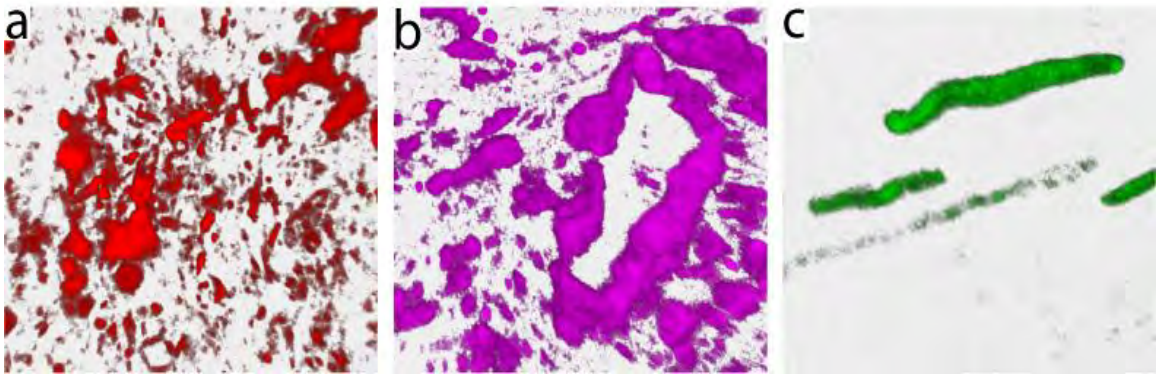

Figure 3.5. Side view of a 3D volume reconstruction of sequential CLSM images of organic matter from (a) postmature Bakken Formation (F); b) postmature Kimmeridge Formation (NS); c) mature Bakken Formation (M). Size of images is 180×180 μm.

Unlike in postmature samples, kerogen in mature Bakken Formation (Fig. 3.4c) still depicts its original depositional spatial character and is localized in lenses that occur parallel to the bedding. The major differences in the spatial nature of kerogen of shale samples are better observed in high magnification 3D volumes reconstructed based on thresholded sequential CLSM images obtained 1µm apart (Figure 3.5). Figure 3.6a-c shows side view of 3D volume of Bakken Formation (Sample F) reconstructed based on 10 sequential CLSM of images obtained 1µm apart.

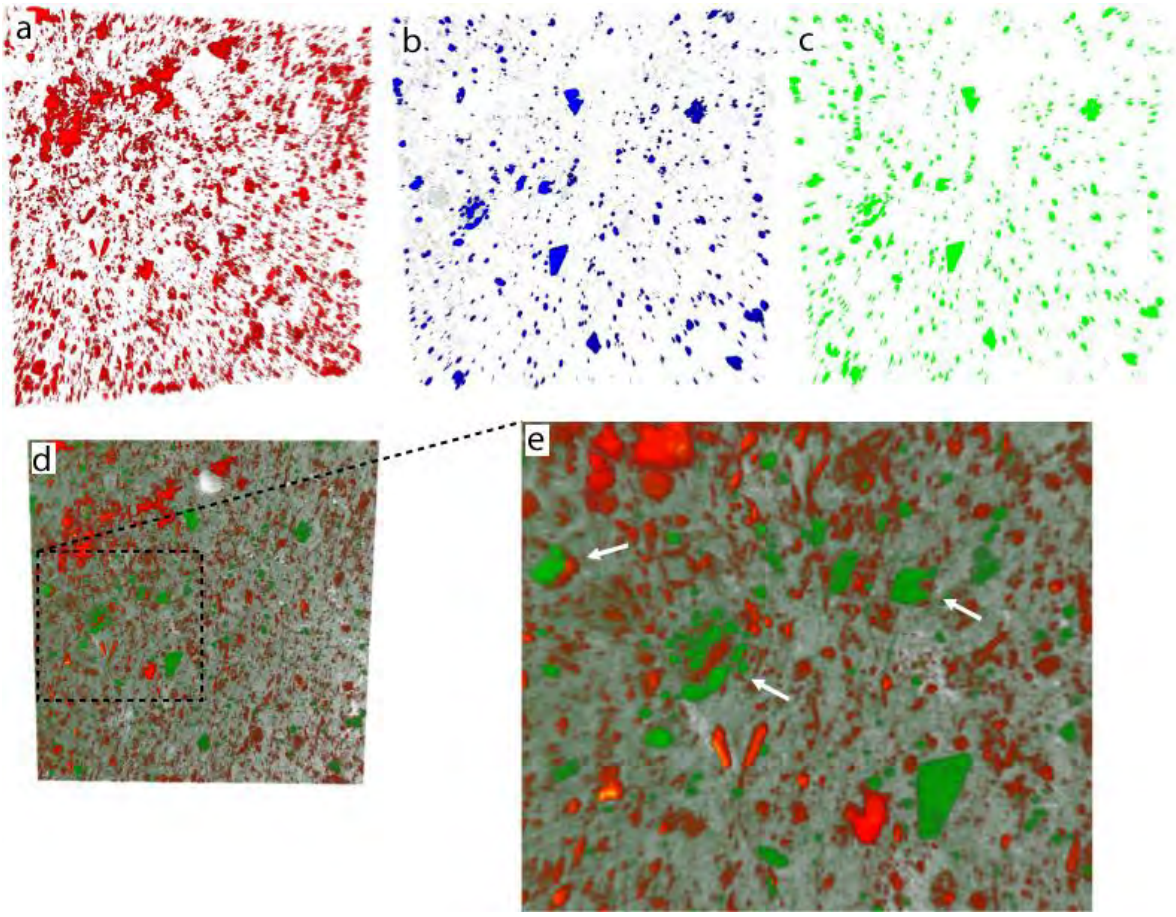

Figure 3.6. 3D volume reconstruction based on 10 sequential CLSM images of organic matter and pyrite of Bakken Formation Sample F. (a) side view of 3D volume of organic matter under red light excitation; (b) side view of 3D volume of pyrite a under blue light excitation; c) side view of 3D volume of pyrite under green light excitation; d) side view of 3D volume of combined organic matter and pyrite; and (e) close-up view of d), arrows indicate partial substitution of organic macerals (red) by framboidal and euhedral pyrite (green). Size of 3D volume is 450×450×9 µm. Distance between two consecutive images is 1µm.

These images are thresholded in order to emphasize three-dimensional character of organic matter in Figure 3.6a (under red light excitation) and pyrite in Figures 3.6b and 3.6c (under blue and green light excitations, respectively). Three-dimensional volumes of organic matter and pyrite are combined in Figures 3.6d and 3.6e and show partial to full replacement of original organic matter by pyrite (shown by arrows).

3.6. Conceptual model of shale evolution and implications for Rock Physics

Figure 3.7 represents a conceptual model of evolution of shale samples with progressive burial and maturation. Initially, at immature stage, organic matter and *stiff* silicate mineral matrix are deposited. As compaction progresses, at a very early stage, porosity is reduced and the pyrite is formed in available pore space, amplifying porosity reduction. With more burial and maturation, preferred orientation of clay particles is achieved, and hydrocarbons generation begins. Originally deposited organic matter is mostly preserved in kerogen lenses with varying degrees of organic matter replacement by both euhedral and framboidal pyrite growth. At this stage (mature: R_o~0.7) and depth (>3km), most of the porosity is lost due to both physical and chemical compaction, pores are occupied by pyrite. Organic matter occurs in bed-parallel elongated lenses scattered throughout the sample and is load-bearing and hence, will contribute to the stiffness of the sample along with silicate mineral matrix. Pore-filling pyrite will reduce matrix porosity and hence permeability dramatically, since it will preferentially grow in the largest available pores. Significant (up to 10%) volume of pyrite, occurring within mineral matrix, given high elastic properties of pyrite (E=380 GPa), might potentially result in increased seismic velocities in pyrite-rich samples compared to those of pyrite-lean samples.

At a later stages (postmature: R_o>1.2), most of the pore space is occupied by pyrite and reworked organic matter filling predominantly elongated pores at grain boundaries. Porosity is reduced below 2%. At this stage, organic matter is finely scattered

throughout the sample without any reference to original depositional bedding and is not load-bearing and hence, will not contribute to the stiffness of the sample nearly as much as silicate mineral matrix.

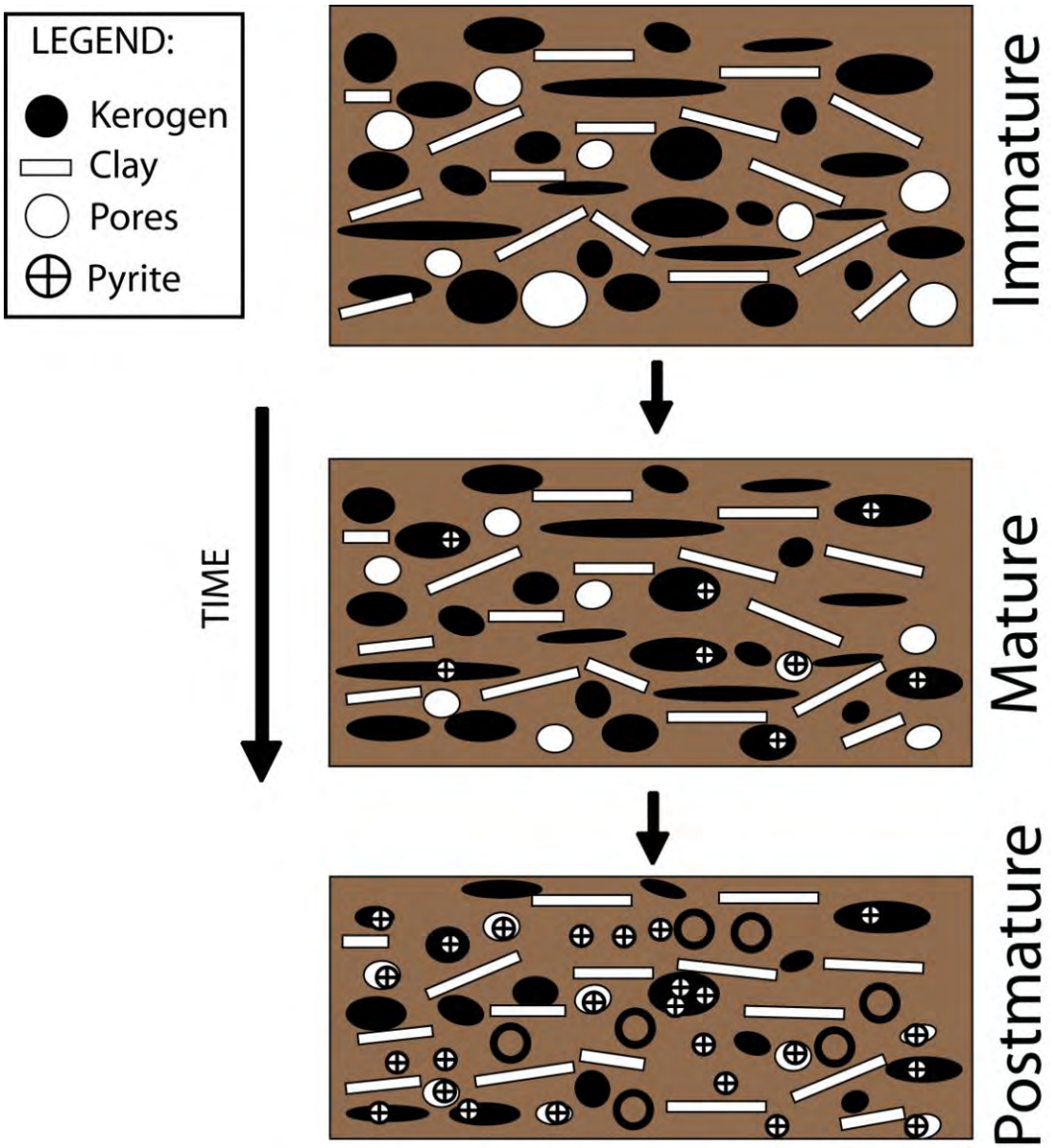

Figure 3.7. Conceptual model of evolution of shale samples.

In order to quantify anisotropy due to the spatial distribution of organic matter in mature and postmature samples, we construct two-dimensional (bed-parallel and bed-perpendicular) cross-correlation functions of kerogen based on the images (Figure 3.8).

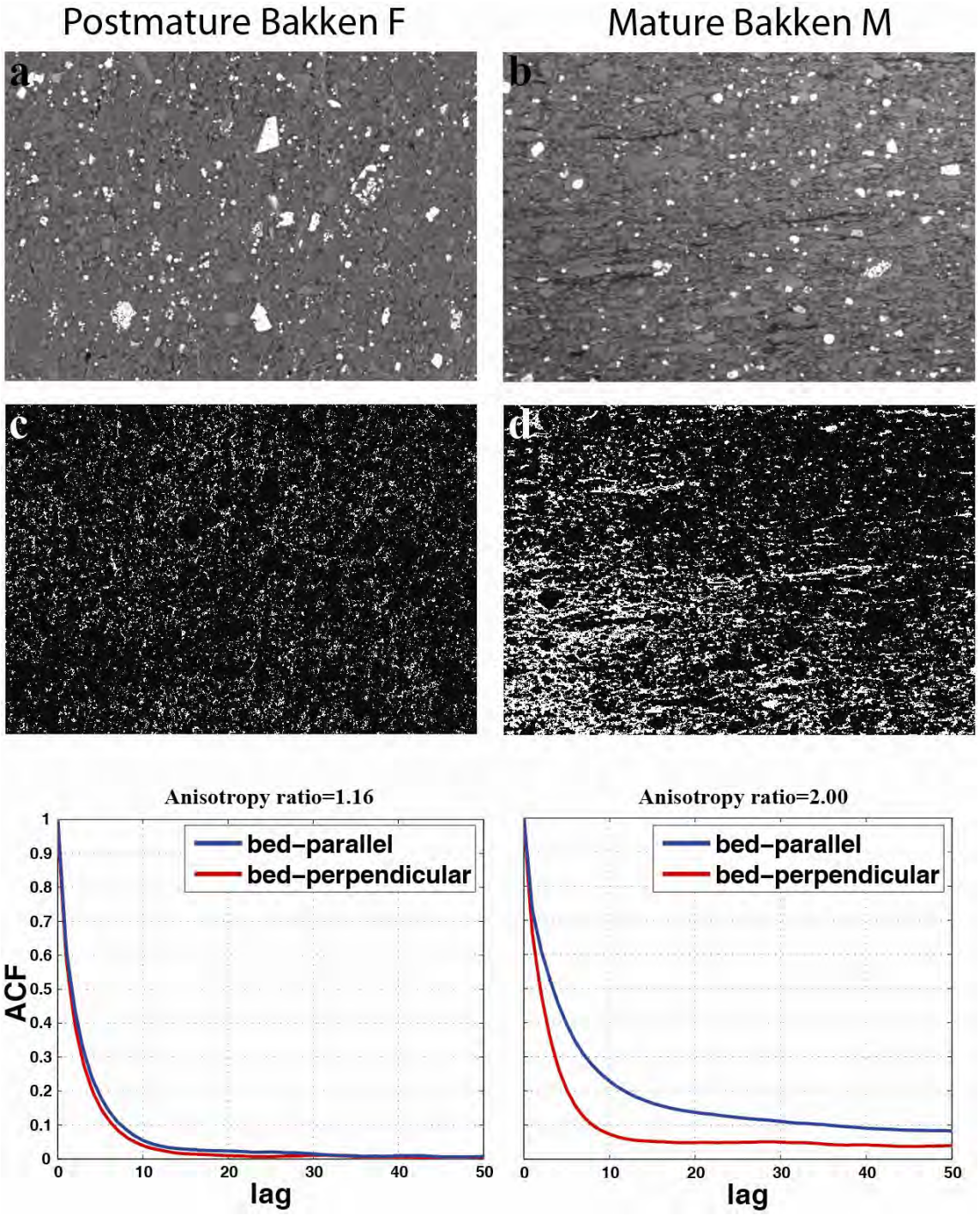

Figure 3.8. a) postmature Bakken Formation sample F, b) mature Bakken Formation sample M, c) kerogen (in white) of postmature Bakken Formation sample F from image (a), d) kerogen (in white) of mature Bakken Formation sample M from image (b), below) corresponding two-dimensional (bed-parallel and bed-perpendicular) cross-correlation functions of organic matter in both samples. Note the difference in correlation function computed in bed-parallel and bed-perpendicular directions for mature sample. In postmature sample this difference is almost absent.

Note the difference in correlation function computed in bed-parallel and bed-perpendicular directions for mature sample, which is almost absent in postmature sample. The computed anisotropy ratio (ratio of maximum range to minimum range) is 1.16 in postmature Bakken Formation sample, and is 2.00 in mature sample. Figure 3.9 shows spread of auto-corrleation function of both samples in all directions. The spread is minimal in postmature Bakken Formation sample suggesting that sample is isotropic in terms of the distribution of organic matter. As expected, in mature sample spread is much larger resulting in strong anisotropy due to the distribution of organic matter.

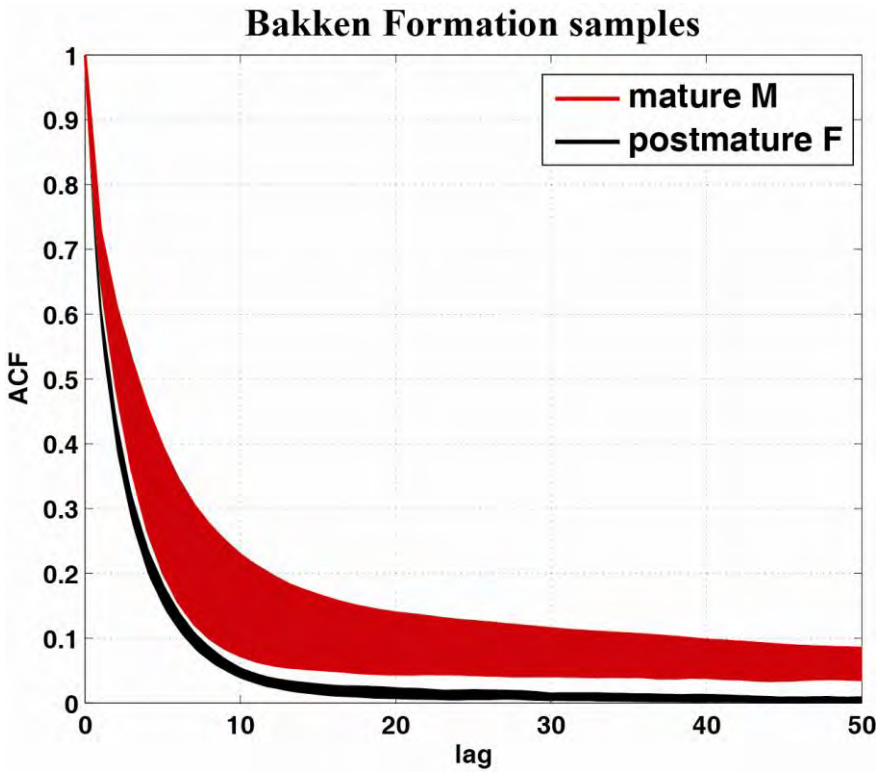

Figure 3.9. Spread of auto-corrleation function of both samples in all directions. The spread is minimal in postmature Bakken Formation sample suggesting that sample is isotropic in terms of the distribution of organic matter. As expected, in mature sample spread is much larger resulting in strong anisotropy due to the distribution of organic matter.

Based on the microtextural observations, it is logical to propose different methodologies for modeling mature and postmature fabric of organic-rich shales. In case of mature samples, two layer composite (Backus averaging) or modified Backus model

approach employed by Vernik and Nur (1992) is appropriate. However, in postmature samples kerogen is not bed-parallel, but finely scattered within mineral matrix and often occupies pores adjacent to quartz, feldspar and clay grains. Therefore, in latter case, Hashin-Shtrikman bounds may be more appropriate. In order to test these ideas and to propose a possible modeling approach based on Rock Physics mixing laws we compare two Bakken Formation source rock samples described above to the larger set of Bakken Formation samples forming a natural maturity sequence for hydrocarbon generation and modeled earlier by Vernik and Landis (1996) and Bandyopadhyay (2009).

Vernik and Landis (1996) combined acoustic velocities and anisotropy measurements with x-ray diffraction mineralogy, Rock-Eval organic geochemical analyses, vitrinite reflectance, and scanning electron microscope observations on 69 cores of hydrocarbon source rocks (including Bakken Formation samples analyzed here) at various stages of maturity collected from eight sedimentary basins. Figure 3.10 shows P-wave and S-wave acoustic velocities measured on dry rock Bakken Formation samples in two orthogonal to one another directions: parallel to bedding, *V(90°)*, and perpendicular to bedding, *V(0°)*.

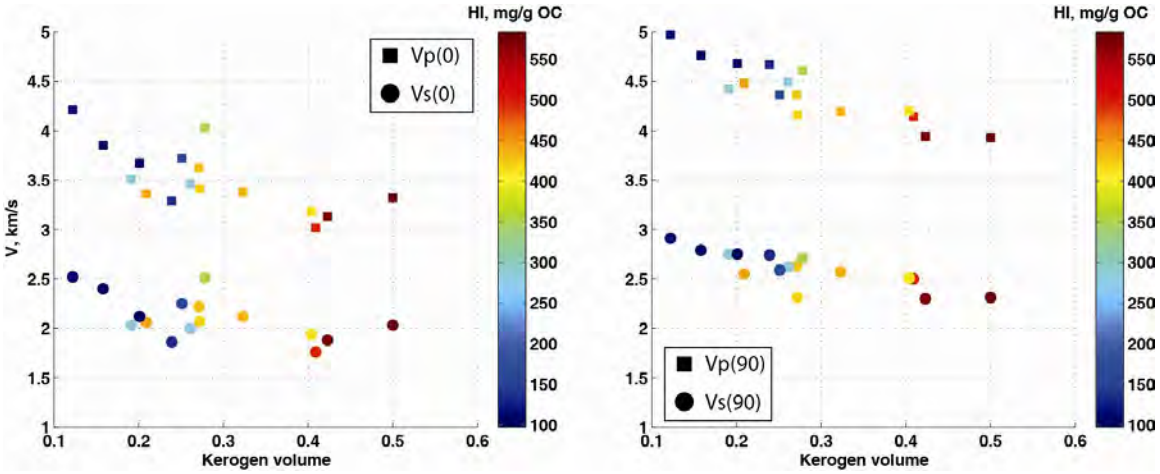

Figure 3.10. P-wave and S-wave acoustic velocities measured on dry rock Bakken Formation samples (P_{eff}=70MPa) in two orthogonal to one another directions: (left) perpendicular to the bedding, *V(0°)*, and (right) parallel to the bedding, *V(90°)*. Colorbar indicates Hydrogen Index. Data Vernik and Landis (1996).

Velocity values are colorcoded by Hydrogen Index, *HI*, an indirect measure of thermal

maturity of source rocks. Vernik and Landis (1996) measured velocities as a function of increasing confining pressure. However, we only analyze measurements obtained at 70MPa effective stress in order to minimize the effect of open cracks. It is clear from the plots that there is strong correlation between increasing maturity and decreasing kerogen volume of Bakken Formation rocks. Velocities within mature source rocks containing reduced amounts of kerogen increase, as their density increases accordingly. It is interesting to note that relative variation in velocity values at a given kerogen volume measured parallel to the bedding, *V(90°),* is less than that in the bed-perpendicular case, *V(90°*). For example, for kerogen volume of 27% in two samples, the difference in $V_p(0°)$ of these samples is ~0.6km/s, with corresponding difference in $V_s(0°)$ of ~0.5km/s.

Briefly recalling the main observation of spatial distribution of organic matter in two Bakken Formation samples, we hypothesize that the bulk modulus of mature sample M (wherein bed-parallel kerogen lenses are observed) should be represented by Reuss lower bound, whereas the bulk modulus of postmature sample F (wherein kerogen surrounds silicate mineral grains) should be represented by Hashin-Shtrikman lower bound. The choice of these particular mixing laws is made based on their physical interpretation of bulk modulus of a two-phase material (in our case of silicate mineral matrix and organic matter). Based on x-ray diffraction, Vernik and Landis (1996) reported average mineralogy (% vol.) and calculated solid mineral matrix density for a set of samples of Bakken Formation. Table 3.2 summarizes x-ray diffraction mineralogy for a set of Bakken Formation samples studied by Vernik and Landis (1996).

Table 3.2. Modal mineralogy (% vol.) of Bakken Formation samples from whole rock XRD analysis by Vernik and Landis (1996).

Lithology	Quartz+Feldspar	Carbonate	Clay	Pyrite	ρ_m, g/cm^3
shale	54	12	31	3	2.75

The Bakken Formation samples are composed of 54% of quartz+feldspar, 12% carbonate, 31% clay and 3% pyrite. Porosity of these samples is below 2%, averaging 0.9%. We therefore ignore porosity, minor pyrite presence and compute Hashin-

Shtrikman as well as Voigt-Reuss-Hill bounds for a mixture of silicate mineral matrix and organic matter.

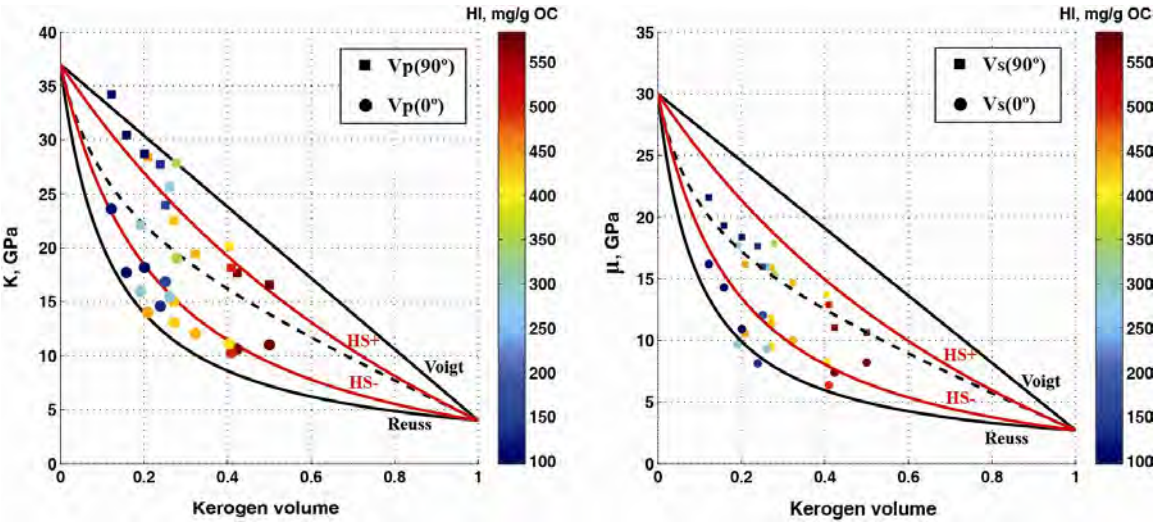

Figure 3.11. Bulk modulus (K) and shear modulus (μ) versus kerogen volume along with Voigt-Reuss-Hill and Hashin-Shtrikman bounds. Colorbar indicates Hydrogen Index. Data Vernik and Landis (1996).

For the stiffest component of the mixture (Quartz+Feldspar), we use average elastic moduli assuming equal presence of quartz and feldspar in Quartz+Feldspar volume (50%-50% vol.) (K=37GPa, μ=30GPa).

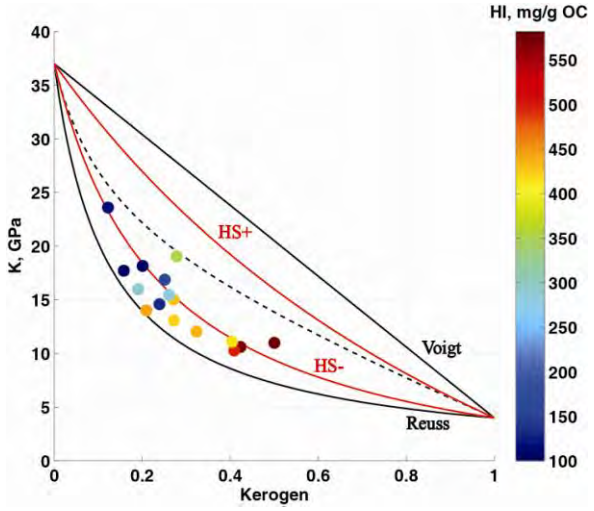

Figure 3.12. Bulk modulus (K) versus kerogen volume for bed-perpendicular direction - Vp(0), along with Voigt-Reuss-Hill and Hashin-Shtrikman bounds. Colorbar indicates Hydrogen Index. Data Vernik and Landis (1996).

For the softest component of the mixture (organic matter), we use average elastic moduli of kerogen obtained from nanoindentation measurements and discussed in detail in the next chapter (K=4GPa, μ=3GPa). Figure 3.11 shows bulk modulus (K) and shear modulus (μ) versus kerogen volume along with modeled Voigt-Reuss-Hill and Hashin-Shtrikman bounds. Figure 3.12 shows the bulk modulus of Bakken Formation samples for bed-perpendicular direction -Vp(0) colorcoded by *HI* along with model predictions. As hypothesized earlier, most of the bulk modulus values fall between Reuss and Hashin-Shtrikman lower bound, which shown in detail in Figure 3.13. On the right panel of Figure 3.13 we mark two analyzed samples by black stars and show that their bulk modulus values are in excellent agreement with the choice of mixing laws.

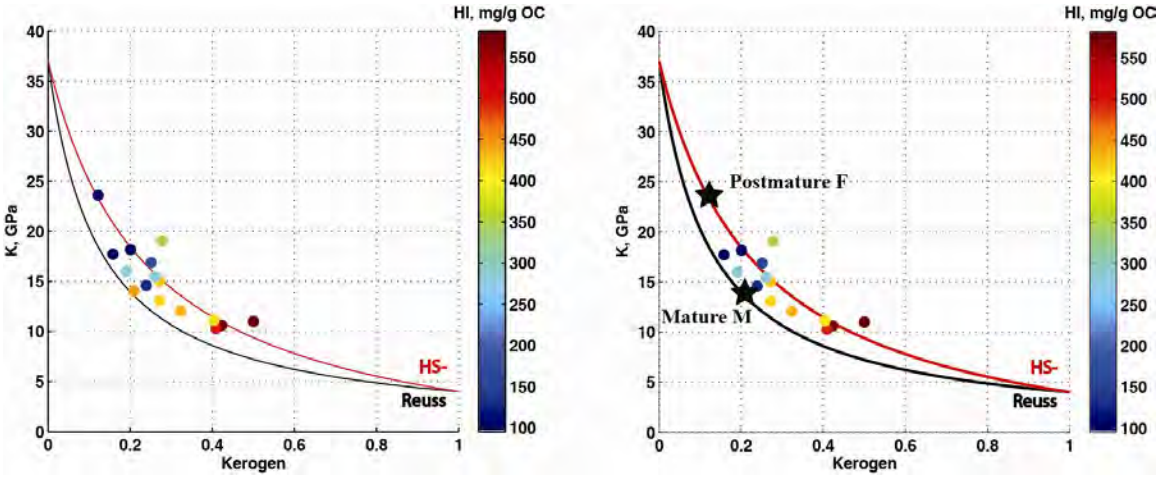

Figure 3.13. (left) Bulk modulus (K) versus kerogen volume along with Reuss and Hashin-Shtrikman lower bounds, (right) same as left with two values corresponding to Bakken Formation samples M and F (marked by black stars). Colorbar indicates Hydrogen Index. Data Vernik and Landis (1996).

In terms of anisotropy, we compute Thomsen's (Thomsen, 1986) anisotropy parameter, ε, which quantifies anisotropy based on the acoustic measurements of P-wave velocity performed by Vernik and Landis (1996) in two orthogonal directions: parallel to bedding, *V(90°)*, and perpendicular to bedding, *V(0°)*. Thomsen's P-wave anisotropy parameter, ε, is then expressed as follows

$$\varepsilon = \frac{V_p(90°)^2 - V_p(0°)^2}{2V_p(0°)^2} = \frac{V_p(90°)^2}{2V_p(0°)^2} - \frac{1}{2} \tag{3.1}$$

Figure 3.14 shows variation of P-wave anisotropy parameter, ε, as a function of organic volume. As Bakken Formation source rocks transform from mature to postmature stage, ε decreases along with decreasing kerogen volume and hydrogen index (<200mg/g OC).

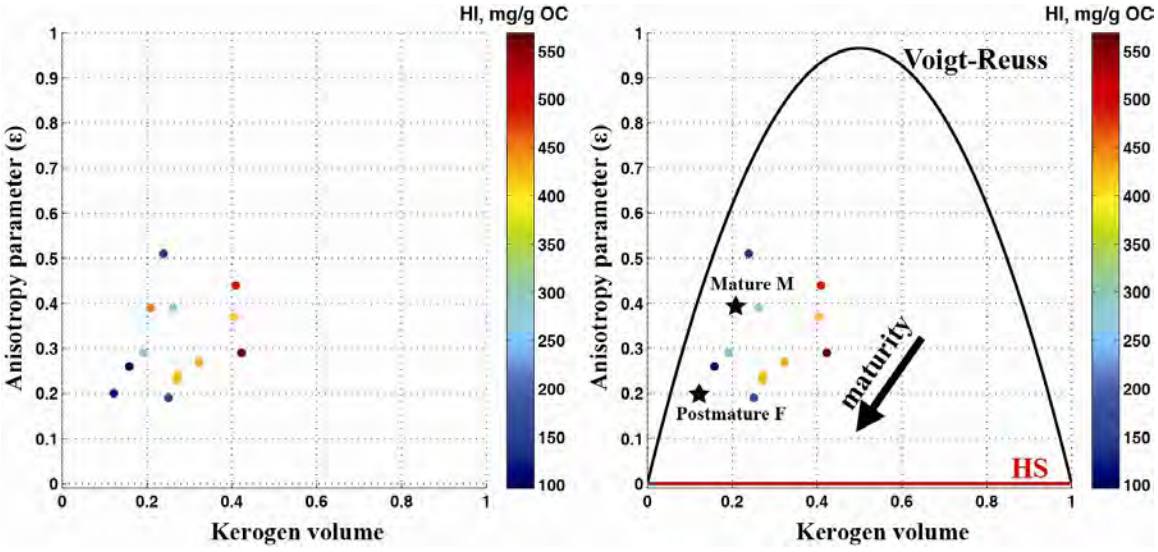

Figure 3.14. (left) Thomsen's anisotropy parameter (ε) versus kerogen volume, (right) same as left with two values corresponding to Bakken Formation samples M and F (marked by black stars) and models based on Voigt-Reuss and Hashin-Shtrikman bounds. Colorbar indicates Hydrogen Index. Data Vernik and Landis (1996).

3.7. Chapter Summary

The microtextures of three shale samples at mature and postmature hydrocarbon generation stages, two from the Bakken Formation and one from the Kimmeridge Formation, are documented. A simple principle of contrasting microfabric observations against each other is used. To gain an insight into shale's intrinsic structure, Scanning Electron Microscopy (SEM) and Confocal Laser Scanning Microscopy (CLSM) based images and subsequent 3D volume reconstruction based on CLSM images is employed. Based on the microstructural observations we establish spatial and temporal link between

organic matter and corresponding maturity stages. Auto-correlation functions computed on mature and postmature sample images show strong anisotropy due to the organic matter in the mature stage, and almost no anisotropy within postmature sample. We then compute Hashin-Shtrikman as well as Voigt-Reuss-Hill bounds for a mixture of silicate mineral matrix and organic matter in order to explain the microtextural observations within two Bakken Formation source rocks and compare them to larger set of Bakken Formation samples forming a natural maturity sequence for hydrocarbon generation. As hypothesized earlier, most of the bulk modulus values of Bakken Formation samples measured in bed-perpendicular direction fall between Reuss and Hashin-Shtrikman lower bounds. Therefore, our choice of mineral matrix and kerogen and corresponding bulk and shear moduli used in modeling satisfactorily describes the data. Furthermore, following these observations, we explain anisotropy variation within two Bakken Formation source rocks.

3.8. References

Ahmadov R., Vanorio T, Mavko G., 2009, Confocal Laser Scanning and Atomic-Force Microscopy in Estimation of Elastic Properties of Organic-Rich Bazhenov Formation, The Leading Edge v. 28, n. 1, p.18-23

Bandyopadhyay K., 2009, Seismic Anisotropy: Geological Causes and Its Implications to Reservoir Geophysics, Stanford University, Ph.D. Thesis, p.254

Hill, R., 1952, The elastic behavior of crystalline aggregate. Proc. Phys. Soc., London A, 65, 349–354

Mann U., 1994, Origin, Migration and Evolution of Fluids in Sedimentary Basins, in Geofluids: edited by J. Parnell, Geological Society Special Publication No. 78 ~Geological Society, London, pp. 233–260.

Radlinski, A.P., Boreham, C.J., Wignall, G.D. and Lin, J.-S., 1996, Microstructural evolution of source rocks during hydrocarbon generation: a small-angle-scattering study. Physical Review B53, pp. 14152–14160

Reuss, A., 1929. Berechnung der Fliessgrenzen von Mischkristallen auf Grund der Plastizitatsbedingung fur Einkristalle. Z. Ang. Math. Mech., 9, 49–58.

Thomsen, L., 1986, Weak elastic anisotropy: Geophysics, 51, 1954–1966.

Tissot, B.P., Welte, D.H., 1978, Petroleum Formation and Occurrence. Berlin-Heidelberg-New York: Springer, p. 699.

Ulm, F. J. and Abousleiman, Y, 2006, The nanogranular nature of shale, Acta Geotechnica, 1, 77-88

Vernik, L., and C. Landis, 1996, Elastic Anisotropy of source rocks: Implications for hydrocarbon generation and primary migration: AAPG Bulletin, v. 80, p. 531-544.

Vernik L. and Liu, X., 1997, Velocity anisotropy in shales; a petrophysical study, Geophysics, 62, 521–532.

Vernik, L., and Nur, A., 1992, Ultrasonic velocity and anisotropy of hydrocarbon source rocks: Geophysics, 57, Issue 5, pp. 727-735

Voigt, W., 1890, Bestimmung der Elastizitatskonstanten des brasilianischen Turmalines. Ann. Phys. Chem., 41, 712–729.

Chapter 4

Nanoindentation in Source Rocks

"I hear and I forget. I see and I remember. I do and I understand."

-- Confucius

4.1. Abstract

We measure Indentation Modulus and subsequently compute the Young's, shear and bulk moduli of source-rock samples from the Bazhenov and Lockatong Formations using a nanoindentation technique. Our approach for elastic-property estimation and mapping couples nanoindentation with scanning electron microscopy (SEM) and confocal laser-scanning microscopy (CLSM). We perform nanoindentaion experiments on areas previously identified as kerogen via SEM and CLSM, and subsequently calculate Young's modulus from Indentation modulus based on force-displacement curves obtained while probing. Consequently, this allows shear- and bulk-modulus

computation using the previously calculated Young's modulus and an assumption of Poisson's ratio of kerogen in the samples. The choice of a reasonable Poisson's ratio is evaluated using sensitivity analysis of Young's modulus to varying Poisson's ratios. Elastic moduli derived from our measurements are then compared to previously published data on organic-rich rocks. Nanoindentation measurements showed kerogen within the Bazhenov and Lockatong Formations to be softer than the surrounding mineral matrix. Indentation modulus of kerogen from the Bazhenov Formation varies between 6 and 11 GPa, whereas for the Lockatong Formation sample it is about 12 GP. Moreover, values of Indentation modulus of kerogen, as well as elastic properties of stiffer minerals as dolomite, quartz and pyrite are in very good agreement with previously published data. Sensitivity analysis of Young's modulus to varying Poisson's ratios of kerogen shows minor dependence throughout the range of Poisson's ratios (ν=0.05-0.45).

4.2. Introduction

Shales are one of the most complicated and intriguing natural materials on earth. Their multiphase composition is continually evolving over various scales of length and time, creating the most heterogeneous class of rocks in existence. The heterogeneities manifest themselves from the submicroscopic scale to the macroscopic scale, and all contribute to a pronounced anisotropy and large variety of shale macroscopic behavior (Ulm and Abousleiman, 2006). Moreover, the effects of the multiphase composition are amplified within organic-rich shales that contain varying amounts of kerogen. Despite significant research into the properties of kerogen, fundamental questions remain regarding how the intrinsic rock-physics properties of the organic fraction affect the macroscopic properties of host shales.

Because we do not fully understand the elastic properties of either the organic matter or the individual clay minerals present in shales, seismic velocity prediction in organic-rich shales remains challenging. Conventional measurements of 'macroscopic' or 'average' properties on core plugs are not sufficient to fully address the degree of property variation within organic-rich rocks. Alternatively, most analyses of organic

matter (kerogen) rely on samples that have been isolated by dissolving the rock matrix. The properties of the kerogen before and after such isolation may be different, and all information about sample orientation is lost. In addition, comprehensive characterization of organic-rich shales has been hindered by several factors: sample preparation is time-consuming, and the nanogranular nature of this rock type makes it difficult to link effective elastic properties to maceral properties, such as elastic moduli, composition, maturity, and quality. These difficulties have prevented us from building large databases, without which we cannot establish the accurate rock-physics models needed for inverting field geophysical data.

One approach to overcome this issue uses atomic-force microscopy (AFM), coupled with confocal laser-scanning microscopy (CLSM) as a tool for visualization and identification of the organic part within shale, and to gather nanoscale elastic-property measurements. AFM-based techniques have been widely used for numerous applications in fields of engineering, nanotechnology, and material science. Recently, AFM-based methods were successfully applied to measure and map elastic properties of natural materials such as fossils (Kempe et al. 2002), shales (Ulm and Abousleiman 2006, Abousleiman et al. 2007), kerogen (Zeszotarski et al. 2004), and clays (Kopycinska-Muller et al. 2007). Generally, AFM-based methods for elastic-property quantification can be subdivided into two categories: those that measure the absolute value of the elastic moduli and those that map the relative variation of the elastic moduli. The first category can be further subdivided into two general approaches of elastic-property measurement: destructive (nanoindentation) and non-destructive (contact mode).

The only study of indirect in-situ (without separation of organic from inorganic part) elastic property measurements of kerogen available in the literature is by Zeszotarski et al. (2004). In their study, they measured the elastic properties of kerogen from Woodford Shale by the nanoindentaion method. However, this method alone does not provide the topological association between the targeted material and its elastic modulus. Our approach applies nanoindentation to regions previously determined to

contain kerogen by application of CLSM. This approach directly measures the elastic response of the examined material (Ahmadov et al., 2009).

There has been a tremendous explosion in the popularity of confocal microscopy in recent years, in part because of the relative ease with which extremely high-quality images can be obtained from specimens prepared for conventional optical microscopy. CLSM was conceptualized in 1953 by M. Minsky and was later used for biological research, chemical analysis, and material testing. CLSM has seen a wide variety of applications, but only very recently has it been applied to studying the morphology of macerals within coals (Teerman et al. 1987) and oil shales (Stasiuk et al. 1998, Vanorio et al., 2008), to thermal-maturity determination (Wilkins et al. 1995), and to characterization of algae fossils (Chi et al. 2006).

4.3. Sample Properties

SEM, CLSM imaging and nanoindentation measurements were performed on samples from two wells tapping The Bazhenov Formation at 3800 m depth and The Lockatong Formation at 549 m depth. At these depths, the measured interval porosity (helium) of the formations is 2.3% and 0.3%, with bulk density of 2.63 g/cm^3 and 2.70 g/cm^3, respectively. Kerogen volume fraction values are 8.7% and 8.2%, respectively. The Bazhenov Formation sample is within mature stage of hydrocarbon generation (Vitrinite Reflectance value of R_o=0.78), whereas The Lockatong Formation sample has already undergone active generation phase (R_o=2.58). The summary of all physical properties of both samples is reflected in Table 1. In preparation for imaging, the samples were cut perpendicular to the bedding to better expose their heterogeneity and then polished to reduce the surface roughness down to 1 to 2 micrometers.

Table 4.1. Summary of petrophysical, geochemical (Vernik and Landis, 1996) and nanoindentation based data for shale and dolomite samples under examination.

Data source and properties	**Bazhenov Formation**	**Lockatong Formation**
Vernik and Liu (1997)		
Depth (m)	3822	549
Density (g/cc)	2.63	2.70
Porosity (%)	2.26	0.30
TOC (%)	2.83	2.84
R_o (%)	0.78	2.58
HI (mg/g)	279	2
Kerogen volume (%)	8.7	8.2
P-wave velocity parallel to bedding (km/s)	4.90	6.19
S-wave velocity parallel to bedding (km/s)	3.08	3.40
P-wave velocity normal to bedding (km/s)	3.82	5.69
S-wave velocity normal to bedding (km/s)	2.56	3.28
This study (nanoindentation)		
M (kerogen), GPa	5.9	11.9
M (pyrite), GPa	256	n/a
M (dolomite), GPa	n/a	125
M (quartz), GPa	92.6	

4.4. Combining SEM, CLSM and Nanoindentation

We performed a series of nanoindentation experiments targeting primarily organic matter, siliceous dolomite, quartz and pyrite minerals. The workflow (shown in Figure 4.1 for Bazhenov Formation sample) for identifying the area of interest is as follows:

1. Identifying the area of interest using SEM images.
2. Confirming the presence of organic matter via CLSM images.
3. Performing nanoindentation measurements within the area of interest.
4. Computing the elastic properties of organic matter, as well as stiff mineral matrix.

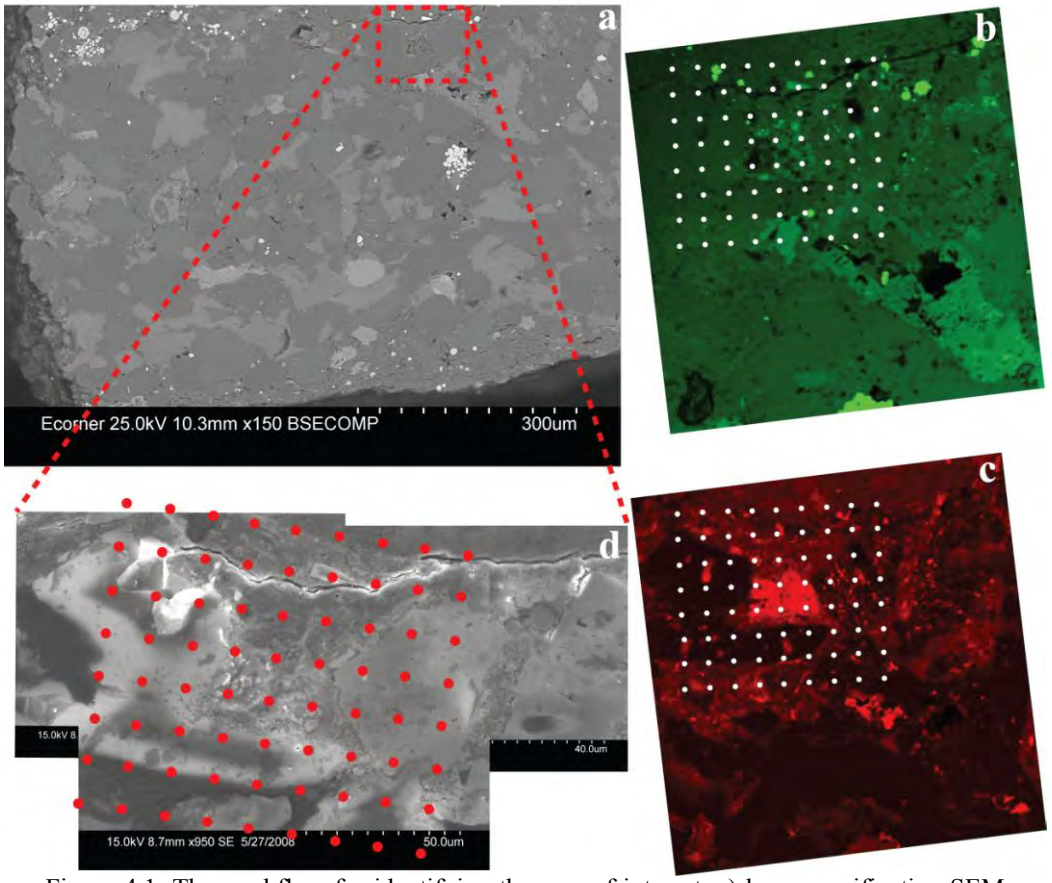

Figure 4.1. The workflow for identifying the area of interest. a) low magnification SEM image of Bazhenov Formation sample; all following images are of the area of interest marked by the dashed red box. b) CLSM image of area of interest using 488nm wavelength (green) excitation. c) CLSM image of the area of interest using 543nm wavelength (red) excitation. d) High-magnification SEM mosaic of the Bazhenov Formation area of interest; indentation points are marked by red dots. Sampling area denoted by white and red dots in Figure 2b and c and 2d respectively is 120×110 μm.

4.5. Principles and Results of Nanoindentation Measurements

All of the nanoindentation experiments were performed using a Hysitron Triboscope two-dimensional transducer mounted on a Digital Instruments Multimode atomic-force microscope equipped with a 100 μm × 100 μm scanner and a diamond indenter tip, a three-sided pyramid (Berkovich geometry) with a tip radius of approximately 150 nm. The white dots in Figures 4.1b and 4.1c, as well as the red dots in Figure 4.1d, mark nanoindentation sampling positions in Bazhenov Formation sample. The position of nanoindentations in Lockatong Formation sample is shown in Figures 4.2a and 4.2b.

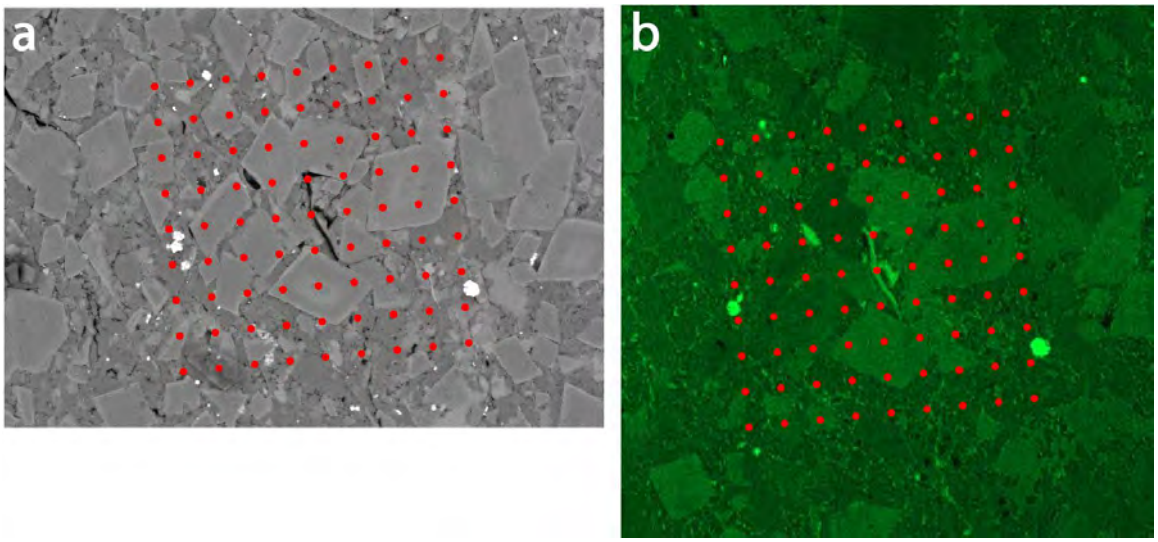

Figure 4.2. The position of nanoindentaions in the Lockatong Formation sample. Indentation points are marked by red dots on a) backscatter SEM photomicrograph and on b) CLSM image obtained under green light excitation. The area of interest in both images is 112×112 μm.

Overall more than 150 nanoindentation measurements (mostly following Cartesian grid) were performed. The distance between two neighboring measurements was 14 μm. This distance corresponds to the minimum that is necessary to avoid influence of mechanical damage from neighboring measurements. The projected tip area as a function of contact depth in the range of interest and the load frame compliance were calibrated using a fused quartz standard following the procedure of Oliver and Pharr (1992).

Determination of physical properties from nanoindentation experiments involves analysis of the generated load-displacement curves. The Oliver-Pharr method is used in this study to calculate hardness and reduced modulus values (Oliver and Pharr, 1992). During loading, the pyramidal indenter equipped with diamond tip is pushed into the sample. A portion of displacement is due to permanent plastic deformation of the sampe, the remainder of the deformation is due to elastic deformation of the sample near the tip. During unloading, it is assumed that all of the displacement is due to pure elastic rebound. The upper portion (upper third) of the unloading curve (Figure 4.3) is fitted to a power-law relationship in order to quantify the slope of the unloading (Oliver and Pharr, 1992).

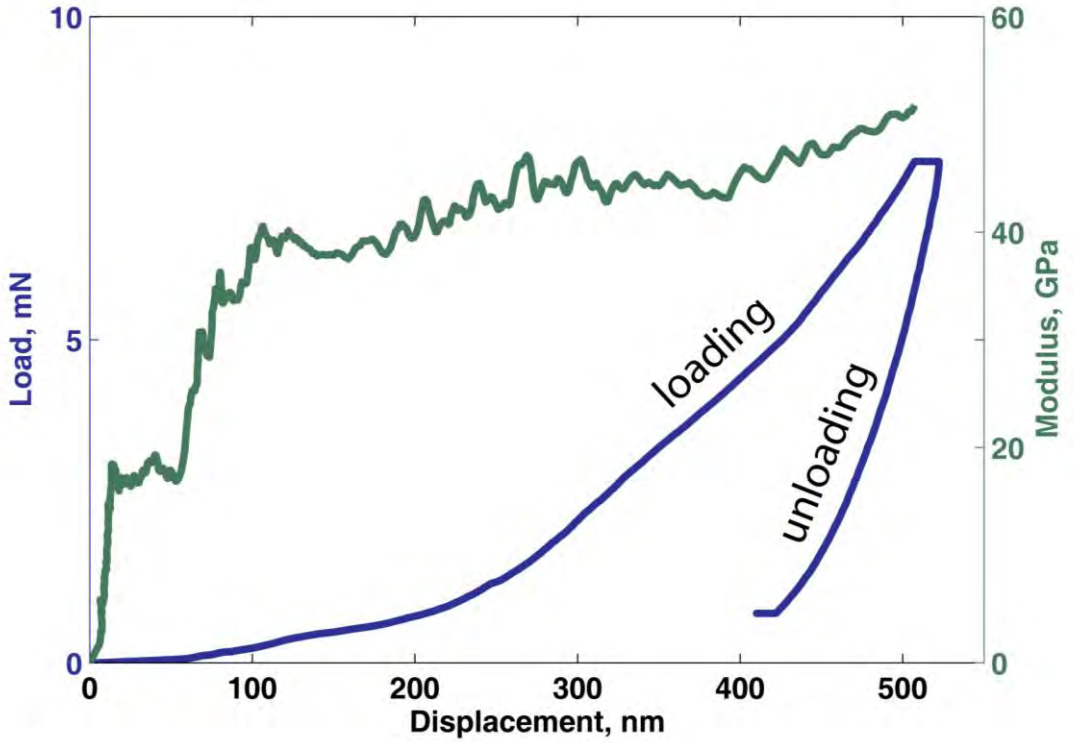

Figure 4.3. Load versus displacement data for one indentation (in blue). Reduced modulus versus displacement data for the same indentation (in green).

The slope of the initial portion of this fit determines the stiffness, S (i.e., $S=dP/dh$, where P is the load and h the displacement). The experimentally measured stiffness, S, and the projected area of elastic contact, A (based on the indentation depth and

determined from the tip area function), are used to determine the reduced modulus, E_r, according to the equation

$$E_r = S\frac{\sqrt{\pi}}{2\sqrt{A}} \tag{4.1}$$

The effect of the non-rigidity of the indenter on the load-displacement behavior is accounted for by the use of a reduced modulus, E_r, through the equation

$$\frac{1}{E_r} = \frac{(1-\nu^2)}{E} + \frac{(1-\nu_i^2)}{E_i}, \tag{4.2}$$

where E and ν are Young's modulus and Poisson's ratio for the specimen, and E_i and ν_i are the same parameters for the indenter. Since the properties of the diamond indenter are known (E_i =1141 GPa and ν_i=0.07), the quantity $E_i/(1-\nu_i^2)$=1147 GPa can be computed. The single nanoindentation measurement, E_r, yields only the combination $E/(1-\nu^2)$, rather than independent measurement of E and ν. From here on, this ratio is referred to as Indentation modulus (M), following the equation below

$$M = \frac{E}{(1-\nu^2)} \tag{4.3}$$

Therefore, Equation 4.2 could be rewritten as following

$$\frac{1}{M} = \frac{1}{E_r} - \frac{(1-\nu_i^2)}{E_i} \tag{4.4}$$

We show below that estimates of Youngs modulus, bulk modulus, and shear modulus can be made assuming various values of Poisson's ratio.

4.6. Consistency of Nanoindentation Measurements

In order to evaluate consistency of nanoindentation measurements as well as to compare elastic properties reported in literature to those obtained here, we performed several indentations within a single sand (quartz) grain within Bazhenov Formation

sample (shown in Figure 4.4). The locations of indentations are marked by white dots arranged into Cartesian grid of 3×3 in the lower right corner of Figure 4.4a (obtained under red light excitation) and by red dots in Figure 4.4b (obtained under green light excitation) and by red dots in Figure 4.4c (backscatter SEM photomicrograph).

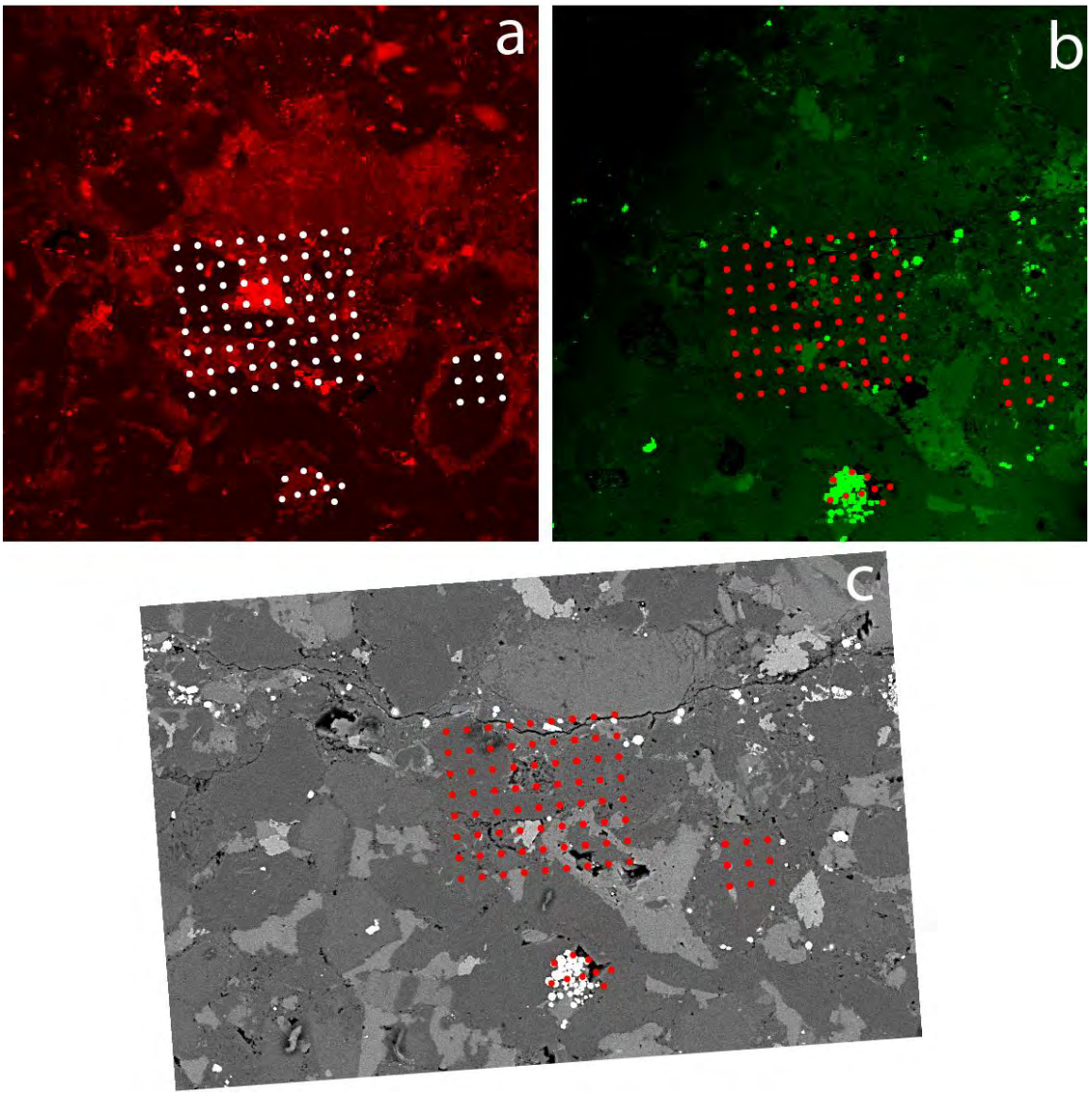

Figure 4.4. The location of all indentations within Bazhenov Formation sample. a) CLSM image under red light excitation, b) CLSM image under green light excitation, c) backscatter SEM photomicrograph. The size of CLSM images is 300 μm × 300 μm.

The results of all nine indentations are shown in Figure 4.5. The load-

displacement curves for all measurements within single quartz grain indicate very low variation in overall behavior. In particular, force needed for amount of displacement is almost identical in all measurements, as are the initial slopes of the unloading curves.

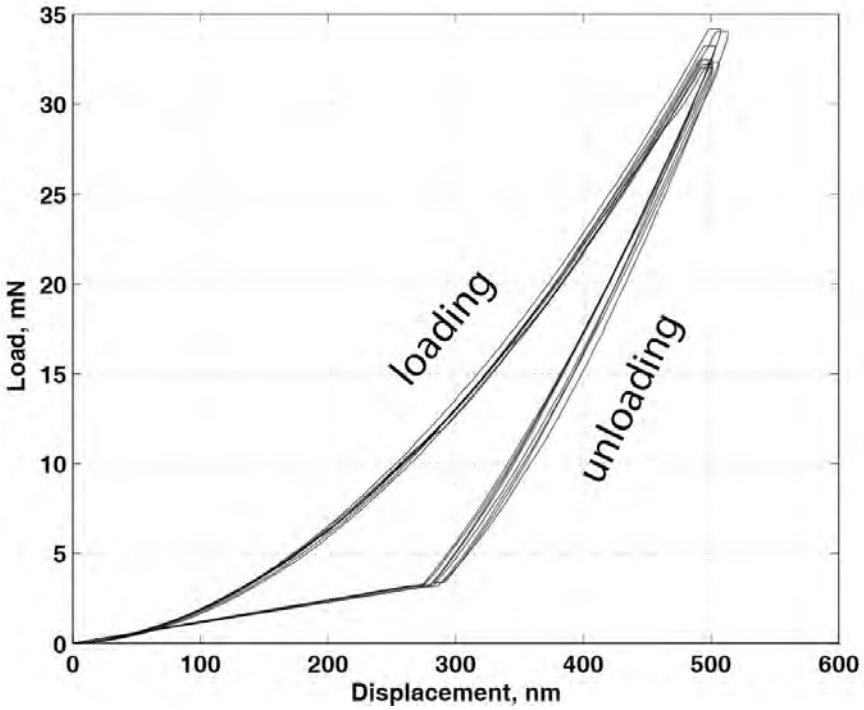

Figure 4.5. The load-displacement behavior for all measurements within single quartz grain found in Bazhenov Formation sample.

We summarize measured Indentation modulus (derived from nanoindentation experiments) and computed Young's modulus based on Poisson's ratio values from *Rock Physics Handbook (RPH)* (Mavko et al., 2009) of kerogen from Bazhenov and Lockatong Formations, as well as moduli of quartz, dolomite and pyrite in Table 4.2.

Figure 4.6 show comparisons of Indentation modulus and Young's modulus obtained from nanoindentation measurements of three minerals, namely quartz, dolomite and pyrite as well as of kerogen to corresponding values published in literature and summarized in *Rock Physics Handbook (RPH)* by Mavko et al. (2009). Poisson's ratio values reported by Mavko et al (2009) were used to arrive at corresponding indentation-derived Young's modulus values via Eqn. 4.3.

Table 4.2. Summary of the measured Indentation modulus (derived from nanoindentation experiments) and computed Young's modulus based on Poisson's ratio values from *Rock Physics Handbook* (Mavko et al., 2009) of kerogen from Bazhenov and Lockatong Formations, as well as moduli of quartz, dolomite and pyrite.

		v (*RPH*)	**M_{NANO}, GPA**	**M_{RPH}, GPA**	**E_{NANO}, GPA**	**E_{RPH}, GPA**
Pyrite		0.15	256.7	311.7	250.2	311.7
Dolomite		0.3	115.8	125.1	109.6	125.1
Quartz		0.07	87.3	93.7	87.0	93.7
Kerogen	**Bazhenov**	0.14	5.9	6.3	5.8	6.3
	Lockatong		11.9		11.7	

Results show excellent agreement for values of Indentation modulus and Young's modulus obtained in laboratory experiments (for kerogen, quartz and dolomite), however, Young's modulus of pyrite obtained from nanoindentation is 18-19% smaller (250 GPa vs. 305-310 GPa) than Young's modulus derived from ultrasonic measurements by Woeber et al (1963) and 18% smaller (250 GPa vs. 306 GPa) than Young's modulus derived from *ab initio* calculations of elastic coefficients for a pyrite crystal structure by Le Page and Rodgers (2005).

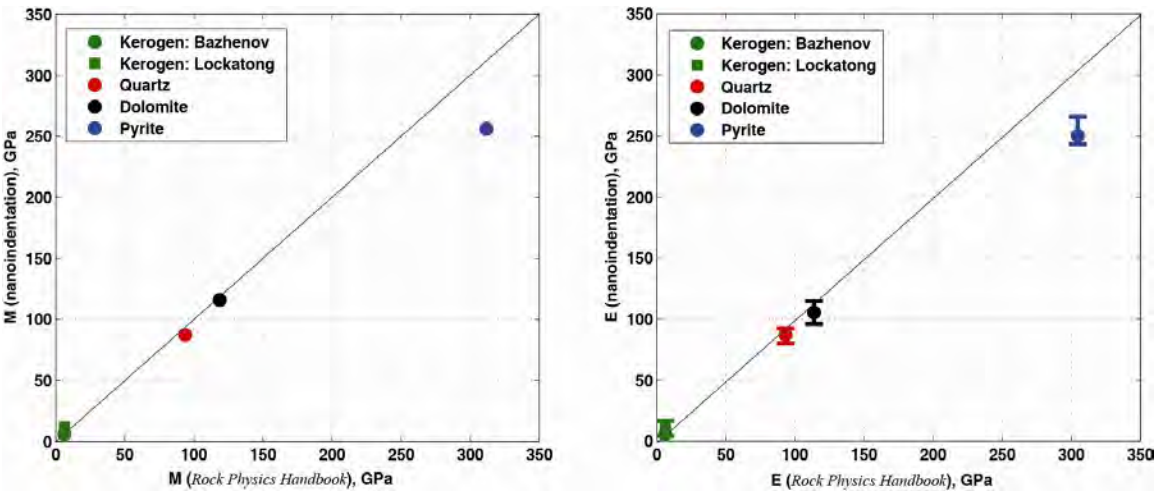

Figure 4.6. left) Comparison of Indentation modulus of several facies (kerogen, pyrite, dolomite and quartz) measured from nanoindentation measurements with Indentation modulus values computed from Mavko et al., (2009), right) Comparison of Young's modulus of several facies (kerogen, pyrite, dolomite and quartz) computed from nanoindentation measurements with Young's modulus values computed by Mavko et al., (2009). Error bars represent Poisson's ratio variation.

The 'softer' Young's modulus value obtained from nanoindentation tests could be explained by the fact that indented area is larger than single crystal of pyrite which results in 'average' elastic response of several pyrite crystals within a framboid and of surrounding background.

Values of Poisson's ratio for kerogen are lacking in the literature. We have used a range of values as well as estimates reported in nanoindentation studies of oil shales by Zeszotarski et al. (2004) and Abousleiman et al. (2007). The only published study wherein nanoindentaion tests are performed directly on the area previously confirmed to contain kerogen is of Zeszotarski et al. (2004). They measured nanoindentation modulus of kerogen from a set of Woodford Shale samples in both parallel and perpendicular to the bedding direction. The results showed (Figure 4.7) almost no anisotropy of Indentation Modulus due to the bedding within Woodford Formation kerogens.

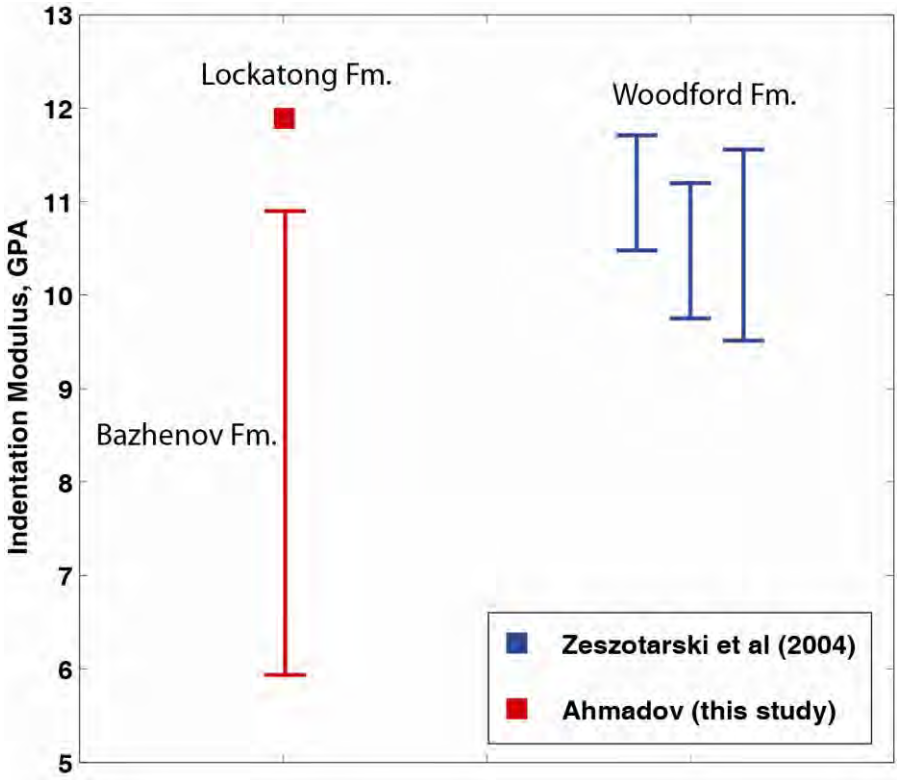

Figure 4.7. Indentation Modulus of organic matter of Lockatong and Bazhenov Formations (this study, for Bazhenov Formation the range is shown by red bar), as well as of Woodford Shale (from Zeszotarski et al., 2004) with ±95% confidence limits.

The lowest computed value of Young's modulus for kerogen within the Bazhenov Formation sample is around 6 GPa, for a corresponding Poisson's ratio of 0.14. Figure 4.8 represents a sensitivity analysis of computed Young's modulus to Poisson's ratio for Bazhenov and Lockatong Formation kerogens with previous nanoindentation studies by Zeszotarski et al (2004) and Abousleiman (2007) of both kerogen and shale, as well as of organic-rich shales analyzed by triaxial tests by Horsrud et al (1998), Dienes (1976), Chong et al (1980) and Dusseault et al (1986). Figure 4.8 (upper panel) shows three curves and area of Young's modulus computed for different Poisson's ratios for kerogens and organic-rich shales based on nanoindentation-derived Young's modulus, whereas the lower panel shows values of Young's modulus of organic-rich shales based on triaxial experiments. Each of these curves corresponds to a single nanoindentation measurement. We have computed variation of Young's modulus in the lower panel of Figure 4.8 in the same manner as for nanoindentation-derived values of kerogen. Young's modulus values of kerogen from Woodford Shale (Zeszotarski et al., 2004) are similar to the values of Lockatong Formation, whereas kerogen of Bazhenov Formation is softer than both Lockatong and Woodford Formation samples. As expected, the Young's modulus is not very sensitive to the variation of Poisson's ratio and theoretically cannot differ from Indentation modulus by more than 25% (according to Eq-n 4.3).

Dienes (1976) and Chong et al (1980) measured Young's modulus of Green River Formation's Mahogany Zone shale samples in both bed-parallel and bed-perpendicular directions using triaxial loading. Samples with more than 50% kerogen (% vol.) showed very small values of Young's modulus on the order of 2-3GPa, whereas those with 20% kerogen had Young's modulus values of 6-11GPa. These values are in good agreement with Young's modulus values (from triaxial experiments) of The Kettle Formation organic-rich shales reported by Dusseault et al (1986) and with organic-rich North Sea shales studied by Horsrud et al (1998). Unlike isotropic Young's modulus of kerogen, Young's modulus of organic-rich shales is anisotropic and higher in the direction parallel to the bedding.

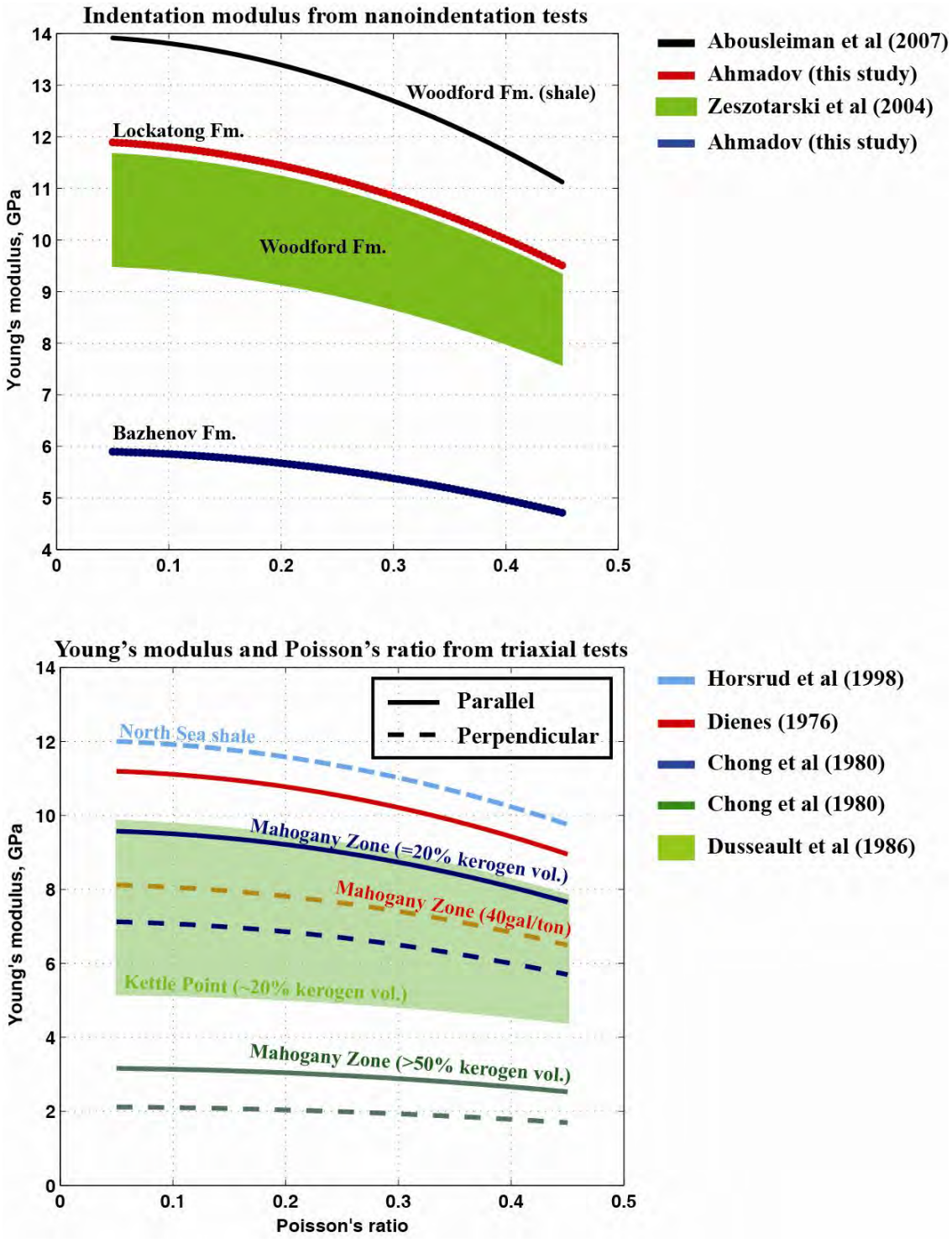

Figure 4.8. Young's modulus sensitivity of kerogen and shale to the range of Poisson's Ratio values. Upper) Young's modulus computed from Indentation modulus derived from nanoindentation tests of kerogens and shale. Lower) Young's modulus of organic-rich shales measured via triaxial loading and modeled according to Equation 4.3.

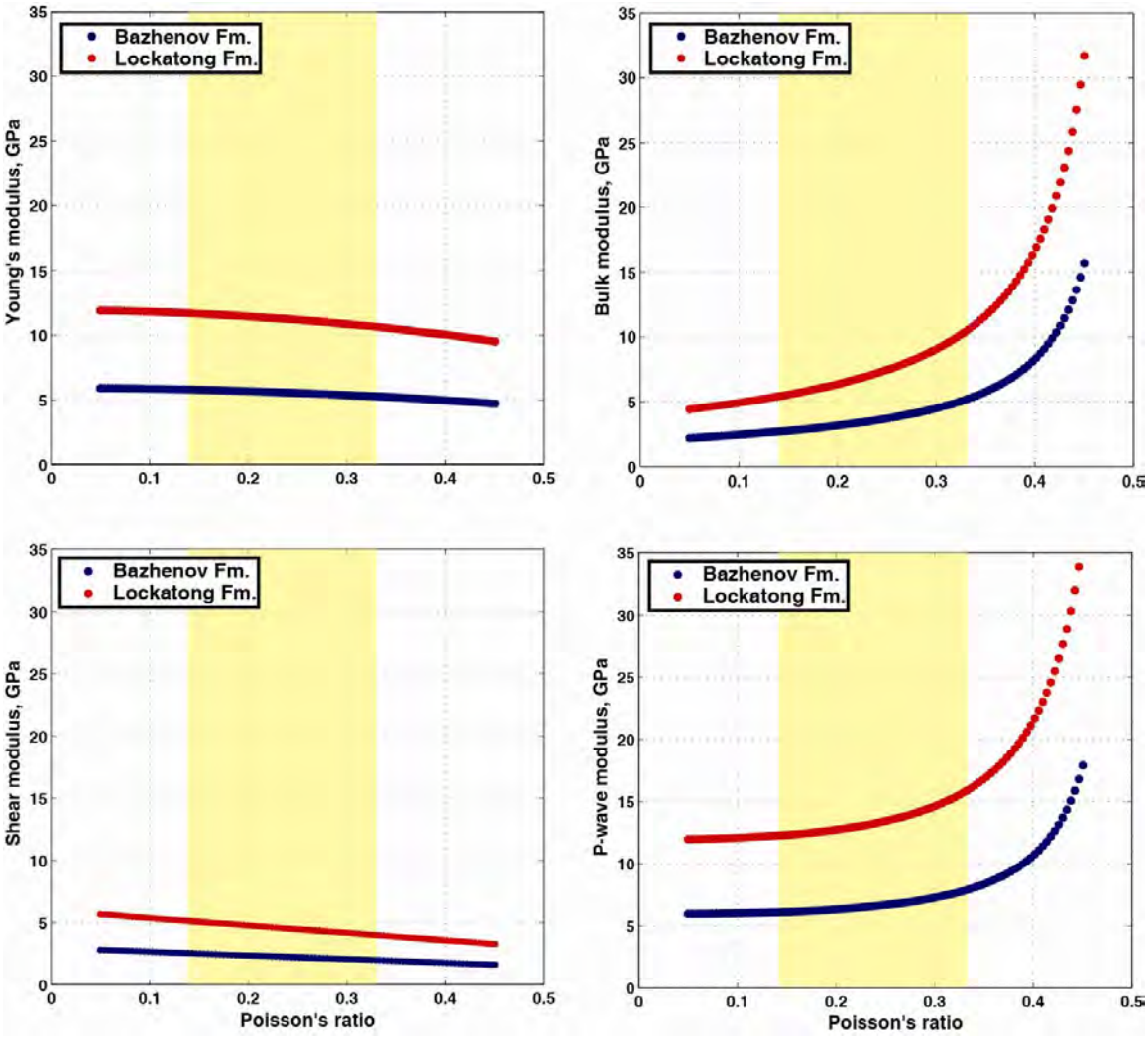

Figure 4.9. Young's, Bulk, Shear and P-wave modulus of Bazhenov (M=5.9 GPa) and Lockatong Formation (M=11.9 GPa) samples as a function of Poisson's ratio.

We have computed Young's, Bulk, Shear and P-wave modulus of Bazhenov and Lockatong Formation samples as a function of Poisson's ratio (Figure 4.9). Since kerogen is isotropic at the scale of the nanoindentation measurements, we use an approach based on the assumption of validity of linear elasticity theory for isotropic material and compute the moduli according to the following equations

$$K = \frac{E}{3(1-2\nu)} \tag{4.5}$$

$$\mu = \frac{E}{2(1+\nu)} \tag{4.6}$$

$$M_{P-wave} = \frac{E(1-\nu)}{(1+\nu)(1-2\nu)} \tag{4.7}$$

Both Young's and Shear moduli slightly reduce as Poisson's ratio increases. However, in the case of both Bulk and P-wave moduli, dramatic increases are reported at Poisson's ratio values approaching the incompressibility limit (ν=0.5). Nevertheless, we confine the region of all studied moduli to Poisson's ratio range between ν=0.14-0.33 (yellow region in Fig. 4.9). This assumption is valid for most of the Poisson's ratio values of organic-rich shales measured by conventional laboratory methods.

Figure 4.10 shows the map of the Young's, Bulk, Shear and P-wave modulus for the Bazhenov Formation sample that result from the nanoindentation experiments targeting the organic matter. The Young's as well as all other elastic moduli are computed by assuming a Poisson's ratio of 0.2. A Poisson's ratio of 0.07 was assigned to the surrounding mineral matrix, which corresponds to pure quartz. Here, organic-rich portions of the sample are characterized by relatively low values of Young's modulus ranging from 6 GPa to 15 GPa. In contrast, areas of the sample not emitting bright fluorescence (as shown in Figure 4.1b and 4.1c) correspond to the mineral matrix (predominantly quartz, clay with some pyrite) which is characterized by higher values of Young's modulus in excess of 60 GPa. The organic-rich portion is characterized by values of bulk modulus ranging between 5 GPa and 15 GPa, whereas the areas of the sample corresponding to the mineral matrix are characterized by bulk modulus values higher than 30 GPa.

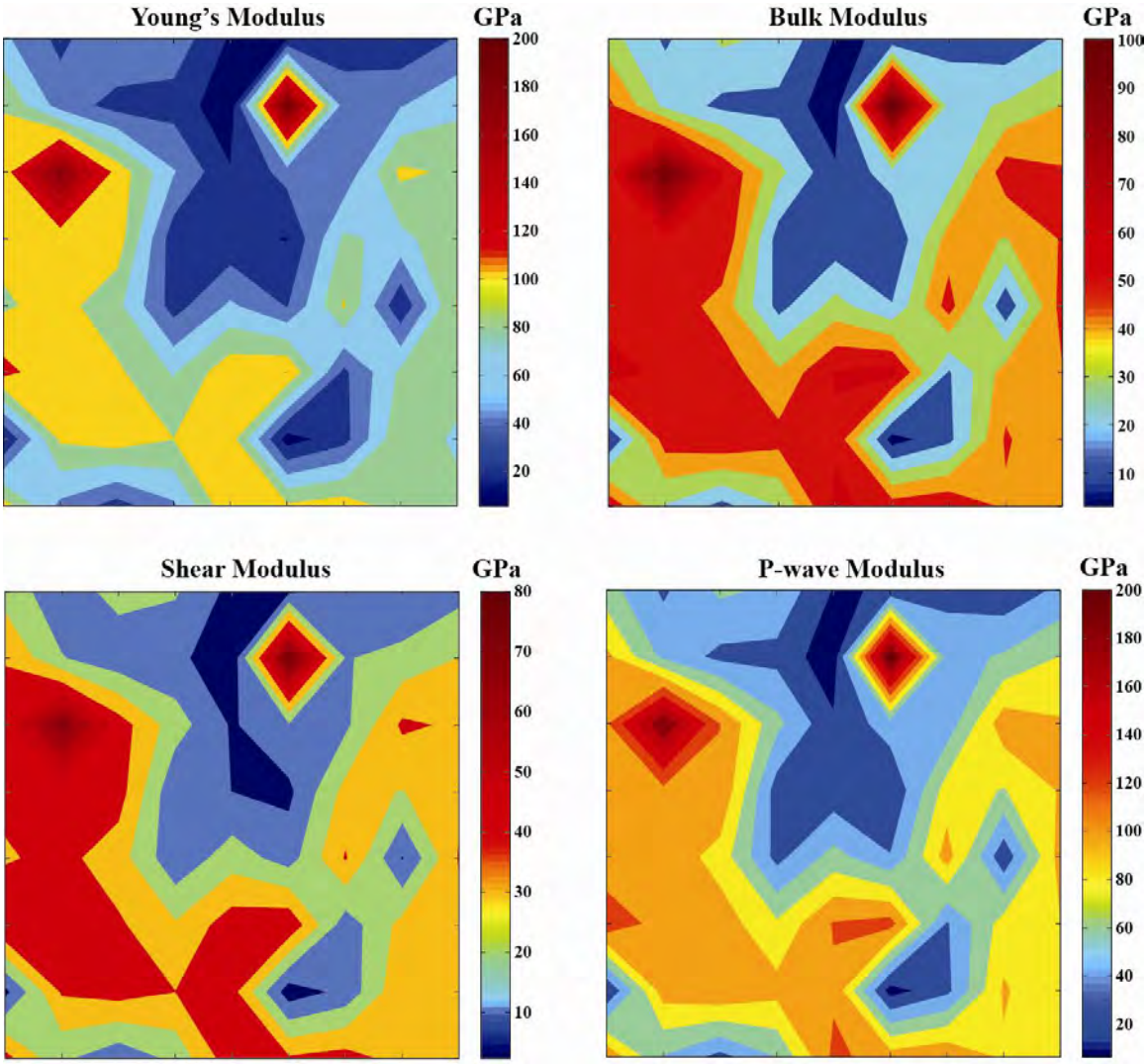

Figure 4.10. Young's modulus map of the area of interest within Bazhenov Formation sample. Organic matter (dark blue) is characterized by low (10-15 GPa) values of Young's modulus. The bar on the right is in GPa. Sampling area is 120×110 μm.

The organic-rich part of the sample is characterized by shear modulus values between 3 GPa and 10 GPa, whereas the areas of the sample corresponding to the mineral matrix are higher than 20 GPa. P-wave modulus of organic matter is between 7 GPa and 25 GPa, whereas the areas of the sample corresponding to the mineral matrix are higher than 40 GPa. Table 4.3 provides a comparison of the elastic properties of kerogen obtained in this study to both the nanoindentation measurements by Zeszotarski et al. (2004) and data from the inversion of ultrasonic measurements (Vernik et al., 1994). For corresponding

values of Poisson's ratio, the elastic moduli of the kerogen from Lockatong and Woodford Formation samples (obtained from nanoindentation methods in this study and by Zeszotarski et al. 2004) show good agreement. The elastic moduli of kerogen from the Bazhenov Formation are more similar to the elastic moduli of the kerogen from the Bakken Formation.

Table 4.3. Comparison of the elastic properties of organic matter from the Bazhenov Formation and Lockatong Formation samples obtained in this study with the elastic properties derived based on nanoindentation measurements (Zeszotarski et al., 2004) and inversion from ultrasonic data (Vernik et al., 1994).

Method: nanoindentation – this study (Bazhenov Fm.)				
v	E (GPa)	K (GPa)	μ (GPa)	$M_{\text{p-wave}}$ (GPA)
0.07	5.9	2.3	2.7	5.9
0.25	5.5	3.7	2.2	6.6
0.35	5.2	5.8	1.9	8.3
0.45	4.7	15.7	1.6	17.9
Method: nanoindentation – this study (Lockatong Fm.)				
0.07	11.9	4.6	5.5	12.0
0.25	11.1	7.5	4.5	13.4
0.35	10.4	11.6	3.9	16.8
0.45	9.5	31.7	3.3	34.0
Method: nanoindentation - Zeszotarski et al., 2004 (Woodford Fm.)				
0.07	10.4	4.0	4.9	10.6
0.25	9.8	6.6	3.9	11.8
0.35	9.2	10.2	3.4	14.8
0.45	8.4	27.9	2.9	31.8
Method: inversion from ultrasonic data -Vernik et al., 1994 (Bakken Fm.)				
0.07	7.3	2.8	3.4	7.4
0.25	6.9	4.6	2.8	8.3
0.35	6.5	7.2	2.4	10.4
0.45	5.9	19.6	2.0	22.3

In order to eliminate the influence of variation of Poisson's ratio of facies (dolomite, quartz, pyrite and kerogen) on elastic moduli, the Indentation modulus variation within the area of interest of the Bazhenov Formation sample is shown in Figure 4.11. The lack of variation in Indentation modulus values within single quartz grain is apparent in Figure 4.11d. Similarly, the corresponding map of the Indentation modulus variation within area of interest of Lockatong Formation sample is shown in Figure 4.12.

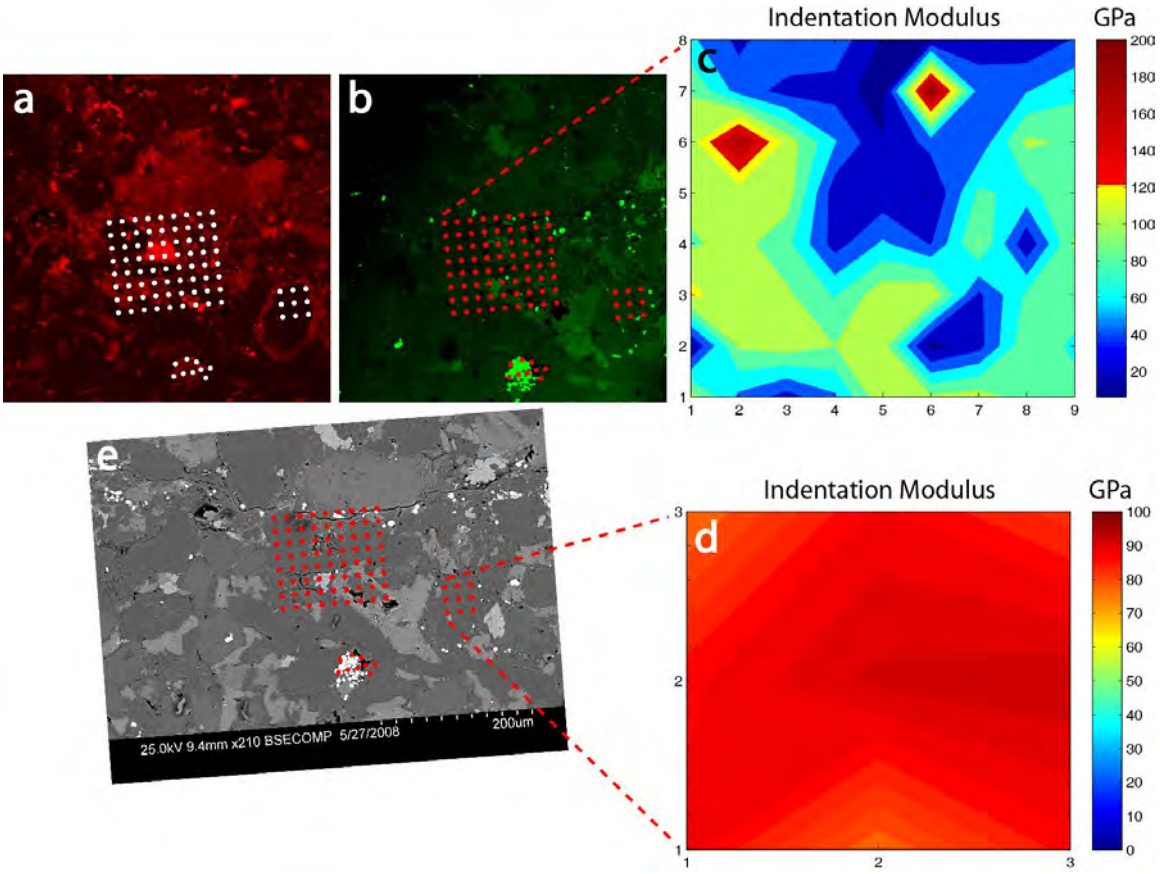

Figure 4.11. The area of interest within Bazhenov Formation sample. CLSM images obtained a) under red light excitation, b) under green light excitation. Indentation modulus maps of c) are containing kerogen, d) quartz grain. e) Backscatter SEM pthotomicrograph. Scale shown on SEM pthotomicrograph.

Table 4.4 shows comparison of Indentation moduli of kerogen from the Bazhenov and Lockatong Formation obtained in this study to those found within The Woodford Shale by Zeszotarki et al (2004).

Table 4.4. Comparison of the Indentation modulus of organic matter within Bazhenov and Lockatong Formations to published data from Woodford Formation (Zeszotarski et al., 2004).

Source	**Zeszotarski et al (2004)**	**This study**	
Formation	Woodford Shale	Bazhenov	Lockatong
M, GPa	9.8-11.7	5.9-10.9	11.9

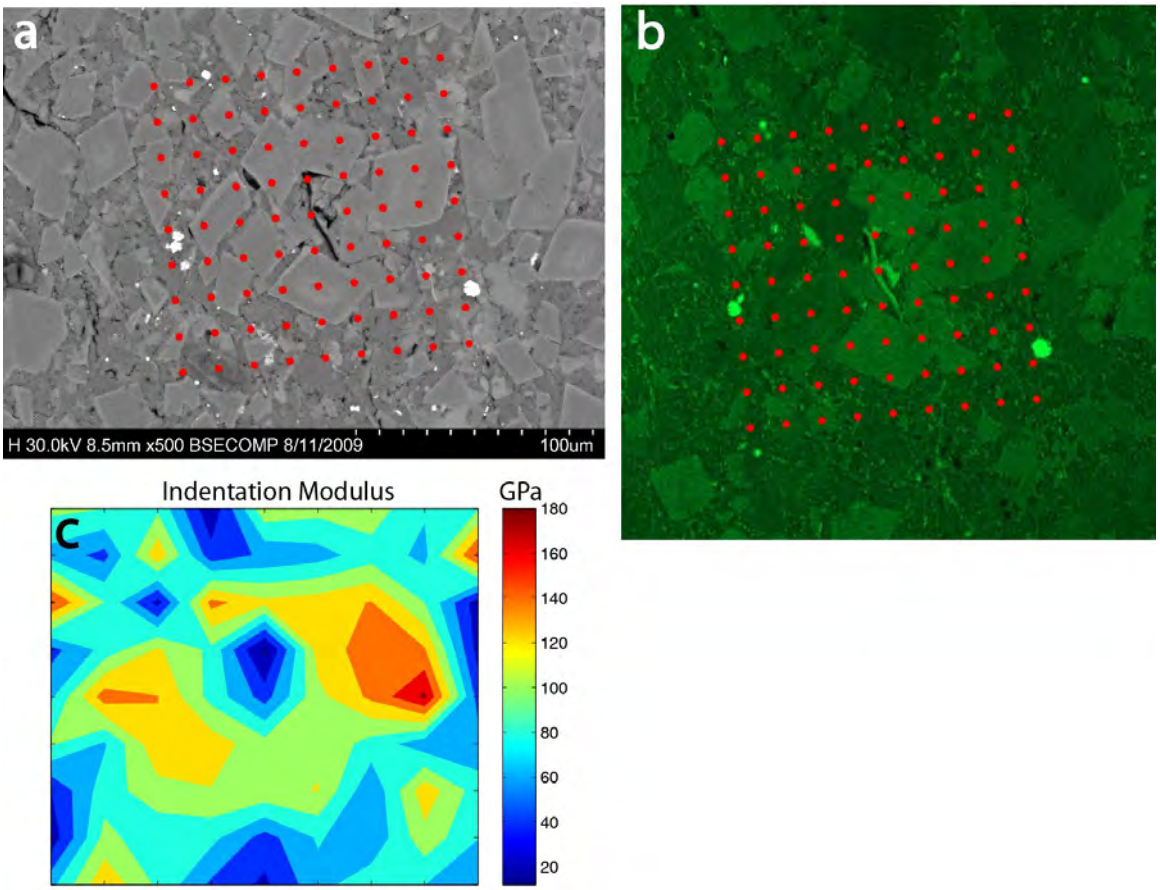

Figure 4.12. The area of interest within Lockatong Formation sample: a) Backscatter SEM pthotomicrograph, b) CLSM image obtained under green light excitation, and c) Indentation modulus map of are containing kerogen. Scale shown on SEM pthotomicrograph.

4.7. Chapter Summary

This chapter discusses a combined application of SEM, CLSM imaging and nanoindentation characterization, which provides the microscopic basis to analyze these macroscopically complex and heterogeneous rock samples. Organic matter was successfully imaged within the matrix of the Bazhenov and Lockatong Formations samples despite inherent lithologic differences of the phases. The experimental system proved capable of determining the physical properties of the kerogen without requiring extraction from the matrix. Nanoindentation measurements showed kerogen within both samples to be softer than the surrounding mineral matrix. In particular, Indentation

modulus of kerogen from the Bazhenov Formation varies between 6 GPa and 11 GPa, whereas for the Lockatong Formation sample it is about 12 GPa. These values are then used to compute Young's modulus, Bulk modulus, Shear modulus and P-wave modulus. Moreover, values of Indentation modulus of kerogen, as well as elastic properties of stiffer minerals as dolomite, quartz and pyrite are in very good agreement with previously published data. Sensitivity analysis of Young's modulus to varying Poisson's ratios of kerogen shows minor dependence throughout the range of Poisson's ratios (ν=0.05-0.45). Both Young's and Shear moduli slightly reduce as Poisson's ratio increases. However, in the case of both Bulk and P-wave moduli dramatic increase is reported at Poisson's ratio values approaching incompressibility limit (ν=0.5). Nevertheless, we confine the region of all studied moduli to Poisson's ratio range between ν=0.14-0.33 under the assumption that is valid for most of the Poisson's ratio values of organic matter and organic-rich shales measured by conventional laboratory methods and by nanoindentation. The assumed Poisson's ratio range between ν=0.14-0.33 yields the elastic moduli values of kerogen for Bazhenov and Lockatong Formation samples in the range of E=6-12 GPa, K=3-11 GPa, μ=2-5 GPa and $M_{P\text{-}wave}$= 6-16 GPa.

4.8. References

Ahmadov, R., Vanorio, T., and Mavko, G., 2009, Confocal laser scanning and atomic-force microscopy in estimation of elastic properties of the organic-rich Bazhenov Formation, The Leading Edge, 28, 19.

Abousleiman, Y. Tran, M. Hoang, S. Alberto Ortega, B. and Ulm, F-J., 2007, Geomechanics field and laboratory characterization of Woodford Shale: The next gas play, SPE paper 110120

Chi, H. M. Xiao, Z. D. Fu, D. G. and Lu, Z. H., 2006, Analysis of fluorescence from algae fossils of the Neoproterozoic Doushantuo formation of China by confocal laser scanning microscope. Microsc Res Tech 69, 253-259.

Chong, K. P., Uenishi, K., Smith, J. W., Munari, A. C., 1980, Non-linear three dimensional mechanical characterization of Colorado oil shale // Int. J. Rock Sci. & Geomech. Abstr., 17, No. 6. P. 339–347.

Dienes, J. K., 1976, Generalized ratios of elastic moduli for oil shale, in Explosively produced fracture of oil shale: Los Alamos Sci. Lab. Tech. Rep. LA-6521-PR.

Dusseault, M.B., Loftsson, M. and Russell, D., 1986, The mechanical behavior of the Kettle Point oil shale. Can. Geotech. J. 23 1, pp. 87–93.

Horsrud, P., Sønstebø, E.F. & Bøe, R., 1998, Mechanical and petrophysical properties of North Sea shales. International Journal of Rock Mechanics and Mining Sciences, 35, 1009–1020.

Kopycinska-Müller, M. Prasad, M. Rabe, U. and Arnold, W., 2007, Elastic properties of clay minerals determined by atomic force acoustic microscopy technique, M.P. André (ed.), Acoustical Imaging, 409–416.

Kempe A., Schopf J. W. Altermann W. Kudryavtsev A. B. and Heckl W. M., 2002, Atomic force microscopy of Precambrian microscopic fossils. Proc. Natl. Acad. Sci. 99, 9117–9120.

Le Page, Y., Rodgers, J. R., 2005, Ab Initio Elasticity of FeS_2 Pyrite from 0 to 135 GPa. Physics and Chemistry of Minerals, 32(8–9): 564–567.

Mavko, G, Mukerji, T. and Dvorkin, J., 2009, The Rock Physics Handbook, Cambridge University Press, p.511.

Oliver W. C. and Pharr G. M., 1992, An improved technique for determining hardness and elastic modulus using load and displacement sensing indentation experiments. J. Mater Res. 7, 1564–1583.

Stasiuk, L.D. Tomica, M. Wong, J. and Pratt, K., 1998, Fluorescence confocal laser scanning microscopy of dispersed organic matter in hydrocarbon source rocks. The Society for Organic Petrology, Abstracts and Programs 15, 88-89.

Teerman, S.C. Crelling, J.C. and Glass, G.B., 1987, Fluorescence spectral analysis of resinite macerals from coals of the Hanna Formation, Wyoming, U.S.A.: International Journal of Coal Geology, 7, 315-334.

Ulm, F. J. and Abousleiman, Y, 2006, The nanogranular nature of shale, Acta Geotechnica, 1, 77-88

Vanorio, T., T. Mukerji, and G. Mavko, 2008, Emerging methodologies to characterize the rock physics properties of organic-rich shales: The Leading Edge, **27**, no. 6, 780–787

Vernik, L., and Landis, C., 1996, Elastic Anisotropy of Source Rocks: Implications for Hydrocarbon Generation and Primary Migration: AAPG Bulletin, 80, 531-544.

Vernik L. and Liu, X., 1997, Velocity anisotropy in shales; a petrophysical study, Geophysics 62 (2), 521–532.

Vernik L., 1994, Hydrocarbon-generation-induced microcracking of source rocks, Gephysics, v. 59, n. 4, p. 555-563.

Wilkins, R. W. T,. Wilmshurst, J. R Hladky, G. Ellacott, M. V.and Buckingham, C. P., 1995, Should fluorescence alteration replace vitrinite reflectance as a major tool for thermal maturity determination in oil exploration?: Organic Geochemistry, 22, 191–209.

Woeber, A.F., Katz, S., and Ahrens, T.J., 1963, Elasticity of selected rocks and minerals. Geophys., 28, 658–663.

Zeszotarski, J.C., Chromik, R.C.. Vinci, R.P. Messmer, M.C Michels, R. and Larsen J.W., 2004, Imaging and mechanical property measurements of kerogen via nanoindentation, Geochim. Cosmochim. Acta. 68(20), 4113.

Chapter 5

Application of Nanoindentation Modulus in Geomechanical Problems

"An experiment is a question which science poses to Nature, and a measurement is the recording of Nature's answer."

--Max Planck

5.1. Abstract

We measure nanoindentation modulus (discussed in detail in the previous chapter) related to the Young's modulus via Poisson's ratio of four commonly occurring phases within source rocks – kerogen, quartz, dolomite and pyrite. Based on the measured

properties of these four phases it is possible to derive P-wave, S-wave and Lamb-wave velocities by estimating Young's modulus and assuming an appropriate Poisson's ratio. The computed velocity values are in excellent agreement with data previously published by Mavko et al (2009). The largest estimated error in velocity values is that of pyrite and does not exceed 10%.

The closure stresses of two- and three-dimensional cracks with wide range of aspect ratios are computed in all phases. The relative difference of stress values for a given aspect ratio within *softest* (kerogen) and *stiffest* (pyrite) phases is in excess of an order of magnitude. The analysis of tensile rock failure conducted herein provides a scheme for computation of stress intensity factors of analyzed fractures. The computed fracture aperture values are in good agreement with previously reported values of Zoback (2007). A thermodynamic criterion of crack propagation due to an applied load according to Griffith (1920, 1924) allows for computation of the tensile stress of a crack as a function of the surface energy per unit area for pyrite, dolomite, quartz and kerogen in three different scenarios: *general case*, *plane strain* and *3-D penny-shaped* cracks.

We analyze conditions for microhydraulic fracturing within organic layers according to Vernik (1994). As results of these computation*s* a relative difference in the maximum aperture of the crack as a function of bounding medium is discussed. The results are in very good agreement with values previously reported by Vernik (1994).

Finally, the deformation of overburden rocks during growth of a laccolith using the theory of bending of a stack of thin elastic plates is analyzed in the framework provided by Pollard and Johnson (1973). Given that elastic properties are combined in the form of nanoindentation modulus, we use this value directly in order to compute flexural rigidity of the layer in overburden.

5.2. Introduction

In brief summary of the previous chapter, we recall that nanoindentation consists of creating contact between a sample surface and an indenter tip of known geometry (in our case – pyramidal Berkovich type) and mechanical properties, accompanied by a

continuous application and recording of change in load, *P*, and depth, *h*. Our tests consist of a constantly increasing load (displacing more sample volume), followed by a short hold and then a constant unloading resulting in a *P*-*h* (load-displacement) curve reported herein (Figure 5.1). In this figure, load-displacement curves for five indentation tests are reported. As expected, much higher force is needed to displace the same volume of material for *stiffer* phases (pyrite, dolomite and quartz) compared to *softer* phases (kerogen of Lockatong and Bazhenov Formation samples). Subsequently, we apply a continuum scale model of the load-displacement curve to reduce the indentation response into two mechanical properties; indentation modulus, *M*:

$$M = \sqrt{\frac{\pi}{2}}\sqrt{\frac{S}{A_c}} \tag{5.1}$$

and indentation hardness, *H*:

$$H = \frac{P}{A_c} \tag{5.2}$$

where $S=dP/dh$ is the (measured) initial slope (upper third of the curve) of the unloading branch of the *P*-*h* curve, *P* is the (measured) maximum indentation load, and A_c is the projected contact area of the indenter on the sample surface which is typically determined as a function of the (measured) maximum indentation depth, h_{max} (Oliver and Pharr, 2004).

Elastic contact mechanics offers a convenient solution for linking the measured indentation modulus, *M*, with the elastic properties of the indented material. The Galin-Sneddon solution (Constantinides et al., 2006) of a rigid, axisymmetric indenter acting on a linear elastic, isotropic, infinite half-space suggests that the indentation modulus is directly related to the Young's modulus, *E*, and Poisson's ratio, *v*, of the studied material:

$$M_s = M = \frac{E_s}{(1-\nu_s^2)} \tag{5.3}$$

where the subscript *s* indicates the indented material. The effect of indenter compliance can be considered by substituting for *M* in Eq. (5.3) the commonly employed (Oliver and Pharr, 2004) result of the Hertz contact solution of two elastically deformable bodies:

$$\frac{1}{M} = \frac{(1-\nu_s^2)}{E_s} + \frac{(1-\nu_{in}^2)}{E_{in}} \tag{5.4}$$

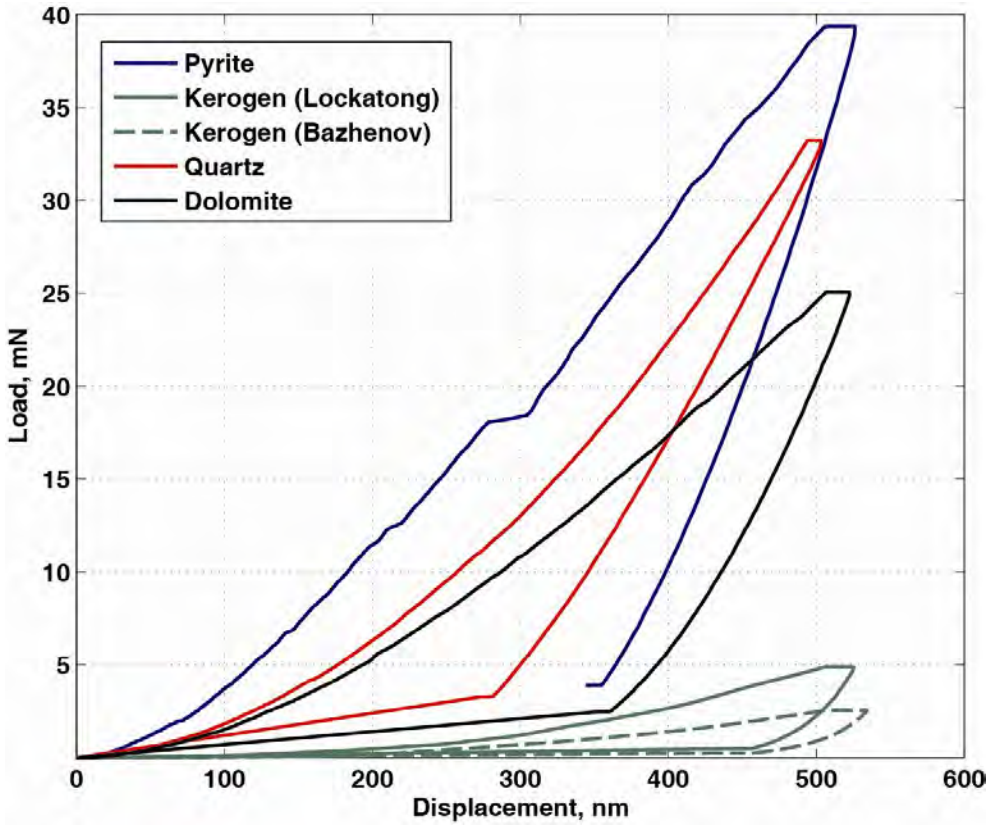

Figure 5.1: Load-displacement curves for five indentation tests. Note, much higher force is needed to displace the same volume of material for *stiffer* phases (pyrite, dolomite and quartz) compared to *softer* phases (kerogen of Lockatong and Bazhenov Formation samples).

where E, ν and E_{in}, ν_{in} are the elastic constants of the studied material and the indenter, respectively. It is important to note that diamond crystals used as indenters are

transversely isotropic and Eq. (5.4) is only approximate. Recently, The International Standards Organization issued a draft international standard (ISO 14577, 2002) which recommend the use of E_{in} = 1140 GPa, ν_{in} = 0.07 for diamond indenters. However, for the purposes of the current analysis, we will employ aforementioned isotropic constants. The elastic properties (Young's, Bulk and Shear) of the individual phases could be computed from the indentation moduli by considering Eq. (5.4) and assuming a Poisson's ratio of studied material. The effect of the Poisson's ratio on the magnitude of E calculated from a given M was discussed in the previous chapter. In this chapter we start by calculating the material elastic modulus M, which does not include any assumption on the Poisson's ratio. It is also interesting to note that after some initial loading (~50nm), the reduced modulus for dolomite and quartz phases reaches a plateau (Figure 5.2), whereas for pyrite modulus constantly reduces and for both kerogen phases constantly increases as a function of increasing load. This effect could be explained by relative difference in projected contact area of the indenter on the sample surface within compared phases. For dolomite and quartz A_c<<grain size of these phases, whereas for pyrite framboids and kerogen, the projected contact area of the indenter on the phase surface is of the same magnitude as the size of these phases. In other words, when a pyrite framboid is targeted, the resulting reduced modulus is expected to drop as a function of increasing load due to the fact that as the indenter displaces more and more pyrite volume the surrounding material starts carrying indenter's load along with pyrite framboid. Since pyrite is much stiffer than any of the observed phases, the drop of the reduced modulus is evident. Contrary to pyrite, kerogen's modulus increases as the indenter displaces more and more kerogen volume. Kerogen is the softest phase, therefore, the effect of the surrounding matrix will result in increasing kerogen's modulus as a function of increasing volume displaced.

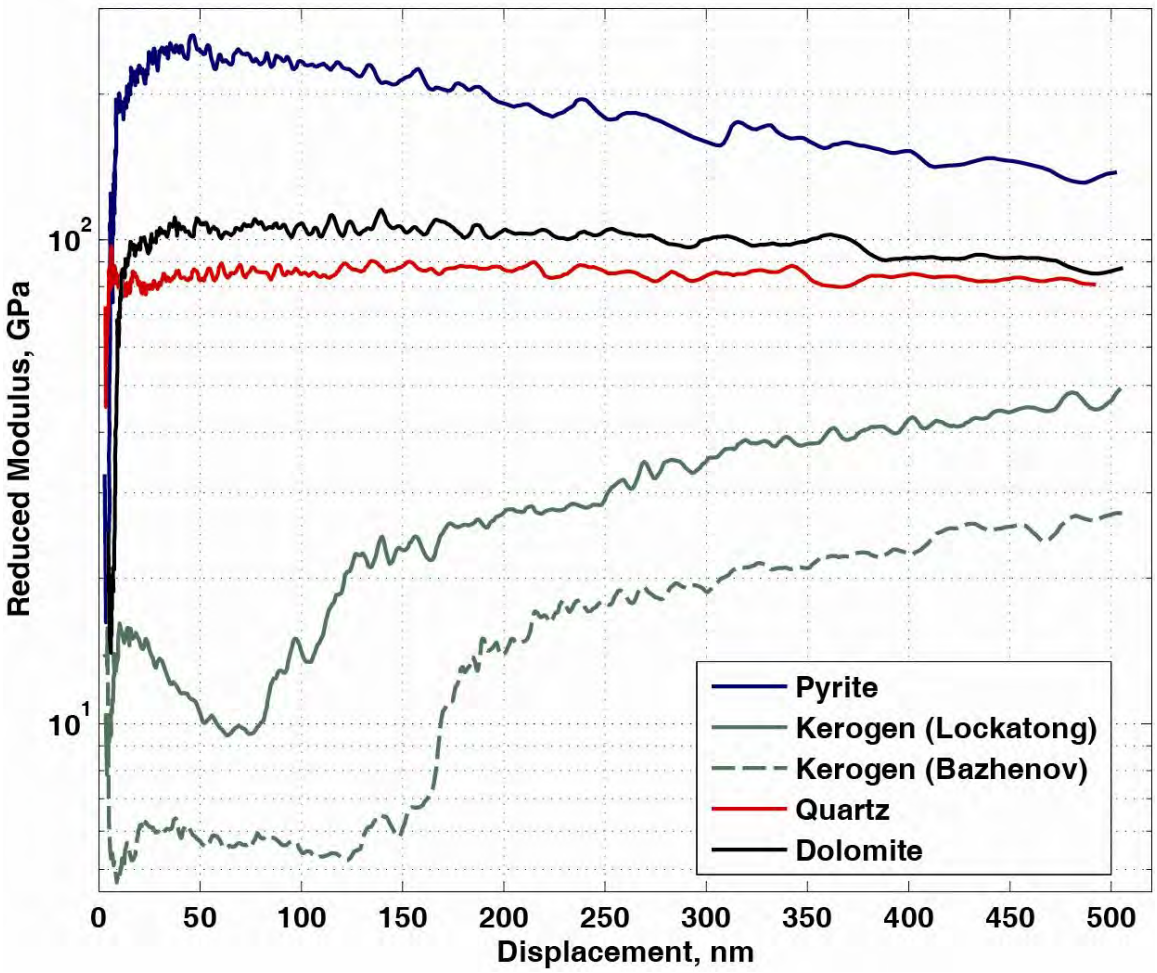

Figure 5.2: Modulus-displacement curves for five indentation tests. Note, after some initial loading (~50nm), the reduced modulus for dolomite and quartz phases reaches a plateau, whereas the pyrite modulus constantly decreases and both kerogen (of Lockatong and Bazhenov Formation samples) phases constantly increases as a function of increasing load.

5.3. Nanoindentation-based velocity estimation

In order to compare nanoindentation derived velocities of different phases to those measured by conventional laboratory techniques, we use values reported by Mavko et al (2009) for pyrite, quartz, dolomite and kerogen (Figure 5.3) phases. The values of both compressional P-wave (V_p) and shear S-wave (V_s) velocities are computed using Eqns. 5.5 and 5.6 for waves in a homogeneous isotropic medium as follows

$$V_p = \sqrt{\frac{K + \frac{4}{3}\mu}{\rho}} = \sqrt{\frac{E(1-\nu)}{(1+\nu)(1-2\nu)\rho}} \tag{5.5}$$

$$V_s = \sqrt{\frac{\mu}{\rho}} = \sqrt{\frac{E}{2(1+\nu)\rho}} \tag{5.6}$$

where ρ is the density and K and μ are bulk and shear moduli of the phase, respectively.

For computation of nanoindentation-derived velocities we use Poisson's ratio values reported by Mavko et al (2009) for all studied phases.

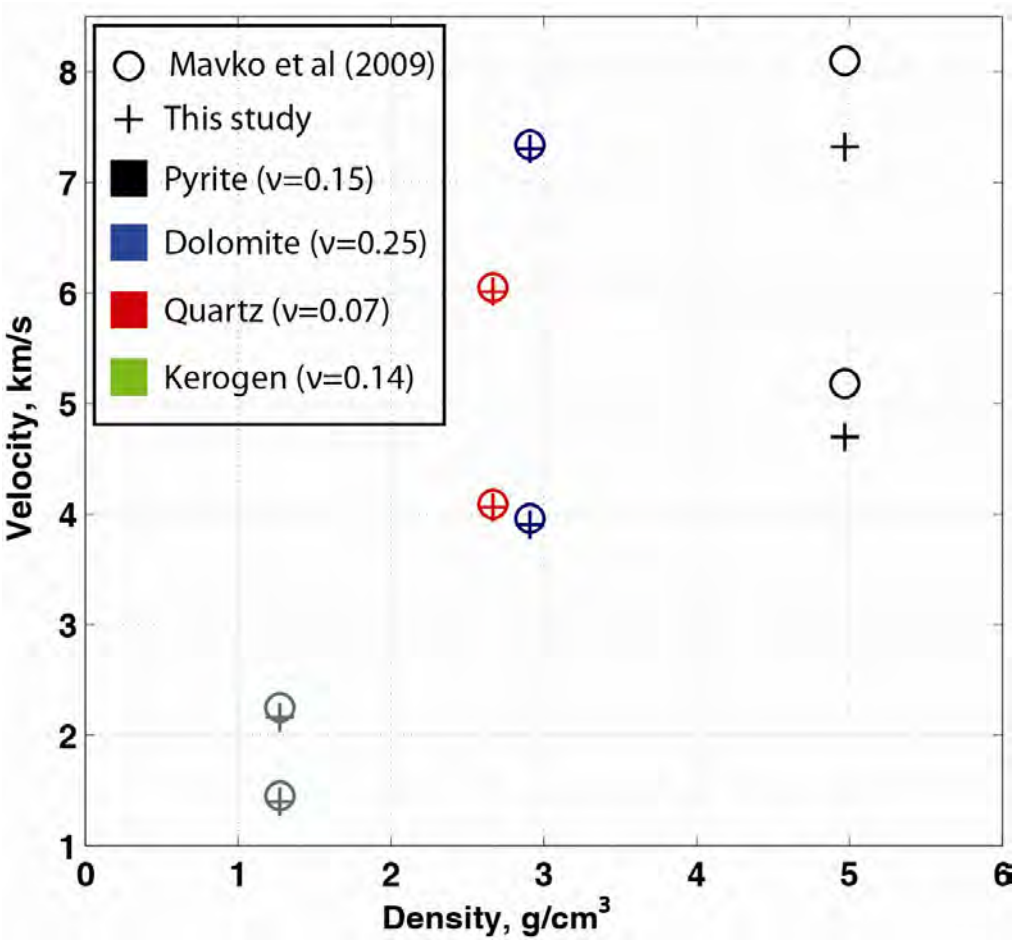

Figure 5.3: Comparison of nanoindentation-derived P-wave and S-wave velocities of different phases to those measured by conventional laboratory techniques reported by Mavko et al (2009). Colors denote phases. Circles denote values from Mavko et al (2009). Crosses are nanoindentation-derived velocities. Higher values of the phase are P-wave velocities, whereas lower ones are S-wave velocities. NOTE: Bazhenov Formation kerogen (M=5.9 GPa) is used for values of kerogen.

The velocity values based on nanoindentation tests for quartz, dolomite and kerogen are in a very good agreement with those reported by Mavko et al (2009). However, the largest deviation is observed for pyrite. Both pyrite's velocities (V_p and V_s) reported by Mavko et al (2009) were measured by Simmons and Birch (1963). Mavko et al (2009) report one averaged value of both velocities computed from three velocity values corresponding to those measured on pyrite crystals oriented in the three principal directions. More precisely, V_p of pyrite reported by Simmons and Birch (1963) is within range of 7.74-8.51 km/s, with V_s range of 4.59-5.71 km/s depending on the principal direction of measurement. Nevertheless, we compute the relative difference in V_p and V_s of all phases (Figure 5.4) from our comparison to corresponding velocity values of Mavko et al (2009). The relative deviation of velocities for quartz, dolomite and kerogen

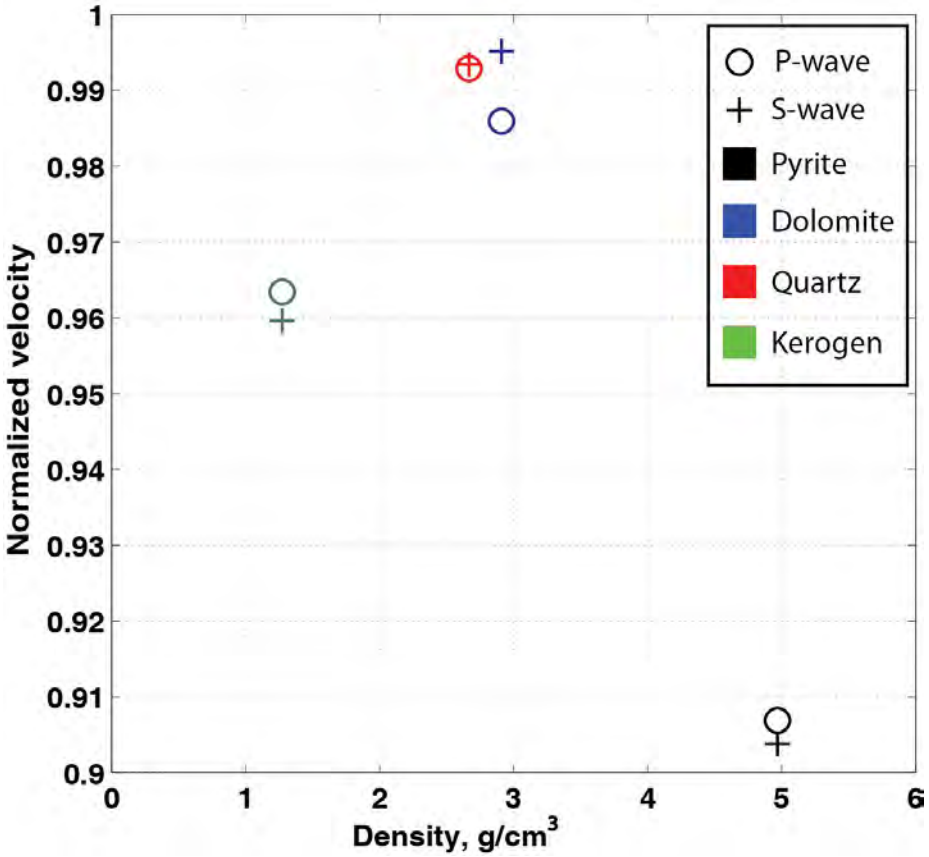

Figure 5.4: The relative difference in V_p and V_s of all phases when compared to those measured by conventional laboratory techniques reported by Mavko et al (2009). Colors denote phases. Circles denote P-wave velocity values, whereas crosses are S-wave velocity values. NOTE: Bazhenov Formation kerogen (M=5.9 GPa) is used for values of kerogen.

is within 4% compared to Mavko et al (2009). Pyrite's velocities are 10% slower when computed from nanoindentation tests compared to velocities reported by Mavko et al (2009).

Other types of waves capable of propagating along free surfaces or along interfaces between different media are reported by Jaeger et al. (2007). Lamb waves are waves of plane strain that can propagate along a plate having traction-free upper and lower surfaces, with displacement components in both the direction of propagation along the plate and perpendicular to the plane of the plate. The detailed discussion of highly dispersive Lamb waves can be found in Viktorov (1967) and Miklowitz (1978). One of the characteristics of these waves is that at wavelengths greater than about ten times the plate thickness, the phase and group velocity of the wave approaches the value (V_{plate}) which is given by Eq. 5.7

$$V_{plate} = \sqrt{\frac{E}{\rho(1-\nu^2)}} = \sqrt{\frac{M}{\rho}} \tag{5.7}$$

which should satisfy the condition of $V_s < V_{plate} < V_p$. The phase velocity decreases with decreasing wavelength, approaching the Rayleigh wave speed for wavelengths less than about half the plate thickness. Similar analysis given for Rayleigh waves (Jaeger et al., 2007) indicates that surface waves in a half-space cannot have a displacement in the *y* direction, in other words, along the free surface but across the direction of propagation as such waves cannot satisfy the traction-free boundary condition. Unlike computation of V_p and V_s, which require *a priori* knowledge of Poisson's ratio of the phase, Lamb-wave velocity (V_{plate}) can be directly obtained from nanoindentation tests based on the Eq. 5.7. Therefore, we compute values of V_{plate} along with V_p and V_s for all phases, and compare them and show that the condition of $V_s < V_{plate} < V_p$ is satisfied (Figure 5.5). It is interesting to note that for all phases, except dolomite, P-wave velocities are almost identical to Lamb-wave velocities. This effect is due to the difference in Poisson's ratios of the

phases. Dolomite, according to Mavko et al (2009), has the highest Poisson's ratio of any of these phases (ν=0.2-0.3).

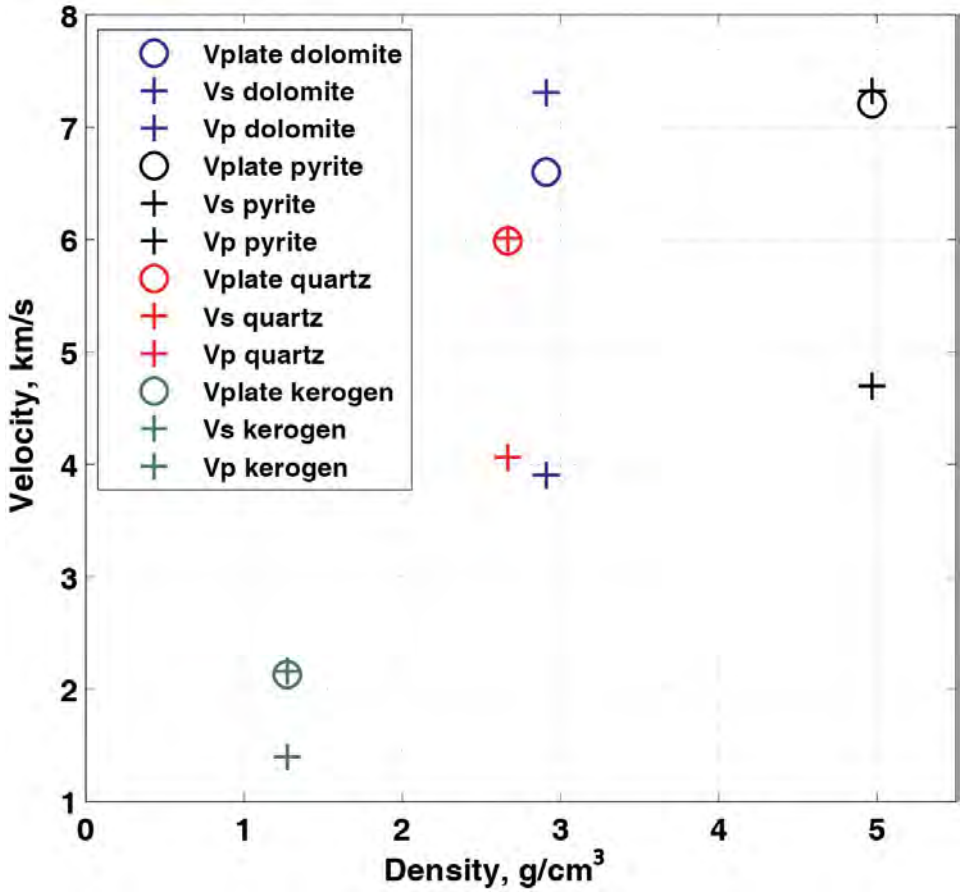

Figure 5.5: Comparison of values of V_{plate} with V_p and V_s for all phases. The condition of $V_s<V_{plate}<V_p$ is satisfied. Note, for all phases, except dolomite, P-wave velocities are almost identical to Lamb-wave velocities. This effect is due to the difference in Poisson's ratios of phases. Dolomite, according to Mavko et al (2009), has the highest Poisson's ratio of all these phases (ν=0.2-0.3). NOTE: Bazhenov Formation kerogen (M=5.9 GPa) is used for values of kerogen.

5.4. *Two-dimensional thin cracks*

Mavko et al (2009) provide a convenient description of a very thin two-dimensional crack in terms of elastic line dislocations, assuming that the crack lays along $-c<x<c$ in the y=0 plane and is very long in the z direction. Under this assumption, the total relative displacement of the crack faces $u(x)$, defined as the displacement of the negative face relative to the positive face, is related to the dislocation density function by

$$B(x) = -\frac{\partial u}{\partial x} \tag{5.8}$$

where $B(x)dx$ is the total length of the Burger vectors of the dislocations lying between x and $x+dx$. The change of stress in the crack plane resulting from introduction of a dislocation line with unit Burger vector at the origin is given by

$$\sigma = \frac{\mu_0}{2\pi Dx} \tag{5.9}$$

where D=1 for screw dislocations and D=(1 – ν) for edge dislocations and μ_0 is the shear modulus. Mode I and mode II cracks could be described by edge dislocations, whereas mode III cracks could be described by screw dislocations.

The stress is the component of traction in the crack plane parallel to the displacement: normal stress for mode I deformation, in-plane shear for mode II deformation, and out-of-plane shear for mode III deformation. Therefore, the stress resulting from the distribution $B(x)$ is given by the convolution

$$\sigma(x) = \frac{\mu_0}{2\pi D}\int_{-c}^{c}\frac{B(x')dx'}{x-x'} \tag{5.10}$$

The deformation for stress-free crack faces under a remote uniform tensional stress, $d\zeta$, acting normal to the plane of the crack is the case of nonfrictional cavities. In this case, the outward displacement distribution of each crack face is given by

$$U(x) = \frac{c\sigma(1-\nu)\sqrt{1-(x/c)^2}}{\mu_0} = \frac{2c\sigma(1-\nu^2)\sqrt{1-(x/c)^2}}{3K_0(1-2\nu)} \tag{5.11}$$

Accordingly, the volume change is given by

$$\frac{d\upsilon_p}{d\sigma} = \pi U(0)ca = \frac{2\pi c^2 a(1-\nu^2)}{3K_0(1-2\nu)} \tag{5.12}$$

Theaforementioned results for displacement and volume change are not limited to cracks of elliptical cross-section and apply to any two-dimensional crack of arbitrary cross-section given that it is very thin and approximately planar.

In the case of a very thin elliptical (in cross-section) crack with half-width *b* in the thin direction, the volume is $\upsilon=pabc$, and the pore stiffness under plane-strain deformation is given by

$$\frac{1}{K_\phi^{'}} = \frac{1}{A}\frac{dA}{d\sigma} = \frac{(c/b)(1-\nu)}{\mu_0} = \frac{2(c/b)(1-\nu^2)}{3K_0(1-2\nu)} \tag{5.13}$$

(Mavko and Nur, 1978) describe another special case of crack of nonelliptical form with initial shape given by

$$U_0(x) = 2b\left[1-\left(\frac{x}{c_0}\right)^2\right]^{3/2} \tag{5.14}$$

where c_0 is the crack half-length and $2b$ is the maximum crack width shown in Figure 5.6. Unlike elliptical cracks that have rounded or blunted ends, this crack has tapered tips where faces make a smooth, tangent contact.

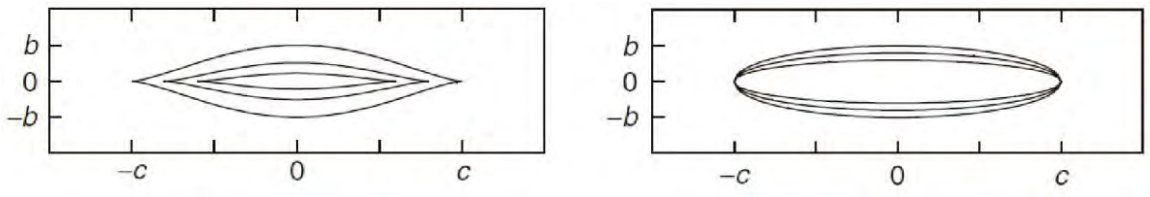

Figure 5.6: left) A nonelliptical crack shortens as well as narrows under compression, right) An elliptical crack only narrows. From Mavko et al (2009).

If pressure, P, is applied, the crack shortens as well as thins, and the pressure-dependent length is given by

$$c = c_0 \left[1 - \frac{2(1-\nu)}{3\mu_0 (b/c_0)} P \right]^{1/2} \tag{5.15}$$

where the deformed shape is given by

$$U(x,P) = 2b\left(\frac{c}{c_0}\right)^3 \left[1 - \left(\frac{x}{c}\right)^2\right]^{3/2}, \qquad |x| \le c \tag{5.16}$$

The main outcome of the smoothly tapered crack tips and the gradual crack shortening is that there is no stress singularity at the crack tips resulting in crack closure at (i.e., $U \to 0$) as the crack length goes to zero ($c \to 0$). Then closing stress (ζ_{close}) is provided by

$$\sigma_{close} = \frac{b}{c}\frac{3E}{4(1-\nu^2)} = \frac{b}{c}\frac{3M}{4} \tag{5.17}$$

where $\alpha_0 = b/c_0$ is the original crack aspect ratio. Eq-n 5.17 is consistent with the usual rule of thumb that the crack-closing stress is numerically $\sim \alpha_0 E$. The exact factor depends on the morphology of the original crack shape. Similarly, the pressure (ζ_{close}) required to close a two-dimensional elliptical crack of aspect ratio α_0 is

$$\sigma_{close} = \frac{b}{c}\frac{E}{2(1-\nu^2)} = \frac{b}{c}\frac{M}{2} \tag{5.18}$$

Figure 5.7 reports the closing stress (ζ_{close}) necessary to close an elliptical crack of initial aspect ratio α_0=0.0001 inserted in a medium that corresponds to one of the four phases reported earlier. A crack within organic matter will require an order of magnitude less closing stress (0.3MPa) compared to those within quartz and dolomite. The stress

required to close the same crack in pyrite will be in excess of 10MPa. It is not surprising that the difference in stress values required to close a crack in *stiffer* phases is within factor of 3, whereas the difference in stresses between *stiffer* (quartz, dolomite and pyrite) phases and *softer* (kerogen) is on the order of magnitude.

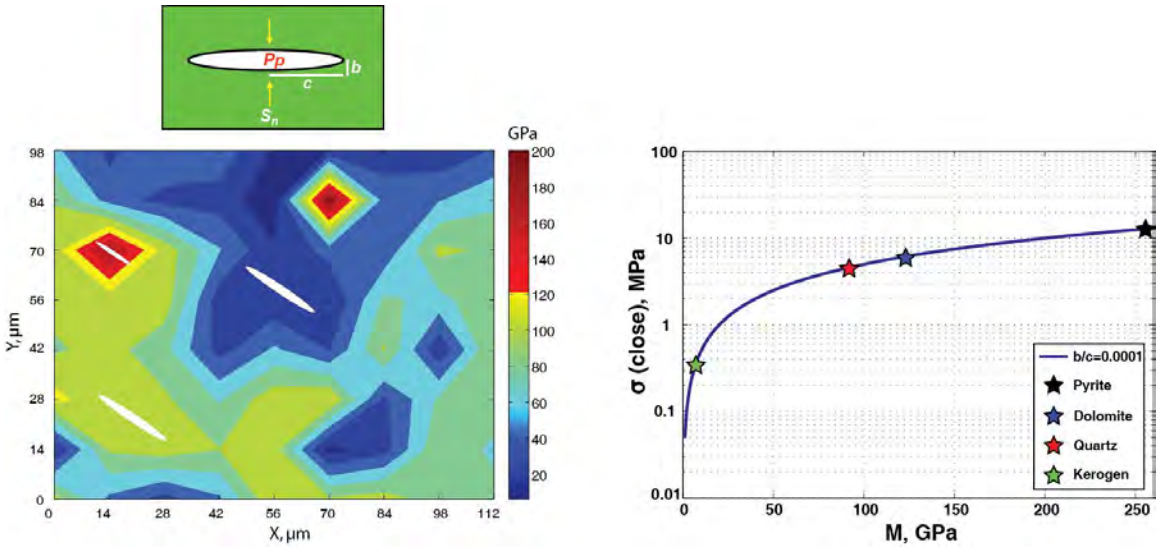

Figure 5.7: left) conceptual rendering of cracks of fixed aspect ratio inserted in a medium of varying elastic properties (colorbar shows value of M), right) closing stress (ζ_{close}) necessary to close an elliptical crack of initial aspect ratio of α_0=0.0001 inserted in a medium that corresponds to one of the four phases.

Another way to display the relationship in Figure 5.7 is to show the closing stress (ζ_{close}) necessary to close elliptical cracks of varying aspect ratios of $\alpha_0=10^{-4}$-10^{-7} inserted in a medium that corresponds to one of the phases reported earlier (Figure 5.8). The same closing stress that will close a crack of a given aspect ratio within a kerogen will only close a crack that has a magnitude higher aspect ratio in *stiffer* (quartz, dolomite and pyrite) phases.

5.5. *Tensile rock failure*

In this section, we will apply nanoindentation-derived modulus to analyze tensile rock failure. The tensile strength of rock is relatively unimportant compared to the compressional strength of rock and the frictional strength of fractures and faults in earth's crust (Zoback, 2007). The previous statement is explained as following: the tensile

strength of essentially all rocks is quite low, on the order of just a few MPa (Lockner, 1995), and given that pre-existing flaws exist in any appreciable volume of rock, tensile strength would be expected to approach zero. *In situ* stress at depth is never tensile. However, tensile fractures can occur around wellbores in some stress states because of the stress concentration at the wellbore wall. Alternatively, when the fluid pressure exceeds the local least principal stress hydraulic fracturing (form of tensile failure) can occur. As a result, this process could lead to the formation of Mode I fractures in rock (opening-mode, planar joints) as illustrated in the Figure 5.6. Even though joints are relatively common in nature, they are unlikely to have a significant effect on bulk permeability in high porosity rocks at depth since they are essentially closed at any finite effective stress. However, the effect is opposite in low-porosity rocks, such as some source rocks, gas shales, igneous and metamorphic rocks, as well as tight gas sandstones. Given that fracture permeability is highly dependent on the aperture of any open fracture at depth, small tensile micro-fractures will have largest effect in on flow within *tight* rocks. The hydraulic fracturing process, when fluid pressure is purposely raised above the least principal stress to propagate a fracture which is then filled with sand or another material as a propant to increase formation permeability, will also result in the extension of a tensile fracture.

Zoback (2007) shows that in the case of hydraulic fracture propagation, the rock strength in tension is essentially insignificant in the fracture extension process. According to the fracture mechanics, the stress intensity at the tip of a planar Mode I fracture is given by

$$K_i = \pi(P_f - S_3)\sqrt{L} \tag{5.19}$$

where K_i is the stress intensity factor, P_f is the pressure within the fracture, L is the length of the fracture and S_3 is the least principal stress. When the stress intensity factor K_i exceeds the critical stress intensity, K_{ic}, or fracture toughness, fracture propagation will occur. Figure 5.9 (upper panel) shows the value of $(P_f - S_3)$ required to cause propagation as a function of fracture length L, for two rock types (Rummel and Winter, 1983): with

high fracture toughness (very strong, low-porosity sandstone or dolomite), and a rock with a very low fracture toughness (poorly cemented sandstone). The lower panel of Figure 5.9 shows the same value of ($P_f - S_3$) required to cause propagation as a function of fracture length for rock types reported by Senseny and Pfeifle (1984). Zoback (2007) notes that while the fracture toughness is important to initiate and initially extend a fracture, once a fracture reaches a length of a few tens of cm, extremely small pressures in excess of the least principal stress are required to make the fracture propagate, irrespective of the rock's fracture toughness. As a result, the most important condition of fracture propagation is that P_f exceed S_3 by only a small amount. Therefore, the strength of the rock in tension is irrelevant after Mode I fracture starts to propagate.

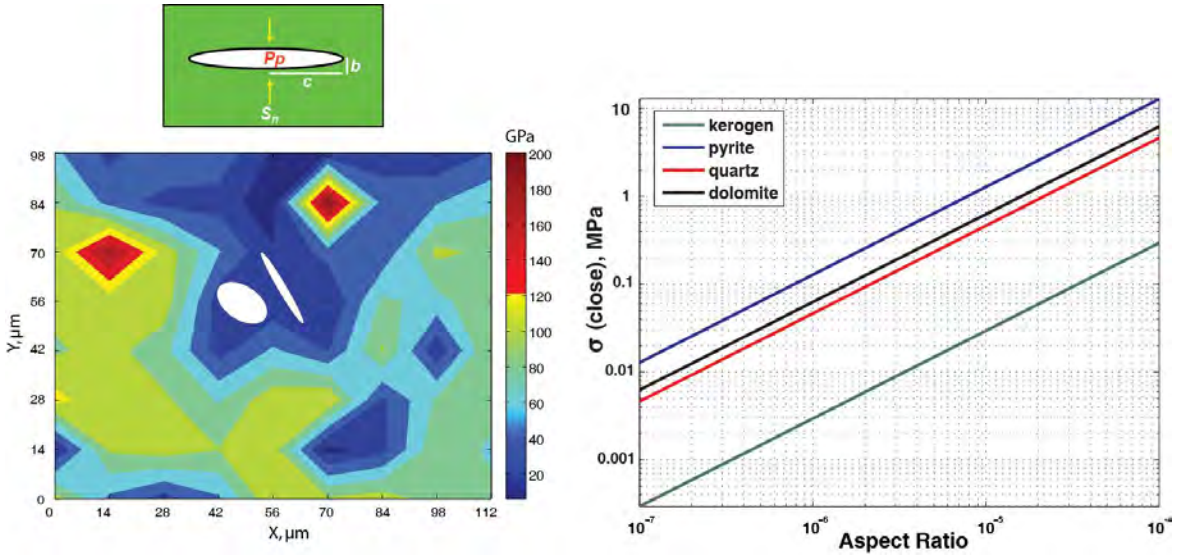

Figure 5.8: left) conceptual rendering of cracks of various aspect ratios inserted in medium of varying elastic properties (colorbar shows value of *M*), right) closing stress (ζ_{close}) necessary to close an elliptical crack of various aspect ratios inserted in a medium that corresponds to one of the four phases.

Contrary to compressional strength, tensile strength does not seem to be dependent on simple effective stress, especially in *tight* (low-porosity/low-permeability) rocks. Schmitt and Zoback (1992) demonstrated in the laboratory that pore pressure acting in granitic rocks had less of an effect on reducing the tensile stress at which failure would be expected. They suggested that as failure was approached, the initiation of

micro-cracks in the incipient failure zone causes pore pressure to drop locally, thus counteracting the effect on strength.

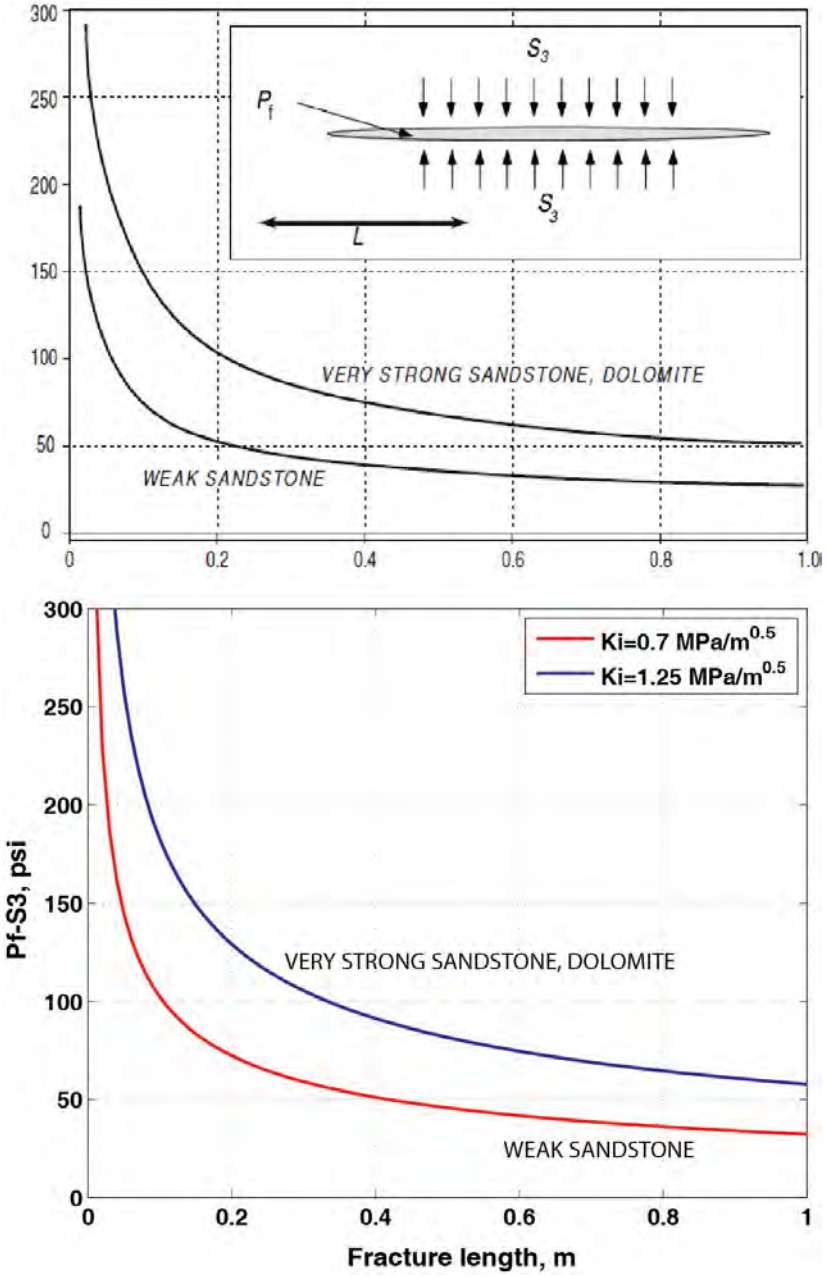

Figure 5.9: upper panel) the difference between internal fracture pressure and the least principal stress as a function of fracture length for a Mode I fracture for rocks with extremely high fracture toughness (such as very strong sandstone or dolomite) and very low fracture toughness (weakly cemented sandstone) from Zoback (2007), lower panel) the same value of (P_f − S_3) required to cause propagation as a function of fracture length for rock types reported by Senseny and Pfeifle (1984).

5.5.1 Fluid flow through Mode I fractures

To consider flow through a Mode I fracture based on a parallel plate approximation for fluid flow through a planar fracture (Nelson and Handin, 1977, Ahmadov et al, 2007), first we define a fluid viscosity, η, the volumetric flow rate, Q, resulting from a pressure gradient, ∇P, that is dependent on the cube of the separation between the plates, b,

$$Q = \frac{b^3}{12\eta}\nabla P \tag{5.20}$$

Next, considering flow through a long crack of length L, with elliptical cross-section, we define maximum separation aperture (b_{max}) of the fracture at its midpoint, given by Zoback (2007)

$$b_{\max} = \frac{2(P_f - S_3)L(1-\nu^2)}{E} = \frac{2(P_f - S_3)L}{M} \tag{5.21}$$

where P_f is the fluid pressure in the fracture acting to open it and S_3 is the least principal stress acting to close the fracture resulting in a flow rate given by

$$Q = \frac{\pi}{8\eta}\left(\frac{b_{\max}}{2}\right)^3 \nabla P \tag{5.22}$$

yielding

$$Q = \frac{\pi}{8\eta}\left[\frac{(P_f - S_3)L(1-\nu^2)}{E}\right]^3 \nabla P = \frac{\pi}{8\eta}\left[\frac{(P_f - S_3)L}{M}\right]^3 \nabla P \tag{5.23}$$

Thus, the flow rate through a fracture in response to a pressure gradient is proportional to the cube of the product of the length times the difference between the fluid pressure inside the fracture and the least principal stress normal to it. When P_f slightly exceeds S_3,

fractures of any appreciable length would be expected to propagate, thereby dropping P_f and causing the fracture to close. In fact, because the static case in the earth is that

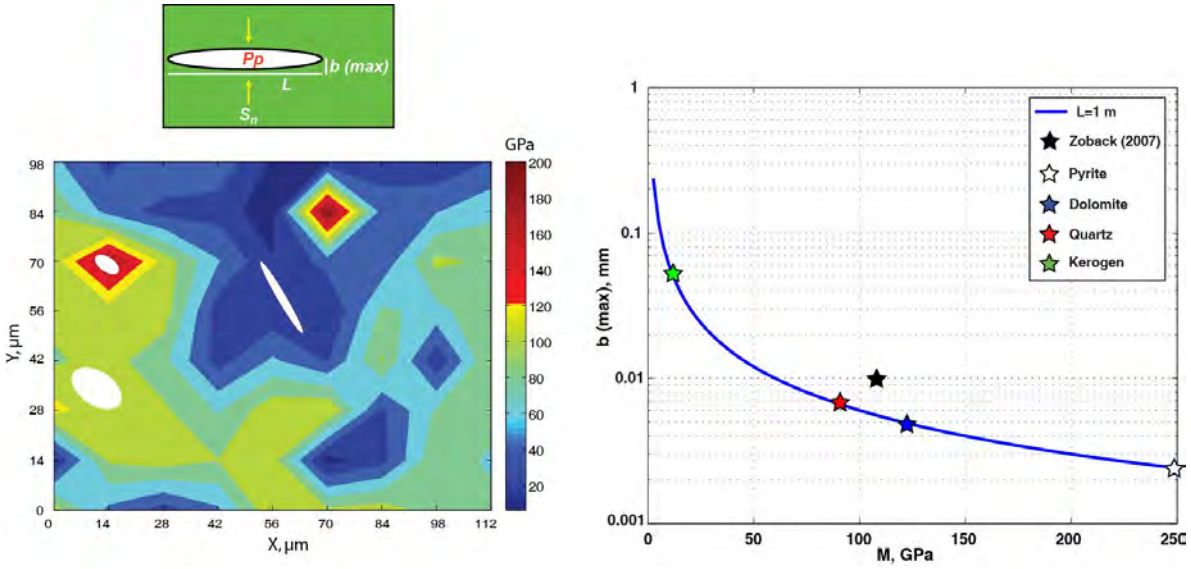

Figure 5.10: left) conceptual rendering of cracks of various aspect ratios inserted in medium of varying elastic properties (colorbar shows value of *M*), right) maximum aperture of 1m long fracture within the analyzed phases compared to the maximum aperture reported by Zoback (2007).

.

$(P_f - S_3)<0$, transient high fluid pressures are required to initiate Mode I fractures (i.e. natural hydrofracs), but following initiation, the pressure is expected to drop and the fractures to close. Hence, only extremely small fracture apertures would be expected. Zoback (2007) considers 0.3 MPa as a reasonable upper bound for $P_f - S_3$ in a one meter long Mode I fracture because of the relative ease with the fracture would propagate (Figure 5.10).

For reasonable values of v and E which are not reported by Zoback (2007), equation (5.21) predicts that the maximum aperture of a Mode I fracture would be on the order of 0.01 mm. Since, Zoback (2007) does not provide elastic properties of the medium in which the fracture is inserted we place it between quartz and dolomite phases in Figure 5.10 for comparison with all phases reported here. As apparent from comparison, the relative location of the case discussed by Zoback (2007) is not crucial; given that medium is *common* sedimentary rock. The aperture value of fractures within quartz and dolomite

phases is in good agreement with values of Zoback (2007). However, in the case of kerogen, the aperture value is an order of magnitude higher compared to *stiffer* phases. Clearly, considering a fracture to be only 1m long is arbitrary, but as L increases, the maximum value of $P_f - S_3$ decreases thereby limiting b_{max} (equation 5.21). Of course, real Mode I fractures in rock will not have perfectly smooth surfaces so that even when they are closed, a finite aperture will remain (Brown and Scholz, 1986) such that in rocks with almost no matrix permeability, closed Mode I fractures can enhance flow.

5.5.2 Tensile stresses in Griffith cracks

Thus far, our analysis has assumed that cracks of a given geometry are present in the rock. Griffith (1920, 1924) derived a thermodynamic criterion of crack propagation due to an applied load. The main idea of his analysis is the recognition that, as a crack propagates, energy is needed to create the new surface area.

Jaeger et al., (2007) consider a thin rock specimen of length L, width b, and thickness t, containing a thin crack of length $2c$ lying perpendicular to the side of length L. In Figure 5.11 a tensile load T is applied to the rock by a hanging mass m connected to

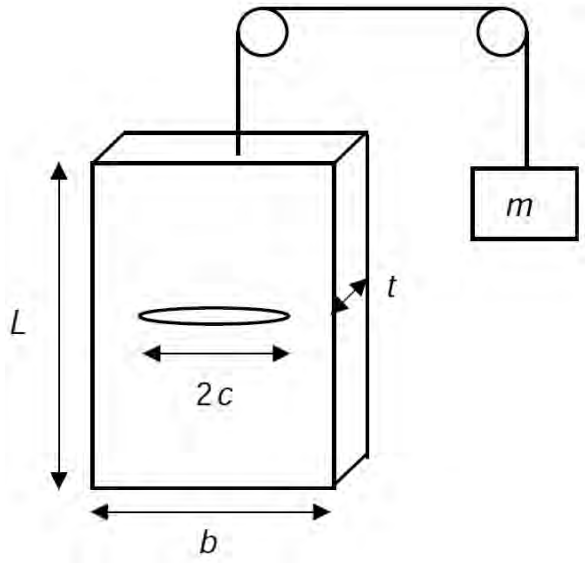

Figure 5.11: Crack extended under constant applied load, used in the derivation of the Griffith criterion from Jaeger et al., (2007).

the rock by a cord that passes over a frictionless pulley. Since the rock slab is very thin and the system is assumed to be under equilibrium, plane stress analysis could be used for the deformation of the rock. The total energy of this thermodynamic system composed of the surface energy of the crack, the elastic strain energy in the rock, and the gravitational potential energy of the mass.

If the crack grows from half-length c to some new half-length, $c+\delta c$, while the load is maintained constant, according to Griffith, the change will only be plausible (thermodynamically) if extension of the crack permits the total energy of the system to decrease. With c treated as a variable, under the condition of all other parameters fixed, and Jaeger et al., (2007) show below that the total energy is an increasing function of c for c less than some critical value c_{cr} and a decreasing function of c for $c > c_{cr}$. Therefore, c_{cr} can be found by maximizing the total energy as a function of crack half-length. The condition is found by solving the Equation 5.24

$$\left(\frac{\partial E_{total}}{\partial c}\right)_T = \frac{dE_{elastic}}{dc} + \frac{dE_{surface}}{dc} + \frac{dE_{gravitational}}{dc} = 0 \tag{5.24}$$

The elastic strain energy stored in the rock is $T^2bLt/2E$, where E is the *effective* Young's modulus of the rock. According to the terms of small-strain elasticity, this energy does not vary with L, therefore it is suitable to use the unstrained length, L_0, wherein the elastic energy can be written as $T^2bL_0t/2E$. Jaeger et al., (2007) found the effective modulus of a rock containing a single fracture lying normal to the loading direction to be $E=E_m/[1 + (2\pi c^2/Lb)]$. If the initial crack is much smaller than the specimen dimensions, the above expression reduces to $E=E_m[1-(2\pi c^2/Lb)]$. Consequently, the first derivative on the right side of (5.24) is computed as follows

$$\frac{dE_{elastic}}{dc} = \frac{dE_{elastic}}{dE}\frac{dE}{dc} = \left(\frac{-T^2bL_0t}{2E^2}\right)\left(\frac{-4\pi E_m c}{bL_0}\right) = \frac{2\pi T^2 tE_m c}{E^2} \approx \frac{2\pi T^2 tc}{E_m} \tag{5.25}$$

and given the fact that E is only slightly less than E_m we substitute it in the end of (5.25). If the surface energy term is considered, surface energy of any crack of surface area A is equal to γA, where γ is the surface energy per unit area. This results in the surface area of a crack of length $2c$ passing through the entire thickness t of the rock slab to be equal to $4\gamma ct$. The second derivative term on the right of (5.24) is thus given by

$$\frac{dE_{surface}}{dc} = 4\gamma t \tag{5.26}$$

The gravitational potential energy of the mass that is responsible for the load of the rock is mgh, where h is the elevation of the mass above some datum related to the deformation of the rock under the condition that if the rock expands by some amount δL, the mass will be reduced by the same amount. The length L of the specimen is given by $L=L_0(1+\varepsilon)=L_0[1+(T/E)]$, where it is convenient to disregard the common convention of *compression=positive* and take the tensile strain as positive. Finally, the third derivative term on the right side of (5.24) can thus be derived as

$$\begin{aligned}\frac{dE_{gravitational}}{dc} &= \left(\frac{dE_{gravitational}}{dh}\right)\left(\frac{dh}{dL}\right)\left(\frac{dL}{dE}\right)\left(\frac{dE}{dc}\right) = \\ &= (mg)(-1)\left(\frac{-TL_0}{E^2}\right)\left(\frac{-4\pi E_m c}{bL_0}\right) = -\frac{4\pi cmgTE_m}{bE^2} \approx -\frac{4\pi cmgT}{bE_m}\end{aligned} \tag{5.27}$$

where the applied load tensile stress T is given by $T = mg/bt$, so (5.27) takes the form of

$$\frac{dE_{gravitational}}{dc} = -\frac{4\pi cT^2 bt}{bE_m} = -\frac{4\pi cT^2 t}{E_m} \tag{5.28}$$

Combining (5.24), (5.25), (5.26), and (5.27) results in

$$\frac{2\pi T^2 tc}{E_m} + 4\gamma t - \frac{4\pi c T^2 t}{E_m} = 4\gamma t - \frac{2\pi T^2 tc}{E_m} = 0 \tag{5.29}$$

We note that Equation (5.29) can be solved for the critical crack length c_{cr} above which, according to Griffith, crack is thermodynamically free to grow at fixed tensile stress T

$$c_{cr} = \frac{2\gamma E_m}{\pi T^2} \tag{5.30}$$

Alternatively, we can consider the quasi-statical load increase and solve (5.29) for the tensile stress T_{cr} at which a crack of initial length c will be able to propagate

$$T_{cr} = \sqrt{\frac{2\gamma E_m}{\pi c}} \tag{5.31}$$

assuming plane strain conditions yields the criterion given below

$$T = \sqrt{\frac{2\gamma E}{\pi(1-\nu^2)c}} = \sqrt{\frac{2\gamma M}{\pi c}} \tag{5.32}$$

while for a three-dimensional penny-shaped crack, the result is

$$T = \sqrt{\frac{\pi\gamma E}{4(1-\nu^2)c}} = \frac{1}{2}\sqrt{\frac{\pi\gamma M}{c}} \tag{5.33}$$

It is interesting to note that the three expressions mentioned above differ only by multiplicative factors on the order of unity. Each of them shows that small cracks will require relatively large stresses to allow propagation, while large cracks can propagate subjected to smaller stresses.

Griffith's criterion (5.31) is a necessary thermodynamical condition that must be satisfied for crack to propagate, however in itself is not sufficient to initiate growth. As a result, the necessary state presumably is that the T at the crack tip must be large enough to break the atomic bonds. However, since the stress concentration at the tip of a small aspect ratio elliptical crack is quite substantial, the latter condition will in practice always be satisfied if Griffith's criterion is satisfied. Figure 5.12 shows computation of the tensile stress as a function of the surface energy per unit area, γ, for phases tested using nanoindentation.

We cover a wide range of γ determined from stable tensile-fracture tests on a variety of rock types and reported by Friedman et al. (1972). In their work, the range of provided values for a set of sedimentary rocks including quartzite, sandstone, granite, marble and limestone is γ=1-12.7 Pa/m. We slightly extend this range in lower-value direction to account for direct measurements of the surface energy based on the Gilman cleavage technique (Gilman, 1960) derived values of γ for quartz and calcite crystals measured by Brace and Walsh (1962), Gilman (1960) and Santhanan and Gupta (1968). Three cases (c=1m) are shown in Figure 5.12, each computed based on (5.31)-(5.33) derived above, corresponding to pyrite, dolomite, quartz and kerogen.

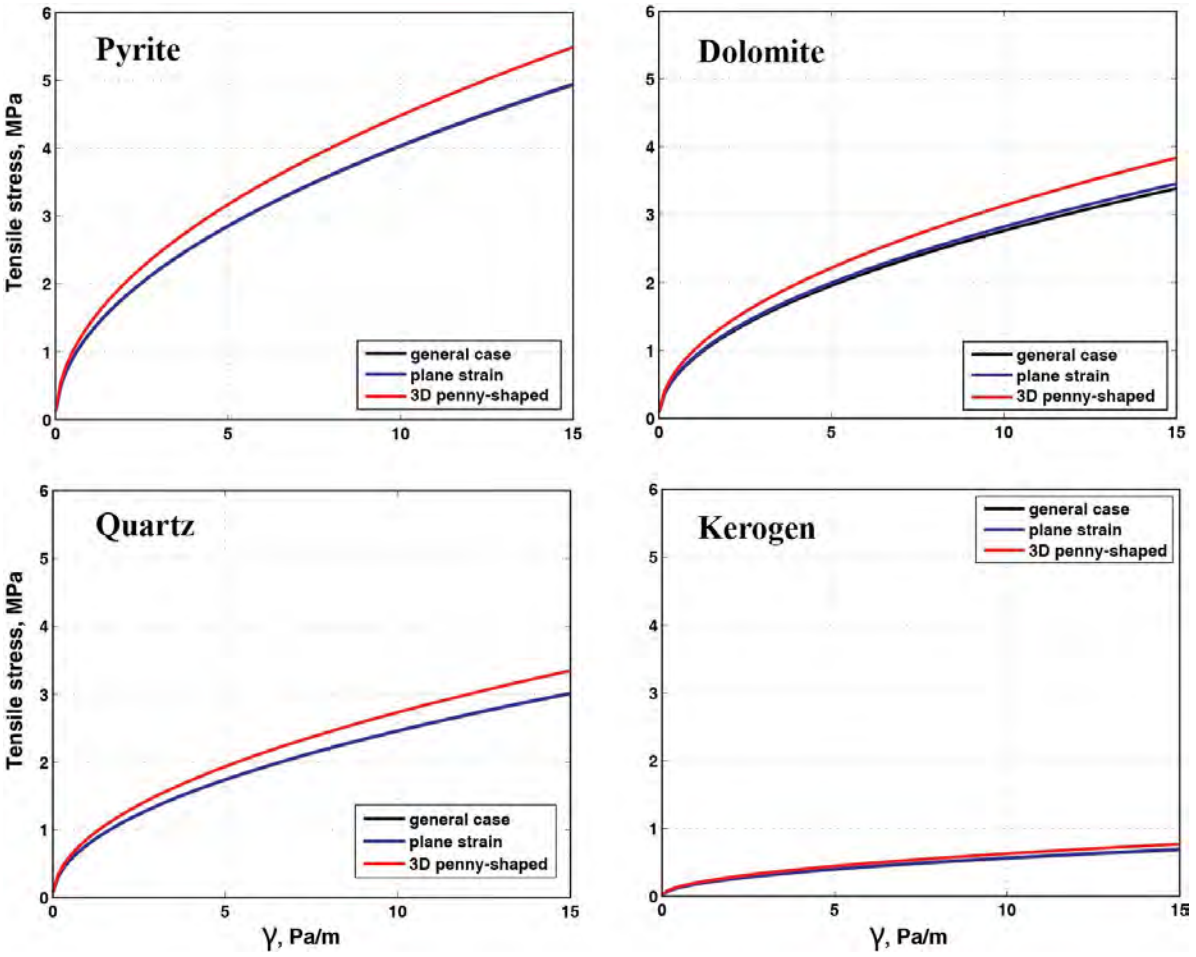

Figure 5.12: Computation of the tensile stress of a 2m long crack as a function of the surface energy per unit area, γ, for pyrite, dolomite, quartz and kerogen in three different scenarios: *general case* (Eq-n 5.31), *plane strain* (Eq-n 5.32) and *3-D penny-shaped* cracks (Eq-n 5.33). Note: *3-D penny-shaped* cracks require higher tensile stresses in all phases compared to other scenarios.

In this particular exercise, the absolute value of fracture length is set to 2m for the ease of computation and in order to emphasize the role of confining medium and relative difference of the tensile stress in three scenarios. The difference we note is twofold: first, there is an order of magnitude difference in tensile stress when all scenarios are compared between the *stiffest* (pyrite) and the *softest* (kerogen) phases. Secondly, in all phases, the quasi-statically increased load (referred to as *general case* in Figure 5.12) scenario is almost identical to the *plane strain* scenario, whereas the *3-D penny-shaped* cracks require higher tensile stresses in all phases.

5.5.3 Conditions for microhydraulic fracturing within organic layers

Vernik (1994) suggests that extensive, bedding-parallel microcracks exist *in-situ* in most mature source rocks undergoing the major stage of hydrocarbon generation and migration based on laboratory measurements of ultrasonic velocity and anisotropy in kerogen-rich black shales of varying maturity. Based on SEM observations of the size of illite platelets (Vernik and Nur, 1992), the maximum size of the long axis of these apparently penny-shaped, fabric-parallel microcracks is taken to be $2c$=6μm, where c is the major semi-axis of the original pore. Briefly recalling that the excess pore pressure needed to overcome the total normal stress for the microhydraulic fracture to initiate is a function of the size, geometry, and position of the flaw as well as the fracture toughness of the host material Vernik (1994) computes dependence of crack major semi-axis on closure stress using principles of the stress intensity at the tip of a planar Mode I fracture using solution similar to Eq-n 5.19 and plotted in Figure 5.13. Fracture toughness of kerogen in the Bakken shale investigated by Vernik (1994) is assumed to be equal to that of a sample of brown coal with similar vitrinite reflectance R_o=0.4-0.6% reported in Atkinson and Meredith (1987) for K_{ic}= 0.006-0.015 MPa. The excess pore pressure for the initial crack half-length of 3μm is found by Vernik (1994) to be in the range 4-8MPa (for the stress configuration and depth corresponding to the Bakken shale samples). Interestingly, in a laboratory experiment by Tissot and Pelet (1971), 10MPa excess pore pressure was recorded in shale under confining pressure until microfracturing caused pressure drop. Jizba (1991) estimates the excess pore pressure that can be generated during kerogen-hydrocarbon transformation reactions in pores with aspect ratio, α=0.01-0.05, and reports a similar range of values. Recalling that given the effective closure stress (ζ_{close}), the major semi-axis c of the crack, and elastic constants of the enclosing material, the typical microcrack aperture can be estimated (Zheltov, 1966; Nordgren, 1972) using Eq-n 5.18 and has been plotted in Figure 5.14. Here, the comparison of the effective crack closure stresses (for all phases under investigation) versus crack aspect ratio for illite and kerogen as confining media reported by Vernik (1994) is provided.

Vernik (1994) used isotropic values of $E_{kerogen}$=8GPa and $\nu_{kerogen}$=0.28 and anisotropic values of illite shale across bedding of E_{illite}=48GPa and $\nu_{kerogen}$=0.25.

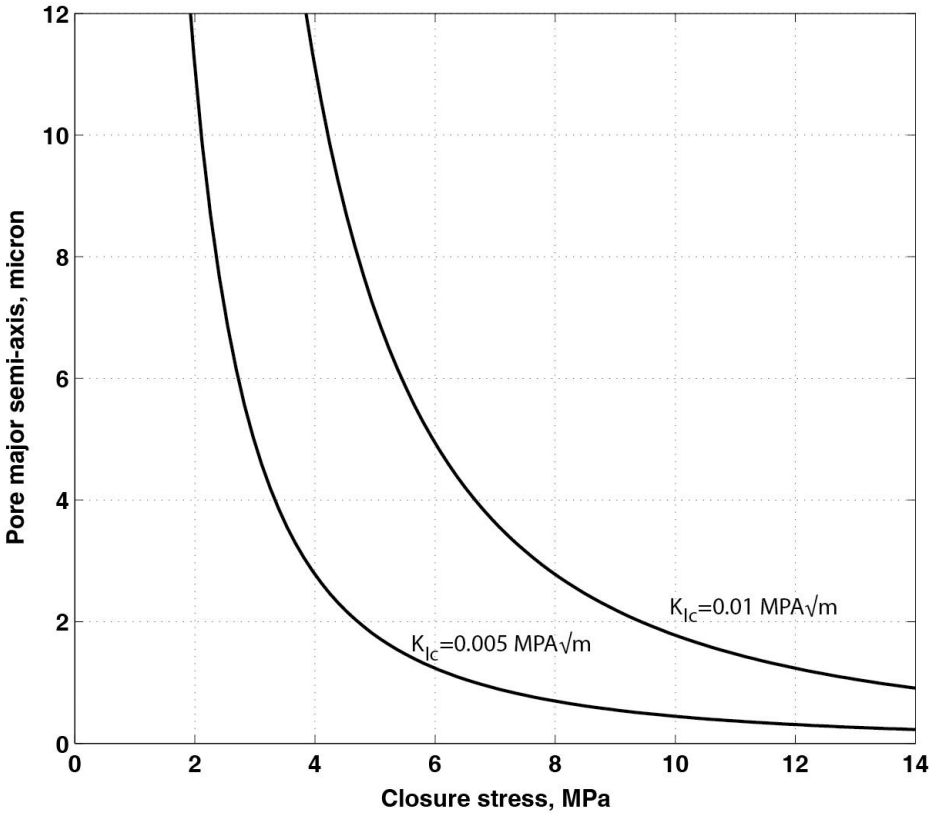

Figure 5.13: Excess pore pressure needed for microhydraulic fracture to occur in the mature black shale versus major semiaxis of the initial pore. From Vernik (1994).

The purpose of the computation depicted in Figure 5.14 is to show a relative difference in the maximum aperture of the crack as a function of bounding medium. The results are in good agreement with values previously reported by Vernik (1994). The microcrack aperture as shown in Figure 5.14 should be in the range 14 to 35 nm if it is enclosed in kerogen or confined to a kerogen-illite interface considered by Vernik (1994) and even larger using elastic properties of Bazhenov Formation sample (marked by green crosses in Figure 5.14). Had the confining media been illite, the aperture for the same range of closure stresses (ζ_{close}), would be unreasonably low (2 to 6 nm), i.e., on the order of the molecular size of some heavy hydrocarbons and even lower in the case of *stiffer* phases

as pyrite, dolomite and quartz. The analysis shown above corroborates the suggestion made by Vernik (1994) that the bedding-parallel microcracks originate and propagate within the weakest constituent of the rock matrix-kerogen assemblage or along interfaces with other mineral phases.

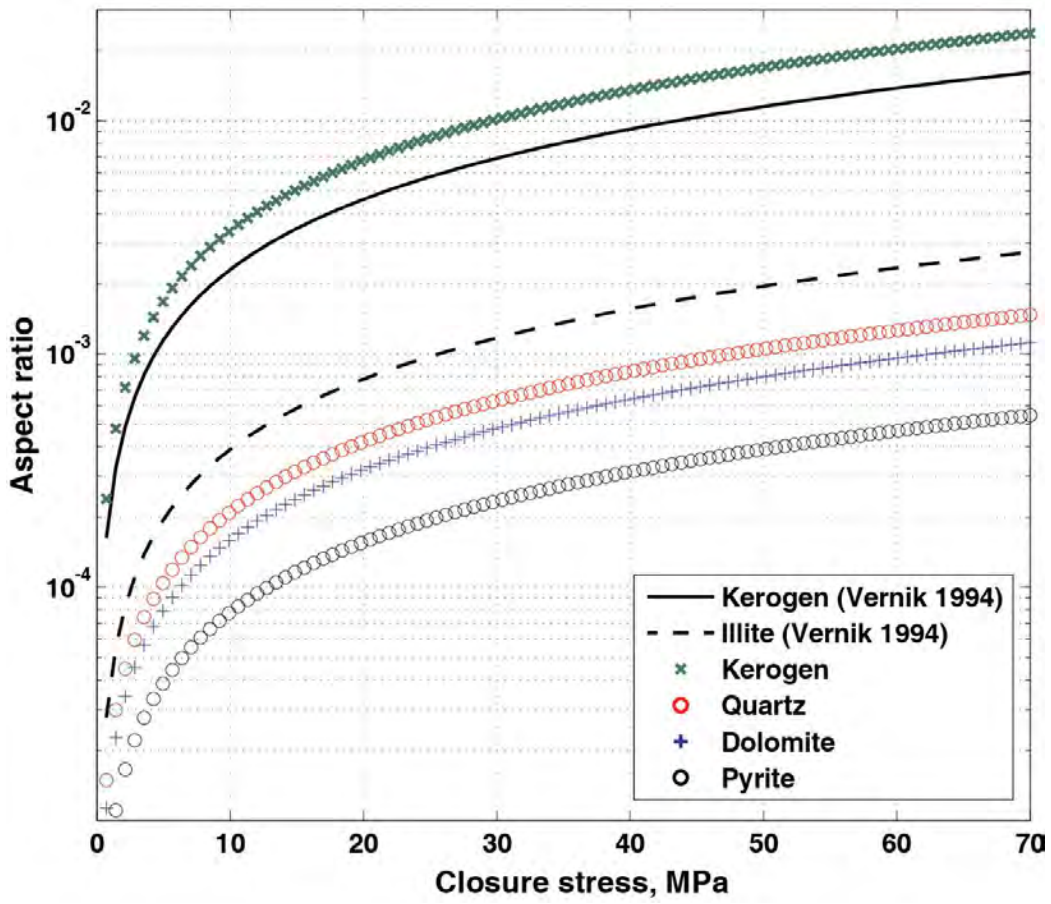

Figure 5.14: Comparison of the effective crack closure stresses (for all phases under investigation) versus crack aspect ratio for illite and kerogen as confining media reported by Vernik (1994).

5.6. *Geological significance of the variables which affect bending*

Pollard and Johnson (1973) analyzed deformation of host rocks during growth of a laccolithic intrusion using the theory of bending of a stack of thin elastic plates. Their theoretical model suggests that lateral spreading of magma is in the form of a sill that

eventually gains sufficient leverage on the overlying strata to deflect them upward and form a laccolith shown in Figure 5.15.

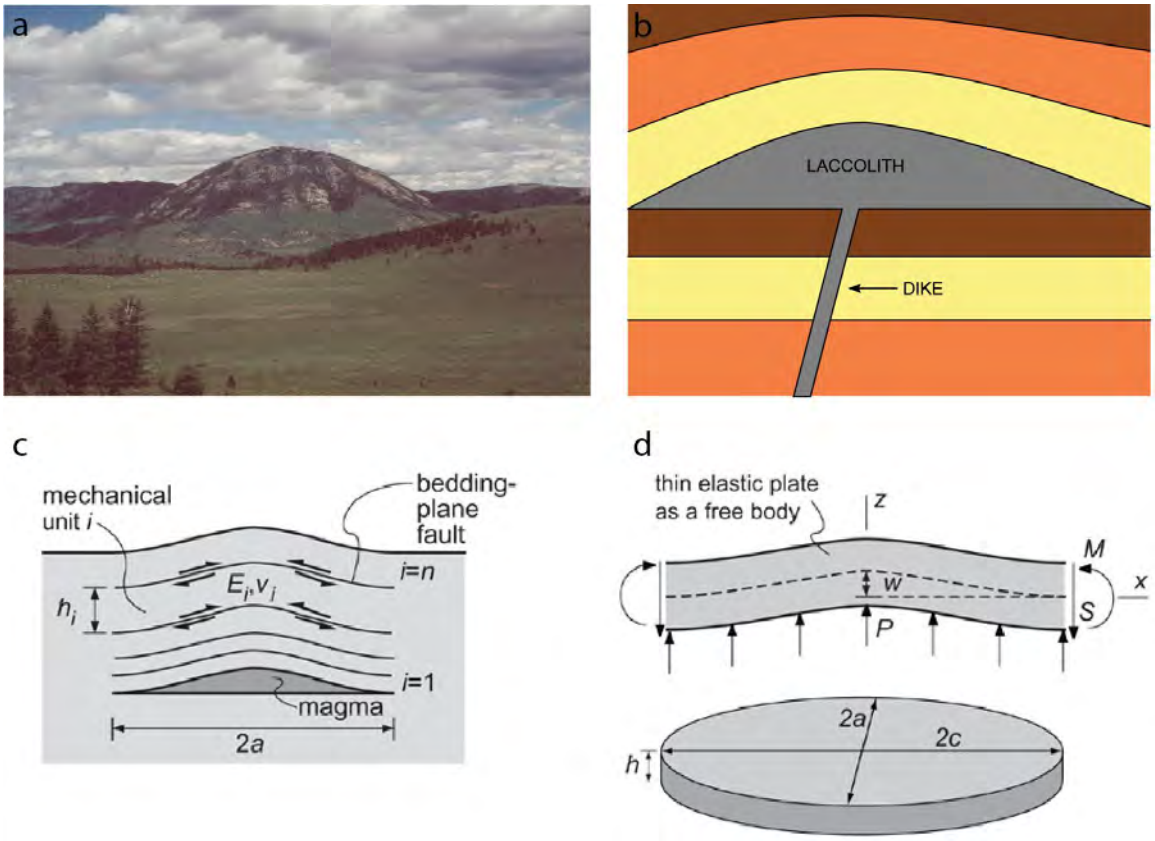

Figure 5.15: a) field-scale photograph of laccolith, b) conceptual model of laccolith growth under increasing magma volume. Idealized model for plate bending over laccolith c) cross section of multiple mechanic units with bedding-plane faults, d) oblique view of plate model for a mechanical unit. Models shown in (c) and (d) are from Pollard and Fletcher (2010).

They note that competence is a term often used in the field by geologists, generally to describe the resistance to deformation of a particular layer of rock and propose the term *flexural rigidity* in order to describe the resistance to deformation of layers over a laccolithic intrusion. Flexural rigidity, R, is defined as:

$$R = \frac{Eh^3}{12(1-\nu^2)} = \frac{Mh^3}{12} \tag{5.34}$$

where h is a thickness of a layer in overburden, E and v are Young's modulus and Poisson's ratio of the layer, respectively. Given that elastic properties are combined in the form of M, it is possible to use this value directly in order to compute flexural rigidity of the layer in overburden. However, it is important to note that nanoindentation derived values represent *phases* and not *rock types*, thus appropriate transforms should be used to convert phase properties into the properties of porous medium with saturating fluids.

5.7. Chapter Summary

We measured nanoindentation (related to the Young's modulus via Poisson's ratio) of four commonly occurring phases within source rocks – kerogen, quartz, dolomite and pyrite. Based on the measured properties of kerogen, quartz, dolomite and pyrite it is possible to derive P-wave, S-wave and Lamb-wave velocities by estimating Young's modulus and assuming appropriate Poisson's ratio. The computed velocity values are in excellent agreement with data previously published by Mavko et al (2009). The largest computed diffrence in velocity values is that of pyrite and does not exceed 10%.

The closure stresses of two- and three-dimensional cracks with wide range of aspect ratios are computed in all phases. The relative difference of stress values for a given aspect ratio within *softest* (kerogen) and *stiffest* (pyrite) phases is in excess of an order of magnitude. The analysis of tensile rock failure conducted herein provides a scheme for computation of stress intensity factors of analyzed fractures. Furthermore, we considered flow through a Mode I fracture based on a parallel plate approximation for fluid flow through a planar fracture and compute maximum aperture of a crack under given stress in all phases. The computed fracture aperture values are in good agreement with previously reported values of Zoback (2007). Alternatively, we derived a thermodynamic criterion of crack propagation due to an applied load according to Griffith (1920, 1924). This allows computation of the tensile stress of a crack as a function of the surface energy per unit area for pyrite, dolomite, quartz and kerogen in three different scenarios: *general case*, *plane strain* and *3-D penny-shaped* cracks. Our

findings suggest that in the case of 3-D penny-shaped cracks, higher tensile stresses are require in all phases compared to other scenarios.

Next, conditions for microhydraulic fracturing within organic layers according to Vernik (1994) were analyzed. Throughout these computation*s* we show a relative difference in the maximum aperture of the crack as a function of bounding medium. The results are in very good agreement with values previously reported by Vernik (1994) and corroborate the suggestion that the bedding-parallel microcracks originate and propagate within the weakest constituent of the rock matrix-kerogen assemblage or along interfaces with other mineral phases.

Finally, the deformation of overburden rocks during growth of a laccolithic intrusion using the theory of bending of a stack of thin elastic plates was analyzed in the framework provided by Pollard and Johnson (1973). Given that elastic properties are combined in the form of nanoindentation modulus, it is possible to use this value directly in order to compute flexural rigidity of the layer in overburden after converting from phase properties to bulk rock properties.

5.8. References

Ahmadov R., Aydin A., Karimi-Fard M. and Durlofsky L., 2007, Permeability upscaling of the fault zones in the Aztec Sandstone, Valley of Fire State Park, Nevada with a focus on the fault slip surfaces and slip bands, Hydrogeology Journal 15, pp. 1239–1250.

Atkinson, B. K., and Meredith, P. G., 1987, Experimental fracture mechanics data for rocks and minerals, *in* Atkinson, B. K., Ed., Fracture mechanics of rock: Academic Press, 477-522.

Brace W. F. and Walsh J. B., 1962, Some direct measurements of the surface energy of quartz and orthoclase, Am. Miner. 47, 1111-1122.

Brown, S. R. and Scholz, C. H., 1986, Closure of rock joints, J. Geophy. Res., 91, 4939–4948.

Constantinides, G., Chandran, K.S.R., Ulm, F.-J., Van Vliet, K.J., 2006, Grid indentation analysis of composite microstructure and mechanics: Principles and validation, Materials Science and Engineering, A 430, 189–202.

Cheng, Y.-T., Cheng, C.-M., 2004, Scaling, dimensional analysis and indentation measurements. Mater. Sci. Eng. R. 44, 91–149.

Friedman M., Handin J. and Alani G., 1972, Fracture-surface energy of rocks, Int. J. Rock Mech. Min. Sci. Vol. 9, pp. 757-766

Gassmann, F., 1951, Uber die Elastizitat poroser Medien. Vier. der Natur. Gesellschaft Zurich, 96, 1–23.

Gilman J. J., 1960, Direct measurement of surface energies of crystals, J. appl. Phys. 31, p. 2208-2218.

Griffith,A. A., 1920, The phenomena of flow and rupture in solids, Phil. Trans. Roy. Soc. Lond. Ser. A, 221,163–198.

Griffith,A. A., 1924, Theory of rupture,in Proc. 1st Int. Cong. Appl. Mech.,C . B. Biezano and J. M. Burgers,eds .,J .Waltman Jr,Delft,pp . 53–63.

ISO 14577, 2002, Metallic Materials – Instrumented Indentation Test for Hardness and Materials Parameters.

Jaeger, J.C., Cook, N. G. W., and Zimmerman, R. W., 2007, Fundamentals of rock mechanics, 4th edition, Blackwell Publishing, Oxford, p.475.

Jizba, D., 1991, Mechanical and acoustical properties of sandstones and shales, PhD. thesis, Stanford University.

Lockner, D. A., 1995, Rock Failure. Rock physics and phase relations. Washington, D.C., American Geophysical Union, 127–147.

Mavko, G. and Nur, A., 1978, The effect of nonelliptical cracks on the compressibility of rocks. J. Geophys. Res., 83, 4459–4468.

Mavko, G, Mukerji, T. and Dvorkin, J., 2009, The Rock Physics Handbook, Cambridge University Press, p.511.

Miklowitz, J., 1978, The Theory of Elastic Waves and Waveguides, North-Holland, Amsterdam.

Nelson R., Handin J., 1977, Experimental study of fracture permeability in porous rock. Am Assoc Petrol Geol Bull 61:227–236

Oliver W. C., and Pharr G. M., 2004, Measurement of hardness and elastic modulus by instrumented indentation: advances in understanding and refinements to methodology, Journal of Materials Research, Vol. 19, No. 1, pp. 3-20

Pollard, D.D., and Fletcher, R.C., 2010, Fundamentals of Structural Geology, Cambridge University Press, Cambridge, p.500.

Pollard D.D. and Johnson A.M., 1973, Mechanics of growth of some laccolithic intrusions in the Henry Mountains, Utah II. Bending and failure of overburden layers and sill formation, Tectonophysics, 18, pp. 311–354.

Rummel, F. and Winter, R. B., 1983, Fracture mechanics as applied to hydraulic fracturing stress measurements, Earthq. Predict. Res., 2, 33–45.

Santhanan T. and Gupta Y. P., 1968, Cleavage surface energy of calcite, Int. J. Rock Mech. Min. Sci. 5, 253-259.

Schmitt, D. R. and Zoback, M. D., 1992, "Diminished pore pressure in low-porosity crystalline rock under tensional failure: Apparent strengthening by dilatancy." J. Geophys. Res., 97, 273–288.

Senseny, P. E. and Pfeifle, T. W., 1984, Fracture toughness of sandstones and shales. Proc. 25th U.S. Symp. Rock Mech., Northwestern University, 1, pp. 390–397.

Simmons, G. and Birch, F., 1963, Elastic constants of pyrite, J. Appl. Phys., 34, 2736–2738.

Tissot, B. P., and Pelet, R., 1971, Nouvelles donees sur les mecanismes de denese et de migration du petrole, simulation mathematique et application a la prospection, Proceedings, 8th World Petroleum Congress, 2, 35-46.

Vernik L., 1994, Hydrocarbon-generation-induced microcracking of source rocks, Geophysics, v. 59, n. 4, p. 555-563.

Vemik, L., and Nur, A., 1992, Ultrasonic velocity and anisotropy of hydrocarbon source-rocks: Geophysics, 57, 727-735.

Viktorov,I. A., 1967, Rayleigh and Lamb Waves: Physical Theory and Applications, Plenum Press, New York.

Zoback, M. D., 2007, Reservoir Geomechanics, Cambridge University Press, The Edinburgh Building, Cambridge CB2 8RU, UK, Published in the United States of America by Cambridge University Press, New York, 464 pp.

Appendix A

Transport Properties of Shales

"Analyze data just so far as to obtain simplicity and no further."

--Henri Poincare

Abstract

We compile published permeability data in shale and contrast these data to classical datasets, including Fontainebleau sandstone, North Sea, and tight gas sandstone laboratory measurements. As expected, shale permeability is much smaller than that in sands and sandstones. Moreover, the fluid transport mechanisms in shale are likely to be different from those in conventional reservoir rocks. The main reason is the very small size of pores in shale, so small that it is often commeasurable with the size of a gas molecule. The main goal of this compilation is to serve as a reference guide for assessing

permeability in new plays as well as a quality-control tool for new physical and computational data.

Introduction

A high-resolution image of shale (Figure A.1) reveals intricate pore geometries quite different from those observed in silica-bearing rocks and even carbonates. Because of the small size of these pores as well as the often disconnected pore networks, the absolute permeability in shale is usually much smaller than in conventional rock.

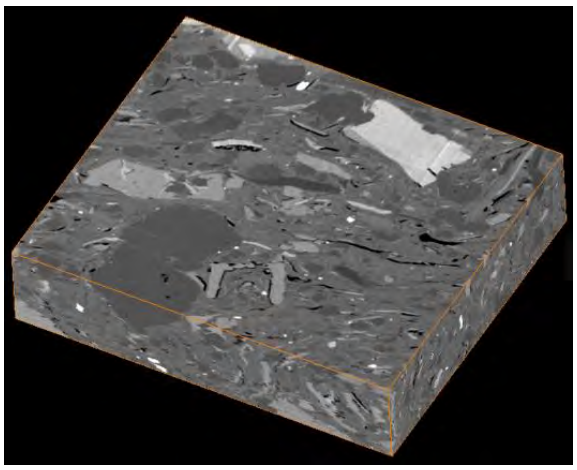

Figure A.1. Pore-scale 3D image of shale (courtesy Ingrain, Inc.). The size of this sample is about 0.01 mm.

There are usually two types of conduits in producing shale: (a) natural and/or human-created fractures through which hydrocarbon flows to the well and (b) the pore space inside the shale matrix. The separation of functions between these two types of conduits is quite distinct. The fractures are usually highly effective flow paths but, by themselves, have almost no storage capacity. On the other hand, the intact (unfractured) shale matrix is where the hydrocarbons reside, but the transport of the hydrocarbons within the matrix and from the matrix to the fractures is highly restricted.

This is why the flow properties as well as porosity of the shale matrix are important in assessing the storage and production potential of a field. This is why here

we concentrate on several results quantifying this matrix permeability (k_m) and its relation to porosity, stress, water saturation and organic component of the rock.

To emphasize the importance of the shale matrix permeability, we quote results from Luffel et al. (1993), who used 3D computer modeling of reservoir performance (Figure A.2) around a typical Devonian shale-gas well from Pike County in Kentucky. These calculations indicate that for matrix permeability $k_m > 10^{-6}$ mD, recovery is independent of k_m. It can be argued that in this case, the productivity is controlled only by the fracture network properties. For $k_m < 10^{-9}$ mD, the recovery is too low to be commercial. In the intermediate range of k_m, between 10^{-9} and 10^{-6} mD, the matrix permeability becomes an important factor affecting recovery.

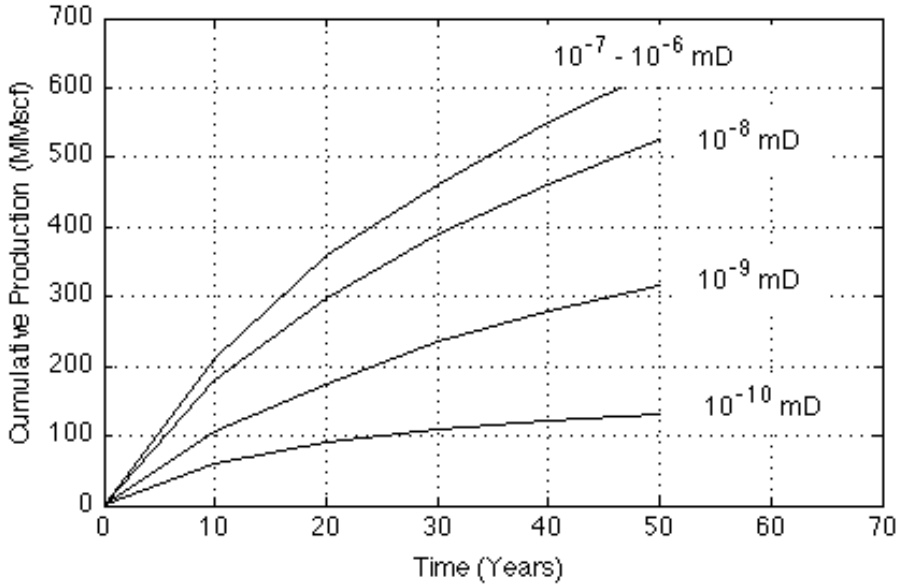

Figure A.2. Numerical simulation of the effect of matrix permeability on cumulative production in a Devonian shale well (from Luffel et al., 1993).

One additional factor that affects the transport of hydrocarbons in the shale matrix is the presence of formation water. The more water is present the smaller the permeability to gas. Some examples given in this compilation focus on this effect.

Benchmark data

Comparison is an effective quantification tool. This is why we feel that in order to better assess shale permeability data we need to compare them to existing permeability data of high-porosityl sands, medium-to-high porosity sandstones, and low-porosity tight

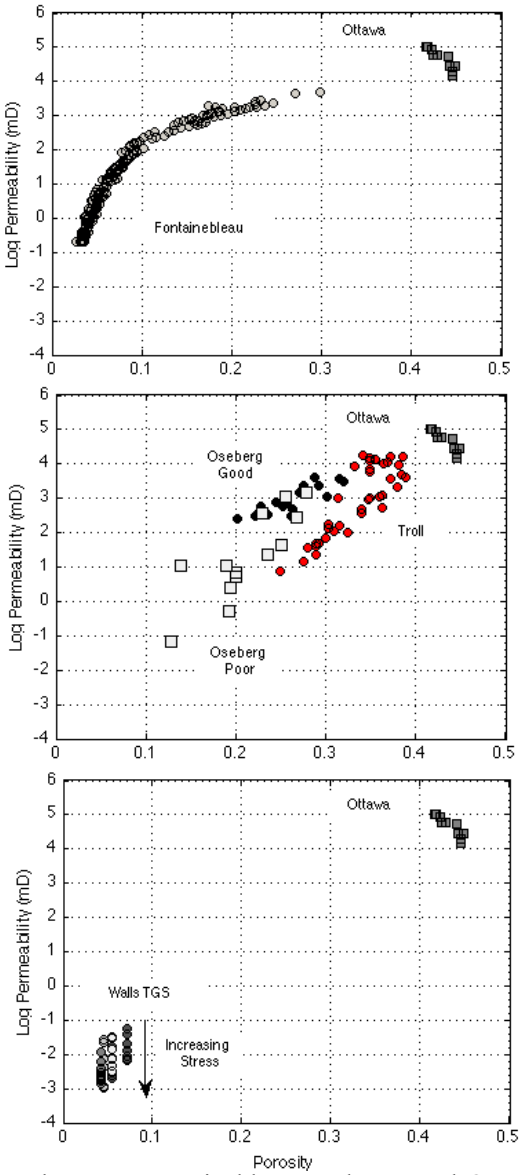

Figure A.3. From top to bottom: Fontainebleau sandstone and Ottawa sand; the Troll and Oseberg data and Ottawa sand; and TGS data and Ottawa sand. The TGS permeability is plotted for varying confining stress whose increase is marked by an arrow. In this dataset, the porosity variation with stress was not recorded and the permeability values are plotted versus the constant porosity measured at room conditions.

gas sandstones (TGS). These benchmark data include the Fontainebleau sandstone data (Bourbie and Zinszner, 1985); sorted Ottawa sands (Estes, 1996); North Sea reservoir sands from the Troll (Blangy, 1992) and Oseberg (Strandeness, 1993) fields; TGS data with permeability measured as a function of confining stress; and Ottawa sand and kaolinite mixtures (Yin, 1992). The Fontainebleau, Ottawa, Troll and Oseberg, and TGS data are displayed in Figure A.3 The summary plot of these data is presented in Figure A.4 with the sand/clay mixture data added. The latter dataset was obtained at room conditions (zero confining stress). The zero-stress porosity of Ottawa sand used is about 0.4, while that of pure kaolinite exceeds 0.6. As the sand is mixed with clay, the porosity of the mixture gradually increases from that of the sand to that of pure kaolinite.

At the same time, the permeability quickly decreases from about 1000 mD in sand to 1 mD in kaolinite. The addition of just small amounts of clay clogs the pores, resulting in rapid permeability reduction. After the clay content reaches 30% by weight, the permeability remains practically the same while the porosity decreases from about 0.4 to 0.6.

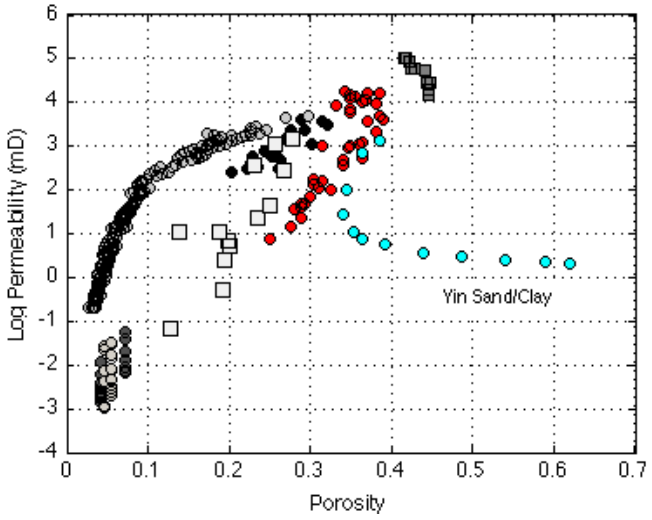

Figure A.4. Summary of the data from Figure A.2 with the sand/kaolinite mixture data added.

This rapid permeability reduction is directly related to the drastic difference in the grain size between sand and clay: in the sand, it is on the order of 0.2 mm, in kaolinite it is usually two orders of magnitude smaller (0.002 mm).

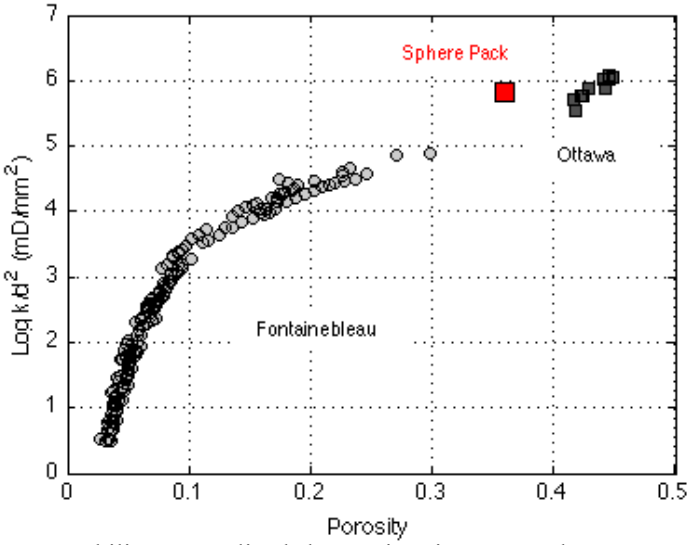

Figure A.5. Permeability normalized by grain size squared versus porosity for Fontainebleau sandstone and sorted Ottawa sand. The red square is placed at porosity 0.36 and normalized permeability 680000 mD/mm^2.

This effect of the grain size on permeability can be readily assessed from the Kozeny-Carman equation:

$$k = 1.38 \cdot 10^7 d^2 \frac{(\phi - \phi_p)^3}{[1-(\phi-\phi_p)]^2 \tau^2}, \tag{A.1}$$

where permeability k is in mD; grain size d is in mm; porosity ϕ is in fraction; and τ is the tortuosity (approximately 2.5). Example of the permeability variation (normalized by the grain size squared) as a function of porosity is depicted in Figure A.5. The red square in Figure A.5 represents 680000 mD/mm^2 experimentally obtained and confirmed on a number of dense random packs of identical near-spherical particles. The porosity of such a pack is close to 0.36.

In the following paragraphs we will provide brief descrition of shale and TGS permeability-porosity datasets and compare them to benchmark data. The complete list of datasets is provided in Table A.1.

Table A.1. List of datasets: their sources, measured lithologies and number of measurements.

Source	Lithology	Measurements
Bourbie and Zinszner, 1985	Sandstone	>50
Estes, 1996	Sandstone	>20
Blangy, 1992	Sands	>10
Strandeness, 1993	Sands	>10
Yin, 1992	TGS, Sand-kaolinite mixture	>10
Nelson, 2009	TGS, sandstones, shales	>10
Soeder, 1998	Shales	8
Sarker et al., 2009	Shales	2
Luffel et al., 1993	Shales	>10
Katsube, 2000	Shales	8
Katsube et al., 2000	Shales	10
Schloomer and Krooss, 1997	Shales, siltstones	25
Byrnes et al., 2009	TGS	>2100
Jizba, 1991	Shales, TGS, sandstones	11
Lewis, unknown	Shales	18
Pathi, 2008	Shales	>20
Yang and Aplin, 2007	Shales	34

Nelson (2009) Dataset

Nelson compiles porosity, permeability, and pore-throat size data for medium- and fine-grained sandstone as well as for tight gas sandstone and shale (Pennsylvanian, Pliocene, Devonian, Jurassic, and Cretaceous) and various source rocks. This summary uses many data sources and reports average porosity and permeability values as well as the minimum, maximum, and average pore-throat sizes. These pore-throat sizes were measured by mercury injection, gas flow, and combined mercury injection and small-angle neutron scattering. The permeability is plotted versus porosity in Figures A.6 to

A.9, where these data are compared to the aforementioned benchmark data. It is clear that the permeability of the shale matrix can easily reach values as small as a few nanoDarcy (10^{-9} D). Figure A.8 displays the Nelson (2009) permeability-porosity data color-coded by the pore-throat size. It seems that the maximum pore-throat size affects the permeability in a more consistent way than the minimum or mean pore sizes.

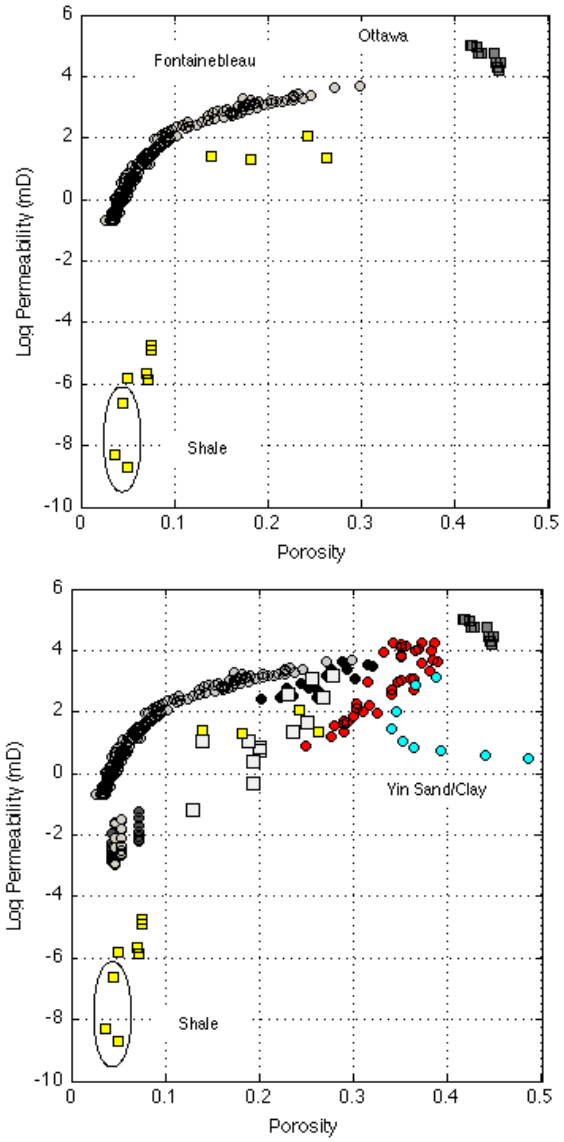

Figure A.6. (left) Permeability versus porosity from Nelson (2009) added to the Fontainebleau and Ottawa data, (right) same data with all benchmark data displayed.

Figure A.9 displays the same dataset where the permeability is plotted versus the pore-throat size and color-coded by porosity. The display on the left, where the permeability is plotted versus the maximum pore-throat size, is, arguably, the most consistent of the three displays in Figure A.9.

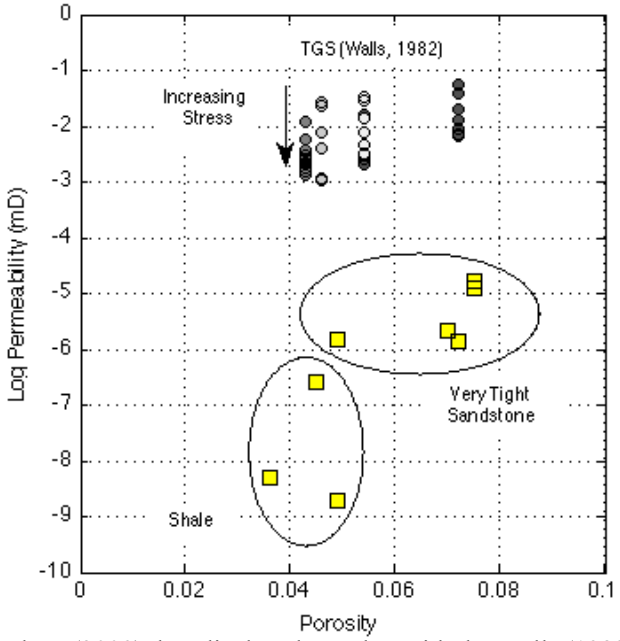

Figure A.7. The Nelson (2009) data displayed together with the Walls (1982) TGS data.

However, it is difficult to make any quantitative conclusions based on these data due to (a) scarcity of the data and (b) vagueness of the meaning of the pore-throat size for the transport and storage properties of shale.

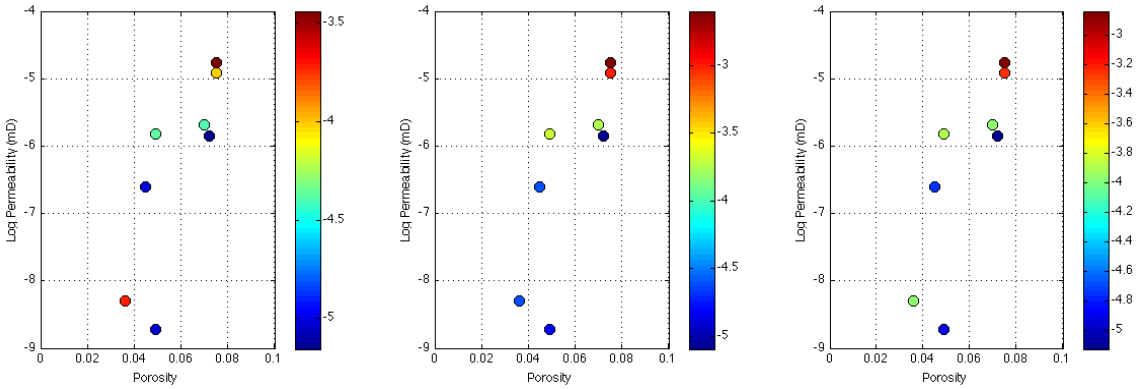

Figure A.8. The Nelson (2009) data. Permeability versus porosity color-coded by the decimal logarithm of the minimum, maximum, and mean pore-throat size (left to right). The throat size is in mm.

Nelson (2009) also quotes Bowers and Katsube (2002) regarding the effect of the confining stress on the total (or storage) porosity and connected porosity, which should strongly affect the permeability. Whereas the increase of the stress by about 50 MPa does not strongly affect the storage porosity, it acts to reduce the connected porosity by a factor 3 to 10. If we assume that the permeability is roughly proportional to the connected porosity cubed, the corresponding permeability reduction has a factor from 30 to 1000.

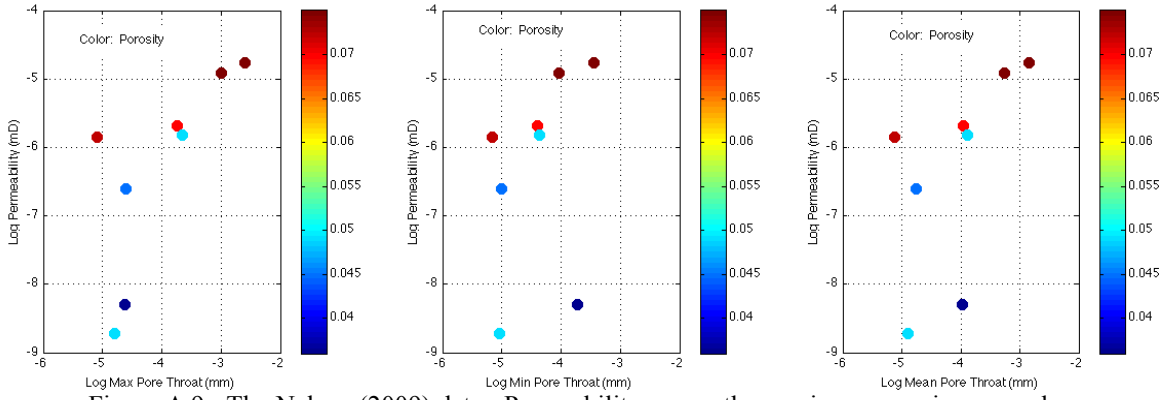

Figure A.9. The Nelson (2009) data. Permeability versus the maximum, maximum, and mean pore-throat size (left to right), color-coded by porosity.

Eastern Devonian Gas shale

Soeder (1988) reports gas porosity and gas permeability versus confining stress in Huron (Ohio) and Marcellus (Morgantown, WV) shale samples. The porosity in most Huron shale samples was so small (< 0.001) that it could not be properly registered. The reason is the presence of petroleum as a mobile liquid phase in the pores of all seven Huron shale samples. It effectively limits the porosity available to gas in this formation to less than 0.002. Accordingly, the gas permeability of the rock matrix is commonly less than 0.0001 mD at reservoir stress. The Marcellus shale sample was free of a mobile liquid phase and had porosity available to gas about 0.1 and relatively high permeability of 0.02 mD. The permeability-stress and permeability-porosity crossplots for the Huron and Marcellus samples are shown in Figure A.10. In spite of the extremely small gas-

occupied porosity and its narrow range, the permeability in Huron shale samples spans almost 7 orders of magnitude. Its reduction with increasing stress is about half an order of magnitude in the higher-permeability samples and an order of magnitude in the smaller-permeability samples. It remains unclear how gas could flow at all through essentially nil pore space.

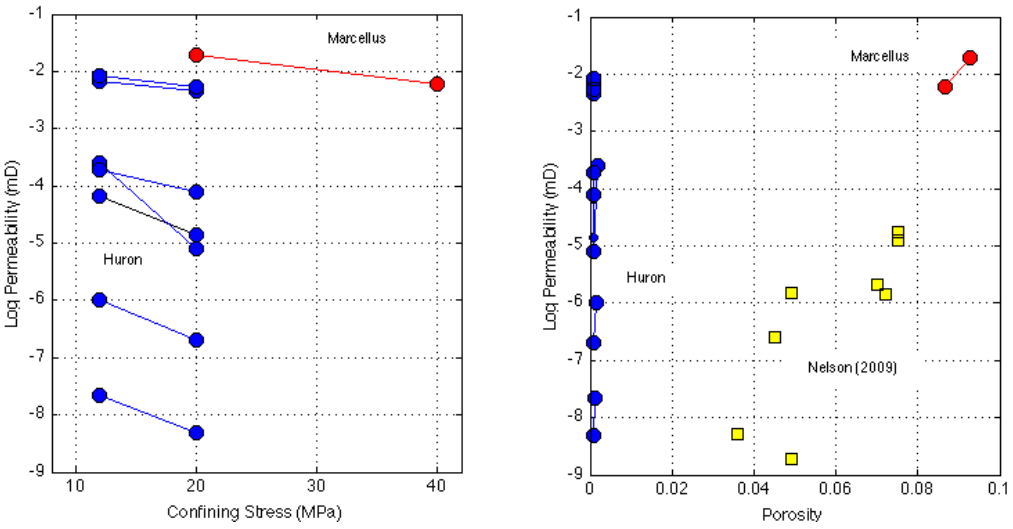

Figure A.10. The Huron and Marcellus shale data according to Soeder (1988). Left: Permeability versus confining stress. Right: Permeability versus porosity with the Nelson (2009) data added (yellow squares). The Huron and Marcellus shale data are plotted for two pressure stations. These points are connected by a line for each sample. Where the porosity was not registered, it was assumed 0.001.

Sarker, Batzle and Lu dataset

Sarker et al. (2009) report constant-rate fluid injection permeability data versus differential pressure on two shale samples. One sample is from the North Sea. Its porosity is not reported by these authors. The other sample is called the Mancos "B" shale with porosity 0.0775 and grain density 2.55 g/cc. This sample is reportedly organic-rich. This may explain the fairly small grain density. The permeability of the North Sea shale was measured at five confining pressure stations, starting at 10 and ending at about 30 MPa. Surprisingly, the permeability shows almost no pressure dependence (Figure A.11). The permeability in the Mancos "B" sample was measured in

the horizontal and vertical directions at three confining pressure stations: 14, 21, and 28 MPa. The vertical permeability is predictably smaller than the horizontal permeability. It is also almost independent of pressure (Figure A.11).

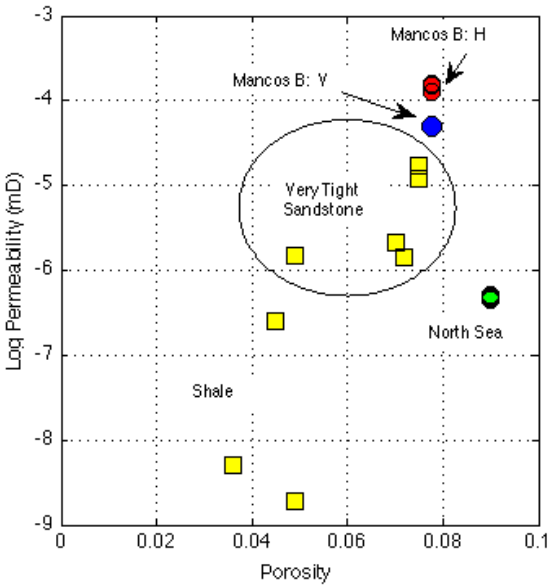

Figure A.11. The Sarker et al. (2009) data (colored circles) compared to the Nelson (2009) compilation (yellow squares). The North Sea shale permeability values (green circles) are ad-hoc placed at porosity 0.09 and plotted for all five pressure stations. The Mancos "B" permeability values are red circles for the horizontal direction and blue circles for the vertical direction.

Luffel, Hopkins, and Schettler Dataset

Luffel et al. (1993) analyze permeability in Devonian crushed shale core chips and cuttings at native water saturations (Figure A.12) using a pulse pressure procedure. The reported porosity is the gas-filled porosity. In this method, shale core samples at in-situ water saturations are crushed, and a narrow sieve cut is used in pulse pressure tests with helium to derive K_m. Advantages of this method are that it is quick to run, inexpensive, and can be used on drill cuttings, and since the shale is likely to part along microfractures and bedding planes during crushing, individual chips are unlikely to contain microfractures. A disadvantage is that the test is run at no overburden stress. Note that there are several other shale properties that utilize crushed samples or cuttings in

their analyses, such as porosity, fluid content, geochemical properties, mineralogy, and adsorption isotherms. However, as will be shown later, shale permeability values obtained by method of Luffel et al. (1993) are 2-2.5 orders of magnitude lower than most of the shale permeability values reported by other authors.

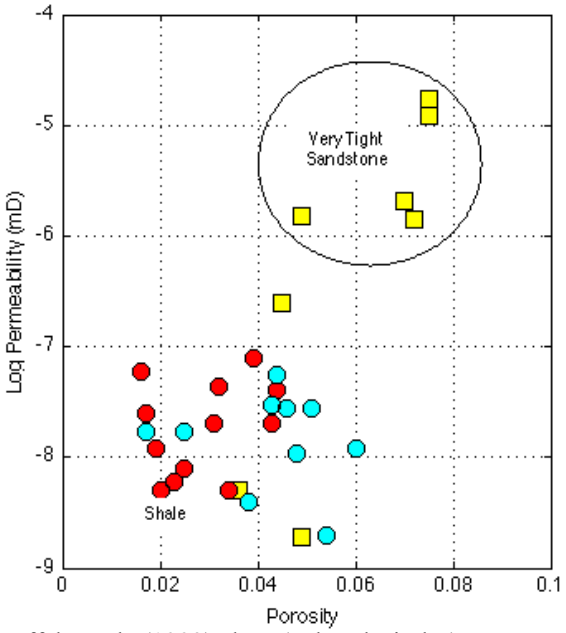

Figure A.12. The Luffel et al. (1993) data (colored circles) compared to the Nelson (2009) compilation (yellow squares). The same-color symbols come from different fragments of the same sample.

Katsube's Shale Dataset

Katsube (2000) is arguably one of handful of authors who present their own scientifically consistent measurements as well as compilations of other author's measurements for porosity and permeability in shale. In addition, the electrical formation factor data are available on the same samples. The main intent of Katsube's work is to quantify overpressure in shale. Nevertheless, his data remain relevant to shale that acts not as a seal but as a producing reservoir.

Figure A.13 displays permeability-porosity and formation factor-porosity data for four shale samples from offshore Nova Scotia. The confining pressure increases from almost zero to over 50 MPa and acts to reduce porosity, permeability and the formation

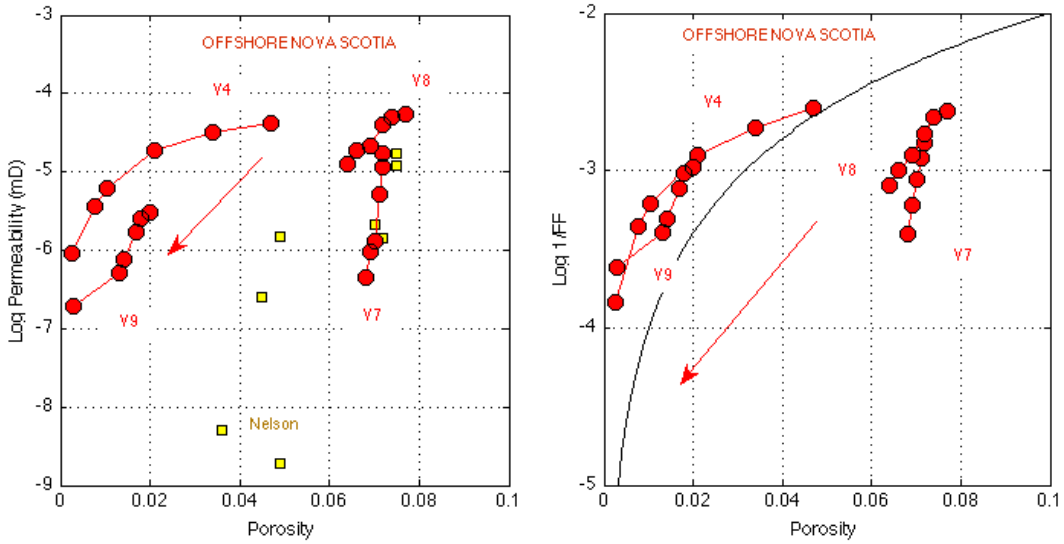

Figure A.13. The Katsube (2000) permeability-porosity (left) and inverse formation factor-porosity data for four Nova Scotia shale samples (red circles connected by lines). The arrows show the direction of applied confining stress, which acts to simultaneously reduce porosity, permeability, and the formation factor. The Nelson (2009) permeability data are shown in the left as yellow squares. The black curve on the right is porosity squared.

factor (F). In the formation factor frame, we plot the inverse formation factor and compare these data to a commonly used equation, $F = \phi^{-2}$ or $F^{-1} = \phi^{2}$.Figure A.14 displays permeability-stress and inverse formation factor-stress plots for the same four samples.

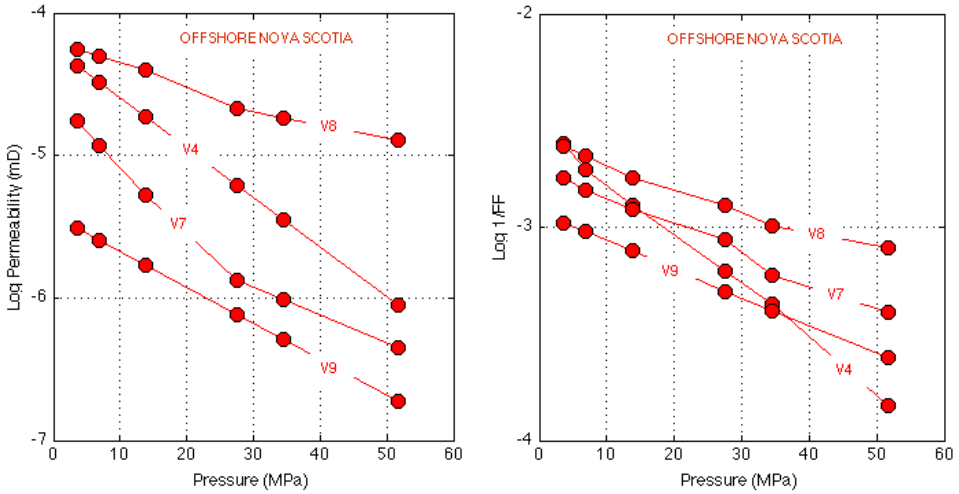

Figure A.14. The stress dependence of the data plotted in Figure A.13.

Finally, in Figure A.15 we cross-plot the permeability and inverse formation factor for these four samples.

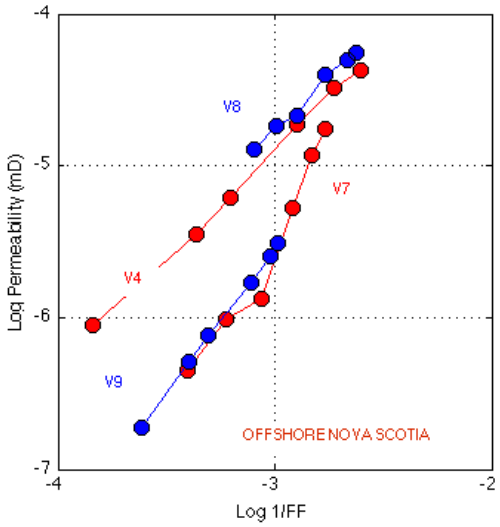

Figure A.15. Permeability versus inverse formation factor for the four samples used in Figure A.13. The direction of the increase in confining stress is from top-right to bottom-left. Different colors are used for better visual separation between the samples.

It is interesting to compare this cross-plot with the same cross-plot for the Yale (1984) sandstone and tight gas sandstone data (Figure A.16).

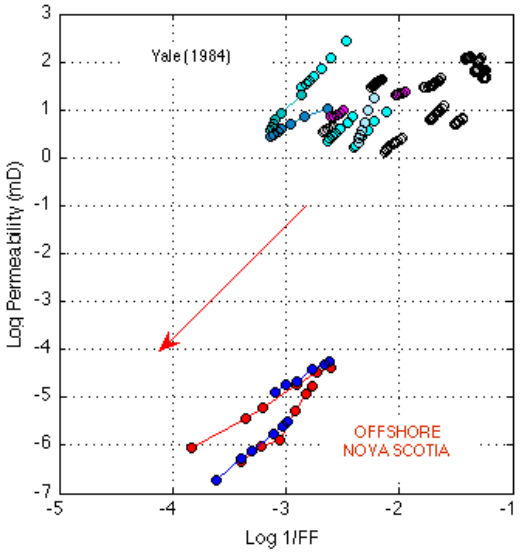

Figure A.16. Same as Figure A 15 but with the Yale (1984) data added (gray and colored symbols). The arrow shows the direction of increase in confining stress.

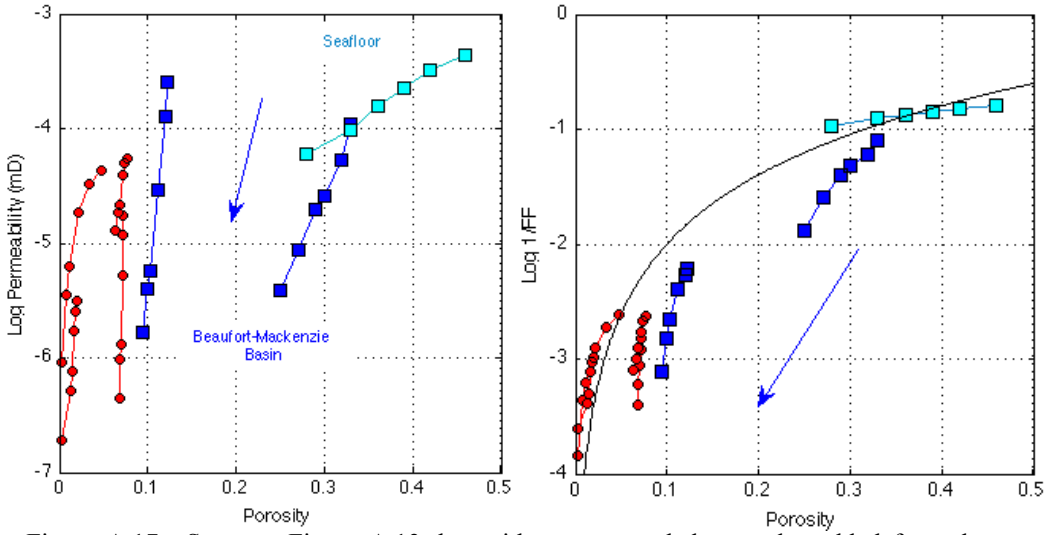

Figure A.17. Same as Figure A.13, but with two more shale samples added from the Beaufort-Mackenzie Basin in Canada (blue) and a seafloor mud sample from offshore Nova Scotia (cyan). These data are shown as squares. The arrow points in the direction of increasing confining stress. The black curve on the right is porosity squared.

Although the formation factor ranges in this shale and in TGS overlap, the respective permeability ranges do not, simply because unlike the formation factor, the permeability strongly depends of the length scale in rock (the grain size), which is much smaller in shale than in TGS.

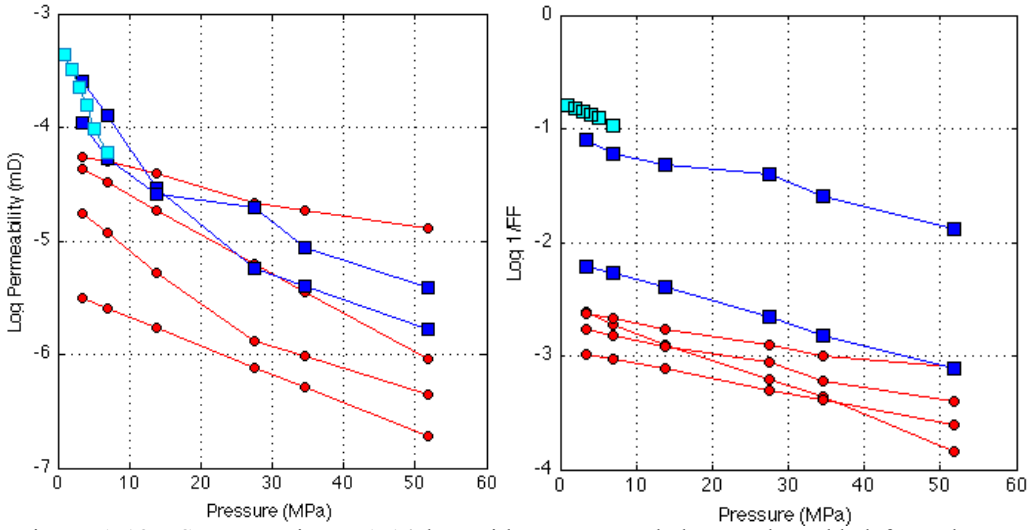

Figure A.18. Same as Figure A.14 but with two more shale samples added from the Beaufort-Mackenzie Basin in Canada (blue) and a seafloor mud sample from offshore Nova Scotia (cyan). These data are shown as squares.

Notice that although the porosity of the two of these shale samples is large, the permeability is still below 0.001 mD, and its range overlaps the range of the permeability of the first four samples (from offshore Nova Scotia). At the same time, the inverse electrical formation factor that is affected more by porosity rather than by the grain size is much larger in high-porosity shale than in the low-to-medium porosity samples. The other three shale samples measured by Katsube (2000) are two medium-to-large porosity samples from the Beaufort-Mackenzie Basin in Canada and a seafloor mud sample from offshore Nova Scotia (Figures A.17 to A.19).

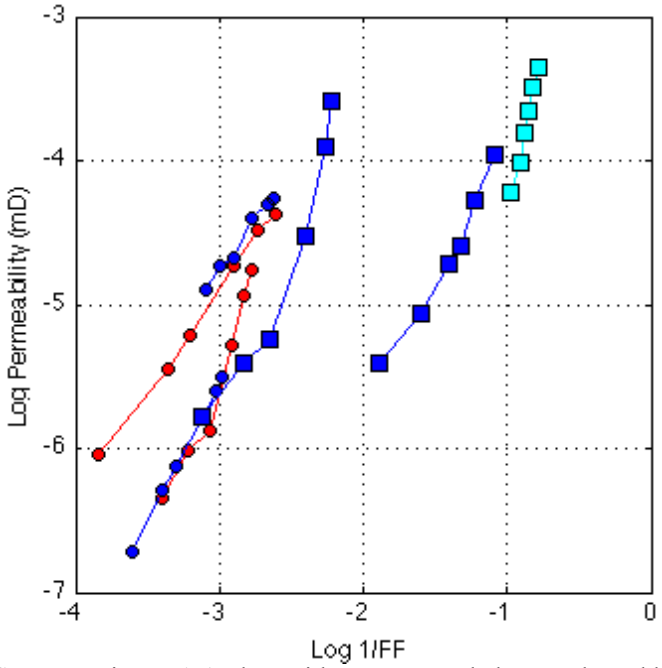

Figure A.19. Same as Figure A.15 but with two more shale samples added from the Beaufort-Mackenzie Basin in Canada (blue) and a seafloor mud sample from offshore Nova Scotia (cyan). These data are shown as squares.

Katsube et al. (2000) Shale Dataset

Katsube et al. (2000) obtained ten shale samples from several Cretaceous stratigraphic units (Colorado Group) of the Western Canada Sedimentary Basin (WCSB) for determination of the effective porosity and apparent formation factor as a function of confining pressure. For nine out of ten shale samples permeability measurements were performed (Figure A.20).

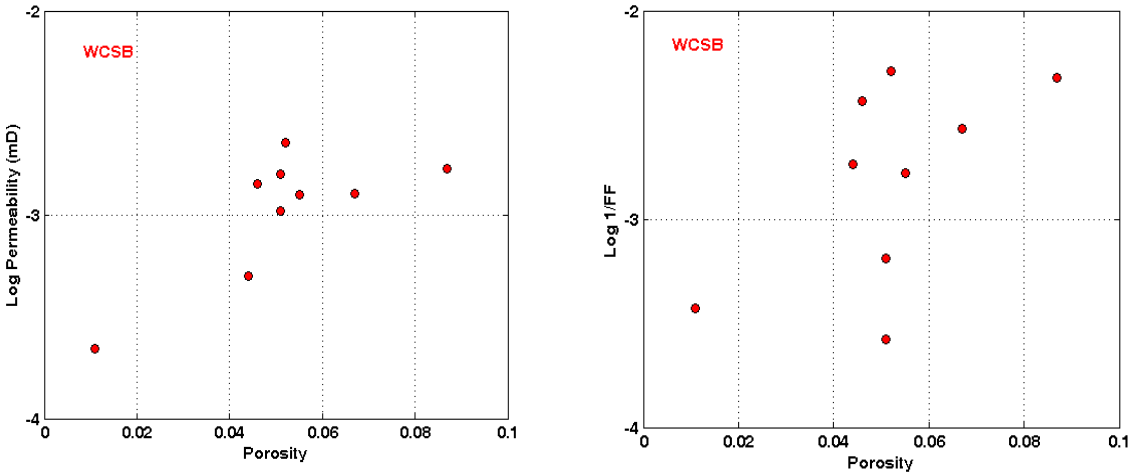

Figure A.20. The Western Canada Sedimentary Basin shale data according to Katsube et al. (2000). Left: Permeability versus porosity for the nine samples. Right: Permeability versus inverse formation factor for the same samples.

The porosity–confining stress and formation factor–confining stress (Figure A.21) data display values and trends that are typical for normal shale, with porosity decreasing and formation factor increasing with increased confining stress, with the exception of the sample cored from siderite concretion (shown by green color in Figure A.21).

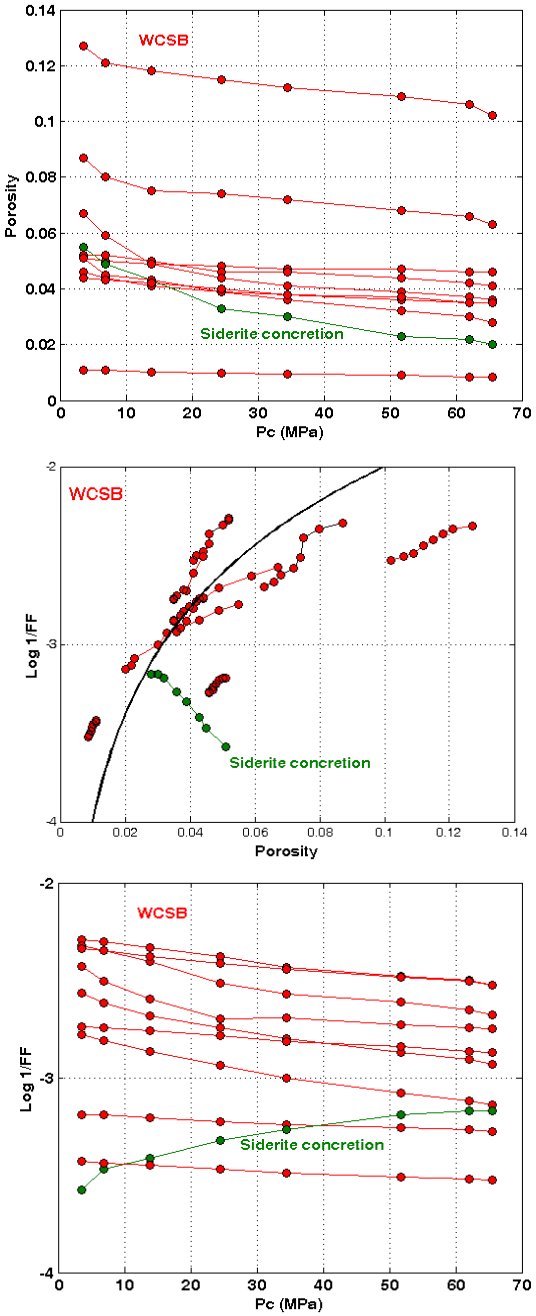

Figure A.21. The Western Canada Sedimentary Basin shale data according to Katsube et al. (2000). Left: Inverse formation factor as a function of confining stress for samples shown in Figure A.20. Middle: Porosity change as a function of increasing confining stress for the same samples. Right: Inverse formation factor versus porosity. The black curve on the right is porosity squared. NOTE: sample cored from siderite concretion (in green) shows drastically different behavior compared to other samples.

Schloomer and Krooss's Shale Dataset

Schloomer and Krooss (1997) analyze low-porosity (<4%) Jurassic shales and mudrocks, as well as fanglomerates (conglomerates derived from fans) and siltstone from the Haltenbanken area offshore Norway and red claystones from Carboniferous and Permian intervals of Northern Germany to study the hydrocarbon sealing efficiency of clastic sediments. Permeability measurements were performed at 15-20 MPa confining pressure (Figure A.22).

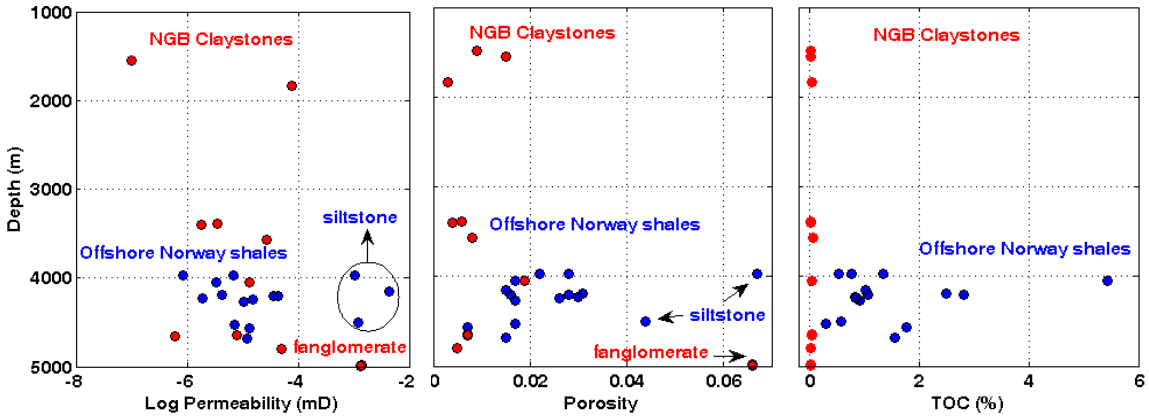

Figure A.22. Offshore Norway (in blue) and Northern Germany (in red) shale, mudrock and siltstone data according to Schloomer and Krooss (1997). Left: Permeability as a function of depth. Middle: Porosity as a function of depth. Right: TOC as a function of depth. The North Germany samples contain trace amounts of organic matter.

The permeability measurements were performed in steady-state mode. Shale samples from both offshore Norway and from Northern Germany show permeability values less than 0.1μD. Siltstone samples from Norway and fanglomerate sample from Germany have at least an order of magnitude higher permeability (except one siltstone sample) and higher porosity (for some samples) compared to shales and mudrocks (Figure A.23).

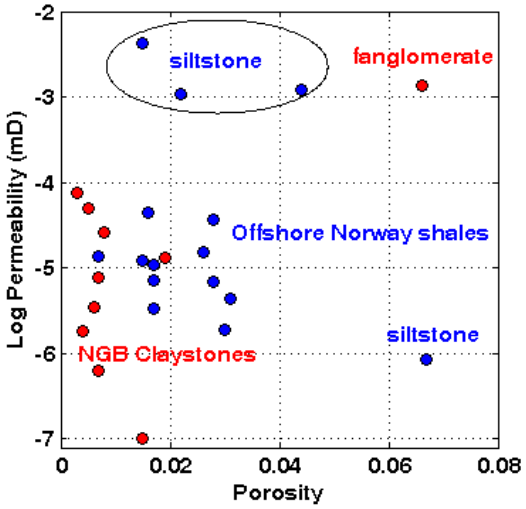

Figure A.23. Offshore Norway (in blue) and Northern Germany (in red) shale, mudrock and siltstone data according to Schloomer and Krooss (1997). Porosity versus permeability for all samples shown in Figure 6.22. NOTE: some siltstone and fanglomerate samples have higher porosities and permeabilities.

Jizba's Shale Dataset

Jizba (PhD Thesis, 1991) reports petrophysical characterization of 88 tight gas sandstones, shaley sandstones and shales from Travis Peak Formation, East Texas. Permeability values reported by Jizba are Klinkenberg-corrected helium measurements at 15-28 MPa confining stress. Volume fraction of clay, as well as of quartz is estimated via point counting in thin sections. Based on the threshold value of clay content equal to 17%, Jizba separates TGS samples from shaley sandstones ($17<V_{clay}<38\%$) and shales ($V_{clay}>38\%$). Therefore, we will analyze properties of 11 samples that contain at least 17% clay by volume (Figure A.24). The effect of clay content on porosity and permeability of both shales and shaley sandstones is investigated in Figure A.25. Permeability values do not correlate to clay content; however, all shale samples ($V_{clay}>38\%$) show at least 2% lower porosity values compared to shaley sandstones of the similar permeability.

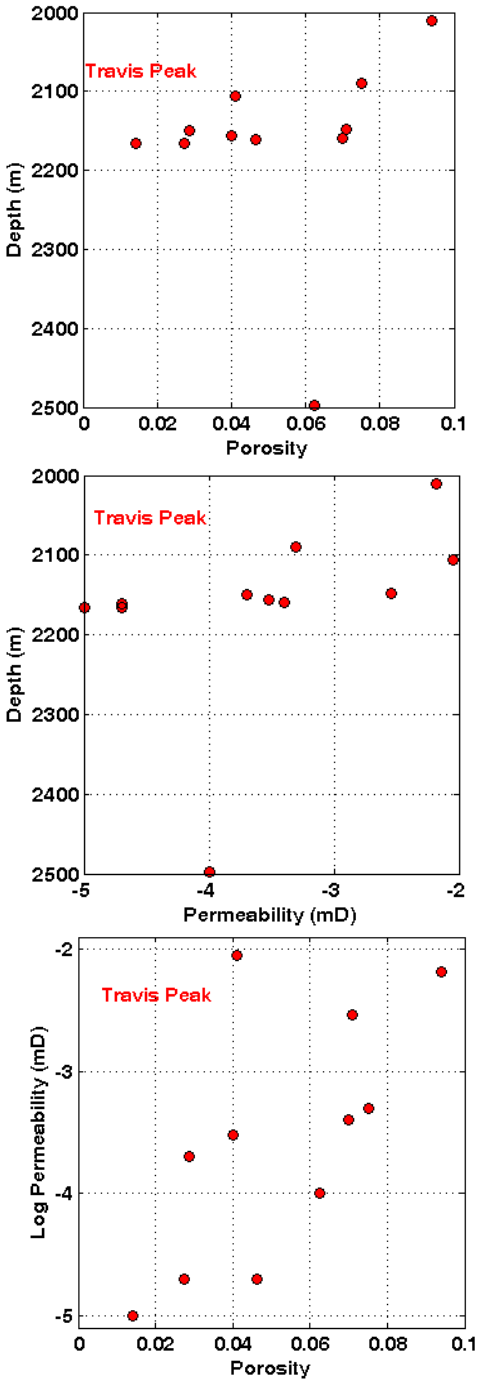

Figure A.24. East Texas shales and shaley sandstones data according to Jizba (1991). Left: Porosity as a function of depth. Middle: Permeability as a function of depth. Right: Permeability versus porosity. NOTE: decreasing permeability correlates with decreasing porosity.

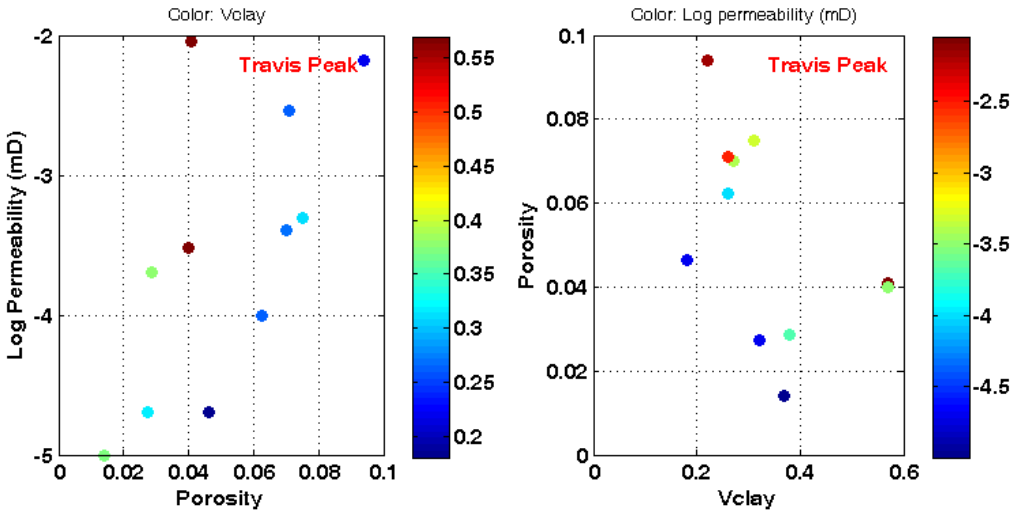

Figure A.25. East Texas data from Figure A.24. Left: Porosity versus permeability colorcoded by clay content. Right: Clay content versus porosity color coded by permeability.

Pathi's Shale Dataset

Pathi (2008) investigated the matrix permeability and rock-mechanical properties of Western Canadian Sedimentary Basin (WCSB) and Woodford shales. The matrix permeability was measured using a pulse-decay experiment. The pulse-decay experiment was employed via triaxial experiments combined with mercury porosimetry, helium pycnometry, Rock-Eval pyrolysis, SEM and X-ray diffraction analysis to measure rock strength, pore size, porosity, total organic content, fabric and composition of samples.

Higher permeability was observed in samples with high clay content, and low permeability was observed in samples with high quartz and carbonate content (Figure A.26). Porosity does not show correlation to permeability in the Western Canadian shales and within the Woodford shales. Even though calcite-rich Canadian shales and quartz-rich Woodford shales have high TOC content, TOC was not seen to affect permeability.

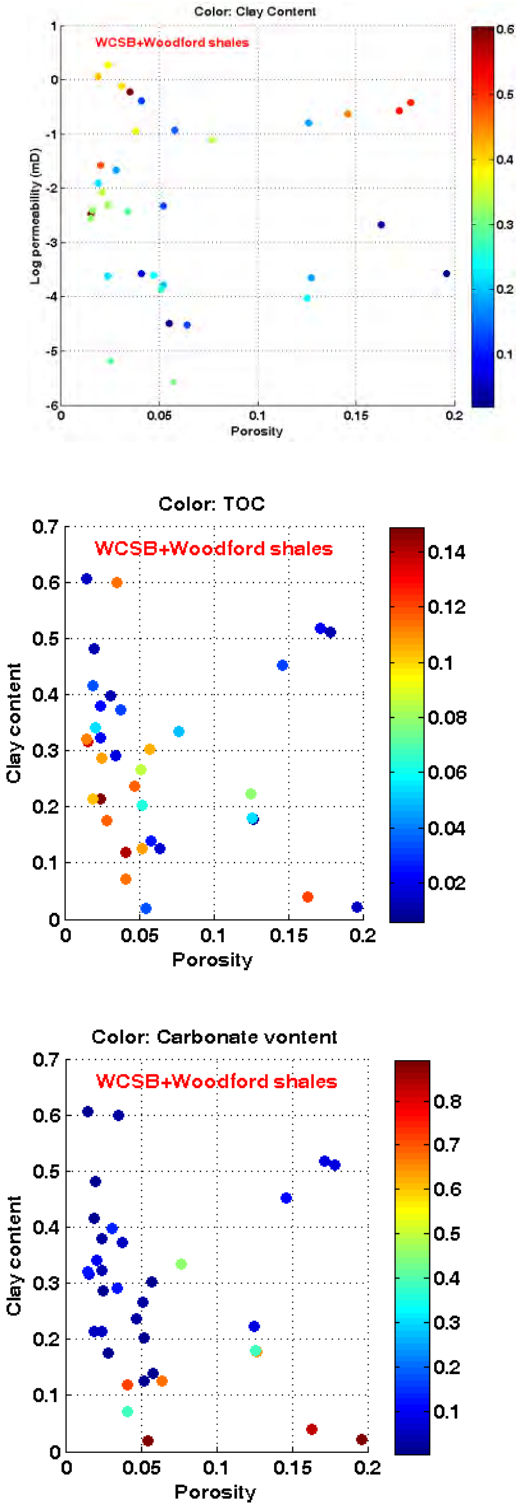

Figure A.26. Western Canada Sedimentary Basin and Woodford shale data according to Pathi (2008). Left: Permeability versus porosity colorcoded by clay content. Middle: Clay content versus pororsity colorcoded by TOC. Right: Clay content versus pororsity colorcoded by carbonate content.

Among the clay-, silica-, and calcite-rich Canadian shales, the calcite- and clay-rich shales had very low permeability (up to 10^{-6} mD) compared to siliceous shales (Figure A.27). The permeability of all shales declines exponentially with increasing effective stress.

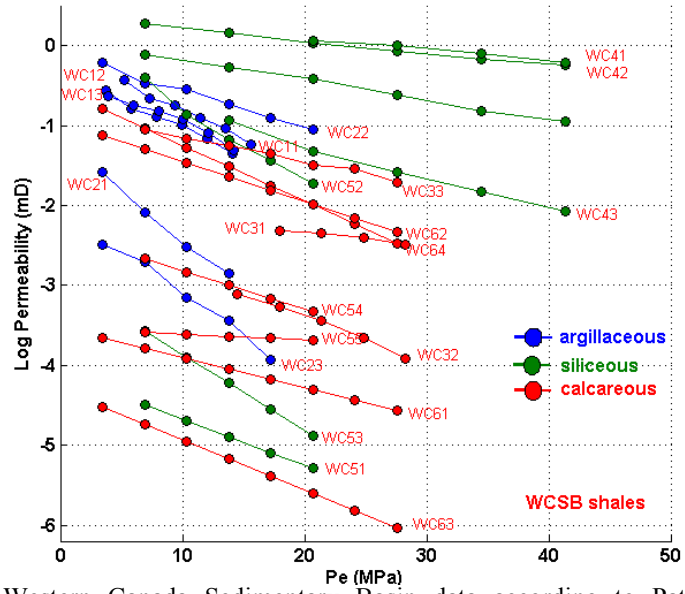

Figure A.27. Western Canada Sedimentary Basin data according to Pathi (2008). Permeability decrease as a function of effective stress for clay-, silica-, and carbonate-rich samples.

Woodford shales (Figure A.28) as well as Canadian shales had very low permeability (up to 10^{-7} mD). All but two samples (WS7 and WS11) exhibit a somewhat similar rate of decrease of permeability as a function of effective stress. Lithologically, samples WS7 and WS11 are following the general trend of minerals and their proportions present within other Woodford shale samples. However, it remains unclear whether drastic reduction of permeability in these samples is a result of preexisting fractures, or is purely a function of matrix permeability behavior.

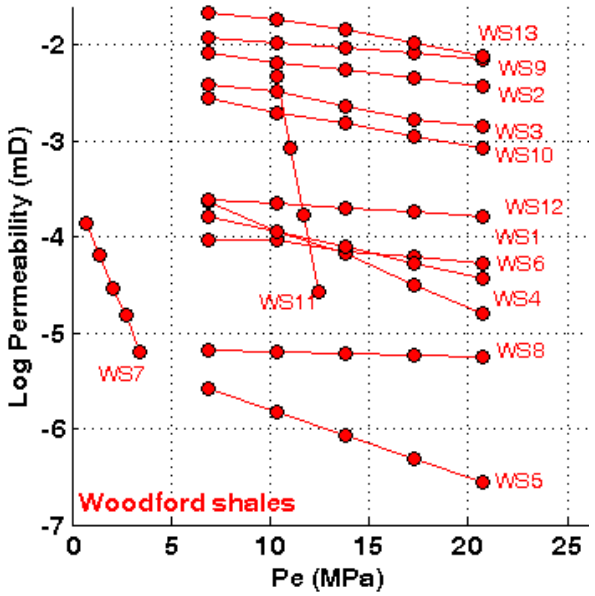

Figure A.28. Woodford shale data according to Pathi (2008). Permeability decrease as a function of effective stress. NOTE: all, but two (WS7 and WS11), samples exhibit somewhat similar rate of decrease of permeability.

Samples that were tested parallel to bedding (shown in red in Figure A.29) had higher permeabilities than samples tested normal to bedding (shown in blue in Figure A.29). Among WCSB shales, the quartz-rich shales showed differences of three to four orders of magnitude for the samples tested parallel to bedding, compared to those tested normal to

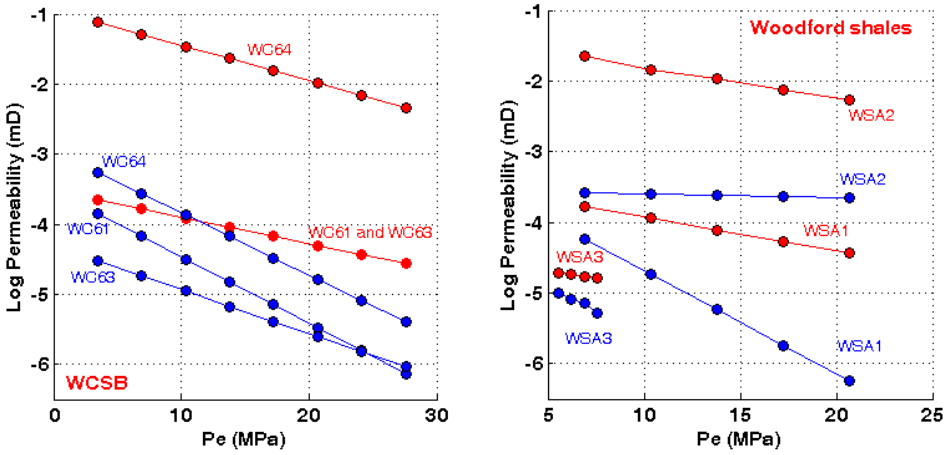

Figure A.29. WCSB and Woodford shale data according to Pathi (2008). Left: Permeability decrease as a function of effective stress for bed-normal (in blue) and bed-parallel (in red) direction. NOTE: for almost all samples, the difference of permeability in a given direction increases as a function of increasing effective stress.

the bedding. The largest anisotropy was found in the clay-rich samples. Clay-rich shales also have a well-developed fabric with a strongly preferred orientation, while the quartz-rich shales had random orientation of the fabric. To better understand permeability anisotropy, we display the ratio of horizontal (K_h) to vertical (K_v) permeability as a function of increasing effective pressure (Figure A.30). For WCSB shale sample WC64, the initial permeability anisotropy is larger than 100 (at P_e=4 MPa), reaching a value in excess of 1000 (at P_e=28 MPa). However, for the rest of the samples K_h/K_v varies between 1 and 100.

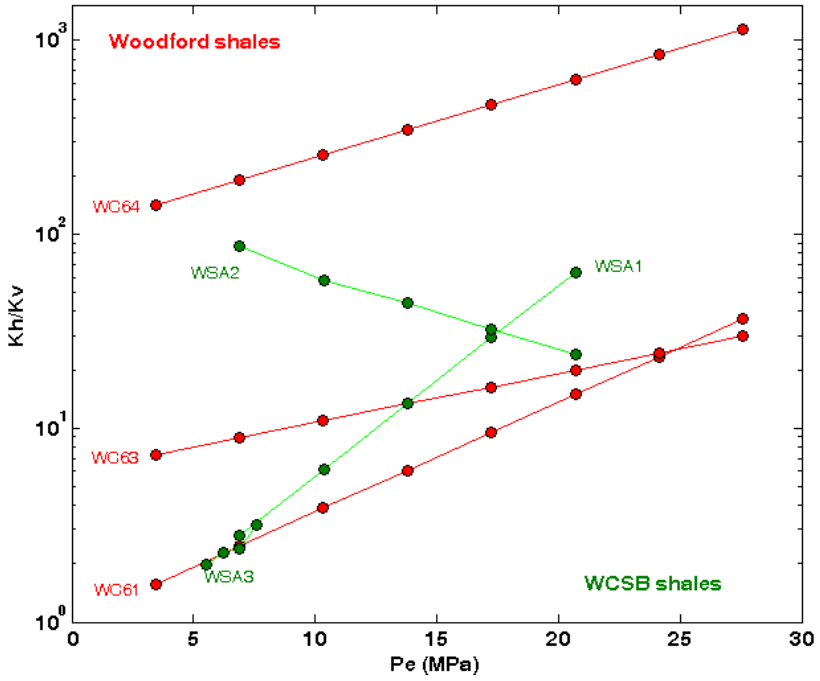

Figure A.30. Woodford shale data according to Pathi (2008). Permeability decrease as a function of effective stress. NOTE: all but two samples (WS7 and WS11) exhibit somewhat similar rate of decrease of permeability.

Yang and Aplin's Shale Dataset

Yang and Aplin (2007) present permeability and other petrophysical data (including pore-size distribution, porosity, particle-size distribution, grain density, specific surface area, total carbon content, organic carbon content, and sulfur content) for

30 deeply buried mudstones. Permeabilities were measured at different effective consolidation stresses ranging from 2.5 to 60 MPa with a 30,000 mg/L NaCl solution. Samples represent a wide spectrum of mudstone types with clay-sized particle (particles less than 2µm diameter) contents ranging from 13 to 66%. Porosities range from 6 to 27% (Figure A.31).

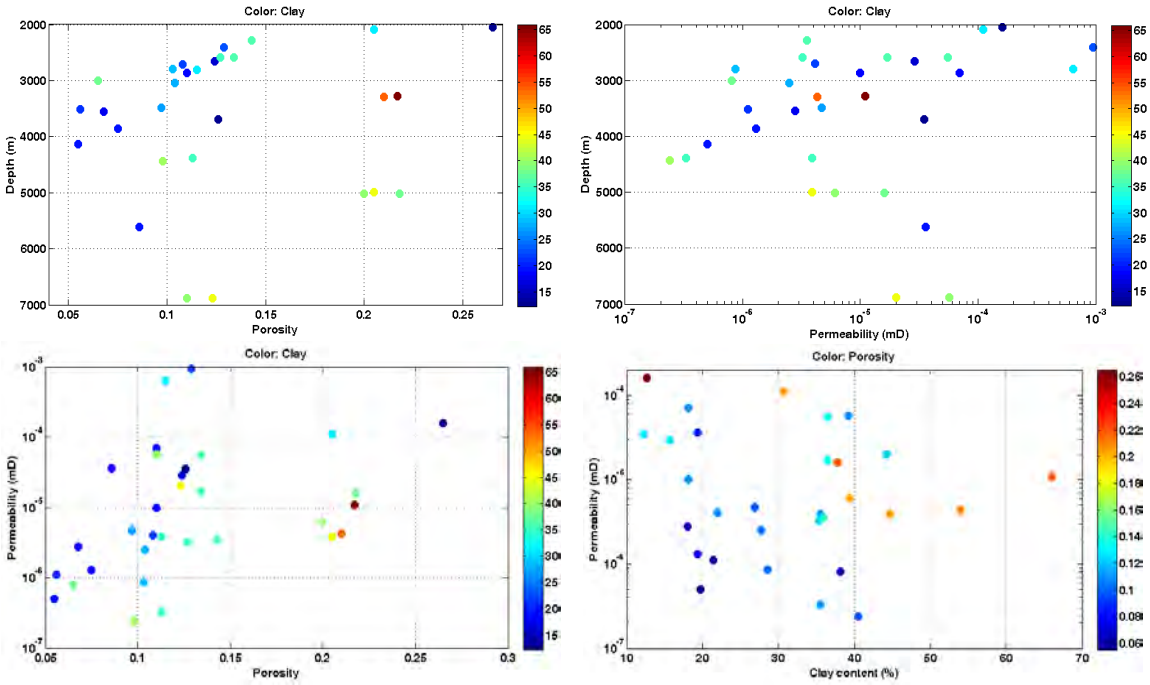

Figure A.31. Shale data according to Yang and Aplin (2007). Upper left: Porosity decrease as a function of depth, color-coded by clay content. Upper right: Permeability decrease as a function of depth, color-coded by clay content. Lower left: Permeability versus porosity, color-coded by clay content. Lower right: Permeability versus clay content color-coded by porosity. NOTE: high clay content samples have higher porosity.

Thirty core samples were selected by Yang and Aplin from 14 North Sea wells, 8 Gulf of Mexico wells, and 1 Caspian Sea well. All wells were at or close to maximum burial. The main sampling criterion was sample quality, since high-quality core material is a prerequisite for the accurate determination of very low permeabilities. Some samples had been recently cored and were wet, but many had dried as a result of storage. The permeability-porosity-depth-clay content cross-plots show a gradual decrease of both

porosity and permeability values, with some outliers at very high depth (~7km). Also, high-clay-content samples tend to have higher porosity.

Mesa Verde Group TGS Data

Byrnes et al. (2009) present a compilation of data from 88 publications by other authors, as well as their own measurements of porosity and permeability in several basins (Washakie, Uinta, Piceance, northern Greater Green River, Wind River, Powder River) of the Rocky Mountain region. TGS are estimated to be approximately 70% of the total TGS resource base and the Mesaverde Group sandstones represent the principal gas productive sandstone unit in the Western U.S.

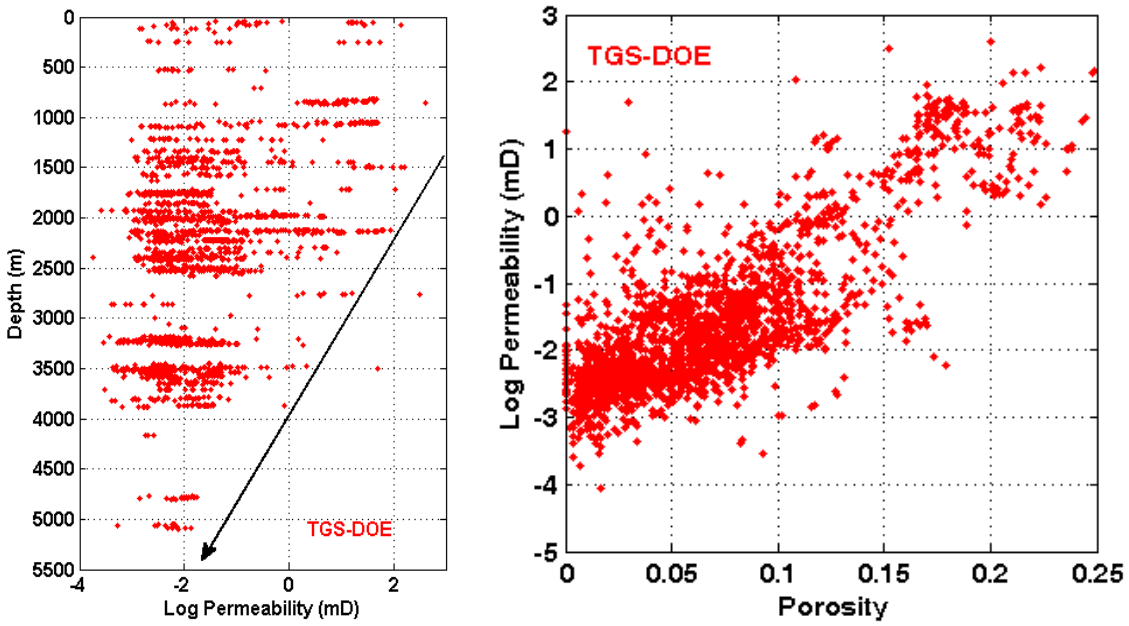

Figure A.32. Tight gas sandstone data from Mesa Verde group according to Byrnes et al. (2009). Left: Permeabilty decrease as a function of depth. Right: Permeability versus porosity. NOTE: strong porosity-permeability relationship.

Altogether, there are >2100 measurements in Mesa Verde Group (MVG) database (Figure A.32). Permeability values decrease to not more than 20μD at depth of 5km. A very strong relationship between porosity and permeability is observed. Low-porosity and TGS samples have higher permeability values than shale samples with corresponding

porosity described in previous datasets. We also note that most of the low-porosity, low-permeability TGS samples come from depth in excess of 2.5km (Figure A.33).

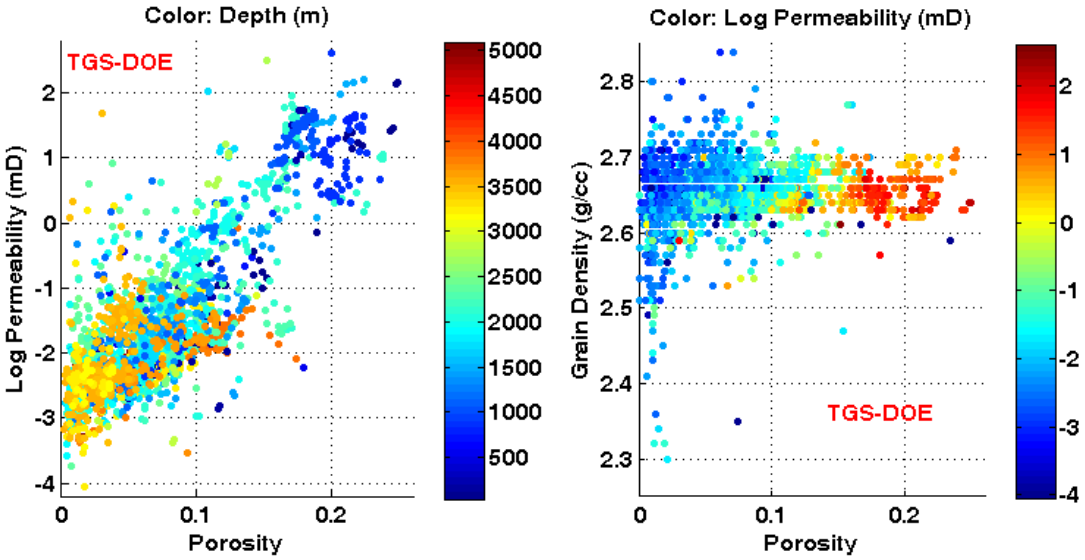

Figure A.33. Tight gas sandstone data from Mesa Verde group according to Byrnes et al. (2009). Left: Permeability versus porosity color-coded by clay content. Right: Grain density versus porosity color-coded by permeability. NOTE: most of the low-porosity, low-permeability TGS samples come from depth in excess of 2.5km.

Summary

We compiled published permeability data in shale and shaley sands and contrast these data to classical datasets, including Fontainebleau sandstone, North Sea sands, and tight gas sandstone laboratory measurements. As expected, shale permeability is much smaller than that in sands and sandstones (Figure A.34). Moreover, shale permeability is smaller than permeability in TGS (for low porosity samples). The main goal of this compilation was to serve as a look-up guide for assessing permeability in new plays as well as a quality-control tool for new physical and computational data.

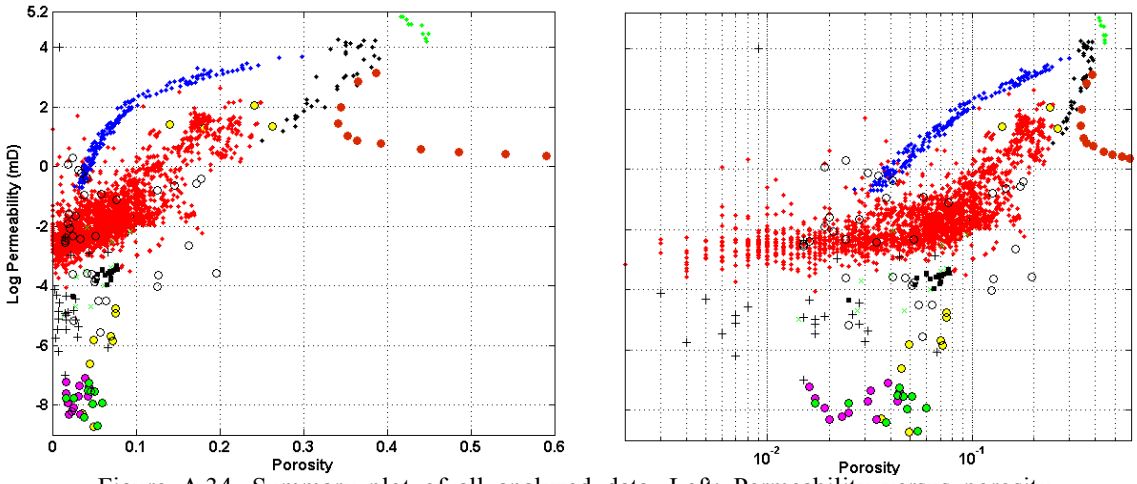

Figure A.34. Summary plot of all analyzed data. Left: Permeability versus porosity. Right: Same as left with porosity on log-scale. NOTE: Luffel's shale data (green and magentacircles) have at least 2 orders of magnitude lower permeability values than values reported by other authors.

References

Blangy, J.-P., 1992, Integrated seismic lithologic interpretation: The petrophysical basis, Ph.D. Thesis, Stanford University.

Bourbie, T., and Zinszner, B., 1985, Hydraulic and acoustic properties as a function of porosity in Fountainebleau sandstone: Journal of Geophysical Research, 90, 11, 524-532.

Bowers, G. L., and T. J. Katsube, 2002, The role of shale pore structure on the sensitivity of wire-line logs to overpressure, in A. Huffman and G. Bowers, eds., Pressure regimes in sedimentary basins and their prediction: AAPG Memoir, 76, 43–60.

Byrnes, P. A., Cluff R. M., and Webb, J. C., 2009, Analysis of Critical Permeability, Capillary and Electrical Properties for Mesaverde Tight Gas Sandstones from Western U.S. Basins: Final Scientific/Technical Report submitted to DOE and NETL, 355.

Estes, C.-A., 1996, Permeability of granular aggregates, M.S. Thesis, Stanford University.

Jizba, D., 1991, Mechanical and acoustical properties of sandstones and shales, PhD. thesis, Stanford University.

Katsube, T.J., 2000, Shale permeability and pore-structure evolution characteristics: Geological Survey of Canada, Current Research paper 2000-E15, 9.

Katsube, T.J., Issler, D. R., Loman, J., and Cox, W. C., 2000, Apparent formation factor and porosity variation with pressure for Cretaceous shale of the Western Canada Sedimentary basin, southern Alberta: Geological Survey of Canada, Current Research paper 2000-E6, 6.

Luffel, D.L., Hopkins, C.W., and Schettler, P.D., 1993, Matrix permeability measurement of gas productive shales: SPE Paper 26633, 261-270.

Nelson, P.H., 2009, Pore-throat sizes in sandstones, tight sandstones, and shales: AAPG Bulletin, 93, 529-540.

Pathi, V., 2008, Factors affecting the permeability of gas shales, Ph.D. Thesis, The university of British Columbia.

Sarker, R., Batzle, M., and Lu, N., 2009, Determination of fluid permeability and specific storage in tight rocks from 1-D diffusion induced constant rate fluid injection, SEG 2009 Expanded Abstracts, 1990-1993.

Schlomer S., and Krooss, B. M., 1997, Experimental characterisation of the hydrocarbon sealing efficiency of cap rocks: Marine and Petroleum Geology, 14, 5, 565-580.

Soeder, D.J., 1988, Porosity and permeability of Eastern Devonian gas shale, SPE Formation Evaluation, March 1988, 116-124 (SPE paper 15213).

Strandeness, S., 1993, Personal communication.

Walls, J., 1982, Effects of pore pressure, confining pressure, and partial saturation on permeability of sandstones, Ph.D. thesis, Stanford University.

Yale, D., 1984, Network modeling of flow, storage, and deformation in porous rocks, Ph.D. thesis, Stanford University.

Yang, Y., and A. C. Aplin (2007), Permeability and petrophysical properties of 30 natural mudstones, J. Geophys. Res., 112, B03206, doi:10.1029/2005JB0042433

Yin, H., 1992, Acoustic velocity and attenuation of rocks: Isotropy, intrinsic anisotropy, and stress induced anisotropy, Ph.D. thesis, Stanford University.